PHYSICS AREA,
THEORY AND NUMERICAL SIMULATION OF CONDENSED MATTER

Friction, tribology and rheology at the atomic scale: from metal nanocontacts to 2D materials and graphene

PhD Thesis

Candidate: Ali Khosravi

Supervisors:
prof. Erio Tosatti
dott. Andrea Vanossi
prof. Giuseppe Santoro

Trieste, November 2023

Contents

Preface

This PhD Thesis comprises quite a vast collection of research activities aiming at addressing curious and unexplained questions, usually inspired by state-of-the-art experiments, in the field of nanotribology and rheology. The thesis divides in three parts and several chapters, each of which focusing on specific themes.

Shortly, in the first part, rheology and nano-mechanics of gold nanocontacts, are explored. Friction and mechanical properties of layered material are presented in part II. Lastly, the third part is a short miscellaneous project on ring population statistics in an ice lattice model. Here, we briefly provide a preface introduction to each part.

Part I: Nanomechanics

Down to the micrometre scale and below, solid metallic materials behave mechanically quite differently from their macroscopic equivalents. when their size is lowered to the micrometre range and below. A higher surface-to-volume ratio, making more surface free energy [1, 2] available for mechanical deformation, results in a fundamentally different behaviour for submicro and nano-sized bodies and contacts. Experimentalists create gold nanojunctions by stretching metallic wires down to the atomic level. They have been known to have an intrinsic string tension, causing under certain conditions the atomic chains to braid up and form magic nanowires when the thickness is very small [1, 2]. The additional fact that the ballistic electrical conductivity of a nanocontact is naturally quantized, makes them the subject of extensive research [3, 4].

The motivation of this part of the thesis is provided by two interesting experiments. First[5], a tuning-fork-based atomic force microscope (TF-AFM) measured the dynamical module of a few-atom thin (average cross sections of N$\approx$ 3 to 20 atoms) gold nanocontact. Their observation gave a surprisingly negative value for stiffness. Second[6], a TEM image of thicker silver nanocontact (starting from N$\approx$ 100) supported by subsequent molecular dynamics simulations [7] demonstrated the plastic stretching and breaking mechanism of such nanocontacts under lateral shearing. Our scope is, first to understand and explain the physics behind these observations, and second to see if possible to come up with new suggestions and predictions for future experiments to help us understand that how rheological properties like negative stiffness may affect the shearing habit of mechanically oscillated solid metal-metal contacts. The baffling large amplitude rheological properties of gold nanocontacts and its shearing consequences should apply, with different parameters, to other ductile metals and in the long run to the dry friction of rough metal-metal mesoscopic and macroscopic contact interfaces.

- Understanding negative stiffness $\rightarrow$ Chapter 1

Negative stiffness in the recent experiments by Comtet et al.[5] on solid gold nano-junctions implied a strange apparent liquefaction under oscillatory strain, completely unanticipated at ambient temperature. In this first chapter, we theoretically demonstrate that even under significant oscillatory strains, realistically generated nanocontacts truly maintain their crystalline structure. Even in rapid oscillatory cycles, tensile and compressive slips of the "necking" and "bellying" types, respectively, do occur, but they recover reversibly. A feature that is unique to nano-sized contacts.

We also show that, counter-intuitively, the residual stress remains tensile after both slips, driving the averaged stiffness from positive to negative, thus superficially mimicking that of a liquid. However, unlike a liquid, rheological softening occurs by stick-slip, predicting largely frequency independent stiffness with violent noise in stress and conductance, properties compatible with experiments.

- How does negative stiffness affect shearing $\rightarrow$ Chapter 2

The way metal interfaces evolve during frictional sliding, and how that evolution can be externally influenced are important questions, yet hard to assess experimentally because contacts are buried and generally inaccessible.

Here we focus on an elementary constituent of a general metal-metal interface, namely an ultrathin individual nanocontact.

In the preceding chapter, we have thus shown a significant rheological softening in mechanical stiffness, when an oscillating tensile force, or torque is present. Here, we conduct realistic nonequilibrium molecular dynamics simulations aimed at detecting to what extent such mechanical oscillations might influence the shearing habit of gold nanocontacts at room temperature. It is found that the shearing evolution is indeed modified with a clear rheological softening introduced by the oscillations. That friction softening however is not quite as strong as, e.g., the thermolubric effect of temperature. Differences emerge for different types of oscillation, but the discrete sudden stick-slip-like advancements connected with the underlying lattice do persist, at least at the shearing velocities and oscillation frequency within simulation reach. The rheological softening that we address is different and should not be mistaken with the usual thermolubricty. The relevance of these results for future experiments will be discussed.

Part II: Layered materials

The study of friction in layered materials, is a emerging field within physics, bridging fundamental principles to real-world applications. Experimental labs has almost always been the origin of important physical discoveries, nevertheless understanding and interpreting the outcomes of experiments is equally a matter of importance. Theoretical approaches such as the Prandtl-Tomlinson (PT) and the Frenkel-Kontorova (FK) model, together with non-equilibrium molecular dynamic (NEMD) simulations are well-suited tools to provide insight into the microscopic origins of friction, offering a deep understanding of the intimate mechanisms at play in materials tribology. Although our interest remains fundamental and academic, such knowledge has direct impact for the design and performance of engineering systems, from nanotechnology to macroscopic machinery, and contributes to the development of advanced lubricants and coatings, enhancing energy efficiency and reducing wear in mechanical systems.

Among layered materials, graphene is unique due to its exceptional mechanical and electrical properties. Its ease of experimental manipulation permits precise fabrication, such as, clamping on sides, growing on easily accessible SiC, and twisted bilayer graphene (TBG). Relative twist angle of two graphene layers, via interface moiré pattern, leads not only to tunable friction, but also to exceptionally interesting electronic properties in TBG, such as the emergence of flat bands at magic angles, offering fertile ground for fundamental research and potential technological applications.
Friction of graphene itself –when used as a slider island or a substrate beneath an AFM tip–, depends on various factors such as: contact area, temperature, sliding velocity, normal load, its commensuration rate with substrate –e.g. twist angle, lattice mismatch–, and clamping and pre-straining layers, et.c.
From all above, we quickly review a few ideas from our colloquium [8] in the brief chapter 3 that are pertinent to this thesis: velocity, temperature, and load dependence of friction. More in the second part of the thesis, we will focus on friction, and other physical properties, of single and/or multi-layer graphene, mimicking two distinct experimental setups, and one theoretical prediction:

- Supported and quasi freestanding graphene → Chapter 4

The research here, has been done in collaboration with the experimental group of prof. Elisa Riedo (NYU). Their experiments [9] measure the hardly accessible interfacial transverse shear modulus of an atomic layer on a substrate. By performing measurements on bulk graphite, and on epitaxial graphene films on SiC with different stacking orders and twisting, as well as in the presence of intercalated hydrogen, we find that the interfacial transverse shear modulus is critically controlled by the stacking order and the atomic layer-substrate interaction. Importantly, we demonstrate that this modulus is a pivotal measurable property to control and predict sliding friction in supported layered materials. The experiments demonstrate a reciprocal relationship between friction force per unit contact area and interfacial shear modulus. Simple 1D sliding friction models that demonstrate how the atomic layer-substrate interaction regulates the shear stiffness and, consequently, the friction dissipation can be used to explain these results. This image fully explains the experimental friction results by taking into account only the shear stiffness resulting from a specific layer-substrate interaction. Other effects, like puckering or electron-phonon dissipation, are not required. These findings provide a method for regulating strain fields and atomic sliding friction for use in band-structure engineering and photonics applications.

- Free standing graphene but supported sides → Chapter 5

Rheological phenomena including indentation, twisting, and wrinkling in deposited and suspended graphene are actively investigated to unravel the mechanical laws at the nanoscale. Most studies focused on isotropic setups, while realistic graphene membranes are often subject to strongly anisotropic constraints, with important consequences for the rheology, strain, indentation, and friction in engineering conditions. Graphene in particular is recognized as the thinnest solid lubricant material and a large amount of work has been dedicated to understand the fundamentals mechanisms of its effectiveness and to unravel parameters relevant to its technological development. Here, experiments performed by our colleagues at University of Modena [10], show how graphene's frictional response to an external indenter is severely altered by conditions of anisotropic suspension, specifically when freestanding graphene is clamped across a long and narrow groove. Results show that the friction coefficient is significant when the tip is sliding parallel to the groove while becoming ultralow in the orthogonal direction. The experimental data suggest that–rather unexpectedly–prestrain of the graphene sheet as a result of clamping is negligible, the key to understand the underlying mechanism is provided by simulations. The paramount mechanism is provided by the extra anisotropic strain induced from indentation under anisotropic constraints, which in turn produces an anisotropic stiffening of the graphene.

- Completely free standing twisted bilayer graphene → Chapter 6

Twisted bilayer graphene (TBG), stands out for its exceptional electronic characteristics at the magic twist angle. While most experimental bilayers are studied in deposited/encapsulated configurations, where the twist-related moiré pattern has no mechanical impact, TBG can also exist in a freestanding form. Here, via simulations and theoretical investigation, we show how, below a critical twist angle $\theta_c \sim 3.7°$, freestanding TBG exhibits an unexpected moiré (2×1) buckling distortion at $T = 0$, leading to the unforeseen collapse of its macroscopic bending rigidity. Moreover, its electronic properties reveal intriguing behavior, with eight narrow bands at the magic twist angle remaining degenerate at zone boundaries, driven by effective single-valley physics. These structural, critical, and electronic findings make freestanding TBG an especially captivating area of research. Our findings in this chapter only offer an understanding of freestanding TBG itself, from mechanical and electronic point of view. Devoid of any external driving force, since studying friction for a freestanding buckled structure is a delicate subject.

While our explicit focus has been on the prototypical case of graphene, many considered experimental protocols and uncovered physical mechanisms (via modeling and simulations) illustrated in this thesis, can be generalized to other 2D membrane-like layered materials as well.

Part III: Other Theoretical Problems

- Ring population statistics in an ice lattice model → Chapter 7

Ordinary ice has a proton-disordered phase which is kinetically metastable, unable to reach, spontaneously, the ferroelectric (FE) ground state at low temperature where a residual Pauling entropy persists. Upon light doping with KOH impurities at low temperature, each molecule nucleates the transition to FE ice with a peculiar kinetic mechanism, recently addressed [11] in a lattice model where the so-called "ice rules" – no less and no more than two hydrogens per oxygen – are enforced. The impurity-driven nucleation process involves the transition of disordered proton rings into ordered rings, making the nucleation efficiency dependent upon the probability distribution of various type of disordered rings. That distribution had been demonstrated by a replica-exchange MC sampling, [11] but no theory had been provided.

We calculate the probability distribution of hexagonal 6-site rings in the disordered state of cubic and hexagonal ice in the same lattice model. The mean-field distribution obtained is in significant agreement with those, slightly different among them, obtained by Monte Carlo simulations. Results are discussed in connection with the equilibrium and non-equilibrium transition from disorder to ferroelectric proton order.

My contribution; disclaimer

Since this thesis comes as a collection of research papers, either published or draft, therefore all contributions is referred to by "We". However I would like to clarify:

- I implemented and carried out the numerical simulations for chapters 1 and 2, and contributed to the theoretical understandings;
- chapter 3 is a short introduction to our collaborative colloquium, to which I contributed by way of general comprehension, discussions, and presenting information;
- I have not performed any of the experiments for this thesis, my contribution in chapters 4 and 5 remains to only performing simulations and contributing to overall theoretical understanding of results;
- in chapter 6 my contribution falls mainly in the second section, electronic structure, and overall understanding of the results. Appendix A contains the home-made code (`LTB+Symm`) for this purpose;
- in chapter 7, my contribution is in the mean-field statistical counting.

Part I

Nanomechanics

Chapter 1

Metallic Nanocontact Rheology

1.1 Introduction

The moment two bodies touch, however gently, they do that first through bridging nanoasperities with possible formation of tiny solid junctions, necks, or nanowires, especially in metals. The ability of nanocontacts in realistic room temperature and vibration-rich conditions to transmit, as it were, mechanical rigidity, represents an issue which, even if delicate and important to basic physics, nanoengineering, and even everyday life, has received insufficient attention. Building on historically important work [12] prototype metallic nanocontacts [13, 14], formed and studied by break junctions, scanning tunneling microscopes (STMs) [15, 16], transmission electron microscopes [17–20] or cold welding [21], have been investigated in past decades through conductance, force measurements and simulations, mostly at low temperatures [13, 14, 22] or other non-standard conditions [17–20]. Even if thermodynamically metastable against spontaneous thinning and eventual breaking [1, 2], metal nanocontacts can be engineered and mechanically controlled to last long enough to be electrically and magnetically characterized by gate and bias voltages. Their realistic room temperature rheology, however, is an open chapter. Because of short lifetimes associated with nanometric structures and the facile changes they can undergo at ordinary temperature, addressing their non-equilibrium rheological properties requires investigations that go beyond the static and cryogenic conditions of most prototype studies.

In their pioneering experimental exploration of oscillatory stress-strain response of ultra-narrow gold nanojunctions, Comtet et al. [5] showed that after the initial small strain (0-5%) elastic response, regular plastic yield occurs first, as expected, around 6-7% strain. Recent work by Liu et al. [23] extended that work to larger cross sections, confirming that with an initially crystalline atomic arrangement inside the nanojunctions, their plastic yield is reasonably attributed to strain-driven slip planes as in macroscopic systems [13, 24, 25]. However, for larger oscillation amplitudes and atomically thin nanocontacts – with conductances $g \approx 3 - 30 g_0$ where $g_0 = 2e^2/h$ – Ref [5] found a further dramatic softening suggestive of apparent liquefaction. The contact effective stiffness with oscillation amplitude above ≈ 0.15 nm drifted from positive to negative, as would befit a gradually melted nanojunction. How and why large dynamic strains – at room temperature but with mechanical heating totally excluded – could usher in the liquefaction of metal nanoasperities is quite puzzling, requiring a more fundamental understanding of their rheology. Besides the conceptual aspects, if indeed a strongly shaken ordinary metal-metal contact were to consist of myriads of liquefied nanonecks rather than of solid junctions, that would hardly be irrelevant to a host of technological issues.

We theoretically investigate here how, at room temperature, a mechanical perturbation such as a vibration, commonplace in many technological applications, will affect and determine the detailed rheological behavior of contacts including stiffness, dissipation and yielding under large time-dependent, e.g., oscillatory stresses and strains. Straight theory is ill equipped to confront this puzzle, owing to both its violently non-equilibrium nature, and its nanometer size scale. It is therefore fortunate that exactly these two features make it directly amenable to non-equilibrium molecular dynamics (NEMD) simulation, which, as we will show, points to an explanation which is different from liquefaction.

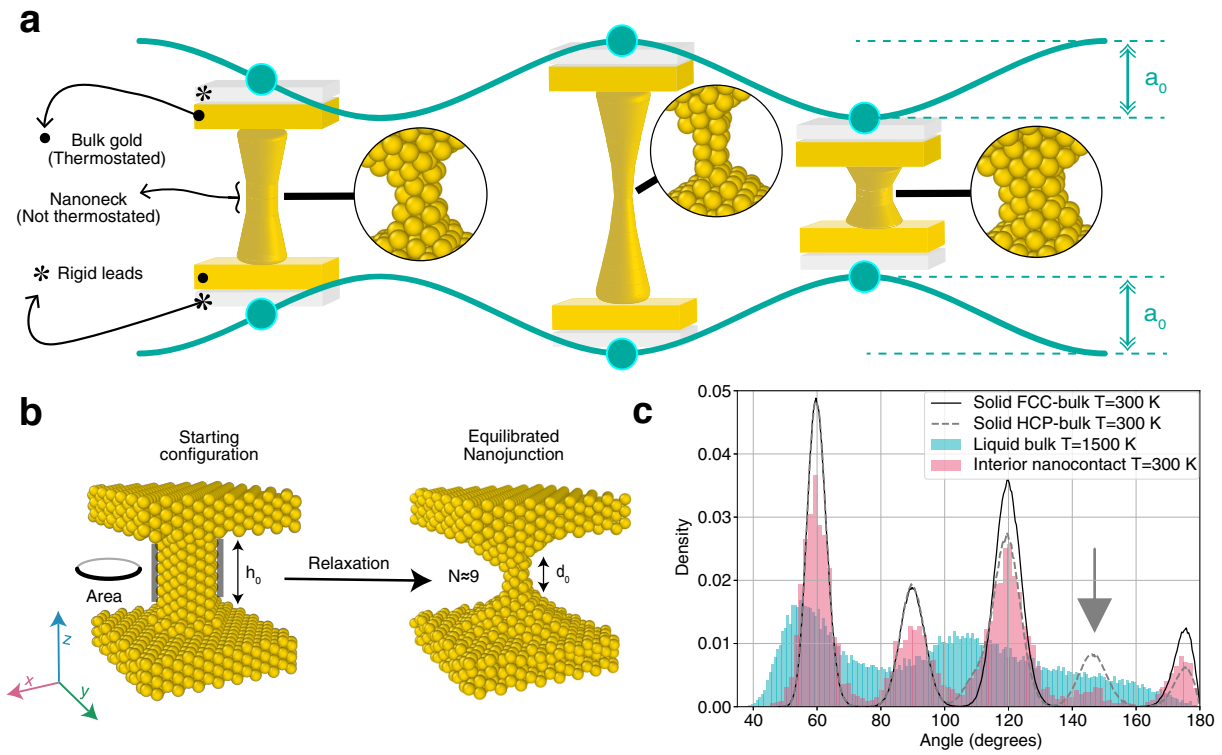

Figure 1.1: Simulated rheology of an oscillating solid metal nanocontact. **a** Sketch of a gold nanojunction under oscillatory strain, exerted through crystalline leads at room temperature. **b** Snapshots of a nanocontact ($N \approx 9$ atom cross section) of initial crystalline columnar shape (left) and quasi-equilibrium working shape obtained after extended structural relaxation (right). Note the anvil-like tips formed on both sides of the effective nanojunction's neck reducing its effective length from h_0 to d_0. **c** Three-body angular distribution of inner core atoms of the relaxed junction measured during ≈ 10 strained cycles at the largest oscillatory amplitude (0.22 nm). The main peaks confirm the survival of fcc structure and coordination of the nanocontact core. The small structure around 147° (arrow) is a signature of the (111) slips.

1.2 Results

We simulated gold nanocontacts suspended between two bulk-like crystalline leads (Fig. 1.1a) whose distance is oscillated as $h(t) = h_0 + a_0 \exp(i\omega t)$, and read the force time evolution (Fig. 1.2) to analyse the mechanical response of a family of nanometer radius model gold junctions, under increasing engineering strain amplitude $\epsilon_0 = a_0/h_0$ (conveniently used, although different from true strain $\epsilon_t = a_0/d_0$ where $d_0 < h_0$ is an effective nanojunction length to be discussed later). All simulations were based on the well documented and reliable force field of Ref.[26]. We focused on initially bulk-structure columnar junctions bridging between two large solid leads, in our case $h_0 \approx 2.75$ nm apart. The initial junction transverse cross section ranged from $N_i = 7 - 40$.

The first important step was to establish a realistic nanojunction shape and inner structure. Both are generally unknown experimentally, and expected to evolve in the course of time [1, 2] with shape evolution routes which depend experimentally on temperature and formation protocols [5, 15–17, 19, 20, 27], and theoretically also on the precise form of interatomic interactions [14, 26, 28–31]. In experimental protocols such as that of Ref. [5], the unknown nanojunction morphology is, through feedback-actuated preservation of a constant average electronic conductance, periodically stabilized to a roughly constant average cross section area of its narrowest neck. Our simulation protocol started with vigorous initial mechanical oscillations and thermal cycling that transformed the initial idealized column into a modified, relaxed, and reproducible structure that did not further evolve within our subsequent working time. That structure, now consisting of a shorter neck-like nanojunction between spontaneously formed anvil-shaped "tips" survived quasi-stable at room temperature and under further oscillations always comprising no less than 10-20 cycles, with amplitudes up to 0.3 nm. Thus no feedback adjustment was required. The nanojunction retained a well defined minimal midpoint cross section (Fig. 1.1b,

right) of area $A \approx N\pi r_0^2$, where $r_0 \approx 0.144$ nm is the atomic radius and $N \approx 4-26$ the atom number inside that cross section – more precisely the number of (110) z-oriented atomic chains crossing that section. In this relaxed configuration, the proper nanojunction length had shrunk from $h_0 \approx 2.75$ nm to a smaller value $d_0 \approx 1$ nm –now excluding the anvils. The relaxed anvil-nanojunction-anvil shape of the overall contact is not specific to any chosen initial h_0; it just took a shorter relaxation time to realize it for the smallest reasonable lead-lead distance, which we therefore adopted.

The protocol proceeded by submitting the thus relaxed nanojunctions to oscillatory strains with frequencies $\omega/2\pi$ spanning three decades 10 MHz-10 GHz. Values which, even if much larger, still as we shall see extrapolate naturally down to experimental frequencies such as 31 KHz (see Fig. 1.3). Preliminary to describing the force results of the simulations, however, the inner atomic structure of the nanojunction and its core is a crucial question to be ascertained. That structure could remain simply fcc crystalline in the first place. It could be glassy – an appealing possibility because glasses are known to liquefy easily under oscillatory strains [32]. Or perhaps the thinnest nanonecks could even possess one of the helically incommensurate coaxial nanotube structures discovered in TEM [17, 19] and theoretically explained [1] by "magic" string tension minima that arise in the course of spontaneous thinning. Alas, all glassy and helical nanojunction structures which were tried did not survive even for the very first few simulation steps. The latter hypotheses should therefore be discarded.

Direct inspection of both the non-oscillating and oscillating nanojunction interiors in the relaxed structure, actually showed them to be approximately crystalline. The signature is provided by the first-neighbour three-body angular correlation function $\rho(\theta)$ of the interior atoms in the central nanoneck portion, defined by carefully excluding atoms in both the tip anvils and the outer nanojunction surface layer, the latter more mobile than the rest. If the nanojunction interior atoms possessed fcc crystalline coordination, $\rho(\theta)$ should show three peaks at 60°, 90°, and 120°; if liquid or glassy, only 60° and 120°; if magic, the pattern should be much more complex owing to incommensurability [1]. The result, shown in Fig. 1.1c shows a clear 60°, 90°, 120° peak sequence, confirming that the inner core of the simulated nanojunction is and remains close to fcc solid throughout, despite room temperature and violent oscillatory shaking. In addition, the presence in the strongly shaken nanowire of a shoulder around 147°, signals ABC to ABA local sliding of (111) planes during the oscillation, to be discussed below and reminiscent of the yielding patterns proposed in experiments [5, 23].

1.3 Reversible yielding

The structure evolution under oscillating strain showed up clearly in the simulation geometry, pictured in Fig. 1.1a, and in Additional Fig. 1.9. As tensile strain amplitude grew, the solid and largely crystalline nanojunction first yielded with a necking local interplane ABC-ABA slip – also causing some thinning. The necking slip took place once the tensile elongation exceeded ≈ 0.16 nm, which is close to $l/(2\sqrt{2}) = 0.144$ nm, half of gold's {110} spacing (the direction of oscillation), where $l = 0.408$ nm is the bulk lattice constant. With some hysteresis, the necking however reversed on the way back, a fast stick-slip-like event made possible on the fly by the subnanometer thickness and by room temperature. In the second half of the cycle, where compression exceeded about the same magnitude in reverse, the nanojunction yielded backwards with an inverse necking, which we dub "bellying", for it is accompanied by a noticeable nanojunction thickening. Again with some hysteresis, bellying finally reversed in the last part of the cycle, the junction returning to its initial state. This simulated behaviour, whose consequences will also be discussed and pictured later in Fig. 1.4, exemplifies how reversible plastic deformation kinetics may emerge as a feature in nanocontacts of metals that are, at their working temperature, sufficiently ductile and sufficiently thin. Similar events were earlier reported in the MD simulations of the Au/Ni system by Landman et al. [33] using EAM potentials. Qualitatively analogous results were also shown by Sutton and Pethica [34] using a Lennard–Jones pair potential. Even in the bulk crystal, a large (110) uniaxial strain favors hcp relative to fcc, and the local sliding associated with the nanojunction yielding transforms local ABC stacking to ABA. (see Additional Fig. 1.9)

1.4 Dynamical force and response function

The structural evolution described underpins the main dynamical output of nanojunctions which we extracted from the oscillatory simulations, that is the instantaneous force $F(t)$ between the leads. Typical NEMD force time evolution at $\omega/2\pi = 50$ MHz are presented in Fig. 1.2 for increasing oscillation amplitudes a_0, for a

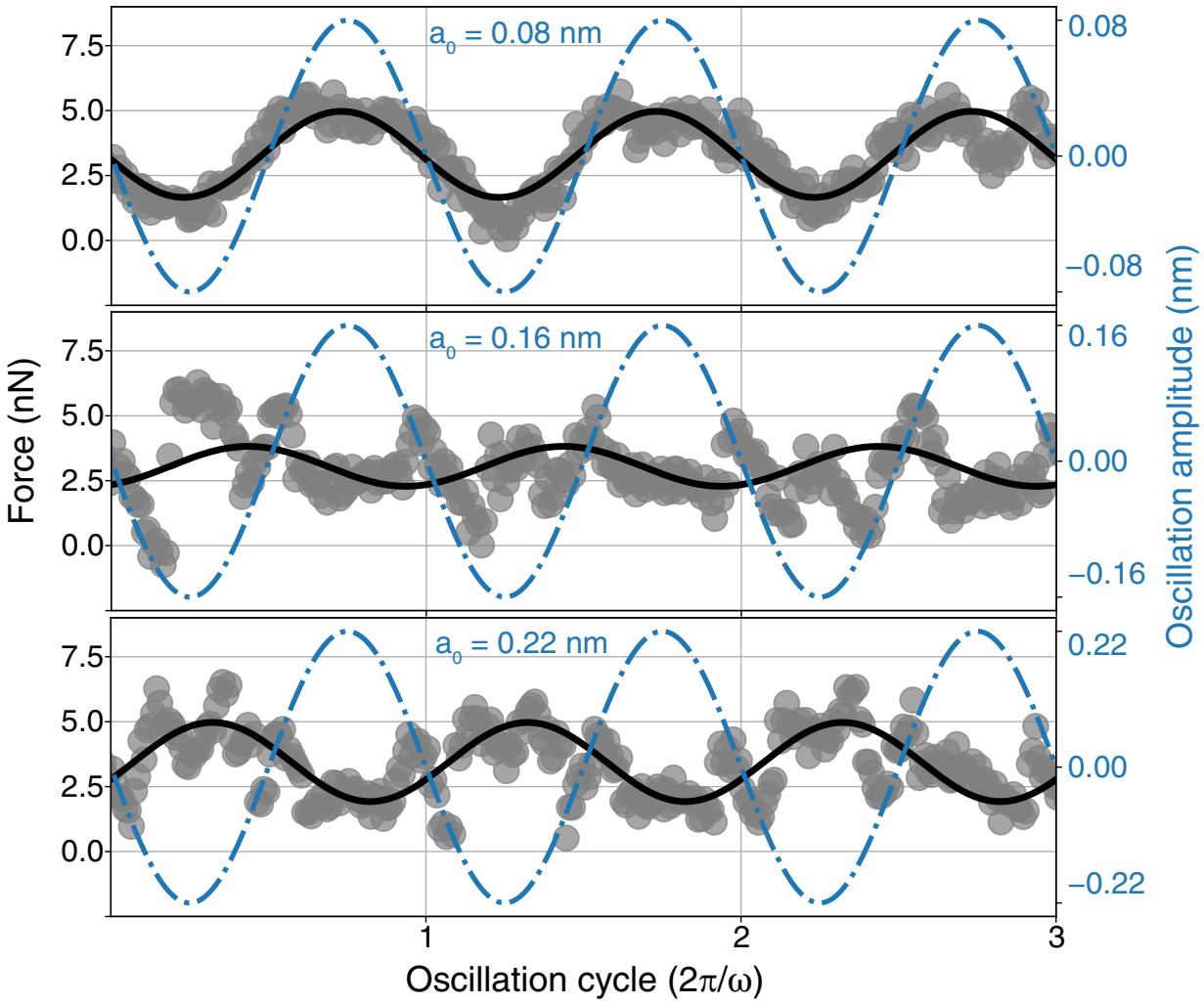

Figure 1.2: Force time evolution under oscillating strain Time dependent force results for the $N \approx 9$ nanojunction of Fig. 1.1b with equilibrated shape, initial $h_0 \approx 2.75$ nm, relaxed neck length $d_0 \approx 1$ nm, average neck cross section area $A \approx 0.6$ nm^2, oscillation frequency 50 MHz, $T = 300$ K. Blue dashed-dotted line: imposed lead-lead oscillating amplitude $a(t)$. Large grey dots: extracted instantaneous force between the leads. Black solid line: sinusoidal fit $F(t) = F_0 + (A\sigma_0)\exp(i\omega t + i\phi)$ of the force. The fit parameter $A\sigma_0$ is the resulting force magnitude. Note the change of rheological response with drastic increase of non-sinusoidal noise at and above $a_0^* \approx 0.16$ nm. Note also the prevalence of tensile (positive) force for all strains (see text). The same plot for the largest size of $N \approx 26$ is shown on Additional Fig. 1.5

nanojunction with relaxed central cross section $N \approx 9$, chosen as the clearest showcase among all cases studied in the range $N \approx 4-26$ (see Additional Fig. 1.5 for the largest thickness). At small amplitudes, the mechanical response was essentially elastic – except for some residual fluctuations (possibly connected with the force field's weak fcc-hcp energy difference [35]) – characterized by a nearly sinusoidal force, and weak phase shift with strain, and thus negligible dissipation. At mechanical yielding, which began rather sharply at a threshold amplitude $a_0^* \approx 0.16$ nm, the force turned noisier (see Additional Fig. 1.7), with sudden jumps associated with the structural interplanar sliding, either necking or bellying, taking place at one point in the nanojunction. From the force, the (conventional) stress magnitude σ_0 was obtained by fitting $F(t)$ in the form $F_0 + \sigma_0 A \exp(i\omega t + i\phi)$ where F_0 represents a background tensile force (string tension) between the leads at zero strain, ϕ the phase shift between the imposed oscillatory strain and the force component of same frequency, and A the narrowest cross section area of the relaxed strain-free nanojunction. The force fit (least squares, same frequency as the

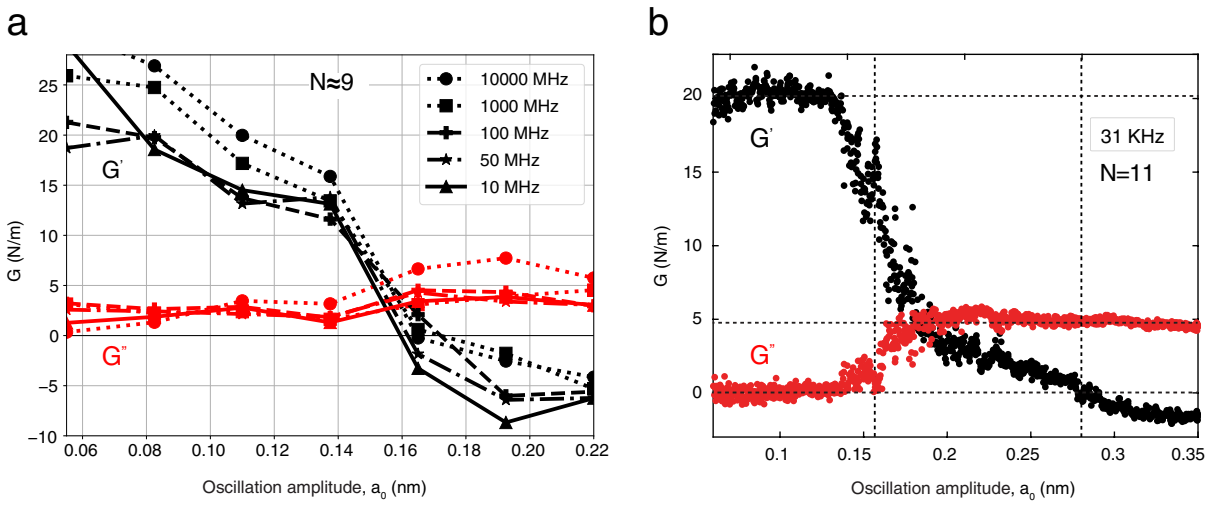

Figure 1.3: Complex dynamical response function. **a** Effective stiffness G' and dissipation G'' at three decades of frequency 10 MHz-10 GHz for a $N \approx 9$-atom cross section nanojunction. Similar results are obtained for different sizes and frequencies (see Additional Fig. 1.6 for the largest size of $N \approx 26$). **b** Experimental data for $N = 11$ at 31 KHz reproduced from [5]. Note the good overall agreement, parameter-free. For lower frequency data at 1 MHz close to simulation limit, see Additional Fig. 1.12

forcing, amplitude and phase as parameters) is not an arbitrary choice, but a mandatory protocol required to extract the same linear response function measured experimentally.

The extracted stress magnitude and phase lead to the complex dynamical rigidity $G = G' + iG'' = (\sigma_0 A/a_0)\exp(i\phi)$ where the average is taken over a sufficient number of cycles. The real part G' is the effective nanojunction stiffness (also called storage modulus), the imaginary part G'' describes mechanical dissipation (loss modulus). From force data obtained in a vast range of frequencies, nanocontact sizes and cross sections we extracted the complex dynamical linear response function G, shown in Fig.1.3a. There is first, as expected, an elastic response at small strains where the stiffness G' is positive and large, and dissipation G'' is, discarding parasitic fluctuations near zero strain (attributable to an excessively small fcc-hcp energy difference, see caption to Additional Fig. 1.6), negligible. As the oscillation amplitudes surpass the yielding magnitude, G' drops and eventually turns from positive to negative, corresponding to the force-strain phase reversal that is visible in the raw data of Fig. 1.2. A corresponding rise of G'' and a noise increase arose at yielding. The large deviations of force from sinusoidal (detailed in Additional Fig. 1.7 and 1.8) are responsible for the noise and underscore the inadequacy of linear response description at and after yielding. We nonetheless focus on the linear response because, even if crude, it permits the simplest assessment of kinetics, as well as direct comparison with experiments. The comparison we found with the experimental complex dynamical rigidity is, even if not perfect, definitely convincing. As shown by Fig.1.3b [5] not only the drift of G' from positive to negative and the dissipation rise are recovered, but also quantitative values of stiffness and yielding strain are in the right range, without adjustable parameters.

We next investigated the oscillation frequency dependence – the response under variable shear rate is a crucial element providing a clear diagnostic of nanojunction rheology, with different outcomes between a yielding solid and a liquid neck. Ranging from 10 MHz to 10 GHz, the simulated frequency dependence of G and its characteristic change of behavior from rigid and elastic to yielding with apparently liquid-like was found in simulations to be essentially nil,(see Fig.1.3a) suggesting that all important slip phenomena take place very fast. This result is coherent with an energy barrier Δ – estimated across a slip, be it compressive or tensile – larger than $k_B T$ by at least an order of magnitude, see Additional Fig. 1.11. Similar to friction, the sharp slips lead to a rheological nanojunction behaviour close to a sequence of nanoscale stick-slip frictional events, known in turn to give rise to a logarithmically weak or negligible velocity dependence of the friction force [36]. The stick-slip-like rheology of simulated solid nanojunctions and their frequency independent response over many

decades can in addition be extrapolated down to much lower oscillation frequencies – such as those used in experiments, presently out of simulation reach – as follows. There must exist by elementary transition state theory a crossover inverse rate, $\omega_L/2\pi$ where $\omega_L \sim \Omega \exp -\Delta/k_B T$ with Ω a mesoscopic attempt frequency scale at which the relevant barrier Δ is thermally overcome during a slip. The basically frequency-independent stick-slip dissipation should persist for oscillation frequency above $\omega_L/2\pi$, and eventually cease below, crossing over to so-called thermolubric viscous sliding, linear with frequency.[37, 38]

In the $N \approx 9$ nanocontact the adiabatic energy jumps at slips suggest energy barriers of $0.2 - 0.4$ eV, while $\Omega \approx 13$ MHz is estimated from real-time force fluctuations close to slips (Additional Fig. 1.11). That predicts a thermolubric crossover frequency estimate $\omega_L/2\pi \sim 600$ Hz for this size and temperature. That justifies extrapolation of high frequency stick-slip behaviour to include experimental tuning fork frequencies like 31 KHz [5], and makes a prediction that might be interesting to verify in future experiments. Our simulations and experiment both show, for all amplitudes above the slip thresholds and up to the largest value, a basically constant G'' (Fig. 1.3). At a single frequency, that could, not unreasonably, be interpreted as evidence of viscous response [5], i.e., $G'' \sim \eta\omega A/h_0$, where η is the viscosity and A the area, independent of amplitude. As a function of the primary oscillation frequency, however, our predicted, nearly frequency independent G'' is very different from this viscous behaviour, at least so long as the frequency does not fall below the thermolubric crossover.

Why there is actually no mechanically induced nanojunction melting in both experiment or simulation is a point already discussed in Ref. [5], but worth re-examining here. Owing to our large oscillation frequencies, one might suppose that melting could in principle occur the large power P provided by the oscillatory strain. In simulation, that power can be evaluated, either as $P = \frac{1}{\tau}\int_0^\tau F(t)\dot{h}(t)dt$ where $\tau = 2\pi/\omega$ is the period, or equivalently as the amount of heat absorbed by the thermostat per unit time. For a nanocontact with a cross section $A \approx 0.6$ nm^2, oscillating with frequency $\omega/2\pi = 50$ MHz and amplitude $a_0 = 0.22$ nm, one obtains a value of $P \approx 1.6 \times 10^{-11}$ W, which, if concentrated on a hypothetical isolated piece of gold of volume $Ad_0 \approx 0.6$ nm^3, would actually melt it in less than 3 cycles. In a nanojunction, heat is, however, conducted away through the suspending tips to the two leads that are held at $T = 300$ K. Owing to the large electronic thermal conductance, estimated via the Wiedemann-Franz relation (valid also in the ballistic regime, that should actually apply here [39, 40]) essentially all heat escapes, leaving only a tiny residue and a temperature increase in the nanojunction that is completely negligible [5]. In our case, simulations actually ignore electronic heat conduction, which in gold is about 95% of the total, thus underestimating the rate of heat escape by a large factor. All the same, the temperature rise in the simulated nanojunction remained negligible, safely below 15 K even at the largest strain amplitudes. The conclusion that the nanojunction does not thermally melt stands therefore absolutely correct. As a further step along that line, considering that a liquid nanoneck could thin down faster than a solid one, we examined the lifetime of $N \approx 9$ nanojunction when T was raised enough to make it locally liquid. Results show (Additional Fig. 1.13) that actual liquid nanonecks at $T > 500$ K should spontaneously evolve and break much faster than any of the experimental feedback and oscillation time scales.

1.5 Intrinsic tensile stress

The agreement of simulated and experimental dynamic response leads us to address with some confidence the question of how a sign change of G' at large strains may arise as result of reversible yielding of a solid nanojunction, and why. Reversibility of yielding is in itself not sufficient to account for that, and some additional element must intervene to make the force jumps at necking and bellying large enough, with accumulation of tensile stress, surprisingly even after compressive bellying. That element, theoretically predicted long ago [1, 2] and recently demonstrated in Pt nanowires[27] is the intrinsically nonzero tensile force - a string tension between the leads – even for a solid nanojunction. In our simulations, tension indeed appeared systematically in all oscillation-free and oscillating nanocontact simulations, as shown by the positive mean force value in Fig. 1.2. Following even the most careful structural relaxation, which canceled the lead-lead force, tensile stress always resurrected immediately afterwards. The bridge-mediated attraction between two bulk-like leads reflects the nanojunction's intrinsic metastability against thinning and eventual breaking. Atoms in the bridge would, if they could, gain free energy by migrating to the leads. Thinning and breaking, averted in experiments by maintaining a constant average electrical current, have no time to occur in the metastable conditions of a

simulation whose duration is much shorter: but the tensile force, transmitted as it were between the leads by the outer nanojunction atoms, is their ubiquitous forerunner. The nonzero average tension force seen in simulations confirm in fact that our rheological results reasonably represent quasi-equilibrium nanojunction conditions. Its value is as it happens, quite easy to predict, ahead of simulations, as follows. Assume a cylindrical nanobridge, solid as well as liquid, with N_t atoms, radius R, length L, and total Gibbs free energy H. The intrinsic lead-lead force is [1]

$$F_i = (H - \mu N_t)/L \tag{1.1}$$

where μ is the bulk chemical potential (at $T = 0$, the cohesive energy) per atom. Considering separate surface and bulk contributions to H, if the bulk could be considered a true solid, and if the nanocontact possessed well defined facets, the free energy difference at the numerator could be written as the sum of the surface stress contributions $(\gamma_i + a_i \frac{d\gamma_i}{da_i})$ where γ_i and a_i are the surface free energy and crystal lattice spacing of the i-th facet. If the bulk was liquid instead, that difference would be just the surface free energy γ. Neither prescription is perfect for our nanocontacts, that are neither real and faceted true solid portions nor liquid necks. We can nonetheless get a rough estimate by ignoring the difference, not large in gold, between surface free energy and facet-averaged surface stress of the main facets, thus treating it as a liquid. That leads to an intrinsic tensile force, or string tension $F_i(R) = 2\pi\gamma R$ that is just the total surface free energy $2\pi RL\gamma$ divided by length L. In our solid simulated junctions this simple force estimate is immediately verified. For example in the $N \approx 9$ nanojunction of Fig. 1.2, where $A \approx 0.6$ nm^2, whence $R \approx 0.44$ nm we obtain, inserting gold's surface energy 0.9 J/m^2 of the force field[26], we obtain $F_i = 2.5$ nN, (4.17 nN using instead the experimental surface energy 1.5 J/m^2) in parameter-free agreement with $F_0 \approx 3.3 \pm 1.0$ nN of the simulation (the confidence interval is connected with force fluctuations in Additional Fig. 1.7). Similarly, for the $N \approx 26$ nanojunction, where $A \approx 1.7$ nm^2 we predict $F_i = 4.2$ nN, (7.08 nN using the experimental surface energy) and observe $F_0 \approx 5.6 \pm 2.2$ nN. This large intrinsic lead-lead attraction, capillary-like but present even across a largely solid nanojunction,[1, 2] should not be forgotten, when interpreting experiments.

The intrinsic tension and its proportionality to radius R represents the second key element to understand the full rheological response. Each time in the cycle the nanojunction undergoes reversible yielding, both necking and bellying, the tensile force and stress undergoes a collapse. Starting from an initially large value which is dictated by the intrinsic tension, down to nearly zero after the slip, whose effect is to cancel essentially the whole force, as demonstrated in Fig. 1.4.

The effect of intrinsic stress on G' can be further demonstrated analytically by e.g., assuming (e.g. for very low frequency ω) a stress-strain behaviour $\sigma(\epsilon)$ that is a hysteresis-free single-valued zig-zag function (see Additional Fig. 1.10)

$$\sigma(\epsilon) = k\epsilon - j_n\Theta(\epsilon - \epsilon_n) + j_b\Theta(\epsilon_b - \epsilon) + \sigma_i \tag{1.2}$$

where k is the elastic stiffness, j_n (j_b) are the necking (bellying) stress jumps, Θ is the Heaviside function, and $\sigma_i = F_i/A$ is the intrinsic stress at zero strain. The effective stiffness G' (strictly real in this case) is the ratio of the Fourier transforms $\sigma(\omega)$ and $\epsilon(\omega)$

$$\begin{aligned} G' &= \frac{2i}{\epsilon_0}\frac{\omega}{2\pi}\int_{-\pi/\omega}^{\pi/\omega} \sigma[\epsilon_0 \exp(i\omega t)] \exp(-i\omega t) dt \\ &= k - \frac{2}{\pi\epsilon_0}[j_n\sqrt{1-(\epsilon_n/\epsilon_0)^2} + j_b\sqrt{1-(\epsilon_b/\epsilon_0)^2}]. \end{aligned} \tag{1.3}$$

The last two terms show how the stress drops j_n and j_b – that are large because of the large intrinsic stress – effectively act to reverse the sign of G' when ϵ_0 exceeds the yielding thresholds ϵ_n and $|\epsilon_b|$ (see Additional Fig. 1.10).

1.6 Discussion

Summing up, we have found that the large-strain rheology of a ductile metal nanojunction, here exemplified by room temperature gold, is dominated by two elements: reversible yielding, and a large size-dependent intrinsic

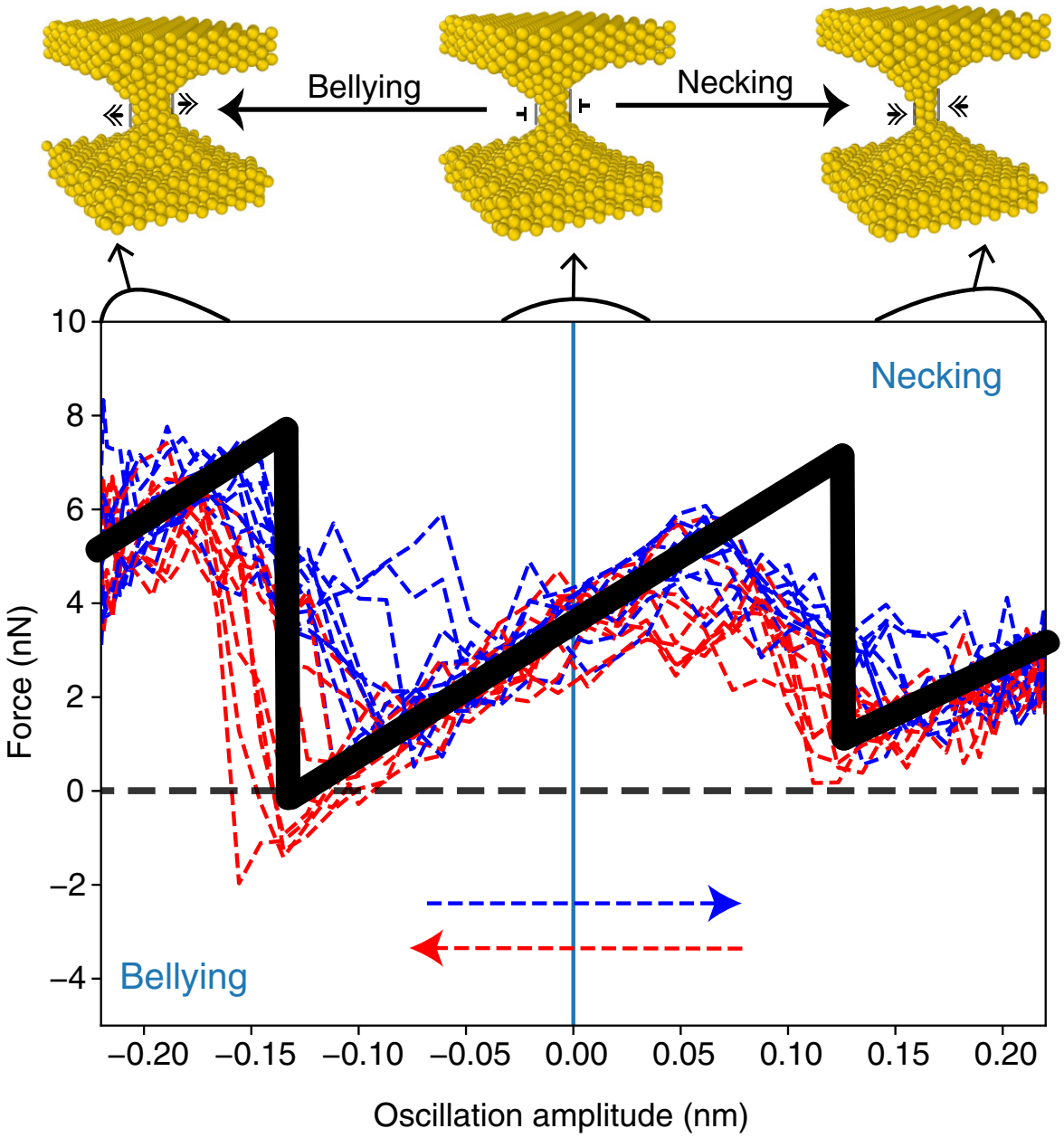

Figure 1.4: Large amplitude force-strain characteristics. Simulation trajectories in the force-strain plane, for the $N \approx 9$ nanojunction at 50 MHz. Blue trajectories: half cycle with positive strain time derivative $\frac{d\epsilon}{dt} > 0$; red trajectories: negative strain time derivative $\frac{d\epsilon}{dt} < 0$. Insets are snapshots frames showing the junction at rest (center), after necking (right) and after bellying (left) Black line: schematic adiabatic zig-zag force-strain characteristics. The straight tract near zero is (ignoring fluctuations) the elastic regime. Major yielding slips occurs at necking and bellying, which are the results of forced tensile and compressive strain, respectively. Note the average tension force dominating the whole cycle, surprisingly including the compressive portion, and the large jumps where the force falls near zero at both slips.

tensile stress, both already apparent in the raw simulation data of Fig. 1.2. The reversible yield slips occur in a basically crystalline structure, as opposed to a conjectured strain-driven liquefaction. The size-dependent tensile stress, predicted to exist in a metal nanojunction in quasi-equilibrium at finite temperature, even if close to a solid inside, causes the stress jumps to be large. The two elements concur to change the sign of the effective stiffness G' from positive to negative, a reversal close to that seen in experiments. The dissipative response G'' at large oscillation amplitudes is predicted to behave as stick-slip friction, that is with weak or negligible

frequency dependence. If the experimental tuning fork frequencies could hypothetically be extended to cover higher values they should directly exclude, we believe, the dramatic linear growth expected for a liquid. If on the other hand the oscillation frequency could hypothetically be lowered enough to reach ω_L, or alternatively if ω_L could be raised enough by increasing temperature, then stick-slip should be found to cross over to thermolubric sliding. A cartoon of the full response in the limit of vanishing ω, for example, is that portrayed in the zigzag model of Additional Fig. 1.10, where G' still switches from positive to negative, whereas dissipation vanishes, $G'' = 0$. A predicted additional consequence of the reversible stick-slip rheology is a large anharmonicity and associated force noise, also be accompanied by conductance noise. Clearly reported in experiments,[5] such a large noise cannot be easily rationalized for a liquid neck.

Investigated here in the specific instance of gold, a very ductile metal at room temperature, the conditions under which a vibration-induced nanojunction softening might occur in different metal contacts of technological importance should be pursued in future studies. Fully developed intrinsic tension in generic nanocontacts might be hampered by slower kinetics in either less ductile metals or ones with larger slip energy barriers (thus showing up only at higher temperatures), where nonetheless the same conclusions about the non equilibrium dynamics of nano and atomic contacts should apply. The mechanical and rheological behaviour under oscillatory strain induced by vibrations of the specific case of gold junctions, expected to be technologically important in electrical contacts [41, 42] – should be of high interest for gold-plated connectors and switches in industrial applications [43, 44], for spacecrafts evolving in microgravity [45] and a multitude of other strongly vibrating contacts. Potential applications beyond the case of gold could play a role in adhesion and friction of vibrating systems, where negative stiffness could alter the mechanical stability, the friction, and the electronic performance of more general metal nanocontacts. Our findings may have major impact in emerging industrial applications such a direct printing of metallic wires at the nanoscale. Indeed the increased stability due to shear induced negative stiffness can prevent mechanical instability of metallic wire and dewetting of surface at the nanoscale providing a novel class of electronic devices.

1.7 Methods

The sub-microsecond simulations were carried out using the Large-scale Atomic/Molecular Massively Parallel Simulator (LAMMPS) open source code [46]. Following previous work by Park and Zimmermann [47], and many other studies, we adopted the realistic embedded-atom method (EAM) gold force field by Foiles et al [26]. The simulation setup consisted of 2042-2516 particles ($N \approx 9 - 26$), with periodic boundary conditions (PBC) in (x,y) plane and free boundary conditions along z axis (the strain axis). The two upper and lower gold leads consist of two fcc rigidly stacked (110) lattice planes. Four thermostating planes consisting of 576 atoms are attached to the leads at each side, joining together with an initial 2.75 nm long column with various thicknesses. The setup is thermally and mechanically relaxed, as shown Fig. 1.1b, finally evolving into a shorter nanojunction subtended between two spontaneously formed anvil-shaped tips. An oscillatory z-displacement is added to the lead-lead distance, causing the nanojunction to undergo a tensile and compressive deformation. Non-equilibrium molecular dynamics (NEMD) simulation is carried out in the framework of Langevin approach at room temperature. In order to minimize the possible influence of this simulating procedure, the thermostat is applied just to the mobile atoms outside the physically relevant region defined by h_0. Besides, we checked that, within a significant range of values of the Langevin damping parameter, rheological response of the system is reasonably independent of its specific choice. The vertical force between two leads are read directly from simulations, the phase shift between force signal and the imposed oscillation is the concern of analysis in this work.

1.8 Additional notes

Here are some supplementary notes in case the reader wants to delve deeper into any particular section.

1.8.1 Robustness of results

Simulations have been performed on nanojunction of varying lateral size in order to investigate the validity of the proposed approach. Almost identical rheological response versus increasing strain oscillations is observed also in nanocontacts with larger mid-junction thickness (here, e.g., $N \approx 26$). The evolution of the force-strain phase differences with oscillating amplitude is shown in Fig. 1.5.

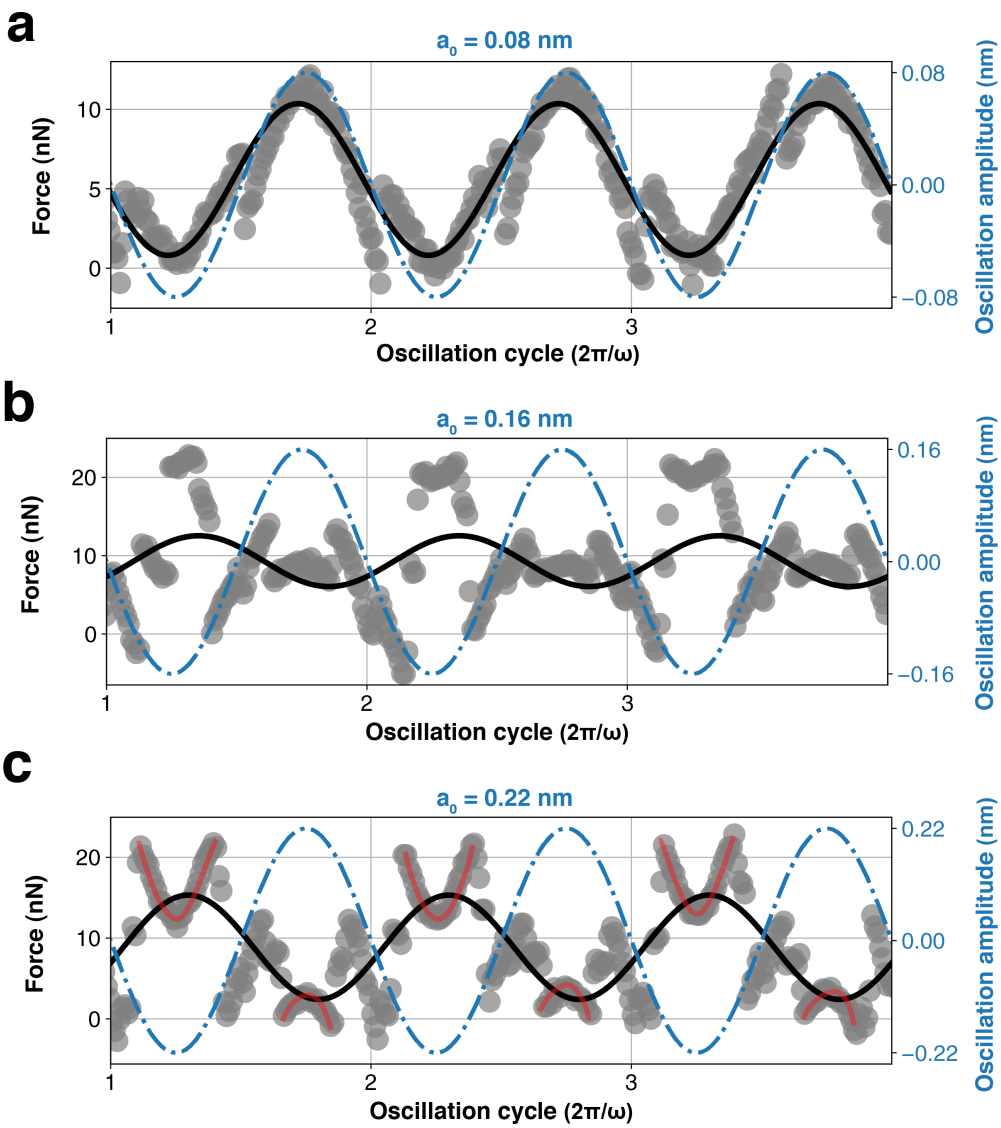

Figure 1.5: Force time evolution of a thicker nanojunction under oscillating strain Time dependent force results (oscillation frequency 50 MHz , T=300 K) for a thicker ($N \approx 26$) nanojunction, with initial $h_0 \approx 2.75$ nm, relaxed neck length $d_0 \approx 1$ nm, and average neck cross section area $A \approx 1.7$ nm^2. Blue dashed-dotted line: imposed lead-lead oscillating distance $a(t)$. Large grey dots: extracted instantaneous force between the leads. Black solid line: sinusoidal fit $F(t) = F_0 + (A\sigma_0)\exp(i\omega t + i\phi))$ of the force. Note how avalanche-like jumps (in red), occurring at the maxima of the driving strain, gradually inverts the sinusoidal fit phase, moving from small **(a)** towards large **(c)** imposed amplitudes. Once again, the prevalence of tensile (positive) force shows up for all strains.

In connection with what is already shown in main text for a thinner nanocontact, Fig. 1.6 displays the

$N \approx 26$ nanojunction force-strain characteristics and the corresponding complex dynamical linear response function, in basic agreement with smaller sizes.

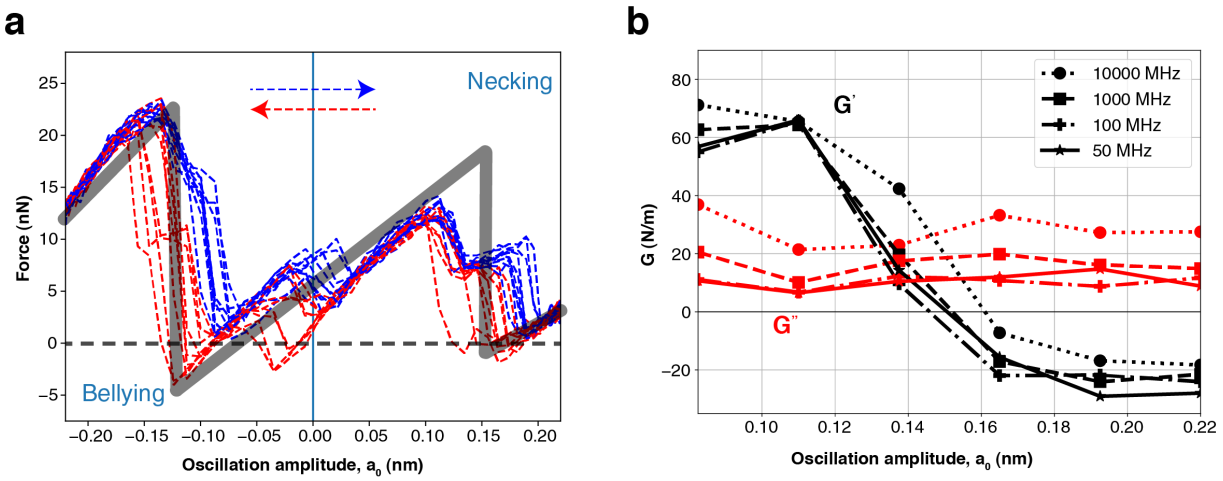

Figure 1.6: Rheology of the thicker ($N \approx 26$) nanojunction at 50 MHz strain rate. **(a)** Large amplitude simulation trajectories of a thick nanojunction in the force-strain plane. Blue trajectories: half cycle with positive strain time derivative $\frac{d\epsilon}{dt} > 0$; red trajectories: negative strain time derivative $\frac{d\epsilon}{dt} < 0$. Black line: schematic (adiabatic) zig-zag force-strain characteristics. At small amplitudes, the straight tract represents an essentially elastic regime, except for some residual fluctuations possibly connected with the force field's small (1.1 $mev/atom$) fcc-hcp energy difference [35]. Major yielding instabilities occurs at necking and bellying ($a_0^* \approx 0.16$ nm), which are the results of forced tensile and compressive strain, respectively. As observed for the thinner nanocontact, the average tension force dominates the whole cycle, including the compressive portion, causing the large jumps where the force falls near zero at the yielding strains. **(b)** Effective stiffness G' and dissipation G'' of the complex dynamical linear response function G. Note how the overall behaviour is frequency independent, one of the evidence for non-liquidity of the junction.

1.8.2 Force fluctuations, nonlinear noise spectrum

The simulated force between the two oscillating leads fluctuates very violently after yielding, and especially at large strain frequencies, where the instantaneous force deviates from the sinusoidal linear response fit.

At all frequencies, and for both thin $N \approx 9$ and thick $N \approx 26$ nanojunctions (see Fig. 1.7), fluctuations tend to rapidly increase toward yielding ($a_0 \approx 0.165$ nm), signaling the gross inadequacy of linear response description beyond the elastic regime.

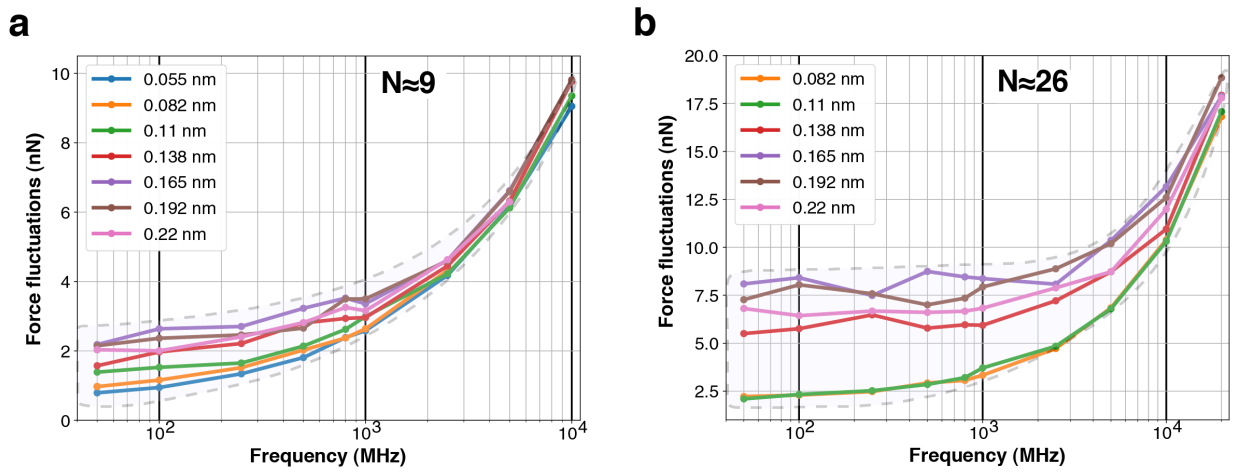

Figure 1.7: Force fluctuations frequency dependence, extracted for different strain oscillation amplitudes for $N \approx 9$ **(a)** and $N \approx 26$ **(b)** nanojunctions, respectively. For each parameters set, data is extracted over many oscillation cycles, considering half width at half maximum of Gaussian distribution of the recorded force signal deviating from its sinusoidal linear response fit.

In addition, we Fourier analyzed the lead-lead force

$$F(t) = \frac{a_0}{2} + \sum_{n=1}^{\infty} a_n \cos(n\omega_0 t) + b_n \sin(n\omega_0 t) \tag{1.4}$$

to obtain the noise spectrum in the two relevant regimes: a) small strain amplitude, where without slips the nanojunction is basically elastic, with positive stiffness and b) large strain amplitude, where the nanojunction deforms with reversible slips and stiffness is negative. As shown in Fig. 1.8 for the nanojunction of $N \approx 9$ the noise spectrum broadens dramatically in stick-slip regime (b), with large higher harmonic contents at $\omega = n\omega_0$ besides the fundamental at $\omega = \omega_0$. The peak n values depend on the oscillation amplitude, reflecting the changeable position of slips within the cycle.

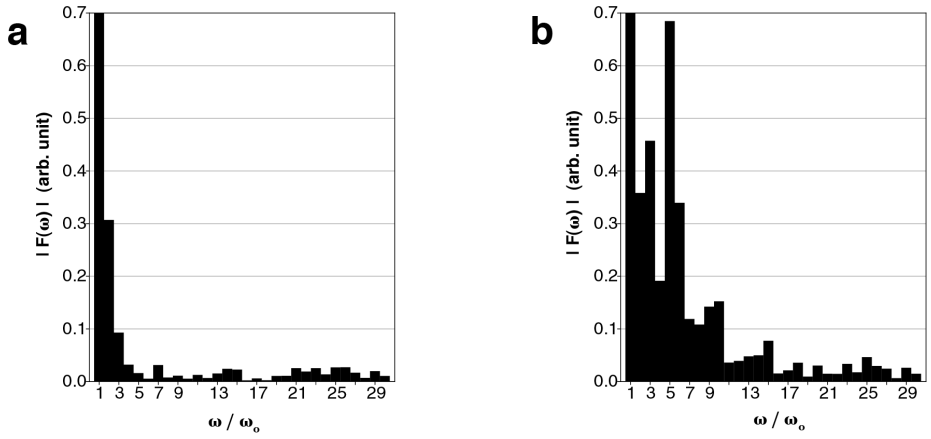

Figure 1.8: Noise spectrum for $N \approx 9$ at small amplitude $a_0 = 0.08$ nm **(a)**, frequency 50 MHz and large amplitude $a_0 = 0.22$ nm **(b)**. The frequency scale shows $n = \omega/\omega_0$. The $|F(\omega)|$ histograms show $\sqrt{a_n^2 + b_n^2}$, normalized so that $F(\omega_0)$ =1. Note the broad-spectrum noise generated by stick-slip at large amplitudes.

1.8.3 Nanocontact structural slips

Here, we show how the force drops, responsible for the zig-zag character in the force-strain trajectories (see Fig. 1.6), are caused by local structural slips. To explore this feature, we perform an oscillatory athermal ($T = 0$)

simulation with strain amplitude $0.22nm$, where layer ordering is easily detectable in the $N \approx 9$ nanowire as shown in Fig. 1.9a.

To verify the structural consequences of avalanche-like instabilities at each strain cycle, we successively determine the angular distribution, now at room temperature, for the $N \approx 26$ nanocontact – central atoms only, excluding surface ones – at 50MHz. Fig. 1.9b reports the angular distribution of the nanojunction structure right when it experiences the largest ($0.22nm$) tensile and compressive strain within the cycle. The shoulder around 147° signals precisely ABC to ABA local sliding of (111) planes after necking. That same feature is missing after the bellying avalanche, where a final fcc structure is restored under compression, a regime where hcp structure is disfavored.

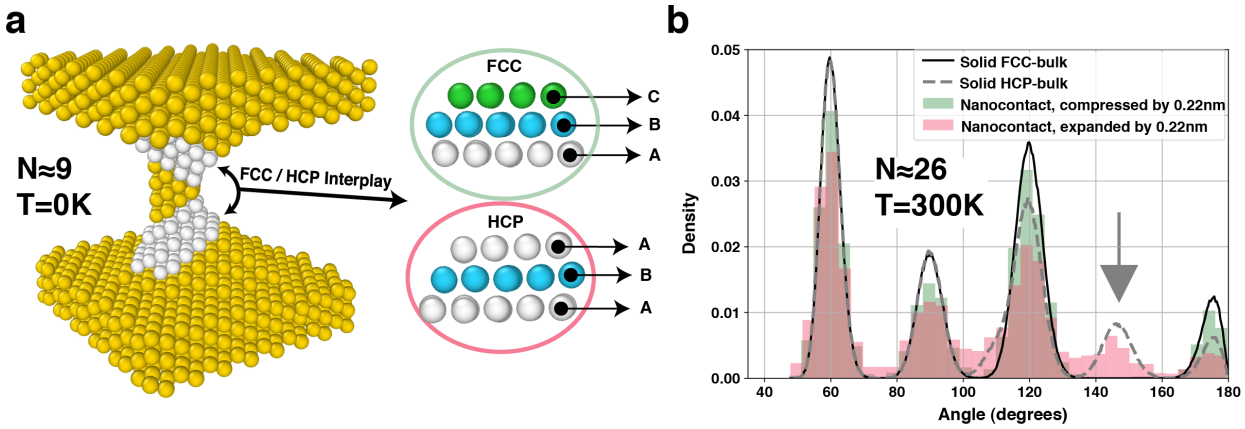

Figure 1.9: Nanocontact structural and interplanar sliding features. **(a)** Local structural slip during a $0.22nm$ strain oscillation for the $N \approx 9$ nanocontact, at zero temperature. **(b)** Angular distribution at maximum compressive/tensile strain (0.22nm) of the thicker $N \approx 26$ nanojunction at 300K. The dark arrow highlights the appearance of a shoulder around 147° signaling the ABC to ABA interplanar local sliding after necking. Simulated frequency is 50MHz.

1.8.4 Zig-zag model

The simple toy model introduced in the main text and characterized by

$$\begin{aligned} \sigma(\epsilon) &= k\epsilon - j_n\Theta(\epsilon(t) - \epsilon_n) + j_b\Theta(\epsilon_b - \epsilon(t)) + \sigma_i \\ \epsilon(t) &= \epsilon_0 \sin \omega t \end{aligned} \tag{1.5}$$

where k is the elastic stiffness, and j_n (j_b) are the necking (bellying) jumps at yield strain ϵ_n (ϵ_b), and σ_i is the intrinsic stress at zero strain, can help us to understand the role of vertical jumps in determining the values of G'. As already mentioned, the effective stiffness can be calculated as ratio of the Fourier transforms

$$\begin{aligned} \epsilon(\omega) &= \frac{\omega}{2\pi}\int_{-\pi/\omega}^{\pi/\omega} \epsilon(t)\exp(-i\omega t)dt = \frac{\epsilon_0}{2i} \\ \sigma(\omega) &= \frac{\omega}{2\pi}\int_{-\pi/\omega}^{\pi/\omega} \sigma(\epsilon(t))\exp(-i\omega t)dt \\ &= \frac{k\epsilon_0}{2i} - \frac{j_n}{\pi i}\sqrt{1-(\epsilon_n/\epsilon_0)^2} - \frac{j_b}{\pi i}\sqrt{1-(\epsilon_b/\epsilon_0)^2} + 0 \end{aligned} \tag{1.6}$$

leading to the formula:

$$G' = \left.\frac{\sigma(\omega)}{\epsilon(\omega)}\right|_{\omega=\omega_0} = k - \frac{2}{\pi\epsilon_0}\left[j_n\sqrt{1-(\epsilon_n/\epsilon_0)^2} + j_b\sqrt{1-(\epsilon_b/\epsilon_0)^2}\right] \tag{1.7}$$

This is the exact equivalent of least square fitting protocol we employed to extract G' from the MD simulations.

For several values of j_n and j_b – renamed simply j here –, Fig. 1.10 shows the zig-zag response of this toy model, and the corresponding effective stiffness G' calculated from Eq. (1.7). The stress jump amplitude j plays a crucial role in determining G' sign reversal. When the applied strain is still within the elastic regime, the overall slope in Fig. 1.10a remains positive; at the yield slips however, both necking and bellying, the stress drops to zero, turning negative the overall slope, and thus G'.

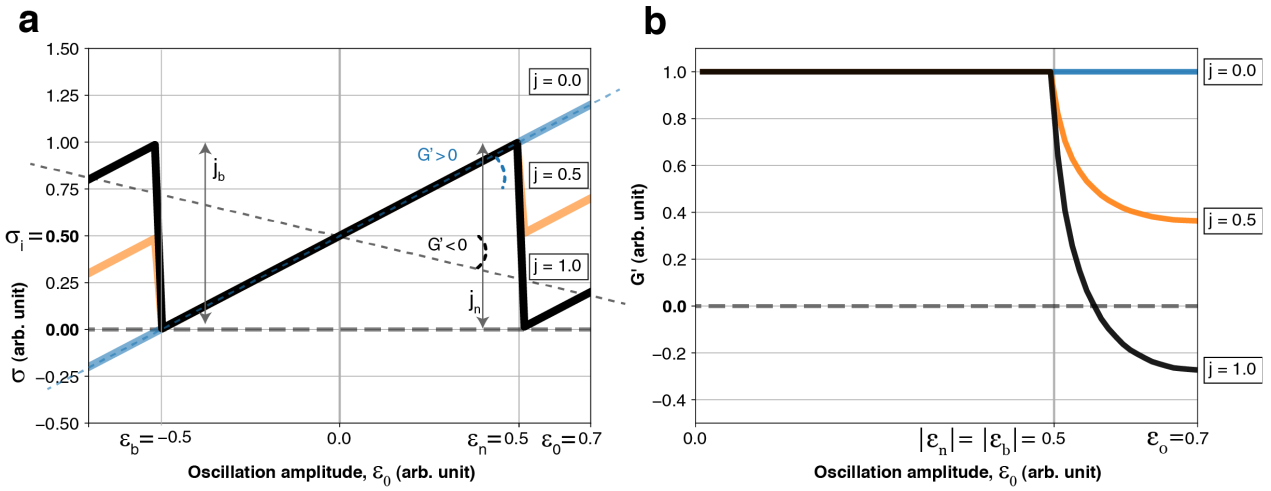

Figure 1.10: Zig-zag stress-strain model for parameters: $j = j_n = j_b$, $\epsilon_n = |\epsilon_b| = 0.5$, $\epsilon_0 = 0.7$, $\sigma_i = 0.5$, and $k = 1$. (a) Model stress-amplitude characteristics, mimicking the avalanche-like slips in the simulated nanojunctions. The overall slope highlighted by dashed lines represents a rough approximation of G'. **(b)** G' calculated using equation Eq. (1.7). Note how G' turns negative for $j = 1$, the value making the stress jumps touch zero, as in simulations. The model demonstrates how a large average tensile stress, imposes also a large value of stress jumps, j –as the result of touching zero– necessarily for G' to turn negative.

1.8.5 Energy barriers and attempt frequency

The regime adopted by each strain-induced slip of the nanojunction may be rationalized by standard transition state theory, where the inverse rate

$$2\pi\tau^{-1} = \omega_L = \Omega \exp -\Delta/k_B T \tag{1.8}$$

is controlled by an energy barrier Δ and an attempt frequency Ω. While both quantities depend on specific nanojunction and its conditions, we obtained an order of magnitude of the barriers from the total energy evolution of the athermal nanocontact of Fig. 1.9a, and extract a rough value between 0.2 and 0.4 ev of the energy jumps, proportional to the barriers (possibly slightly underestimated by the force field), associated with single slips (Fig. 1.11a). We also ran a 300K non-oscillatory simulation of the nanocontact ($N \approx 9$), pre-strained by -0.12 nm, a regime where unbellying slip occur erratically and attempt oscillations are more conspicuous. The analysis of Fig. 1.11b-c yields an estimated $\Omega \sim 13.3$ MHz for the attempt frequency of the N=9 nanocontact. Assuming qualitatively therefore, a barrier of 10 $k_B T$ and an attempt frequency Ω as found we obtain a crude crossover frequency estimate $\omega_L \sim 600$ Hz.

1.8.6 Heat conductance

The heat conductivity of a metal such as gold is largely electronic. Thus the mechanical heat generated inside the junction by oscillatory strain is basically conducted away by electrons at the Fermi surface. The heat conductance in the bulk metal is related to electrical conductance through the Wiedemann-Franz relation. For our nanojunctions, however, since their typical length is smaller than the electron's mean-free-path –37.7 nm for gold[48]–, electrical conductance is ballistic, and not diffusive as in bulk. It has been conclusively shown that the Wiedemann-Franz relation holds also in ballistic nanochannels[39, 40], which for the nanojunction with cross section $N \approx 9$ at 300K for instance, gives:

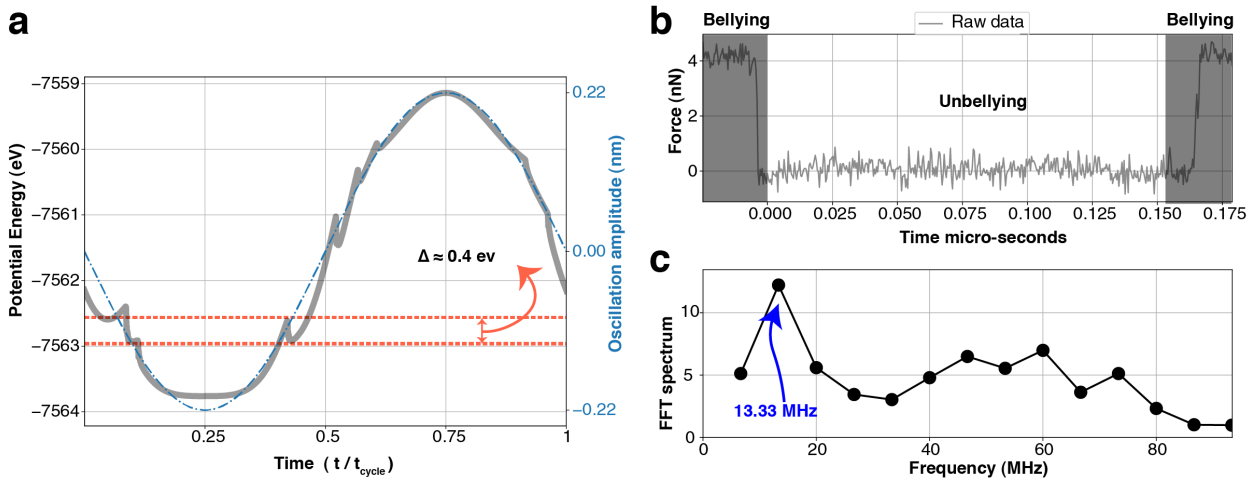

Figure 1.11: Analysis of the force noise and energy jumps near and following an "unbellying" slip. (a) Evolution of total energy during an adiabatic strain oscillation at T=0 in the $N = 9$ junction. Two orange dashed lines show a typical energy barrier of a single slip, e.g., bellying. The jumps provide an order of magnitude of the slip energy barriers. **(b)** Raw force signal from simulation at T=300K **(c)** Fourier spectrum of force, showing weak attempt frequency oscillations centered at $\omega = 13.3$ MHz

$$\kappa_{ballistic} = N \times \frac{\pi^2 k_B^2 T}{3h} \approx 2.56 \times 10^{-9}\ WK^{-1} \tag{1.9}$$

Using this value, we can estimate what would be the increase in temperature in an ideal nanojunction, in presence of the ballistic electronic heat conductance. With a mechanical Joule power of 2 ev/cycle $\sim 1.6 \times 10^{-11}$ W in the case of $N \approx 9$ while oscillating with amplitude of 0.22 nm at frequency of 50 MHz, the expected temperature increase would be

$$\Delta T = \frac{1.6 \times 10^{-11}}{2.56 \times 10^{-9}} \approx 0.006\ K \tag{1.10}$$

In our MD simulations the electronic conductance, responsible for about 95%[40] of total heat conductance in a real gold nanojunction, is of course absent. Moreover, we only thermostat the two thin solid lead slabs supporting the whole contact of length h_0 (see Fig. 1). Unsurprisingly we observe a higher simulated temperature rise of the interior nanocontact than that estimated above, but still below 15 K, thus unable to cause melting, and altogether irrelevant.

1.8.7 Low frequency simulations

For a qualitative check and validation of our results, we lower the frequency down to 10 MHz and 1 MHz, performing in the latter one oscillation cycle only. Less accurate as that result is, the response function extracted and shown in Fig. 1.12 shows that the overall conclusions drawn in text remain valid. Specifically, the reversible yield slips, the sign change of G' with frequency independent G" at large amplitudes are confirmed.

1.8.8 High temperature nanocontact lifetime

The experimental time scale to control the contact size is many orders of magnitude larger than the life time of a heated nanocontact. We conclude experimental nanocontacts are always solid.

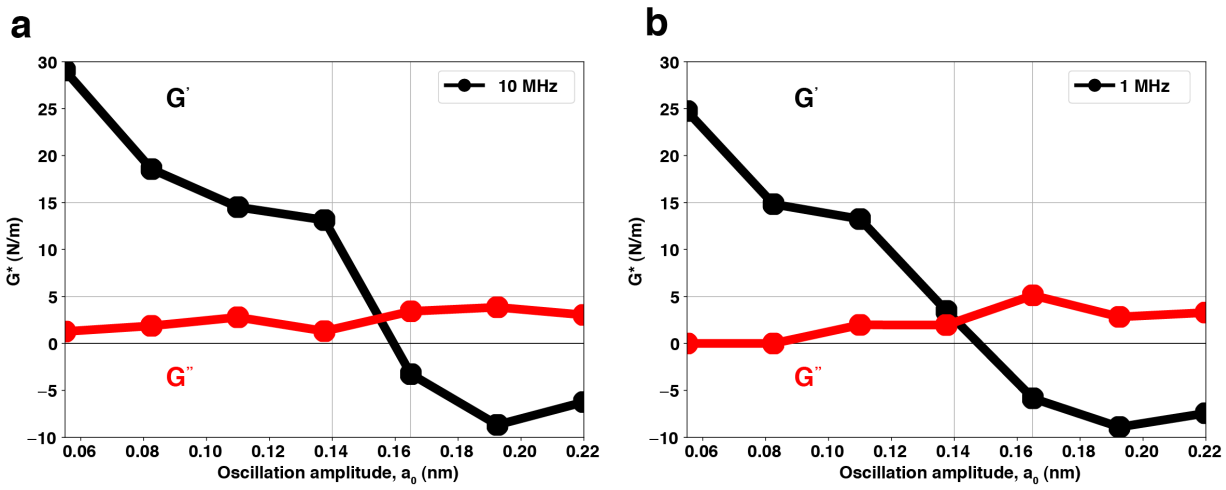

Figure 1.12: Complex dynamical linear response function G, for nanocontact $N \approx 9$. **(a)** 10 cycles, 10 MHz **(b)** 1 cycle, 1 MHz

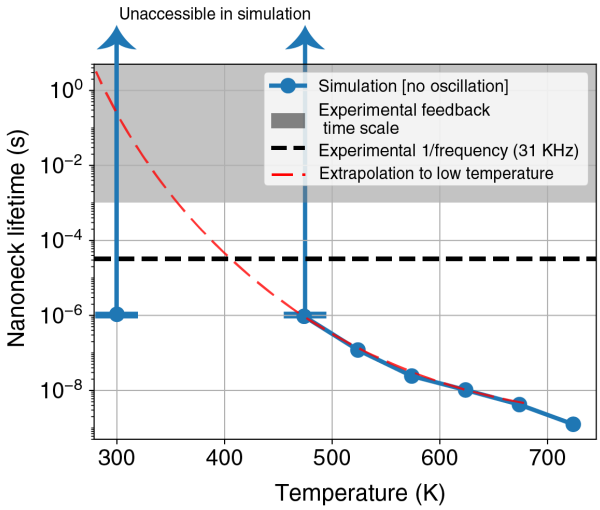

Figure 1.13: Nanocontact lifetime of a $N \approx 9$ **nanocontact obtained as a function of temperature without vertical oscillation, simulation duration is less than** 1μ **sec.** Black dashed line and grey band are the time period and experimental feedback time range used in Ref. [5]. Red dashed line: lifetime extrapolation at low temperatures. Liquid nanonecks at $T > 500$ K break extremely fast, while already at 400 K the lifetime would be shorter than the experimental feedback time.

Chapter 2

Rheological Softening of Metal Nanocontacts Sheared under Oscillatory Strains

2.1 Introduction

In the past two decades, studies of dry friction and wear [49] have repeatedly shown how rapid load oscillations may cause a strong increase of lubricity between inert solid interfaces that do not merge or cold weld. Theoretical arguments [50–53] essentially based on idealized Prandtl-Tomlinson models qualitatively suggested how, under these conditions, the externally imparted oscillations cause an easier disentanglement between facing asperities. Here we are concerned with interfaces, such as those between ductile metals, where the local contact inevitably involves merging and/or cold welding, thus forming narrow solid bridges in correspondence with facing asperities, as discussed in classic literature [54–56].

At present, the detailed rheological evolution of such interfaces under shearing friction is insufficiently explored. For this situation, an "inert interface" type of model [50–53] is in principle inadequate, and a new approach is called for.

Metal-metal nanocontacts, often crystalline, are reported in electron microscopy data, most commonly in noble and near-noble metals [6, 18–20]. Experimental TEM images [6, 57] in oscillation-free sliding metal contacts also demonstrate a high degree of crystallinity of the bridging contact. The formation and presence of nanocontacts is also underlying the conductance of electrical metal contacts, whose overall Sharvin conductance might be roughly estimated as $G \sim NN_cG_0$ where $G_0 = 2e^2/h = 12.9\ (kOhm)^{-1}$, for N widely spaced nanocontacts in parallel, each of minimal cross section consisting of roughly N_c atoms. Generally, nanocontacts interact with each other due to the combination of roughness and elasticity, as outlined in phenomenological models (see [58, 59]). When the interface is forced to slide under applied shear stress, the sparsely distributed nanocontacts are stochastically sheared, broken, and reformed with mechanical friction and wear.

The shearing of single metal nanocontacts has already received attention in literature. Sato et al.[6] studied it experimentally in Ag. More recent non-equilibrium molecular dynamics simulation by Wang et al.[7] remarkably rationalized these results. Both studies showed that the shearing of a contact between two relatively large size asperities proceeds by what one might call atomic stick-slip, as expected for sliding among two crystal planes at the contact's middle cross section. The shearing slips were seen to evolve from single atomic steps at the beginning of shear, developing to multiple steps close to breaking. That evolution was also accompanied by a gradual weakening of the average shear stress before breaking. No kind of oscillatory perturbation was considered in these early studies; the large contact cross sections studied would anyway have left little room for any rheological effects such as those we intend to pursue here for much narrower nanocontacts, such as those recently studied experimentally[5] .

With that goal in mind, we pursued simulation studies of the shearing of a model thin gold nanocontact, where one anticipates that an applied oscillation should have an effect. Underlying and motivating this study is the recently discovered phenomenon of a seemingly liquid-like collapse of mechanical impedance as a result

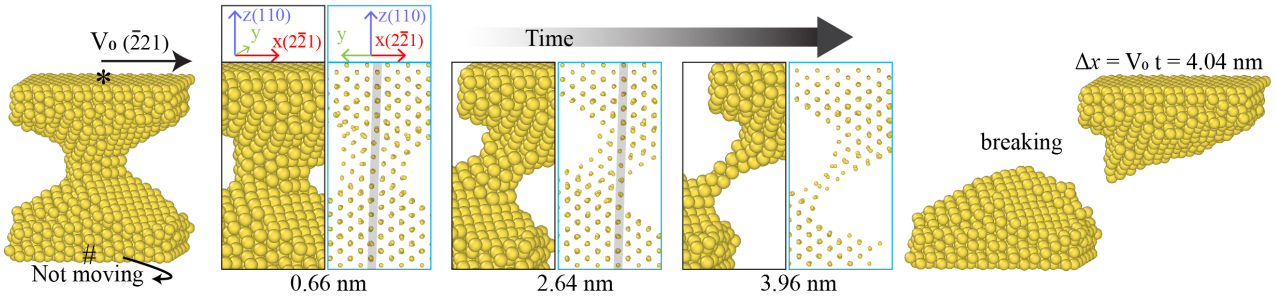

Figure 2.1: Shearing nanocontact with constant velocity of 0.02 m/s, no oscillations applied. Between 0.66 nm and 2.64 nm, in total four events of stick-slip, results in narrower contact with four extra 111 layers in between. Two additional stick-slip events produce an umbilical braiding chain of gold atoms (4 atoms thick), owing to the inability to preserve crystallinity. Black and blue frames show the same moment of shearing from two different perspective. Gray and almost vertical shaded lines, show that 110 chains maintain their vertically after each slip. Detailed pictures of shearing with oscillations are provided in Additional note 2.7.1.

of strong strain oscillations in gold nanocontact at room temperature[5]. That puzzling phenomenon was very recently shown [60] not to involve melting, but rather to be due to a reversible stick-slip-like plastic evolution of the solid and crystalline nanocontact, coupled with an ever-present string tension.[1, 2] Together, these are the two elements that lead to the observed negative nanocontact stiffness – only apparently liquid-like , caused by oscillations in a crystalline nanocontact.[60].

We simulated the transverse shearing of the ultra-thin gold nanocontact, first without, then with vertical or rotational strain oscillations of fixed frequency and increasing magnitude, 2.1. Without oscillations, the shearing proceeds by atomic steps, apparently stick-slip-like. Additional oscillations of increasing magnitude do rheologically decrease the average yield shear stress. However, even at the largest oscillation magnitudes, where the effective tensile stiffness G' has become negative [60], the stick-slip-like shearing behaviour is never completely eliminated. In agreement with that, the time-averaged frictional shear stress remains in most cases poorly velocity-dependent, despite the rapid internal nanocontact evolution induced by oscillations.

As we shall describe in Section 2.2, the oscillation-softened nanocontacts indeed experience some reduction of mean shearing friction, without actually losing the stick-slip like atomic steps. The nanocontacts still maintain, despite strong imparted oscillations, their solid crystal structure during all phases of shearing.

Noise and fluctuations, mechanical, acoustical and electrical, also accompany and reflect the shearing process. As shown in Section 2.3, the analysis of that noise is particularly interesting and revealing for a nanocontact sheared in presence of rotational oscillations. Section 2.4 presents the dependence of shearing friction upon velocity and temperature, which results in agreement with stick-slip expectations. Section 2.5 will show how the complex dynamical response function (i.e., the conventional stiffness and damping) evolves during shearing. Our final considerations, including prospectives for a proper "rheolubric" transition from stick-slip to smooth shearing at sufficiently low velocities and oscillation frequencies, conclude the paper in Section 2.6.

2.2 Nanocontact shearing simulations

We conducted non-equilibrium molecular dynamics (NEMD) simulations including a standard Langevin thermostating at room temperature. The simulation setup included approximately 2500 atoms (Fig. 2.1). The upper and lower gold leads were composed of two FCC rigidly stacked (110) lattice planes. Four thermostated planes, each consisting of 576 atoms, were attached to the leads on each side, connecting them with an initial column-like nanocontact shape of approximately 2 nm in length. With the present choice of crystal orientation, the column is made up of first-neighbour (110) atomic chains, a crystallographic choice that yields a nanocontact particularly robust and resistant to thinning and breaking. After careful relaxation and annealing, surface atoms migrated and the column turned into the more realistic long-lived shape of Fig. 2.1. The narrowest transverse cross section of the relaxed nanocontact comprised $N_c \sim 26$ atoms. Electrically, that would correspond to about

N_c ballistic channels. Many such ultrathin nanocontacts could of course be similarly generated and studied. As shown in previous work [60], their rheological behaviour is however essentially equivalent. We argue therefore that studying just one should suffice to address their generic shearing behaviour.

To minimize the possible influence of Langevin damping on the subsequent NEMD dynamics, the thermostat was only applied to the mobile atoms well outside the physically relevant nanojunction region. Additionally we verified that, within a significant range of values of the Langevin damping parameter, the rheological response of the system was reasonably independent of the specific choice. The whole setup was thermally and mechanically relaxed before the shearing simulations. Shearing was performed by moving the upper lead with a constant velocity $V_x = 0.02m/s$ along the $(2\bar{2}1)$ direction (our x-axis), orthogonal to the initially vertical (110) nanocontact axis. Shearing was also carried out at increasing velocities, from 0.02 to $0.2m/s$. When it was accompanied by oscillations (to be introduced below), either vertical or rotational, the frequency of oscillations was generally set at 1 GHz. These large velocities and frequencies, forced as they are by current computational limits, are of course generally higher than those expected from experiments. Our previous experience [60] however showed that the rheological behaviour of gold nanocontacts at room temperature remained the same across many orders of magnitude of these parameters. In particular, a loss of so-called necking-bellying jumps in favour of a smooth rheological evolution of a nanocontact of this size is not expected until a very low oscillation frequency of order 600 Hz. A further point worth stressing here is that none of the rheological manoeuvres realized in the present simulations, and *a fortiori* in experiments,[5] implies a rise of temperature. All heat produced by shearing and by oscillations is effectively removed to the thermal bath, which stabilizes room temperature. Therefore no change of friction should or could be attributable to a hypothetical onset of "thermolubricity"[61].

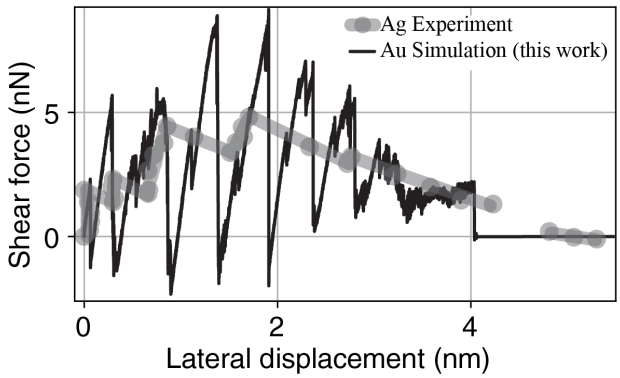

Figure 2.2: Instantaneous shear force for a nanocontact from simulation (black) for Au, and experiment (gray) for Ag (re-plotted from Ref [6]). Note the stick-slip advancement mode for Au, and the average friction force for Ag, both similar apart from a different force jump magnitudes. An important difference is the step length magnitude, variable in the thick experimental Ag contact, but fixed and quantized in the much thinner simulated nanocontact. As explained in text, the latter reflects the surprising atomic stick-slip of a generally oblique nanocontact, a feature lost in a thicker contact.

The starting point: shearing without oscillations

In the first of set of shearing simulations,we applied a lateral constant velocity $V_x = 0.02m/s$ to the upper lead, without oscillations. The shear force evolution between the two leads shown in Fig. 2.2 (black) is read off the simulation, showing the sawtooth profile typical of stick-slip advancing steps, through which the nanocontact shearing takes place. As the shearing proceeded, the nanocontact gradually deformed into a narrower and narrower oblique junction, thinning down and eventually breaking apart, see Fig. 2.1. The stick-slip-like jump size, with constant magnitude close to 0.5 nm, is shown by the green bar in the force signal Fig. 2.3**a**.

Structural examination, detailed in Fig. 2.1 showed that each slip is due to a sudden shear-induced elongation. The nanocontact rearranges, by thinning down while adding at each slip one extra (111) plane, actually a solid slice, to its length. Shearing slips are therefore entirely akin to the oscillation-induced necking jumps earlier reported with vertical oscillations and no shear.[60]. That being ascertained, the partially sheared nanocontact

becomes increasingly oblique at first sight by a continuous amount as the shearing proceeds. Thus the question arises, if the nanojunction obliqueness grows continuosly, why do shearing slips strictly retain the atomic step length prescribed by the two leads, as if the nanocontact remained vertical?

Although not visible in Fig. 2.1, the answer is structural (see Fig. 2.8a) and quite interesting. Oblique and slanted as it is, the nanocontact *always retains unbroken vertical (110) atomic chains that connect the two leads*. At the each slip, the sudden necking rearrangement, while increasing by one the number of (111) cross section planes, stops precisely once at the earliest distance where unbroken (110) vertical atomic chains can reform. And that is precisely the $(2\bar{2}1)$ lattice spacing in both leads, that is $2\sqrt{3}R$, where $R = 0.148$ nm is gold's atomic radius. The rationale behind this unsuspected shear slip quantization therefore appears to reflects jumps between successive adhesion energy minima, which the surviving unbroken (110) chains realize between the two leads after each slip.

It is instructive to compare this profile with the experimental shearing force profile, Fig. 2.2 (gray) measured in the past for a much thicker silver nanocontact [6]. The experimental shearing force also exhibits stick-slip steps. It has an overall nonmonotonic magnitude from initially small to maximum after a few slips, to a final decline before breaking. That behaviour had already been described and understood by simulations [7]. We superpose it here to our own nanocontact shearing simulation, so as to highlight similarities and differences. Even if our cross section area is much smaller, the overall similarity is still remarkable, including atomic stick-slips and force magnitudes, despite the two different metals, Au and Ag.

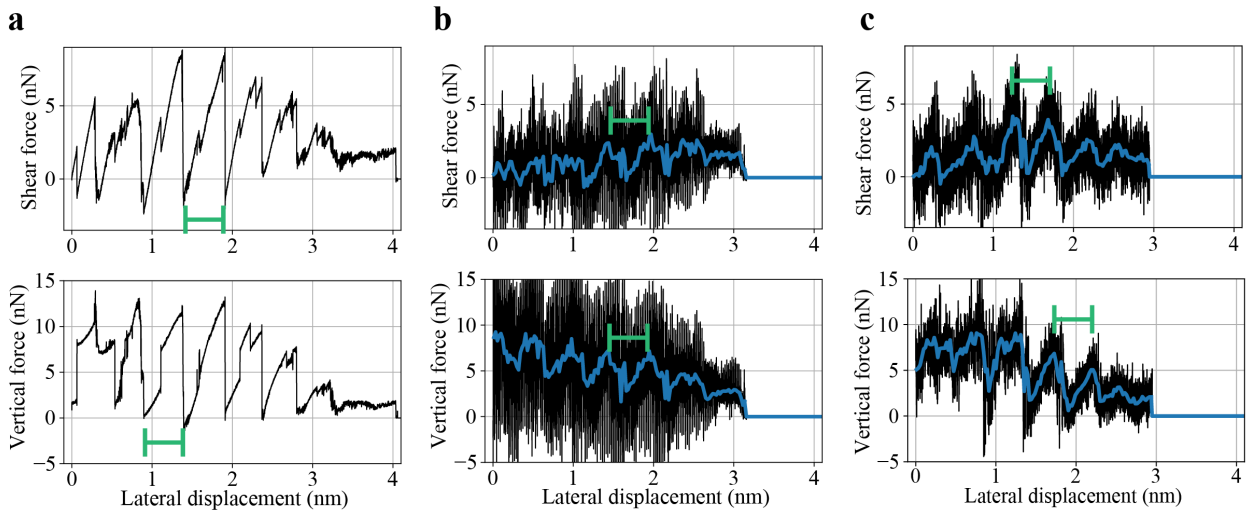

Figure 2.3: Horizontal and vertical forces of simulated shearing of the Au nanocontact of Fig.1. (a) No oscillations; (b) Large vertical oscillation ($a_0 = 0.22nm$); (c) Large twist oscillation ($\theta_0 = 30$ degrees) Blue lines are averages drawn for better visibility. Green bars show the length of slips. Its value ≈ 0.5 nm reflects the Au lattice spacing $a\sqrt{3}$ in the $2\bar{2}1$ sliding direction.

On the other hand, there are important differences. Our thin nanoconct shear slips are all atomic and, as explained above, correspond to a single step in the $(2\bar{2}1)$ direction. That differs from the evolution from single to multiple slips of the thicker Ag contact, where no quantization is detectable. Another difference is the magnitude of force jumps, which is much larger in the simulations. This very likely reflects vastly different relaxation times and mechanical stiffnesses of experimental and simulation shearing setups. One advantage of the stiff simulation setup we adopted is to emphasize direct access to *noise*, which is paramount in stick-slip shearing. The shearing noise in our simulation was strong, both in the (horizontal) x-directed shearing force and in the (vertical) z-directed force, see Fig. 2.3**a**. That is actually quite natural, for more than one reason. First, the vertical string tension, established and steady during the sticking period, must undergo a jump at each slip, while returning to a steadier, slightly smaller value at next sticking, when unbroken (110) chains reform, of course less numerous. Another is the decreasing level of parallelism of the slipping layers to the x-direction of shearing.

Shearing with vertical oscillations

In the subsequent main set of simulations we applied an oscillatory z-displacement $A(t) = a_0 \sin \omega t$, symmetrically to both leads. Increasing oscillation magnitudes a_0 were explored, reaching values up to $a_0 \sim 0.22$ nm where prior to shearing the nanocontact stiffness rheologically turned from positive to negative.[60]. The nanojunction zone underwent an oscillating tensile/compressive deformation. For small amplitudes, that simply added an oscillating noise on top of the signal of the previous case –see Additional note 2.7.2. At higher amplitudes $a_0 > 0.22$ nm, deformations are known to develop necking and bellying jumps, which repeat reversibly in each cycle of oscillation during shearing. The intrinsic string tension [1, 2], (thanks to which even a solid nanocontact resists breaking at necking and heals at bellying), maintains in this condition a large average tensile force. These are the two elements that drove the rheological softening of the contact prior to shearing. They remain at work during shearing while, in the course of time, the nanocontact thins down while maintaining its stick-slip advancing behaviour.

Fig. 2.3**b** shows the extreme case of $a_0 = 0.22nm$ vertical oscillation amplitude. The overall effect of oscillatory necking/bellying [60] is to make the nanocontact cross section narrower after each slip. It survived in spite of that, continuing to exert its string tension between the two leads. That kind of "live" behavior makes a ductile metal contact really different from rigid unreactive models. Despite such a violent and large oscillation amplitude at frequency of 1 GHz, stick-slip shearing still persisted (blue line in Fig. 2.3**a**), its characteristic length (green bar) the same as the previous case of shearing without oscillation.

Shearing with rotational ("twist") oscillations

In a subsequent set of simulations, instead of vertical oscillations, we mutually rotated the two leads with an oscillatory twist of the form $\theta(t) = \theta_0 \sin \omega t$ while at the same time actuating the shearing without any other perturbations. Because the stick-slip advancements reported in the two previous subsections were connected with interplanar 2D lattice slidings, a reasonable expectation was that oscillatory twists might deeply alter the shearing mode. The force profile of shearing with a torsional oscillation as large as $\theta_0 = 30°$ is shown in Fig. 2.3**c**. The shearing is visibly smoother. The nanocontact breaks earlier, confirming that twist oscillations disturb shearing more effectively than oscillating strains. Yet, even in this more disruptive case, the average frictional force is not much smaller. Importantly, and to some extent surprisingly, the stick-slip shearing habit persisted with the same atomic step length (green bar) as in the two previous cases. In order to minimize possible artifacts, we performed additional simulations adding an initial nonzero twist the the oscillatory one, as shown in Section 2.5. Despite differences of details and noise, the stick-slip shearing habit was found to persist even in that case. Only by pushing θ_0 to values as large as 60° was it possible to recover a smooth shearing habit.

Vertical force and string tension

In all shearing conditions, the stick-slip jumps of the friction force are systematically accompanied by even stronger jumps of the lead-lead normal force. An important feature of vertical forces that the nanocontact transmits, between the two leads (Fig. 2.3), is its systematically positive average value. That just reflects the natural string tension, which a ductile metal nanocontact will display in all finite temperature conditions, rationalized as follows. In a hypothetical liquid junction, the total free energy, minimized by reduction of the surface area, gives rise to capillary attraction between the two partner bodies. A solid crystalline nanocontact does not possess bulk capillarity, yet the mere chemical potential difference felt by an atom between the junction (an unfavoured site) and a bulk solid lead (a more favourable site) has consequences. The first is that atoms will slowly but inevitably drift thermally from the junction to the leads, provoking thinning and eventual breaking. The second is to create a thermodynamically based string tension between the leads qualitatively similar to that of a liquid neck, despite the inner crystallinity of the nanocontact [1, 2]. At every horizontal slip, the vertical force jumps in phase with the horizontal force, the nanocontact behaving as an oblique stretched spring. The magnitude of vertical force jumps is almost a factor 2 larger than the shear counterparts. The vertical force average – the underlying string tension – gradually drops as the shearing proceeds, clearly due to progressive thinning of the nanocontact prior to breaking, shown by Fig 2.1.

The vertical force traces of Fig. 2.3 complements the simultaneous information on the evolution under the oscillatory perturbations by the horizontal force on the shearing process. The first element is the persistence of vertical jumps approximately in phase with, and nearly twice as large than, the horizontal shear slips. As the shearing proceeds, the progressive drop of the vertical force average with tensile oscillations, and even more with twist oscillations, is stronger than without oscillations.

2.3 Shearing noise analysis

The previous Section presented the global picture of the rheological effect of oscillations on the shearing habit of a thin nanocontact. More quantitative insights can be obtained by Fourier analysing both shear (horizontal) and vertical force traces of Fig. 2.3. That also permits addressing the large mechanical noise which accompanies the shearing.

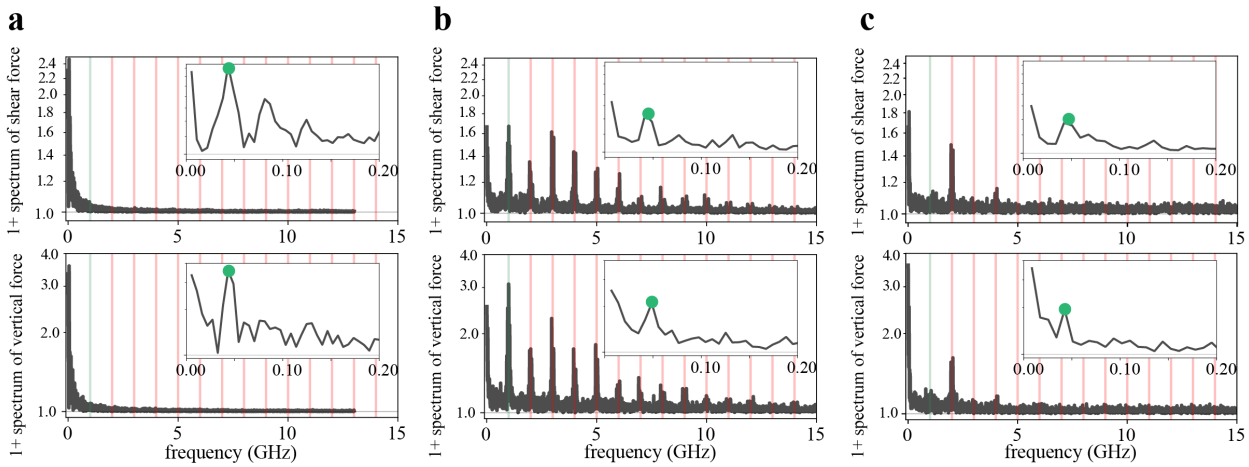

Figure 2.4: Spectrum of Fourier transform associated to Fig. 2.3 for (a) non-oscillatory shearing contact (b) extreme vertical oscillation ($0.22nm$) while shearing, (c) extreme rotational oscillation (30 degrees) while shearing. For better visibility, the y-axis is scaled logarithmic and the spectrum is shifted by $+1$. Inset is zoom-in low frequency interval. Green dot shows the stick-slip peak at ≈ 42 MHz, signaling the length-scale in Fig. 2.3. Note that the integer peaks are coupled with the stick-slip frequency –see Additional note 2.7.3.

Fig. 2.4 shows the spectrum of Fourier transform of the force traces of Fig. 2.3. The initial shearing without oscillations presents a single peak around ≈ 42 MHz (marked with green dot in the inset). That is the washboard frequency of atomic stick-slips $f_w = V_x/\lambda$, where $V_x = 0.022m/s$ is the simulated sliding velocity and $\lambda \approx 0.5$ nm is the atomic stick-slip length along $2\bar{2}1$ (marked with the green bar in Fig. 2.3). In the shearing with oscillations, either vertical or rotational, a weaker washboard frequency peak survives, even in extremely large oscillation amplitudes. Therefore the oscillations do not cause true rheolubricity in the shearing of the nanocontact. This weakening marks nevertheless a rheological softening of the shearing habit. That is due to the rapid oscillation-induced reversible plastic deformations, taking place while the slower shearing takes place. These plastic deformations were found to consist of necking-bellying for tensile oscillations [60], while they consist of interplanar angular locking-unlocking for rotational oscillations.
In both of these two cases –see Fig. 2.4**b,c**–, a high frequency noise appears in the form of higher harmonics of the imparted oscillation (1 GHz in the case shown). The sinusoidal imposed oscillation elicits a strong non-linear response. Qualitatively, we may associate the total number of peaks showing up to the number and intensity of rearrangements that the nanocontact needs to undertake in order to preserve its crystalline structure after each stick-slip events.

These nonlinear noise peaks offer a potential structural information insight. With rotational oscillations in particular, different combinations of n-th harmonics, such as odd or even, appear and disappear based on the relative crystalline orientation of the two leads. As shown in Fig. 2.4**c**, when upper and lower leads have the same crystal orientation, Fourier shear force peaks possess only even harmonics. That is because the shearing

slip generally takes place while the nanocontact is maximally twisted. The nanocontact spends the longest time near that top dead point, where the originally straight (110) chains are subjected by twist to a very costly "braiding". For vanishing average static twist Φ =0, there are two equivalent top dead points per rotational oscillation cycle. The shear force time dependence can be crudely assimilated to

$$p(t) = \mid \sin(\omega_0 t) \mid \tag{2.1}$$

As a result, Fourier shear force peaks only at twice of fundamental frequency ω_0, even harmonics.

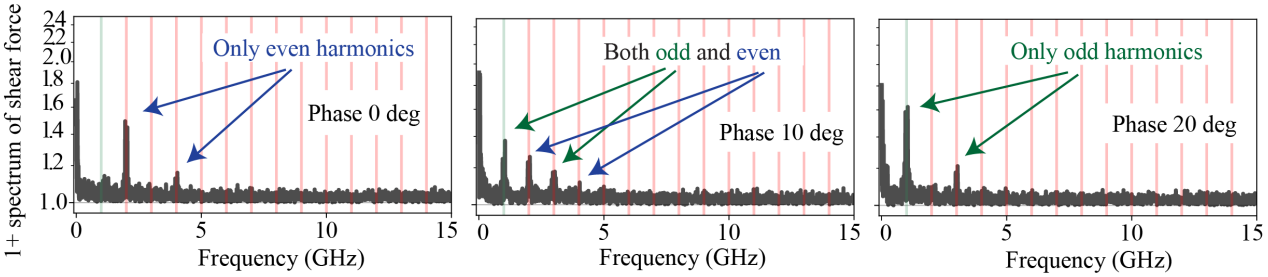

Figure 2.5: Fourier analysis of the force noise during shearing accompanied by a rotational oscillation ($\theta_0 = 30°$), for different crystal orientation, phase Φ of the two leads . Left, Φ =0, perfect alignment of the upper and lower leads (same as in Fig. 2.4c), where only even harmonics appear. Middle, intermediate misalignment Φ= 10°, where both odd and even harmonics are nonzero. Right, large misalignment Φ= 20°, where only odd harmonics appear.

The misalignment around a vertical axis of the upper lead crystal orientation with respect to the lower one, brought an interesting change. Increasing misalignments Φ= 10° and 20° yielded, as shown in Fig. 2.5, a clear evolution of noise spectral peaks. With Φ= 10°, both odd and even harmonics were nonzero. By increasing the misalignment to Φ= 20°, even harmonics disappeared and only odd harmonics remained. The main effect of the average misalignment Φ is to make the two top dead points, $\theta(t) = \theta_0 \pm \Phi$, inequivalent. Since shearing slips take place preferentially near maxima of $|\theta(t)|$, there is an imbalance of probability in favour of the positive top dead point versus the negative one. At the large misalignment Φ =20 degrees, the negative top dead point slip probability drops to essentially zero. This interesting asymmetry, results in a kind of 50% duty cycle, with a time dependence of the shear force closer to a "rectified" form

$$p(t) = (1/2)(1 + \text{sign}[\sin(\omega_0 t)]) \tag{2.2}$$

The Fourier transform of Eq.(1) has peaks precisely at $(2n + 1)\omega_0$.

For more general parameters θ_0 and $\pm\Phi$ of the rotational oscillations, the inequivalent efficiency of the two dead points directly reflects in the even-odd peak distribution of the noise Fourier transform. A distribution which, on the other hand, is relatively independent of the oscillation frequency ω_0. These results could be further developed for possible applications such as discovering the crystal orientations of nanocontacts, a feature usually only visible by TEM for unburied setups.

The present analysis is limited to mechanical noise, but the underlying structural phenomena suggest extrapolating mechanical noise to electrical current noise as well. As expected, and also shown by recent experiments [62], tensile force and conductance jump simultaneously at each of the successive contact thinning events that precede breaking. That is clearly explained by the drop in the nanocontact minimal cross section. The separate smooth evolution of force and current between the jumps are less correlated, with conductance as stable as the cross section, and pulling force building up to reach the thinning point.

2.4 Velocity and temperature dependence

We can now return to our initial motivation. Namely, discovering to what extent external mechanical oscillations, tensile or angular, could transform, without extra help by temperature, the shearing habit of a thin

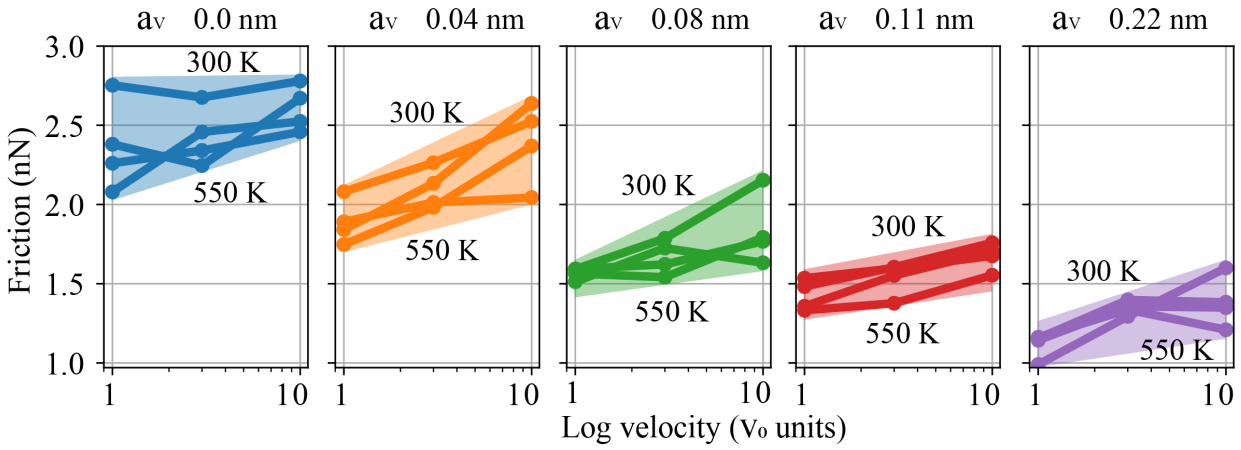

Figure 2.6: Shear friction force as a function of velocity v_0. Our lowest velocity (same in all cases in the main text) was $v_0 = 0.022$ m/s. Each line refers to a given temperature T and vertical oscillation amplitude a_0.

nanocontact from stick-slip to viscous – a process we called "rheolubricity". The velocity dependence of frictional shear, logarithmic for stick-slip, linear for viscous sliding, can provide the most direct diagnostic.[36] To verify this further velocity hallmark, we ran additional simulations at a variety of speeds and temperatures.

The average frictional shearing stress, conventionally defined as the midpoint average of horizontal force traces such as those of Fig. 2.2 and 2.3, was extracted and plotted versus velocity in Fig. 2.6 for various vertical oscillation amplitudes and for increasing temperatures. Each line represents the velocity dependence of friction at a given temperature and vertical oscillation amplitude a_v. The simulation thermostat always applied to the leads and not to the nanocontact) ensures in all cases that the mechanical heat introduced by oscillations and shear is completely completely conducted away. These further simulations were too limited in number to be statistically accurate; the resulting uncertainty is represented as a shaded area comprising upper and lower temperatures used. While that spread could not permit detailing a delicate logarithmic velocity dependence, the overall behaviour is clearly and undoubtedly much weaker than linear, in agreement with the persistence of stick-slip already reported in the previous sections. Results for twist oscillations, (not explored at this stage) are also expected to be similar. In conclusion, coherently with the previous sections, the mechanical oscillations do bring a noticeable amount of rheological softening of frictional shearing, but no proper rheolubricity at the frequencies considered. As will be mentioned in Conclusions, that outcome might only change at extremely low oscillation frequencies, outside of the range accessible to direct simulation.

2.5 Dynamical response function

In the course of shearing, a nanocontacts undergoes a structural evolution that rheologically affects its mechanical properties. Our imposed oscillatory perturbation, $p(t) = p_0 \sin \omega t$, elicits dynamically a certain response, in general not sinusoidal. Although not really a linear response, the (generally large) sinusoidal component $r(t) = r_0 \sin(\omega t + \phi)$ can be used and is used[5] as a mechanical impedance – a dynamical response function. For a vertical oscillation, $p_0 = a_0$, and $r_0 = f_0$, the latter is the best fit to the sinusoidal part of the vertical force intensity. Note the response of interest (Fig. 2.3) is very noisy at room temperature which requires averaging over several cycles in order to get a reliable fit (in our case, 10). The ratio $G = G' + iG'' = (f_0/a_0)\exp(i\phi)$ is the complex dynamical response function, whose real and imaginary parts are technically referred to as storage module (more commonly "stiffness"), and loss module.

In the rotational case, $p_0 = \theta_0$, while $r_0 = \tau_0$, the latter is the sinusoidal best fit to the torque intensity, and the corresponding response function $G_\theta = G'_\theta + iG''_\theta = (\tau_0/\theta_0)\exp(i\phi)$. These are the complex dynamical response whose evolution we wish to explore during the nanocontact shearing.

Results are shown in Fig. 2.7. All modules undergo dramatic up-down evolution in the course of shearing.

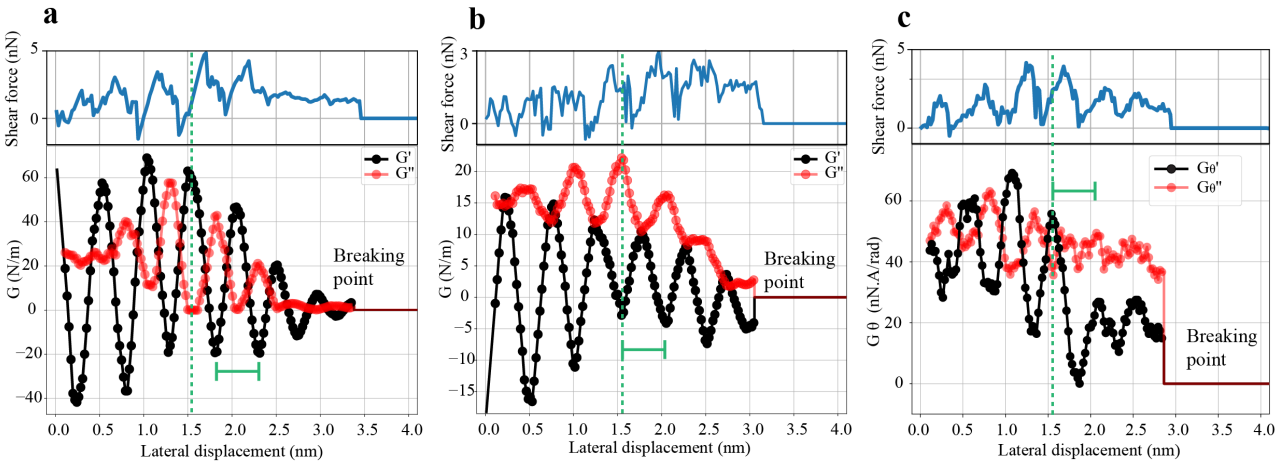

Figure 2.7: Evolution of the complex dynamic vertical response G for shearing with vertical oscillation with amplitude (a) $a_0 = 0.08nm$ (b) $a_0 = 0.22nm$, and (c) complex dynamic rotational response for shearing under rotational oscillation $\theta_0 = 30°$. Green marks indicate the periodicity of slip, same as in Fig. 2.3, and 2.4. The green dashed line is matching the extermums of dynamical module with almost middle of each stick-slip. The nanocontact is essentially elastic after each slip. Blue curve, is showing the shearing force as function of displacement. Please note G (G_θ) is calculated with vertical force (torque).

Opposite extrema of stiffness G'_θ and loss module approximately coincide with the mid point of the shear force slips – the green dashed line.

For the rotational oscillation, stiffness remains always positive, independent of amplitude θ_0, and it's undulation has its maximum stiffness almost at matching points along $2\bar{2}1$ direction of AB layers ≈ 0.5 nm. However for the vertical case, the story is different and depends on oscillation amplitude a_0.

For small $a_0 = 0.08$ nm (Fig. 2.7a), the stiffness G', initially positive, follows a simultaneous occurrence of stick-slip as shearing without oscillation or with rotational oscillation – see the force profile in Fig. 2.3 or Fig. 2.7a,c. For large $a_0 = 0.22$ nm, the stiffness G', initially negative owing to the large tensile oscillation [5, 60] undulates between positive and negative values as successive slips carry out the shearing. This response is reversed by a phase π, relative to that of rotational or small vertical oscillation, whose both having initial positive stiffness. It can be seen, from the shear force profile in Fig. 2.7 stick-slip is also shifted by half of it's usual periodicity 0.5/2 nm, or π. To understand the reason we have to look into the lattice structure. Shown in Fig. 2.8a, the lattice periodicity along $2\bar{2}1$ direction is 0.5 nm. However, projected from vertical direction 110, it is also possible to have alternate match of A with B instead of AB.

This is an interesting consequence of negative stiffness [1]. The contact is spending the long must of its resting time, during oscillation at dead point of each cycle, whose owning to negative stiffness results in slanted layers visible in direction $2\bar{2}1$ Fig. 2.8 previously know as necking and bellying. This analogy results in the alternate match of A with B as the minimum energy coordinates for the stick-slip to occur.

[1] To validate our understanding of negative stiffnessG', extra simulations are performed with no shearing but two simultaneous oscillation along vertical and orthogonal direction (y). See Additional note 2.7.4.

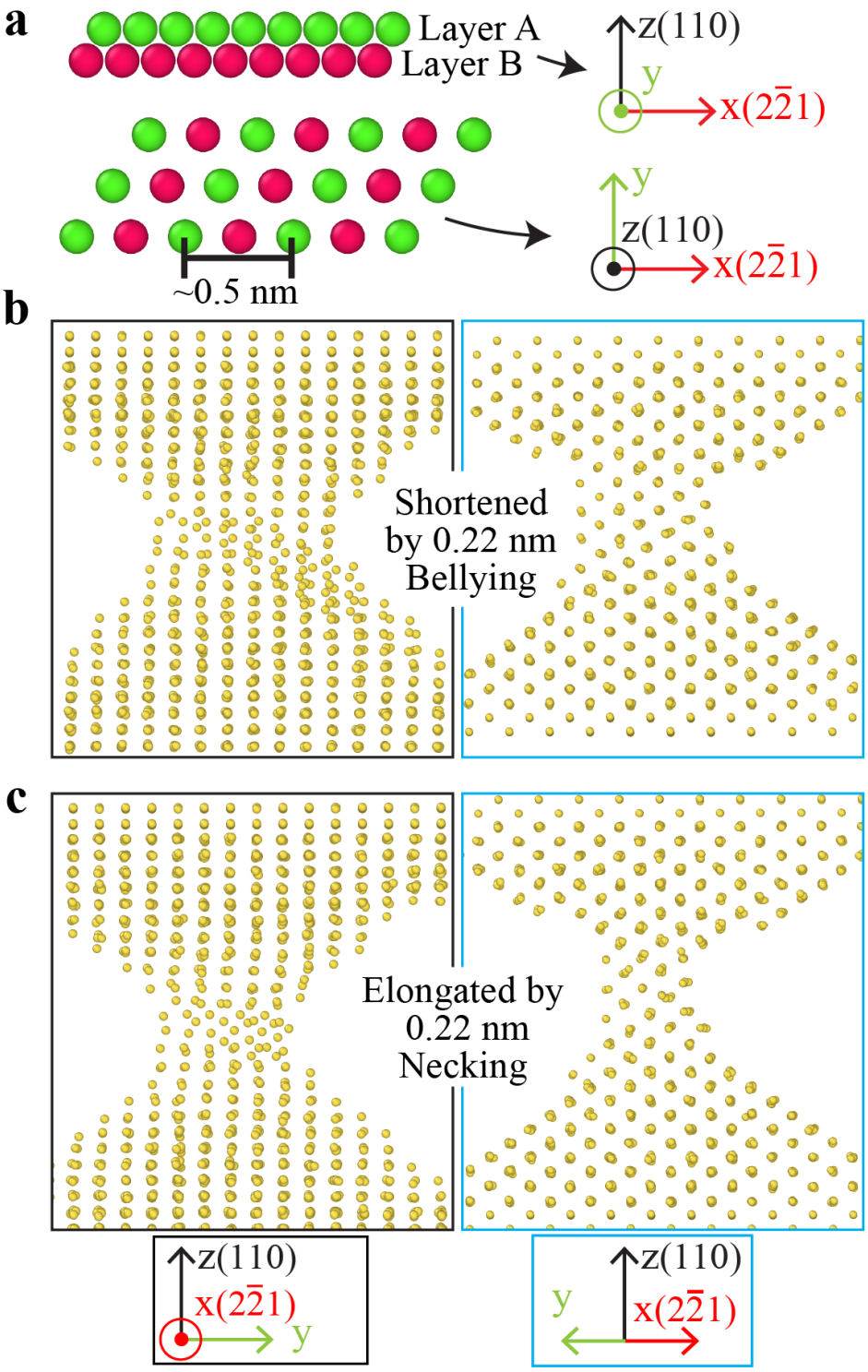

Figure 2.8: (a) The lattice structure, green and red represent A and B layer in the 110 direction. In the case of negative stiffness, A prefers to match with B and B with A, an alternation. (b) and (c) are showing the twinning moment occurring reversibly at each cycle of vertical oscillation near the dead-points where the contact spend must of it's time. This only occurs when the vertical oscillation amplitude is large enough (here 0.22 nm) giving rise to negative stiffness [60]. This particular layer arrangement shifts the stick-slip points by half the lead's surface lattice spacing $(1/2)a\sqrt{3} = 0.25$ nm, thus altering solution of AB matching BA, while maintaining the verticality of 110 chains. Panels (b) bellying, and (c) necking moments from two different angle.

2.6 Discussion and conclusions

Underlying this work is the broad question, to what extent the rheological friction softening caused by imparted oscillations might or might not resemble those of temperature. As is known from simple models, temperature has a weakening effect on dry friction. In particular, the energy barriers that give rise to stick-slip can be thermally overcome with a crossover to smooth sliding at high temperatures - a regime appropriately dubbed *thermolubric*[37]. The oscillation-free shearing of a crystalline nanocontact does, as we have shown, proceed by sudden advancement-induced rearrangements akin to stick-slips. It is thus natural to wonder whether, by analogy, an additionally imparted mechanical oscillations might similarly drive a crossover to a hypothetical *rheolubric* regime where sudden rearrangements and stick-slips could give way to smooth, liquid-like shearing. We have presented arguments backed by realistic simulations showing that mechanically imparted high frequency oscillations - either vertical, or rotational - while softening rheologically the frictional shear evolution of an ultrathin gold nanocontact, do not suffice to produce rheolubricity, i.e., to turn the nature of the shearing process from stick-slip to fully smooth and viscous. That failure goes hand in hand with the known persistence of a crystalline structure in the oscillated nanocontact which opposes a smooth shearing shearing. Crystallinity is unexpectedly robust also thanks to the pervasive string tension present in the nanocontct in all conditions.

The persistent stick-slip nature of shearing entrains a number of consequences. First, and unmistakable, the velocity dependence of friction is much weaker than linear as would be expected for viscous sliding. Our simulated velocity dependence is indeed compatible with the logarithmic dependence typical of stick-slip. Second, there is a strong mechanical shear noise, with nonlinear mixing between the washboard and oscillation frequencies. As an interesting side note, the predicted Fourier spectrum of shear noise with rotational oscillations may change from only even to only odd overtones depending on the relative crystalline orientation of the two leads. That is an unanticipated result of potential value for structural diagnostic. Accompanying all the above, during the stick-slip shearing the nanocontact complex dynamical modulus – stiffness and loss module – jumps dramatically at each slip. As a result of planar alternation, their phase shifts by π in the case of negative stiffness, experimentally an observable element.

A relevant question to be discussed before closing is the domain of validity of these results, based as they are on simulations with relatively large shearing velocities and extremely large oscillation frequencies. What if these velocities and frequencies were much lower? Thermodynamics actually demands that shearing at sufficiently low velocity should necessarily reach the thermolubric regime, where stick-slip must disappear.[8, 37] Similarly, oscillating a nanocontact at a sufficiently low frequency should wash out the necking-bellying phenomena, with crossover to a smooth, nearly adiabatic evolution [60]. Simulations cannot approach these low frequency and velocity regimes, but extrapolations are nonetheless possible as follows. Concerning frequency, it was estimated in the past that the crossover oscillation frequency for a nanocontact such as that studied here should be around 600 Hz. Therefore, even for very modest oscillation frequencies, from kHz to MHz, the stick-slip scenario just presented should still hold – of course with numerical modifications in case of different nanocontact sizes. Similarly, by equating the washboard frequency $\sim V_x/a$ to the crossover frequency (600 Hz in our case) we estimate a low velocity limit ≈ 300 nm/s, where stick-slip shearing should turn thermolubrically viscous. Nevertheless, the nature of rheological softening, is different from that of thermolubric.

The above estimates suggest a speculative experimental proposal in conclusion of this work where rheolubricity was sought and not found within the parameter ranges of our simulations. Suppose a nanocontact shearing experiment was initially started at a velocity just above the crossover velocity, without oscillations. The shearing would be stick-slip as described. If subsequently at that point the oscillations were turned on, the regime should change, with a transition from stick-slip to viscous shearing. The same result could be obtained at constant velocity by switching oscillations from above to below the crossover frequency. Rheolubricity seems therefore attainable in future experiments.

2.7 Additional notes

2.7.1 The evolution of breaking junction

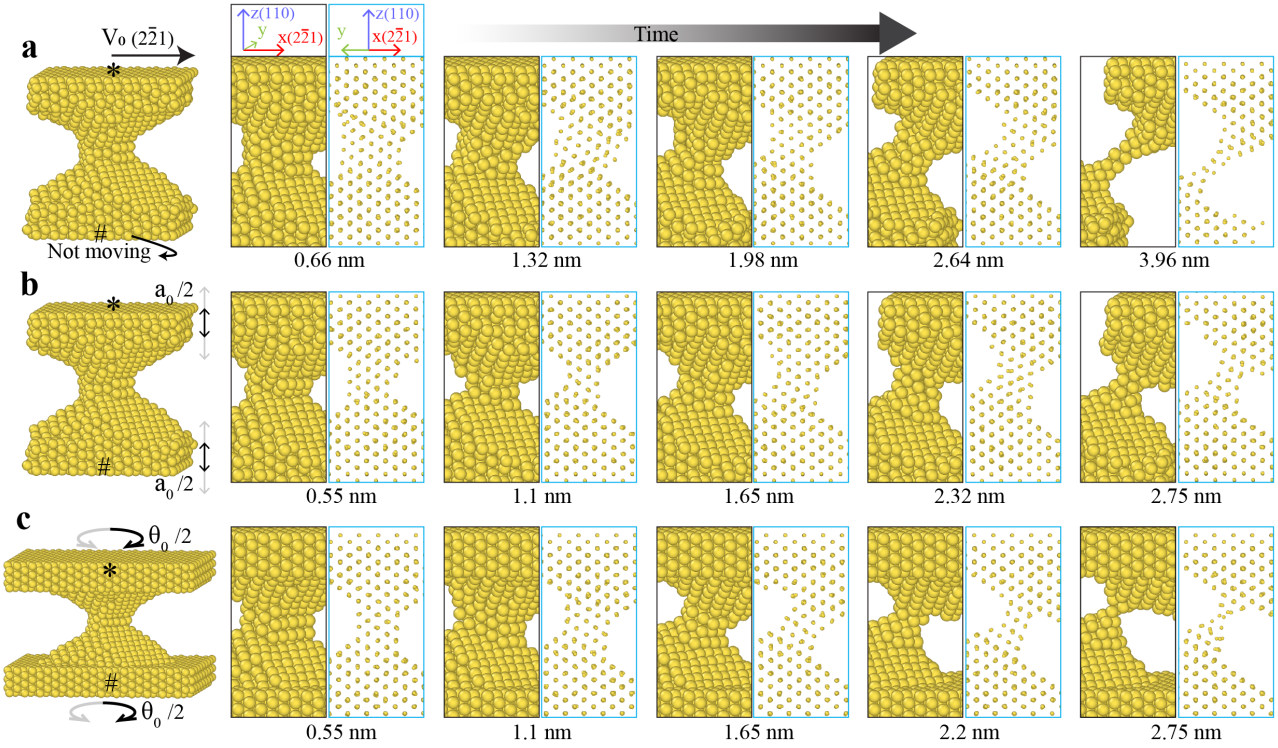

Figure 2.9: Lattice structure evolution. (a) While shearing without oscillation, the same as identical to Fig. 2.1; (b) with vertical oscillation a_0=0.22 nm ; and (c) with rotational oscillation θ_0 = 30 degrees. Black and blue frames show the same moment of shearing from two different perspective. Shearing velocity V_0 = 0.02 m/s; frequency of oscillation in both vertical and rotational case set is 1 GHz

2.7.2 Small vertical oscillations

In Fig. 2.10 we show how the effect of small oscillations, 0.04 nm and 0.08 nm is building up a noise in the original signal of shearing without vertical oscillation. This rheological noise is reducing the average friction overall – see the orange line.

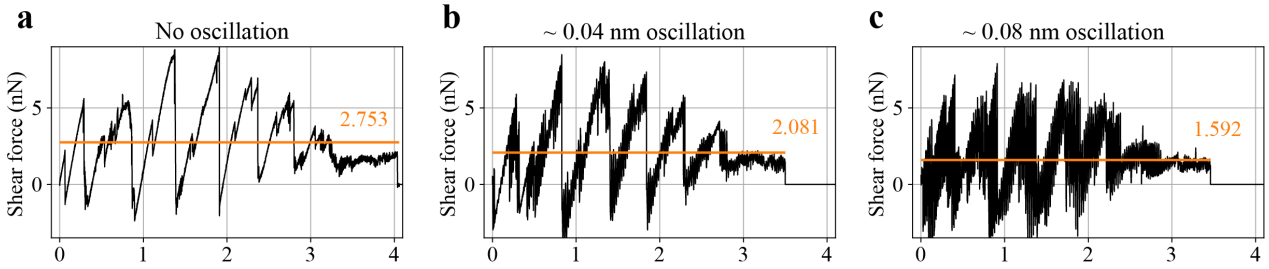

Figure 2.10: Shear force signal for (a) shearing without oscillation (b) with vertical oscillation of small amplitudes 0.04 nm (c) and 0.08 nm

2.7.3 Coupling of washboard and oscillation spectra

It is interesting to analyse the fine frequency structure of our shearing force spectra. As the inset in Fig. 2.4 shows, the washboard frequency is that the of stick-slip peaks, ≈ 42 MHz. The external oscillation peaks are at the higher frequency of 1 GHz. Owing to the strong nonlinearity of the system, and to the high shearing velocity, $0.022m/s$ in our simulations, the two phenomena couple and interfere, and the two frequencies mix. As a result, all oscillation-related peaks are split by the much smaller washboard frequency, as shown in Fig. 2.11. In experiments with much lower sliding velocities, the coupling should be reduced. If moreover much lower oscillation frequencies could be used, the nanocontact rhelogical behaviour could evolve from necking/bellying to adiabatic, whereby all high frequency peaks would disappear altogether. Based on an order of magnitude calculation, the crossover frequency of the current nanocontact is estimated to be 600 Hz.

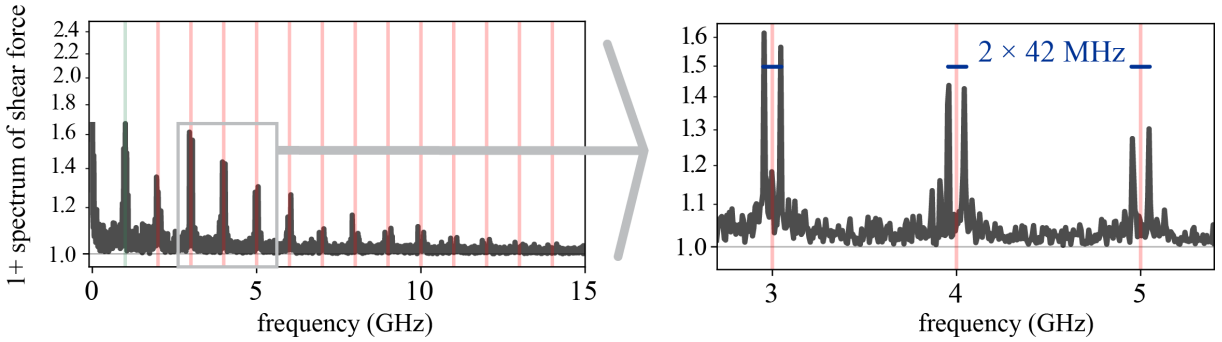

Figure 2.11: Frequency analysis of shearing force accompanied with large vertical oscillation of $a_V = 0.22nm$, the same case as in Fig. 2.4b. The zoom-up in the right, shows a hidden overcoupling feature, with separation of twice the stick-slip frequency, ≈ 42 MHz. This feature should disappear in experiment, without eliminating the rearrangement peaks.

2.7.4 Evolution of vertical G with lateral oscillation

This time, we run a series of simulations of the same contact oscillated laterally (y direction) and vertically (z), but with no shearing. Results confirm our understanding of negative G', turning its sign once it's accompanied with large lateral oscillation.

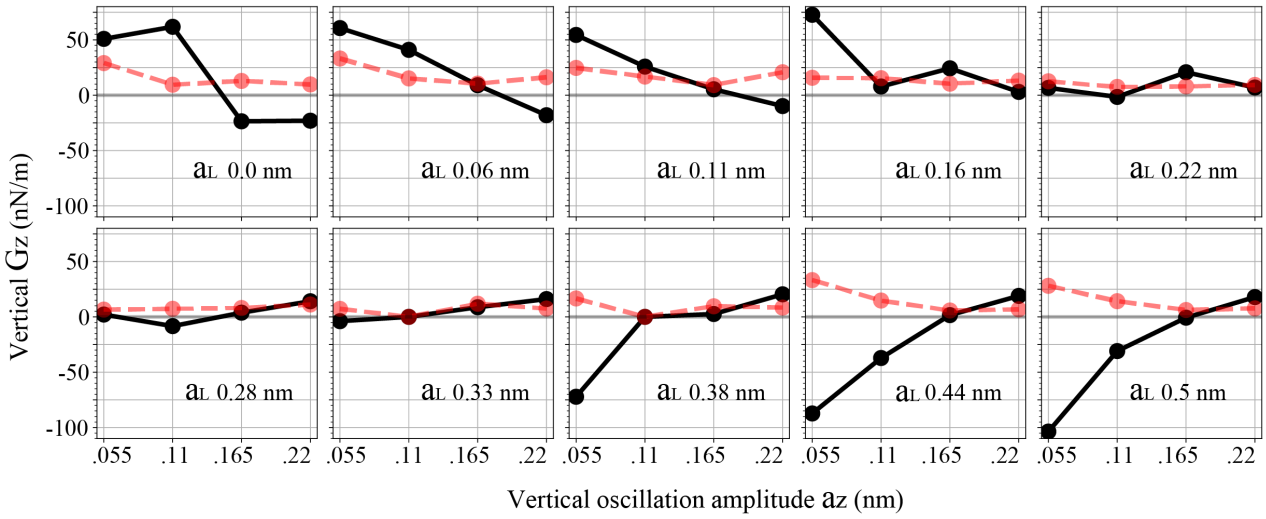

Figure 2.12: Vertical G as function of a_z, in the presence of lateral oscillation a_L. Black line is the real part of dynamical module, G' and red is the imaginary part G''

Part II

Layered Materials

Chapter 3

Colloquium: Sliding and Pinning in Structurally Lubric 2D Material Interfaces

3.1 Introduction

Besides the electronic properties of graphene-like 2D materials that attract most of the attention [63–68], their mechanical, tribological and rheological characterization must in parallel be physically understood and controlled [69] for many reasons. A first, practical one is that mutual sliding of two juxtaposed 2D material layers is known to be quite easy, owing to their weak interlayer van der Waals interaction. Beyond that, mutual incommensurability of 2D materials interfaces can lead to ultra-low sliding friction, a property known as "superlubricity" [70, 71]. That property makes it naturally attractive for energy saving and potentially for lifetime increase. Good lubricity makes them promising for the application in micro/nano electromechanical systems, e.g., micro/nano-generators and nano-oscillators [72–75]. Another one, more substantial, is that our current understanding of "superlubricity" is still too vague. On the whole, the friction's connection to incommensurability and rotation is as we shall see a source of surprises.

A host of questions arise about the facile sliding of these incommensurate 2D crystalline interfaces, or alternatively on their mechanical pinning against shear. The exceptional in-plane robustness coupled with great out-of-plane membrane-like flexibility are brand new elements. Another one is the unusually important adhesion between the very flat layers. These elements make 2D materials interfaces different from other frictional systems [76] as 3D solids [56, 77–79], adsorbed layers and clusters [80–83], colloid monolayers [84–88], etc. For nano to mesoscale, the size and temperature dependence of static friction of 2D material contacts, as well as their comparison with that of (velocity-dependent) kinetic friction generally differs from classic macroscopic laws in a way that is currently addressed case by case. The widespread concept in the sliding of crystalline interfaces is structural lubricity between incommensurate faces [89–92], generally believed to imply superlubricity [36, 71, 93–96]. It should be noted that this term is nowadays used with different meanings in physics and in engineering.

Standard superlubricity [90], which is adopted in the colloquium as synonymous to ***structural superlubricity*** [92], can be defined for infinite defect-free systems as an *unpinned*, free sliding state. That is a state where the static friction F_s – the smallest force needed to initiate the sliding motion – is mathematically zero even down to $T = 0$. In the real world of course everything has finite size, even without defects. The edges destroy the slider's perfect translational invariance, inevitably causing static friction. However, if the slider's bulk is structurally superlubric and defect-free, F_s scales as A^α with $\alpha \leq 1$. For $\alpha < 1$ we shall refer to this real-world cousin of structural superlubricity as ***structural lubricity***. Despite the celebrated early detection of superlubricity [97, 98] in structurally lubric twisted graphene flakes and graphite interfaces [71, 98–106] and theoretical work [107–112], the community remains in need of a broadly applicable roadmap applicable to the sliding of 2D layered materials.

Below is a list of some questions that seem currently open and/or debatable, which are discussed in the colloquium:

What is the origin of friction and how are static and kinetic friction related at 2D materials interfaces? What kind of area, temperature, velocity and load dependence of interface sliding friction should one generally anticipate? Specifically, different experiments report different scaling of friction with area A^α, with exponent α ranging from 0 to 1. What is the origin of this dispersion? What role does the extreme 3D anisotropy of these poorly extensible, yet very flexible and easily corrugated membranes play? Why is it that structurally lubric 2D material experimental sliders generally exhibit a logarithmic velocity dependence (the earmark of stick-slip) [113–115], instead of a linear one (the earmark of smooth sliding)? Can temperature (or load) bring about a change between high and low friction states?[61, 116] And what are numerically the actual friction coefficients of the 2D materials interfaces? Is the differential friction coefficients, generally used for 2D materials, really adequate?

I briefly revisit some concepts from our colloquium [8] in this chapter, with no conclusion, since they are appropriate for the subsequent chapters.

3.2 Velocity and temperature

The stacking of a 2D material onto its substrate is a crucial information in order to understand its frictional sliding behaviour. Incommensurate crystalline stackings are expected to be, when perfect and unbounded, structurally superlubric. As was said above, in that state the static friction is zero, because lateral forces totally cancel out. More often and practically, 2D crystalline interfaces are at best structurally lubric. In that state, the incommensurate sliding layer is pinned to the substrate, due to edges or other impurities. In this case, three regime for velocity dependence of friction are expected, namely stick-slip, thermolubric, and ballistic.

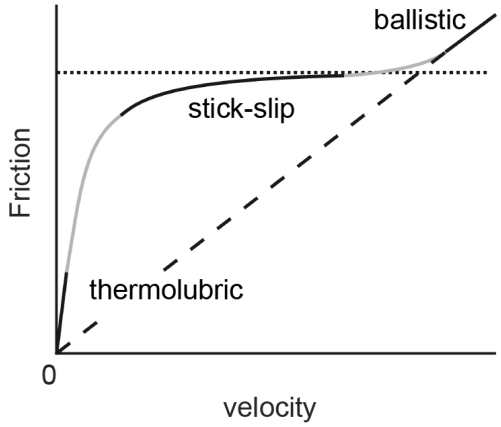

Figure 3.1: Three friction regimes of a pinned structurally lubric contact as a function of velocity: thermolubric, stick-slip, and ballistic; sketch reproduced from [61].

Stick-slip generally implies a weak logarithmic velocity dependence, roughly $F_\mathrm{k} \propto (\ln v)^\gamma$ with $2/3 < \gamma \leq 1$ [37, 113–115, 117–120]. The well-known qualitative reason for this weak dependence is that increasing velocity just increases the frequency of stick-slips but basically not the average frictional force.

The two other regimes, thermolubric and ballistic, emerge.As sketched in Fig. 3.1, drawn after Ref. [61], stick-slip friction turns viscous when velocity is either high or low enough, for two opposite reasons. At high velocity, typically when the kinetic energy exceeds the largest energy barrier energy $\frac{1}{2}Mv^2 > U_0$, barriers lose their grip, and friction turns “ballistic" [121], a regime where friction rises linearly with velocity. Conversely, at the low velocity limit and nonzero temperature, a nanoslider has ample time to thermally diffuse back and forth across barriers. In that condition Einstein’s viscous drift regime applies – a regime also referred to as “thermolubric" [61, 116].

In all the experiments in the following chapters 4 and 5, shearing and slider velocities are in the range of μm/s, whereas achievable velocities in simulations are typically closer to m/s, that is six orders of magnitude higher. Luckily we can still continue to use these simulations, as long as we understand the physics behind them and their validity regime. In this case both experiment and simulations are in the same stick-slip window.

Temperature dependence will also differ in these three regimes.

Medium and low speed stick-slip friction: In this regime, as temperature increases, friction is expected to gently decrease by terms roughly like $-\ln T$ [37, 117, 120]. This behavior is attributed to thermal fluctuations aiding in overcoming energy barriers, leading to a negative temperature dependence that corresponds to the logarithmic velocity dependence of stick-slip [122, 123].

Ultra-low speed thermolubric and viscous friction: In this regime, friction decreases much faster than logarithmic as temperature rises. Here, the externally forced drift is a weak perturbation of thermal random walk, and frictional damping (ζ) follows Einstein's relation $\zeta = k_{\mathrm{B}}T/D$, where D is the diffusion coefficient. The exponential growth of $D \propto \exp(-W/k_{\mathrm{B}}T)$ with temperature (Arrhenius-like behavior) overcomes the linear growth of ζ with temperature.

High speed ballistic friction: In this regime, friction is predicted to grow linearly with temperature, as phonon scattering of a fast slider –as exemplified *e.g.,* in ref [121]– is enhanced by the growing dynamic corrugation of the interface at higher temperatures.

3.3 Load

Historically, the load dependence of sliding friction is characterized by the friction coefficient $\mu = \frac{\text{friction force}}{\text{normal load}}$, a key parameter in tribology dating back to da Vinci and Amontons [124, 125]. In rough interfaces, increased friction with load is linked to larger contact area and enhanced role of interface corrugation. However, at the nanoscale, the load-dependent behavior is system-specific and typically non-linear.

In the 2D layered material interfaces, friction does not show a linear relationship with the applied load. Even at zero external load, a finite frictional force is present due to physical adhesion effects, such as van der Waals attractions and electrostatic interactions, which make the pinning effect of edges and impurities felt, even in structurally lubric interfaces. Such adhesional forces easily cancel each other at rough interfaces [126–129]. The adhesion pressure, indicated as P_{adh}, plays a significant role in shaping the friction-load curve [130]. The friction coefficient (μ), defined as the ratio of the frictional shear stress ($\tau = \frac{\text{shear force}}{\text{contaxt area}}$) to the total normal pressure:

$$\mu = \frac{\tau}{P_{\mathrm{ext}} + |P_{\mathrm{adh}}|} \tag{3.1}$$

provides a more appropriate measure of friction in nanoscale.

It is important to note that, in the following chapters 4 and 5, load is exerted by an external AFM tip. Although the formula in (3.1) is meant for layered material rather than for a tip on substrate, the adhesion P_{adh} between substrate layers are negligible, and the friction coefficient there is independent of that.

Chapter 4

Relation between Interfacial Shear and Friction Force; Quasi-freestanding Graphene

4.1 Introduction

Two-dimensional (2D) materials, such as graphene, are usually exfoliated onto or directly grown on a substrate, which can change the 2D material's chemical, electronic and mechanical properties [131, 132]. Furthermore, intercalation of atoms between the substrate and 2D layers is a common methodology to tune the properties of 2D films [133–136]. Interlayer and layer-substrate interactions are usually probed by investigations of their electronic properties, for example, by using angle-resolved photoemission spectroscopy [133], or by studying the strain with Raman spectroscopy [137, 138]. Recently, interlayer elasticity has been probed by atomic force microscopy (AFM) and has shown a high sensitivity to the presence of intercalated water in graphene oxide [134].

An important property of the interface between the substrate and 2D layer is the interfacial transverse (out-of-plane) shear modulus [139], G_{int} , measured from the in-plane strain experienced by the top atomic layer when a shear force, parallel to its surface, is applied to the atomic layer while the substrate experiences an opposing force. This shear modulus, which is conceptually similar to the c_{44} elastic modulus in graphite [140, 141], is critically related to the chemistry, order and structure of the interface [141], and it is of key importance to understanding the strain-controlled electronic and optical properties [142], as well as the frictional behaviour, of 2D materials [105]. It is also relevant for a broad spectrum of applications [143–147]. Unfortunately, there are very few theoretical and experimental studies on the transverse shear modulus of 2D multilayers [148, 149], and no reported measurement or calculation of the interfacial transverse shear modulus of a single atomic layer on a substrate, to the best of our knowledge.

Here, we show how to measure and control the interfacial transverse shear modulus of one and two supported atomic layers on a substrate (Fig. 4.1a,b). In particular, we investigate monolayer (1 L) and bilayer (2 L) epitaxial graphene films grown on the Si face of SiC(0001) [150], where a typical buffer carbon layer (BfL) sits in between graphene and SiC (Ref. [150]; for example, 1 L/BfL/SiC in Fig. 4.1c); in addition, we investigate 1 L and 2 L quasi-free-standing epitaxial graphene films on H-terminated SiC(0001) (Refs. [151, 152] ; 1 L/H − SiC in Fig. 4.1d), and twisted 10 L epitaxial graphene grown on the carbon face of SiC$(000\bar{1})$ (Ref. [153]; twisted 10 L/SiC in Fig. 4.1e). Finally, we compare the above samples with bulk highly oriented pyrolytic graphite (HOPG) where the graphitic planes have an AB stacking order (Fig. 4.1f) with a small mosaic angle. The experiments show that the interfacial shear modulus is critically controlled by the stacking order, the atomic layer-substrate interfacial interaction and the substrate shear stiffness. Furthermore, we show that G_{int} , and therefore the associated 2D layer interaction with the underlying substrate, is a key physical and measurable property to control and predict sliding friction in supported 2D films, a topic that has produced a large amount of fundamental yet somewhat controversial studies [99, 104, 131, 154–156]. In particular, for all the above-described graphitic systems, we observe a reciprocal relationship between the friction force per unit contact area and the interfacial transverse shear modulus. This reciprocal relationship also emerges from simulations using the Prandtl-Tomlinson (PT) model. These findings are further rationalized by simplified one-dimensional (1D)

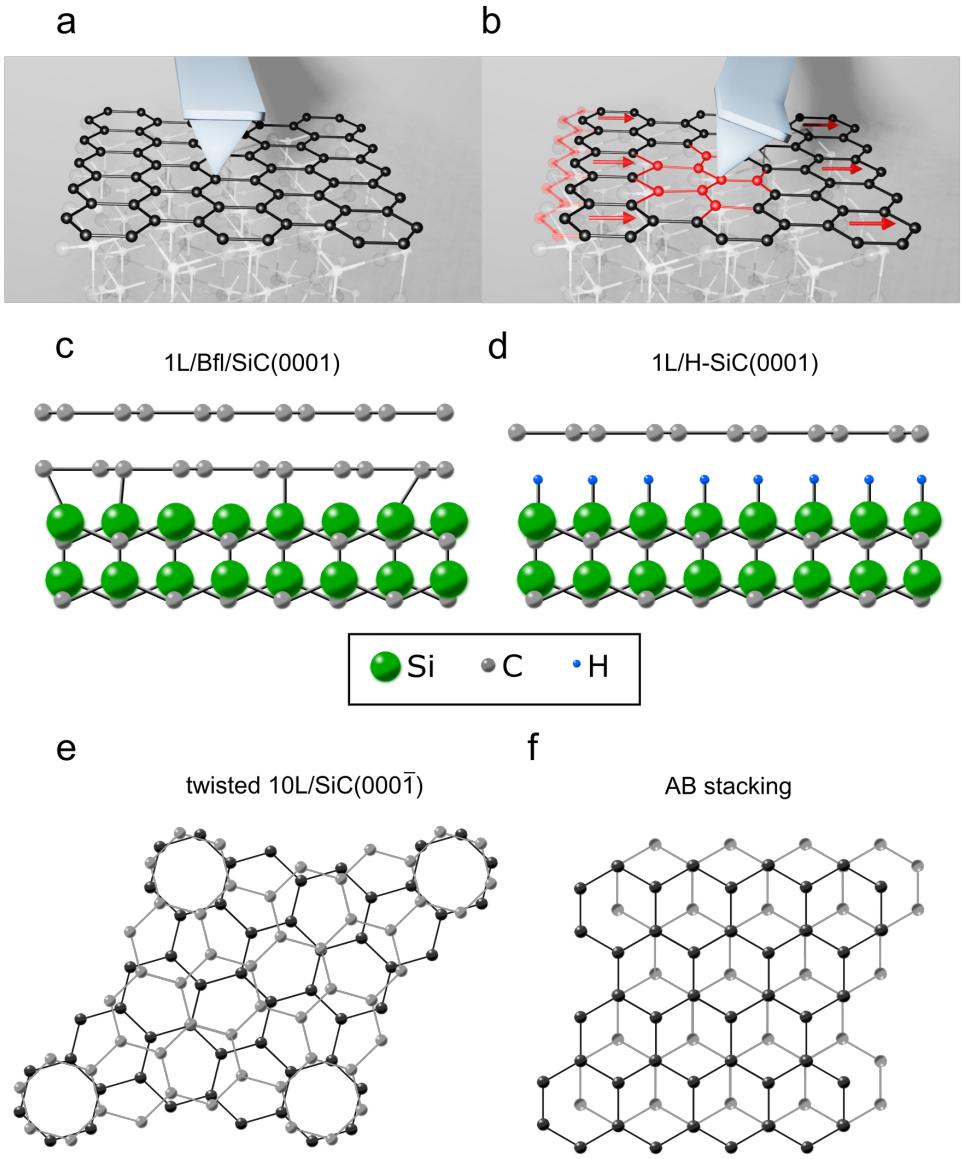

Figure 4.1: Interfacial transverse shear modulus experiment. a,b, Scheme of the interfacial shear modulus experiments. Initially, an AFM tip is brought into contact with a graphene layer sitting on a substrate (a). The AFM tip is then oscillated in-plane while in contact with the graphene surface, causing rigid moving of the graphene atomic layer in an elastic regime (no slipping; b). c, Scheme of one epitaxial graphene layer on the conventional graphene-like buffer layer on SiC(0001). d, Scheme of one quasi-free-standing graphene layer on SiC(0001) after hydrogen intercalation. e, Scheme of stacking between two graphene layers in the case of twisted 10 L/SiC(000).f, Scheme of AB stacking, the most favourable stacking between two graphene layers.

simulations of a tip sliding over a Frenkel-Kontorova (FK) harmonic chain, which mimics the graphene layers, in the presence of a sinusoidal 'substrate' potential mimicking the graphene-substrate pinning. An increase in the amplitude of the substrate potential is shown to be related to an increase in the interfacial transverse shear stiffness. Accordingly, a larger interfacial shear stiffness and larger potential amplitude decrease the tip-induced lateral deformation and associated dissipative events, resulting in lower friction-a mechanism that differs from those proposed so far for 2D materials.

4.2 Experimental data

Existing measurements

The interfacial shear modulus of different types of epitaxial graphene films and HOPG is investigated by experimentalists by modulated nano-shear (MoNS) methods (Fig. 4.1a,b), which have been conceived from the modulated nanoindentation (MoNI) method [134, 157–159]. MoNS experiments are performed on epitaxial graphene films with different thicknesses, substrates and stacking orders, as well as on bulk HOPG. In particular, we investigate four different types of epitaxial graphene films on the Si face of SiC, namely, monolayer and bilayer epitaxial graphene films on the buffer carbon layer (for example, 1 L/BfL/SiC in Fig. 4.1c), and hydrogen-intercalated monolayer and bilayer quasi-free-standing epitaxial graphene films (for example, 1 L/H − SiC in Fig. 4.1d). We also investigate ten layers of twisted epitaxial graphene grown on the C face of SiC (Ref. [153]; twisted 10 L/SiC in Fig. 4.1e) and bulk HOPG. Fig. 4.2 shows the measured curves of lateral contact stiffness versus normal load, $k_{\text{cont}}^{\text{lateral}}$ (F_{N}), for each sample, where the solid lines represent the mean values obtained from multiple experiments in different sample regions and the shaded areas represent the standard deviation obtained from these multiple experiments. The obtained values of G_{int} are averaged and summarized in Table 4.1. The experiments reveal that G_{int} in epitaxial graphene grown on the Si face of SiC increases from 190MPa for 1 L/BfL/SiC graphene to 217MPa for 2 L/BfL/SiC graphene. First, we notice that the obtained G_{int} values are close to the values of the transverse shear modulus (c_{44} constant) of bulk turbographite, where the layer stacking is random, that is, between 180 and 350MPa (Refs. [141, 160]), and also close to the values of the interlayer shear modulus of non-supported multilayer graphene, about 400 ± 250MPa (Ref. [149]). This observation suggests that the measured G_{int} is not related to extensive stretching of the covalent bonds within the graphene layer, or to the associated, much stiffer in-plane shear modulus of graphene, about 0.5TPa (Ref. [161]). Second, we observe the same G_{int} dependance on the number of layers in both non-intercalated and H-intercalated graphene samples grown on the Si face of SiC. The interfacial shear moduli of 1 L/H − SiC and 2 L/H − SiC are 217MPa and 246MPa, respectively. The ratio between monolayer G_{int} and bilayer G_{int} is equal to 0.88 for both non-intercalated and intercalated graphene, which corresponds to an increase of 14% for 2 L with respect to 1 L. This identical layer dependence of G_{int} suggests that the origin of this increase is the same in both intercalated and non-intercalated graphene.

The interfacial shear modulus dependency on the stacking order is demonstrated in a study in the literature [162], where the authors study the transverse shear modulus (c_{44}) of graphitic systems using density functional theory calculations. These calculations show that the transverse shear modulus increases when moving from a random graphenegraphene stacking of the layers to a perfect AB stacking. In our experiments, where the tip indentation is below 1, we measure G_{int} , which is the transverse shear modulus of the top atomic layer with respect to the underneath material (or substrate). Therefore, based on the above density functional theory simulations, we conclude that 2 L epitaxial graphene, which has perfect AB stacking, has a larger G_{int} than 1 L epitaxial graphene, which is sitting on a rough graphene-like layer with a mixture of sp^2 and sp^3 bonds [163]. Indeed, several experiments in the literature [164–166] show that bilayer graphene grown on the Si face of SiC has an AB stacking order. On the other hand, single-layer graphene on a buffer layer presents a mixture of AB-like and AA-like stacking orders [167]. Furthermore, twisted 10 L/SiC graphene films grown on the C face of SiC have a peculiar stacking sequence (Fig. 4.1e) where adjacent layers are rotated relative to each other, with a 30°(R30) or ±2.20° ($R2^{\pm}$) rotation from the SiC bulk (1010) direction [153]. The MoNS measurements show that G_{int} (1 L/BfL/SiC) < G_{int} (twisted 10 L/SiC) < G_{int} (2 L/BfL/SiC). This result can be understood in terms of the energy landscape of the stacking order. Larger values of G_{int} are found in 2 L/BfL/SiC because the perfect AB Bernal stacking order is the most stable stacking, while twisted 10 L/SiC has a unique, highly ordered stacking of non-Bernal rotated graphene planes that is less energetically favourable than AB stacking, and finally 1 L/BfL/SiC has a disordered mixture of AB-like and AA-like stacking [167] that gives the lowest G_{int} values, in agreement with the density functional theory simulations [141].

On the other hand, to understand the results of the H-intercalated samples, we consider the interaction of the top layer with the underneath layer or substrate. In 2 L/H − SiC, the first graphene layer sits on top of a H-terminated SiC surface [168], while the second layer is again forming an AB (Bernal) stacking structure with the underlying first layer [169]. As discussed above, the stacking misorientation of 1 L graphene on H − SiC is the origin of a decreased G_{int} compared to the ordered AB stacking of 2 L graphene on H − SiC. While stacking order has a strong impact on the transverse shear modulus, other material properties are clearly important, such as more broadly the strength of the interaction of the top 2D layer with the underlying layers or substrate, and the in-plane shear stiffness of the 2D layer, which in this work is constant since we are considering only

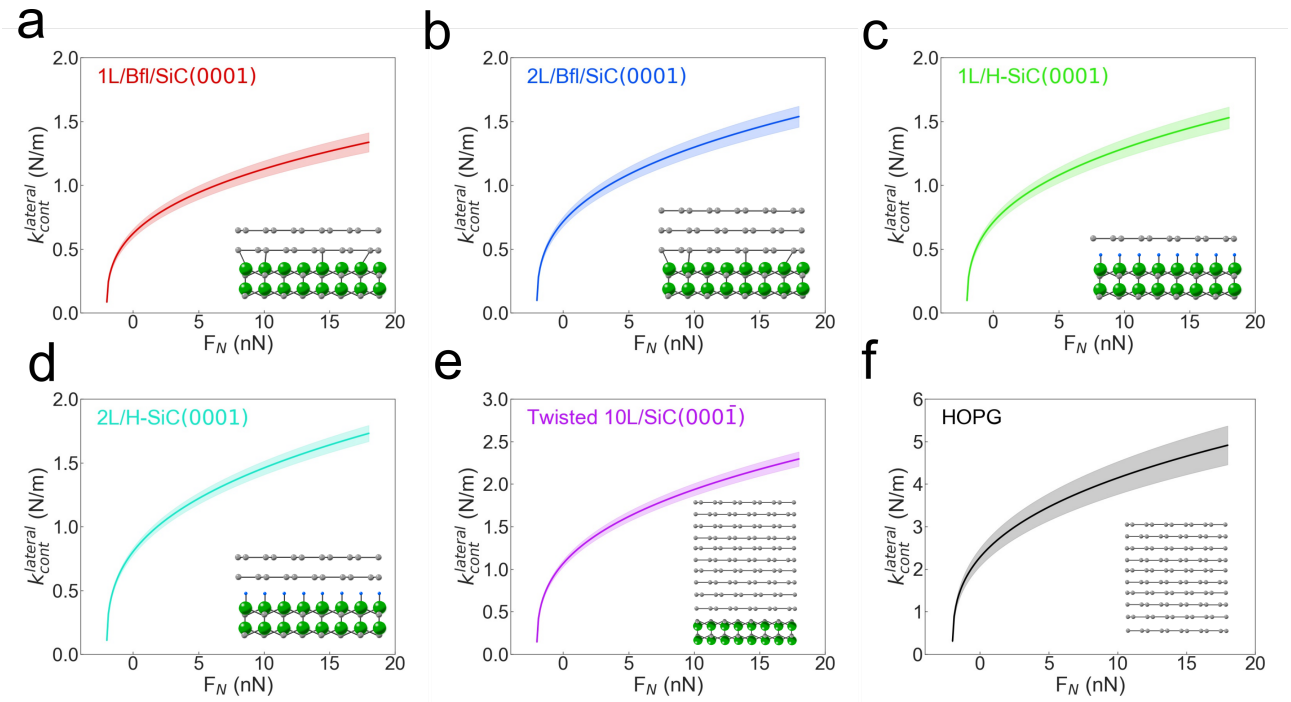

Figure 4.2: Interfacial shear modulus measurements. a-f, Contact stiffness ($k_{\text{cont}}^{\text{lateral}}$) versus normal load (F_{N}) obtained from the MoNS measurements for 1 L/BfL/ SiC(0001)(**a**), 2 L/BfL/SiC(0001)(**b**), 1 L/H − SiC(0001)(**c**), 2 L/H − SiC(0001)(**d**), twisted 10 L/SiC(000) (e) and HOPG (f). The solid lines represent the mean values obtained from multiple experiments in different sample regions, and the shaded areas represent the standard deviation for these multiple experiments. The insets show the schematics of the respective crystal arrangement of the six samples.

graphene layers. Since the Raman spectra (not shown here) indicate that the graphene samples with and without hydrogen intercalation present a similar structure and quality, we conclude that G_{int} changes because of different graphene-substrate interfaces. In particular, the 30% increase in G_{int} after hydrogen intercalation could be explained by ajamming effect due to the H atoms at the graphene-SiC interface, which could provide a source of pinning that is more important than that of the buffer layer, and therefore hinder the shear of the top atomic graphene layer. In the case of 2 L films on H-terminated SiC, the effect of the bottom layer's hindered shear propagates to the top layer, increasing the overall shear stiffness of 2 L/H − SiC compared to 2 L/BfL/SiC. The shear stiffness of the substrate is also of key importance. For example, in HOPG, the top graphene layer sits on another graphene layer with AB stacking order in respect to the layer below. Therefore, G_{int} of the very top layer is increased by the larger interfacial shear modulus of the underneath layer.

Measurements formulation

During a typical MoNS experiment, after a silicon AFM tip is brought into contact with a sample at a specific initial normal load ($F_{\text{N}} = 10 - 20\text{nN}$) controlled by the AFM feedback loop, the cantilever holder is driven

Graphene	G_{int} (MPa)	$\mu\left(\times 10^{-2}\text{nN}^{1/3}\right)$	σ(MPa)
1L/BfL/SiC(0001)	190	2.3	23.3
2L/BfL/SiC(0001)	217	1.4	14.0
1L/H-SiC(0001)	217	1.4	14.2
2L/H-SiC(0001)	246	0.9	9.1
Twisted 10L/SiC(000$\bar{1}$)	206	3.7	15.0
HOPG	441	0.7	2.8

Table 4.1: The values of the interfacial transverse shear modulus (G_{int}), friction coefficient (μ) and friction force per unit contact area (σ) for the different graphene samples

by a lock-in amplifier to oscillate parallel to the graphene surface, with a sub-angstrom oscillation amplitude. The sub-angstrom lateral oscillations are applied to the AFM tip holder via a piezoelectric stage at 2.213kHz controlled by a lock-in amplifier while the tip is sticking in contact with the sample surface (no slip). The variation in lateral force at each normal load is recorded during AFM tip retraction from the sample until complete withdrawal from the surface is achieved, at a rate of 0.9nNs^{-1}. Because of such small oscillation amplitudes and the presence of adhesive forces, during the oscillation, the tip apex is always sticking to the surface of the sample (no slipping), and it induces a lateral shear in the sample underneath in a purely elastic regime, as shown in Fig. 4.1b. In this sticking regime, when static friction prevents the tip from sliding, the force per unit displacement necessary to shear the top atomic layer in respect to the substrate is proportional to the effective interfacial shear modulus [170], G^*_{int}, defined as

$$G^*_{\text{int}} = \left(\frac{2 - v_{\text{tip}}}{G_{\text{tip}}} + \frac{2 - v}{G_{\text{int}}} \right)^{-1} \tag{4.1}$$

where v_{tip} and v are the Poisson's ratios of the AFM tip material and graphene sample, respectively, while G_{tip} and G_{int} are the interfacial transverse shear moduli of the AFM tip material and graphene sample, respectively. By measuring the lateral force (ΔF_{L}) experienced by the cantilever during the oscillation Δx, while the tip is sticking, in contact with the sample surface, it is possible to obtain the lateral stiffness of the tip-sample contact, $k^{\text{latel}}_{\text{cont}}$, following the equation [170]

$$\frac{\Delta F_{\text{L}}}{\Delta x} = \left(\frac{1}{k^{\text{t}}_{\text{lever}}} + \frac{1}{k^{\text{lateral}}_{\text{cont}}} \right)^{-1} = k^{\text{lateral}}_{\text{total}} \tag{4.2}$$

where $k^{\text{t}}_{\text{lever}}$ is the torsional spring constant of the AFM cantilever ($k^{\text{t}}_{\text{lever}} = 70.7\ \text{N m}^{-1}$). Furthermore, G^*_{int} is

$$k^{\text{lateral}}_{\text{cont}} = 8 G^*_{\text{int}} a, \tag{4.3}$$

where a is the tip-sample contact radius and G^*_{int} is defined in Eq. (4.1). Contact mechanics equations [170] can then be used to calculate a from the normal load and the adhesion force F_{adh} :

$$a = \left(\frac{3 R_{\text{tip}}}{4 E^*} \left(F_{\text{N}} + F_{\text{adh}} \right) \right)^{1/3} \tag{4.4}$$

where R_{tip} is the tip radius and E^* is the effective transverse Young's modulus of the tip-sample contact [157–159]. During the MoNS experiments, F_{adh} is directly measured from the $k^{\text{lateral}}_{\text{cont}}$ versus load curves (Fig. 4.2) as the lowest load at which the contact is lost [134], while E^* is measured via MoNI for each sample.

The lateral contact stiffness is then measured at different decreasing loads, while retracting the tip from the initial contact load (1020nN), until complete detachment from the surface is achieved at $F_{\text{N}} = F_{\text{adh}}$. The G_{int} is then obtained by fitting the experimental $k^{\text{lateral}}_{\text{cont}}$ (F_{N}) curves with the following equation:

$$k^{\text{lateral}}_{\text{cont}} = 8 \left(\frac{2 - v_{\text{tip}}}{G_{\text{tip}}} + \frac{2 - v}{G_{\text{int}}} \right)^{-1} \left(\frac{3 R_{\text{tip}}}{4 E^*} \left(F_{\text{N}} + F_{\text{adh}} \right) \right)^{1/3} \tag{4.5}$$

We perform MoNS experiments on multiple areas of the six sample surfaces, acquiring more than 60 curves of $k^{\text{lateral}}_{\text{cont}}$ versus F_{N} for each sample (Fig. 4.2). The obtained interfacial transverse shear moduli G_{int} are averaged and summarized in Table 4.1 and Fig. 4.3a.

Moreover, the friction coefficient μ for each graphene sample is obtained by fitting the respective friction curve using the nonlinear equation [171]

$$F_{\text{L}} = \mu \left(F_{\text{N}} + F_{\text{adh}} \right)^{2/3} \tag{4.6}$$

Here, F_{adh} is the adhesion force and μ is the friction force coefficient. More details about the friction experimental set-up and results are in given in [9].

4.3 Relationship between friction force and interfacial shear modulus

The frictional behaviour of 2D materials has been so far ascribed to the so-called puckering effect [99, 131], electron-phonon coupling [104] and surface roughness [172], or to a combination of these factors. Based on our results, we can discard mesoscale to nanoscale roughness as the main driving force. Indeed, experiments measure similar values of surface roughness across all the samples (not shown here). Regarding the puckering and electron-phonon coupling effects, while they certainly play a role, the results reported here clearly indicate that the key parameter controlling friction in epitaxial graphene, and likely other supported 2D materials, is the interfacial shear modulus and the 2D layer-substrate interaction. For example, while 2 L/BfL/SiC and 1 L/H-SiC are different in many aspects (for example, different numbers of layers, different stacking order and different interface with the substrate), for a balancing of effects, their interfacial shear modulus is similar, and indeed also their friction per unit area, confirming the key importance of G_{int} in determining the frictional behaviour of the 2D system. Furthermore, the ratio between G_{int} of 2 L and G_{int} of 1 L is the same for both non-intercalated and intercalated graphene samples, as it is the ratio between the corresponding friction coefficients. Finally, we note that the number of layers does not fully explain the observed behaviour; indeed, the friction per unit area in twisted 10 L/SiC has an intermediate value between that of 1 L and 2 L non-intercalated graphene films on SiC, while HOPG (very large number of layers) has the lowest value of friction per unit area.

To investigate the relationship between friction and interfacial shear modulus, in Fig. 4.3 a we plot F_{F}/A as a function of G_{int} for all the experimentally investigated samples, and we fit the experimental data with different analytical functions. Surprisingly, we find that a two-parameter reciprocal function fits all the experimental data extremely well, with a statistical coefficient of determination, R^2, equal to 0.989 (more details on the published supplementary [9]). In particular, all the experimental data points fall on the following reciprocal curve (Fig. 4.3a):

$$\frac{F_{\text{F}}}{A} = \frac{\alpha}{G_{\text{int}} - \beta} \tag{4.7}$$

where α and β are obtained from the fitting to the experimental data, and have the respective values of $864 \pm 71\text{MPa}^2$ and $153 \pm 4\text{MPa}$. To investigate the origin of the relationship between G_{int} and F_{F}/A, and to find a physical interpretation of the experimentally observed reciprocal fitting function, in the next paragraph we perform a series of simulations based on the PT model [38, 61, 173]. While the experiments show that G_{int} and the associated interaction of the top 2D layer with the underlying substrate (for example, stacking order and layer-substrate interfacial forces) are key elements controlling nanoscale friction in 2D materials, other properties could have an important impact. For example, surface chemistry is clearly a key property affecting the tribological properties of a material; therefore, if comparing different 2D materials (for example, graphene versus BN), the chemistry needs to be considered, as well as the intrinsic shear modulus of the 2D layer and possible differences in puckering. However, when keeping the chemistry fixed (only graphitic samples were measured) and varying other parameters such as substrate stiffness, substrate interaction, number of layers and stacking order, we are able to demonstrate a general relationship between G_{int} and F_{F}/A.

4.4 Friction force simulations

To investigate the physical origin of the relationship between G_{int} and F_{F}/A and to find a physical interpretation of the experimentally observed reciprocal fitting function, we develop simple friction models. In particular, to simulate the friction force probed by a sliding AFM tip on a surface, we first use a Prandtl-Tomlinson model (PT) [38, 61, 173], where a nano-tip is dragged by a spring over a corrugated energy landscape (Fig. 4.3b-d). In the PT model, the total potential energy $U(x,t)$ at position x and time t of the system is described by

$$U(x,t) = \frac{1}{2} k_{\text{total}}^{\text{lateral}} (x - vt)^2 + V_{\text{tip-layer}}(x) \tag{4.8}$$

Here the first term on the right-hand side represents the potential energy stored in the total lateral spring constant of the cantilever-tip contact system, $k_{\text{total}}^{\text{lateral}}$ (Eq. (4.2)) when the tip is sliding with velocity v $\left(v = 1 \text{ m s}^{-1}\right)$; more discussions about the velocity influence on the contact lateral stiffness can be found in the literature [174]. The second term, $V_{\text{tip-layer}}(x)$, is potential energy, which describes the energy barrier that the tip has to overcome to slide over the periodic lattice of the sample surface. As discussed in Eq. (4.1) through Eq. (4.3), the value of G_{int} is directly related to the value $k_{\text{total}}^{\text{lateral}}$.

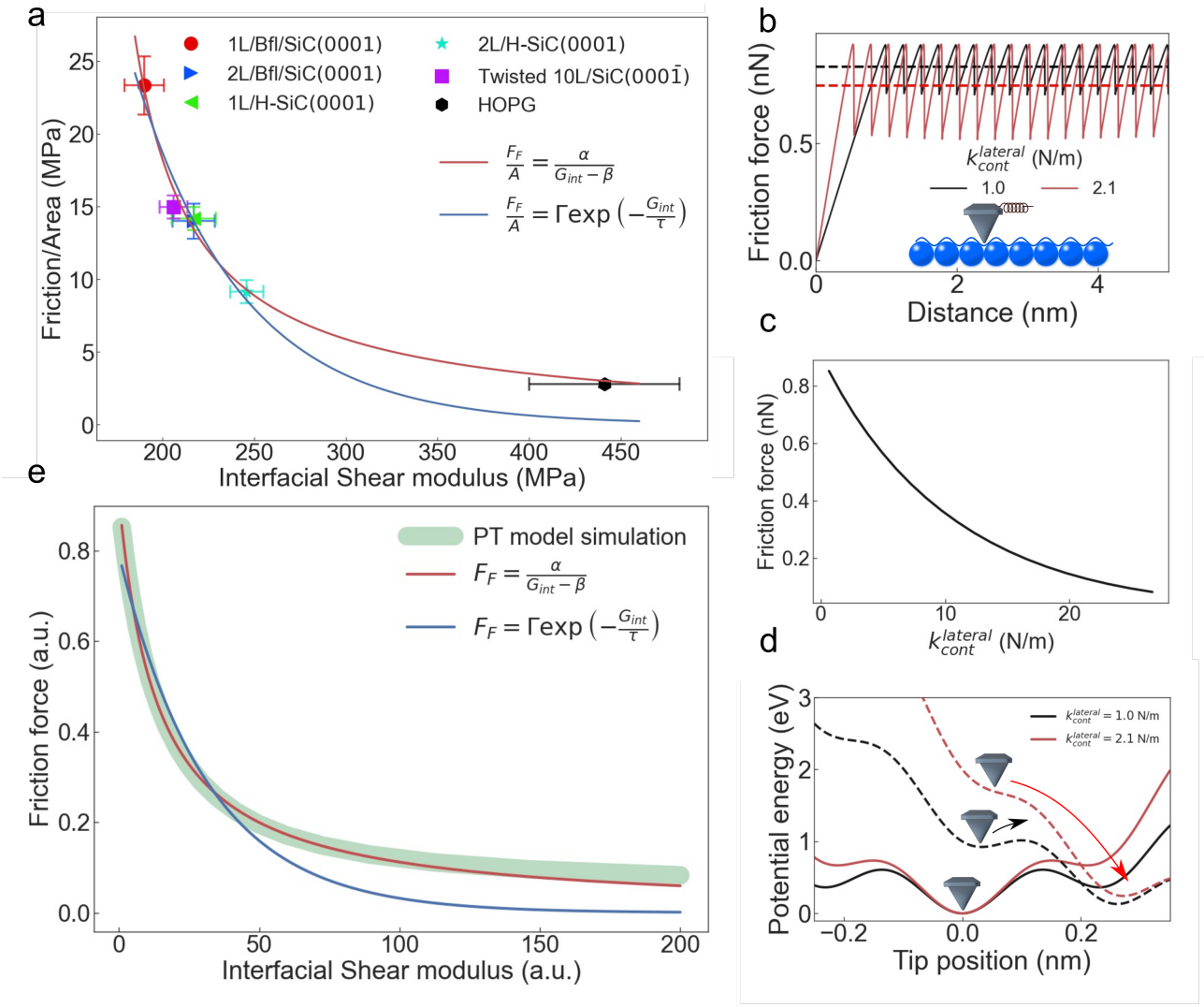

Figure 4.3: Friction force and interfacial shear modulus relationship. a, Experimentally measured friction force per unit contact area as a function of the measured interfacial transverse shear modulus for the different samples. The red solid curve represents the fitting curve described in Eq. (4.7), while the blue solid curve is a two-parameter exponential decay fitting function. b, PT modelling of the friction force as a function of tip sliding distance. The dashed lines show average values of friction force. The inset shows a cartoon of the PT model, where the tip slides on a fixed potential representing the graphene-plus-substrate system. c, Average friction force as a function of the contact lateral stiffness calculated from the PT model.d, PT potential energy (Eq. (4.8)) as a function of the AFM tip position, according to the PT model. The solid curves represent potential energy at $t = 0$ s and the dashed curves show potential energy at $t = 0.5$ s. The arrows indicate the future movement of the tip, while for $k = 1$ N/m the tip starts to slide, the same tip for $k = 2.1$ N/m still has to overcome an energy barrier.e, PT simulations of friction force as a function of the interfacial shear modulus, and fitting functions. The red solid line represents a two-parameter reciprocal function, while the blue solid line represents a two-parameter exponential decay function.

The time evolution of the system, as sketched in the inset of Fig. 4b, with the total potential energy (Eq. (4.8)) is obtained from the solution of the equation of motion [38, 173]

$$m\ddot{x} = -\frac{\mathrm{d}U(x,t)}{\mathrm{d}x} - m\eta\dot{x} \tag{4.9}$$

where m is the mass ($m = 501.40 m_{\mathrm{carbon}}$, where m_{carbon} is the atomic mass of carbon), η is the damping parameter ($\eta = 1.88\mathrm{ps}^{-1}$)[175], $\dot{x}$ and $\ddot{x}$ are the first and the second time derivative of position, respectively. The total potential is described by Eq. (4.8), where the $V_{\text{tip-layer}}$ potential is described by the following equation:

$$V_{\text{tip-layer}}(x) = V\left[1 - \cos\left(\frac{2\pi}{a}x\right)\right] \tag{4.10}$$

Here, V is the amplitude of the tip-layer potential. The friction force is calculated by

$$F_{\text{F}} = k_{\text{total}}^{\text{lateral}}\left(X(t) - x(t)\right) \tag{4.11}$$

where $X(t) = vt$ is the coordinate of the pulling spring and $x(t)$ is the tip coordinate. The steady-state value can be calculated as a time average of the friction force. The numerical solution of Eq. (4.9) is obtained using a Python code with a time step of 2.5ps.

To understand the experimental F_{F}/A versus G_{int} curves of Fig. 4.3 a, we show PT simulations for systems having different G_{int} values. The values of F_{F} versus G_{int} obtained from the simulations are plotted in Fig. 4.3e, showing a trend very similar to the one found in the experiments (Fig. 4.3a). In particular, the simulated curve can also be fitted very well with a two-parameter reciprocal function ($R^2 = 0.999$). As in the experiments, the PT model demonstrates that for higher G_{int} values, steady-state friction has lower values, due to a larger amount of energy stored elastically during the sticking regime, and a smaller amount dissipated during slip. This can be easily seen in Fig. 4.3d, where we show the potential energy of the system ($U(x,t)$ in Eq. (4.8)), represented by a corrugated parabola, as a function of the tip position, for two different values of G_{int} . The curves indicate that when the tip starts sliding (slip event) on a sample with larger G_{int} (corresponding to larger $k_{\text{cont}}^{\text{lateral}}$), the same tip for the same position of the pulling spring (coordinate 'distance' in Fig. 4.3b), for a sample with lower G_{int} , still has an energy barrier to overcome before starting to slide. Consequently, the friction is larger for smaller G_{int} .

Although this simple PT model rationalizes the experimental results, it fails to explain the origin of increased stiffness. Therefore, we develop a Frenkel-Kontorova (FK) model with a repulsive tip on top of it, enabling us to understand the rule of in-plane corrugation.

The epitaxial graphene is mimicked with one dimensional FK harmonic chain (k_0), and a substrate is described by rigid sinusoidal potential of amplitude U with the same spacing as the chain at rest. a_0. The internal potential of harmonic atomic chain is

$$U_{\text{int}} = \frac{k_0}{2}\sum_n \left(x_{n+1} - x_n - a_0\right)^2 \tag{4.12}$$

And the substrate potential with amplitude U and the same periodicity a_0 is

$$U_{\text{sub}} = \frac{U}{2}\sum_n \left[1 - \cos\frac{2\pi x_n}{a_0}\right] \tag{4.13}$$

A point "tip" of mass M and coordinates (X_t, Z_0) interacting with chain atoms x_i through a purely repulsive potential scaling as $1/\text{R}_\text{n}^6$, giving to a interacting potential with the chain as

$$U_{\text{tip}} = \sum_n \frac{\varepsilon}{\left(\left(X_t - x_n\right)^2 + Z_t^2\right)^3} \tag{4.14}$$

Where ε is the potential parameter, X_t and Z_t are the coordinate of the tip. Note that x_n is strictly one dimensional and any vertical movement is not allowed for the harmonic chain.

The tip is dragged by a spring (k_{lever}^t) whose pulling velocity is gradually increased to reach a constant steady state value v. Vertical movement of the tip Z_t is allowed by a second hard spring (k_{Z}^t), while the chain is constrained to one dimensional X motion only, as would befit a membrane whose adhesion to a substrate is much larger that its corrugation barrier against sliding. The tip harmonic potential is

$$U_{\text{lever}} = \frac{1}{2}k_{\text{lever}}^t\left(X_t - vt\right)^2 + \frac{1}{2}k_{\text{Z}}^t(Z_t - Z_0)^2 \tag{4.15}$$

Where Z_0 is the initial vertical coordinate of the tip.

Overall, the total potential energy of this system can be written as:

$$U(x,t) = U_{\text{int}} + U_{\text{sub}} + U_{\text{tip}} + U_{lever} \tag{4.16}$$

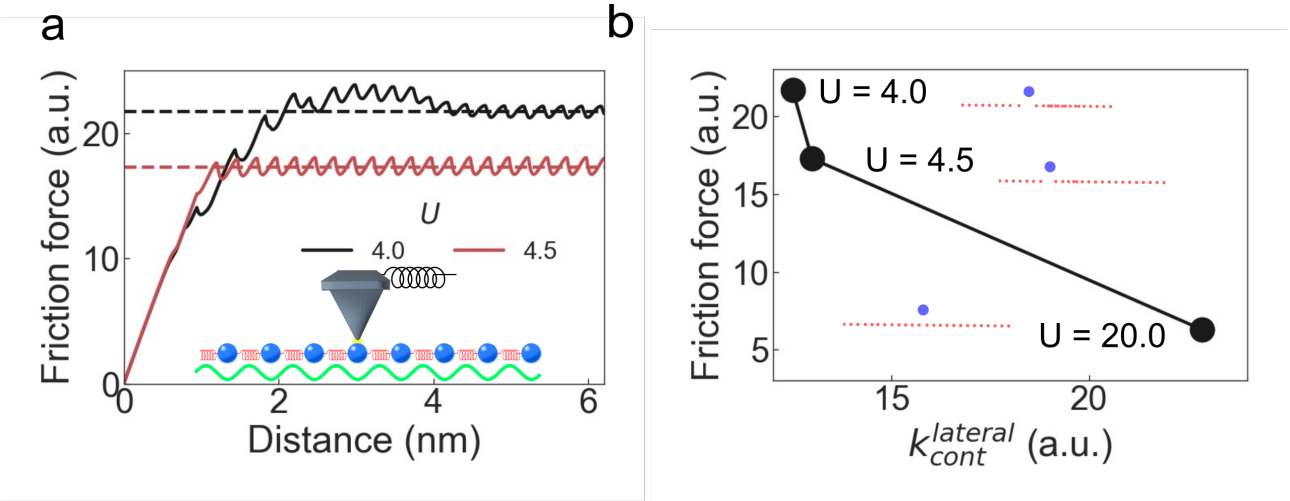

Figure 4.4: Friction force FK modelling. a, FK modelling of the friction forces as a function of tip sliding distance. The inset shows a cartoon of the FK model, where the tip slides on top of a 1D chain of springs (representing the graphene atoms), which moves on top of a fixed potential (representing the graphene-substrate interaction). The dashed horizontal lines show average values of friction force. b, Commensurate FK model simulations showing how the increase of the substrate periodic interaction potential amplitude (U) acts to increase the lateral contact stiffness, which is related to G_{int} , in turn leading to a decrease of friction, similar to the experiments. The sliding simulation snapshots (blue circle, right-moving tip; red dots, layer atoms; periodic potential not shown) illustrate how an underlying decrease of tip-induced deformation size accompanies the frictional evolution.

Describing analytically the friction associated with this potential is, unlike the PT model, not an easy task. Therefore, in this case we perform non-equilibrium molecular dynamics simulations with a home-made code. Periodic boundary conditions are enforced, and the chain as a whole is long enough to prevent sliding – 120 atoms. Thus, all frictional deformation of chain atoms is localized: compressed in front of the tip and stretched behind it. The dissipated energy is removed by a Langevin damping gamma. A stick-slip advancement is found in all cases, but a particular choice of parameters is made so as to obtain a useful cartoon for the extraction of interfacial shear stress.

The chain which is pinned against sliding by an amount controlled by the magnitude U of the layer-substrate interfacial potential for three situations: weak U represents qualitatively 1 L/BfL/SiC; intermediate U represents twisted 10 L/SiC, 2 L/BfL/SiC and 1 L/H$-$SiC; and strong U represents sliding on HOPG. The resulting friction force model evolution of Fig. 4.4a shows the initial elastic displacement with overall stiffness $k_{\text{total}}^{\text{lateral}}$, from which the contact lateral stiffness $k_{\text{cont}}^{\text{lateral}}$ is extracted (Eq. (4.2)), followed by atomic stick-slip events. Steady-state friction as interfacial shear stiffness, which in turn causes the decrease in friction, since fewer atoms are displaced and fewer 'bonds' with the graphene layer are broken (insets in Fig. 4.4b).

In this cartoon model, we demonstrated an example where a non-puckering substrate is able to compress and expand both behind and ahead of a giant tip. Results shows that the origin of increasing stiffness that causes the friction to decrease, is in the in-plane corrugation of the substrate.
Moreover we perform an additional set of simulations with a marginally different set of parameters that are appropriate for a smaller regime of U. Here as a side note, we can define an effective stretching length as the initial tip displacement in the following form, where the friction force approaches the steady state value

$$\frac{F(X = L_{eff})}{< F >} \approx \ln(2) \tag{4.17}$$

The frictional force $F(X)$ in Fig 4.5b depicts the model frictional evolution as a function of the driving X, shown for a weakly corrugated substrate (small U) and a stronger corrugated one (large U). The stiffness increase and the associated decrease of average friction plotted in Fig. 4.5 confirm the main points suggested by experiments. Remarkably, there is an almost perfect coincidence of friction and effective stretching length (Fig. 4.5d) elucidating how the corrugation-driven growth of interfacial shear stiffness, results in a nonlinear

reduction of the effective shear length L_{eff} which drops exactly like friction, controls the overall tribological behaviour of this model.

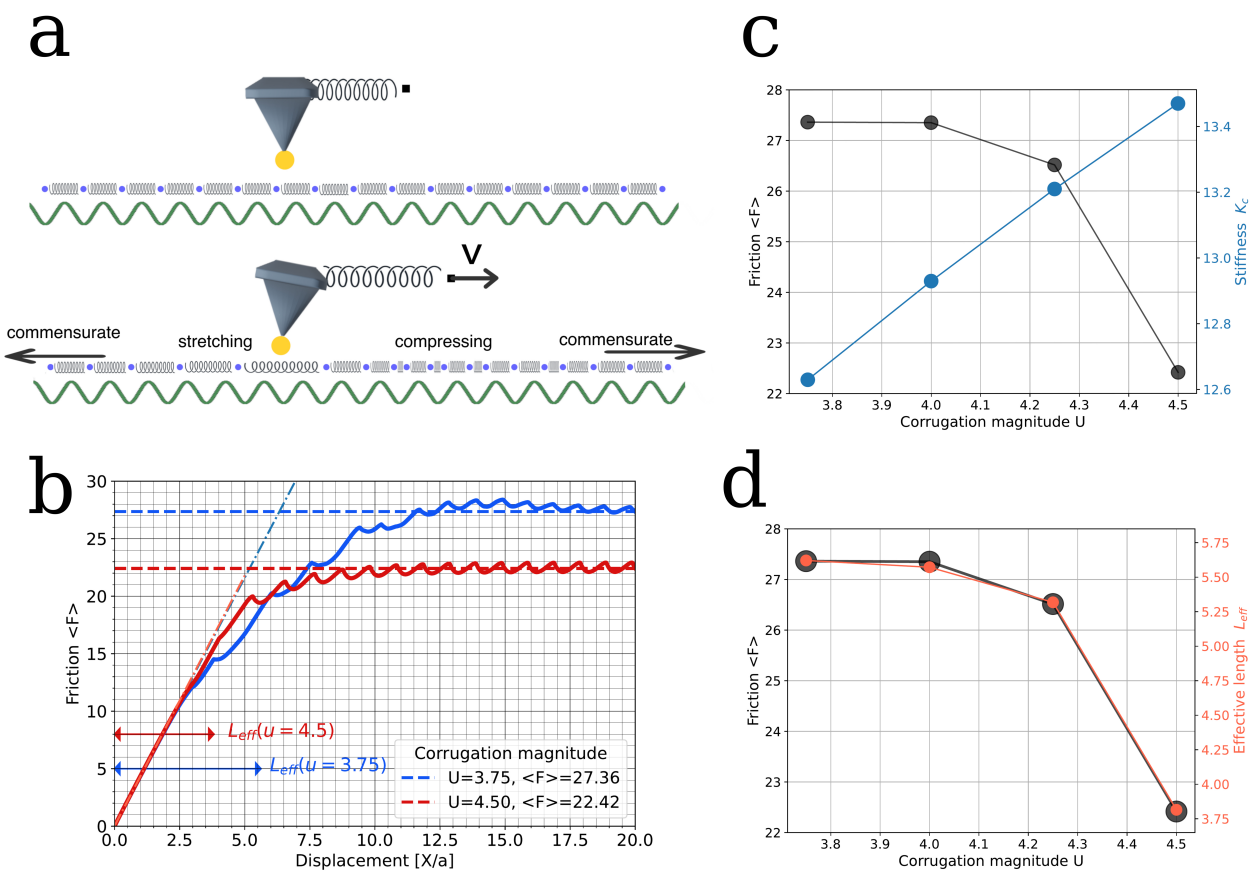

Figure 4.5: MD friction force simulations second set of parameters. (a) Sketch of the 1D simulation model. Note that a small chain portion behind the tip is stretched, another in front is compressed and, most importantly, both are dislodged out of registry with the substrate. (b) Friction evolution as a function of the pulling spring coordinate. The straight lines near the origin are the slopes dF/dX from which interfacial shear stiffness is extracted (see text), and are not as close. The effective shear length L_{eff} drops strongly for a stronger substrate, corresponding to the shrinking size of the local deformation. (c) variation of steady state friction and shear stiffness for increasing substrate corrugation. The reverse behavior of the two quantities is similar to experiment.(d) the effective length and friction behave identically as the corrugation magnitude changes in this model.

4.5 Conclusions

By using the sub-angstrom resolution MoNS method, experiments measured the interfacial transverse shear modulus of atomically thin epitaxial graphene layers on SiC, as well as bulk HOPG. We show that this modulus is a key property of the interface between a single atomic layer and the underlying substrate, and is critically controlled by the chemistry, stacking order and structure of the graphene-substrate interface, as well as the shear modulus of the substrate. Importantly, we demonstrate that the interfacial shear modulus is a pivotal measurable property to control and predict sliding friction in supported 2D films. Indeed, we observe a general reciprocal relationship between the friction force per unit contact area and the interfacial shear modulus for all the investigated graphitic structures, including twisted graphene and bulk HOPG. These results can be explained by simple 1D sliding friction models, which show that the atomic layer-substrate interaction controls the shear stiffness, and therefore the resulting friction dissipation. This picture explains in full the experimental friction

results by considering only the shear stiffness originating from a given layer-substrate interaction, without the need to invoke other effects, such as puckering, or electron-phonon dissipation. These results can be generalized to other 2D materials and represent a way to control atomic sliding friction and to manipulate strain fields for band-structure engineering and photonics applications.

Chapter 5

Anisotropic Friction and Rheology of Suspended Graphene

5.1 Introduction

The rheological and frictional behavior of pristine graphene has attracted much fundamental and technological interest during the last decade. From the mesoscale down to the atomic level, a great research effort is underway to unveil the physical mechanisms underpinning the indentation, twisting, wrinkling, and crumbling phenomena [134, 176–182] of this extraordinary membrane. The exceptional hardness (Young's modulus around 1 TPa and intrinsic in-plane strength of 130 GPa [180]), the extreme ability to elastically sustain tensile strain up to at least 20% [183], and its large out-of-plane membrane-like flexibility make graphene the forefront prototype material for the design of innovative systems and structures with controlled intrinsic properties [184]. Graphene has been integrated into several hi-tech electronic devices such as organic light-emitting diodes [185, 186], strain sensors [187–191], wearable devices [192–194], and micro- and nanoelectromechanical systems [195]. Understanding and exploiting strain-induced effects in 2D layered materials in general is nowadays a fast-growing topic in both fundamental and applied research, given that many of its intrinsic properties can be tuned by mechanical deformation. While the tunability of transport and optical properties under strain has been extensively addressed [196–200], the microscopic tribological behavior as a function of the applied strain and boundary conditions has received far less attention [201–203]. Graphene tends to conform to the morphology of the supporting surface when deposited over a hosting substrate and the tribological response of the layered coating significantly depends on the layer-substrate interaction [99, 204, 205]. At the same time, different experimental realizations of supported graphene have highlighted the importance of 2D layer strain on the overall tribological and electronic behavior [206–209]. To disentangle these effects and shed light on their origin, suspended graphene represents an ideal system. Recently, free-standing graphene has been investigated by Zhang *et al.* [201], who found a reduction of friction with increasing strain in a suspended and isotropically strained graphene sheet with atomic force microscopy (AFM) measurements. Complementary atomistic simulations showed how this tensile prestrain reduces the membrane flexibility thus decreasing the impact of the tip, hence reducing the friction.

Here we go beyond the isotropic setup in Ref. [201] and study the friction behavior of graphene suspended and fixed at the edges of a long narrow groove. We observe with remarkable reproducibility that the frictional dissipation of the graphene membrane measured by our sliding AFM tip turns anisotropic, with a differential friction coefficient (COF) typically three times higher parallel to the groove axis compared to orthogonal axis. This occurs with negligible prestrain in our system, as confirmed by Raman measurements. Molecular dynamics (MD) simulations reveal that the sliding-friction anisotropy is ruled by the interplay between the tip-indenting action and the boundary conditions. The strain-free, asymmetric suspension condition is responsible for the anisotropic indentation pattern shape and rheology of the membrane, quantitatively explaining the observations. Our results rationalize the often-overlooked aspect of nonisotropic constraints in nanoscale systems, with important implications for realistic engineering setups.

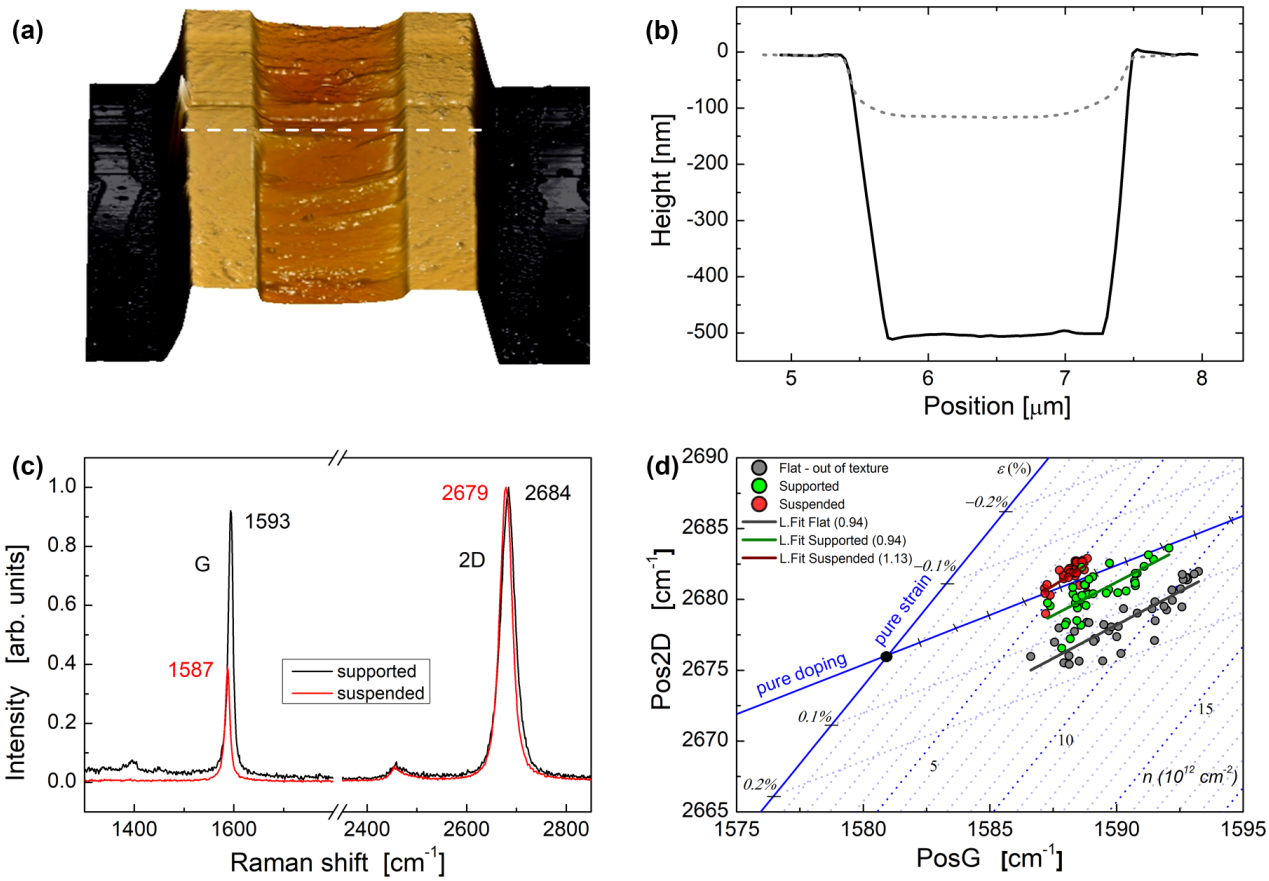

Figure 5.1: AFM imaging and Raman characterization of single-layer CVD graphene anisotropically suspended. (a) Three-dimensional topography image and (b) relative line profiles of CVD graphene deposited on a single groove. White dashed line in (a) indicates the line profile in (b). Equilibrium configuration between graphene and underlying substrate indicates a complete conformation and clamping on the flat crests enclosing the groove and a total suspension at the center of the groove. (c) Raman spectra comparison of supported graphene (black) and suspended graphene (red). Note the typical redshift of G and 2D peak positions on suspended graphene. (d) Correlation plot of Pos2D vs Pos$G$ peaks showing data from supported graphene (gray) and data within the patterned area which include supported graphene on the crest and suspended graphene (green and red, respectively). Lines represent the linear fit from supported graphene (gray line, slope 0.94), graphene on crest (green line, slope 0.94), and from suspended graphene (red line, slope 1.13). Neutrality point indicated by the black dot at position (1581.6 and 2676.9 cm^{-1}) in the Pos2D versus Pos$G$ correlation plot, and the additional axes to quantify strain and doping are taken from Ref. [209].

5.2 Experimental data

Sample characterization

The suspended graphene was obtained by depositing a commercial single-layer chemical vapor deposition (CVD) graphene on a standard silicon dioxide-based calibration grating array.

Briefly, a commercial single-layer CVD graphene was deposited over the calibration grating by wet transfer process. The calibration grating comprises a central patterned area and a surrounding flat region. The pattern consists of long, parallel, and equally spaced grooves (crest-to-crest distance: 3 μm, valley width: 2 μm, step height: 500 nm). After transfer, the external flat region is fully covered by single-layer graphene that we refer to as supported graphene in the following. On the contrary, the sample surface over patterned area displayed regions where the graphene adhered to the substrate and regions where it hung fully suspended via clamping on the top of the crests, see Fig. 5.1(a). AFM 3D topography and corresponding line profiles in Fig. 5.1(a-b) reveal an excellent conformation of graphene sheet over the crests and the complete suspension in the region between them. In particular, the AFM profiles before and after deposition [solid and dashed lines in Fig. 5.1(b),

respectively] indicate that graphene tends to mechanically relax to a configuration where a small fraction adheres to the sidewalls of the groove.

The graphene membrane was then characterized by Raman spectroscopy, a well-established method used to quantify the purity, thickness, and strain of graphene films [209–212]. Fig. 5.1(c) presents the typical Raman spectra obtained from analyzing both the supported graphene (black line) and suspended graphene (red line) of the deposited graphitic film. The shape of the two prominent G and 2D peaks (both symmetric Lorentzian line shape, and width $W_G = 12\ \mathrm{cm}^{-1}$ and $W_{2D} = 33\ \mathrm{cm}^{-1}$, respectively) indicates a high quality, single-layer suspended graphene film [210–213]. The absence of the disorder-related D peak near 1350 cm^{-1} on the suspended part and the weak intensity on the supported one indicate that CVD graphene film is composed of large, defect-free single-crystal domains. The downward shift of both peaks positions in the suspended regions with respect to the supported graphene is evident and indicative of the different extent of both deformation and doping effects [210] in the two regions.

To disentangle doping and strain effects, we performed extensive Raman maps on graphene on the patterned area and graphene supported on the surrounding flat silicon region. Each map comprised about 80 points where we measured and fit Raman spectra to obtain G and 2D peak positions (Pos$G$ and Pos2D in the following). We computed the Pos2D/Pos$G$ correlation shown in Fig. 5.1(d) following the protocol developed by Lee *et al.*[209]. Pos$G$ and Pos2D are linearly correlated even within an ideal graphene sheet because of the ubiquitous presence of doping and strain effects. The slope of the linear distribution is indicative of the relative importance of either doping or strain effects. The solid blue lines in Fig. 5.1(d) represents the linear pure-strain axis with slope 2.2 and the pure-doping axis with slope 0.7 , respectively [209]. The two axes cross at the neutrality point marked by a black dot at position (1581.6 and 2676.9 cm^{-1}) [209]. While on the doping line only positive values are physically meaningful, the convention adopted for strain evaluation is to indicate as a negative value the compressive strain that moves the peak towards higher frequencies and as a positive value the tensile strain inducing shift in the opposite direction [214]. The gray dot and the related gray line represent data from supported graphene while green and red data come from graphene over the patterned area. Data from supported graphene (gray symbols) indicate only a very slight tensile strain as well as a hole-doping effect, consistent with the literature for supported CVD graphene [211]. Raman spectra acquired from graphene within the pattern split into two sets with different slopes (green and red symbols). The green dots show a trend compatible with the reference signal (supported graphene) and, hence, they are attributed to the crest region, where graphene is supported. Indeed, the fitted slope [green and gray lines in Fig. 5.1(d)] is 0.94 in both cases, a value consistent with the literature [211]. By contrast, the red data are representative of suspended graphene: They group close to the doping axis so that the extrapolation towards strain axis indicates a negligible prestrain. Indeed, the linear fit yields a slope of 1.13 consistent with the value of 1.09 reported by Gajewski *et al.* [211] for suspended graphene. Hence, our sample presents no prestrain, probably because the portion of membrane adhering to the sidewall of the groove is small and its effect negligible.

Measurements

Following the structural results of the Raman spectroscopy analysis, the membrane rheology was proved by friction force microscopy (FFM) (Fig. 5.2). FFM scans in two opposite directions were performed on a $1-\mu\mathrm{m}^2$ area, corresponding to the central region suspended between two crests [blue square in Fig. 5.2(a)]. By tilting the sample 90°, the same area was first scanned in the direction orthogonal to the groove axis and then in the one parallel to the groove axis, as indicated in the right side of Fig. 5.2(a) by black and red arrows, respectively. The same area was analyzed in both directions with positioning accuracy of the order of 100 nm [215, 216].

Care has been taken to analyze regions free from preexisting extended wrinkles, which are clearly identifiable due to the strong contrast they produce on the lateral force signal [217]. On the contrary, ripple effects on graphene either of an intrinsic type or induced by tip or point defect [218] cannot be resolved since the induced elastic deformations during FFM measurements are larger with respect to ripple corrugation.

The measured frictional dissipation F was found to depend strongly on the scanning direction: The friction force recorded during scans parallel to the groove was typically three times that the orthogonal, at the same load P [see Fig. 5.2(b)]. The orthogonal vs parallel friction increase was then measured at different loads, from about 25 nN down to the negative pull-off force. Fig. 5.2(b) reports the typical friction vs load behavior observed in several different spots on the membrane. The differential friction coefficient dF/dP (COF) was evaluated for each friction vs load curve and used as a representative parameter of the membrane anisotropic response. Fig. 5.2(c) summarizes the statistics of our multispot analysis, revealing a remarkably consistent threefold increase from orthogonal to parallel scanning direction.

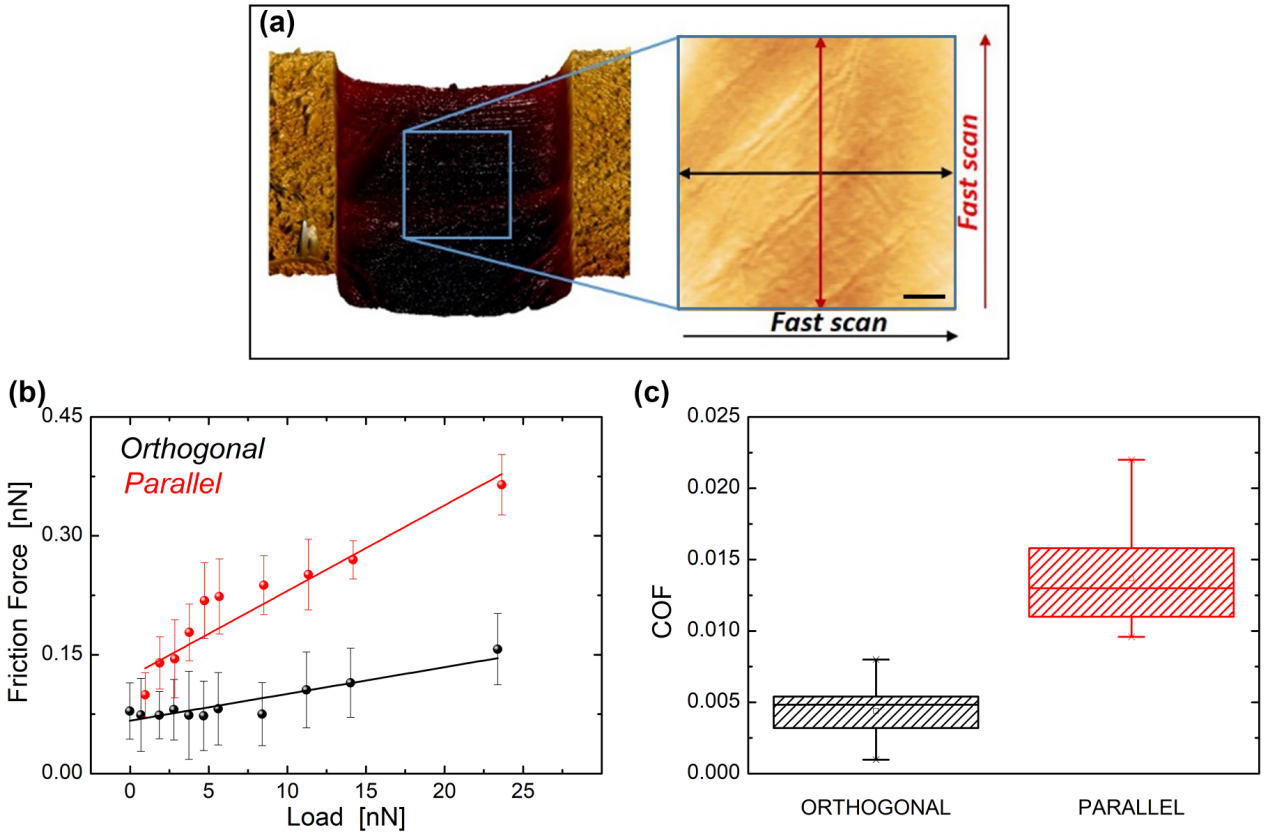

Figure 5.2: Direction-dependent friction response of suspended CVD graphene. (a) Three-dimensional topography reconstruction of freestanding CVD graphene over single groove and 2D zoom of the region analyzed by FFM (blue square: $1 \times 1 \mu m^2$); the two scan directions are represented with double-headed arrows (black for the orthogonal and red for the parallel, respectively). Scale bar corresponds to 150 nm. (b) Friction force as a function of load applied to free-standing CVD graphene with groove axis oriented orthogonal (black) and parallel (red) to the fast scan direction; circles represent experimental data with their error bars and continuous lines are the respective linear fit. (c) Boxplots of COF for orthogonal (black) and parallel (red) scans; counting corresponds to 12 different regions for orthogonal scans and to 19 for parallel scans, respectively.

In particular, we notice that along the orthogonal direction the extremely low COF values are in agreement with those measured by Deng *et al.* on single-, bi-, and trilayer graphene suspended on micrometer-size circular hole [219] and confirmed recently by Zhan [201]. These values approach that of thick graphite [220], suggesting the absence of important elastic deformation effects. Comparison with graphene-supported systems is nontrivial since the specific tribological behavior depends on the substrate on which the graphene is deposited [201, 221]. In general, the higher the adhesion towards the substrate the lower the out-of-plane deformation effect and the lower the friction coefficient [104, 222]. Our results, summarized in Fig. 5.2(c), reveal that along the orthogonal direction the membrane behaves like a graphene layer with minor load-induced out-of-plane deformations, while along the parallel direction load-dependent deformation effects seem to become increasingly important.

The FFM scans were performed over hundreds of nanometers, providing the mesoscopic tribological response arising from a nanoscale contact. Over this length scale the atomistic stick-slip events cannot be detected by our equipment. Nevertheless, the atomistic nature of the dissipation can be indirectly assessed from the velocity dependency of the COF. We found that halving and doubling the sliding velocity yielded the same COF. This velocity independence of friction in both directions is the fingerprint of the stick-slip regime, whereas a viscous dissipation would yield a linear dependence [223].

5.3 Simulations

In order to understand the atomistic mechanism underlying the microscopic experimental measures, we consider the minimalistic model sketched in Fig. 5.3(a), which retains the experimental features assumed to be at the origin of the observed behavior. The stick-slip regime indicated by the experiments suggests that the fundamental dissipation mechanism should be captured by the Prandtl-Tomlinson (PT) model [224, 225], allowing for the tip to be reduced to a point-like object [blue dot in Fig. 5.3(a)] sliding over a corrugated energy landscape. The cantilever was modeled as a mass moving at constant velocity v_{drag} [red square in Fig. 5.3(a)], dragging the tip via a spring of constant K (see a benchmark of the model parameters at Refs. [10, 46, 201, 226]).

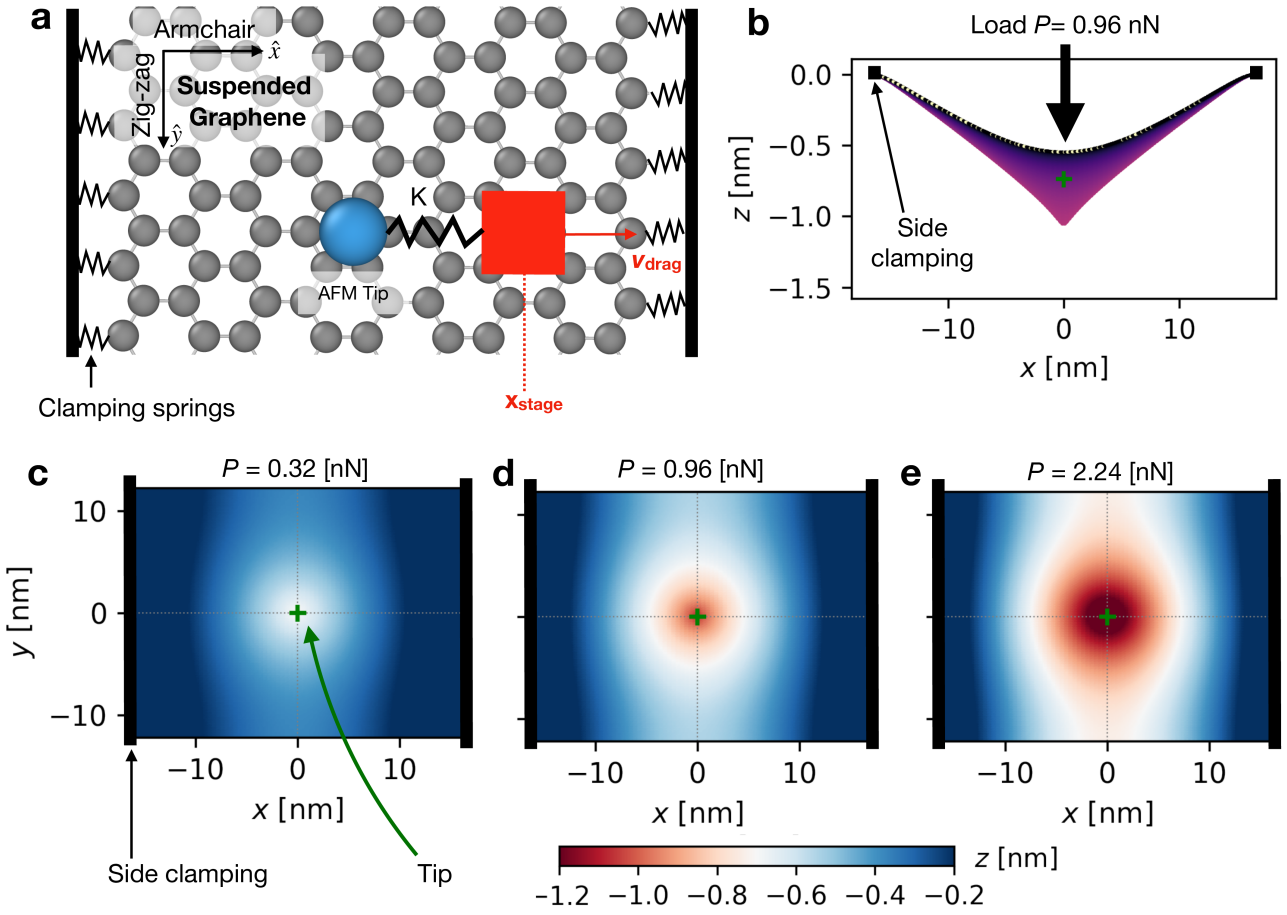

Figure 5.3: (a) Model setup. Free-standing graphene membrane is clamped along the edges in the y direction at fixed x coordinate, consistently with experimental orientation in Fig. 5.1(a). Clamping is realized by attaching a stiff spring ($Q = 1602$ N/m) to each edge carbon atom in a $0.25 - $ nm region. As reported in the top left corner, the zigzag edge is clamped while the armchair one is free (Our results and conclusion is independent of the choice of orientation –see [10]). Prandtl-Tomlinson tip (blue sphere) indents the membrane under a constant vertical load (along z). Mimicking a minimal AFM setup, the tip is attached to a moving stage (red cube), representing the massive cantilever, translating at constant velocity v_{drag}. Side- (b) and top (c)-(e) views of the indentation profile. Purple region in (b) reports the position projected on x and the black squares indicate the position of the clamps. Note that the axes in (b) are not in scale, i.e., the deformation of the membrane is accentuated for visual aid. (c)-(e) Top view of the indentation profile for increasing loads, as reported at the top of each plot: The tip (green cross) indents the center of the membrane and the system is relaxed Color scale in (c)-(e) reports the vertical deformation of the membrane, as indicated by the color bar at the bottom. Black bar at the sides indicates the position of the clamps, as in (a). Gray dashed lines in (c)-(e) mark the reference $x = 0, y = 0$, as a guide to the eye. Height of each C atom of the membrane has been linearly interpolated on a finer grid for clearer visualization.

Construction of the substrate in the PT model (i.e., the 2D membrane on which the tip slides) was key in

this model, as it needed to capture the deformable nature of the suspended graphene sheet while at the same time preserving the atomistic nature of the contact–a smooth membrane cannot yield a stick-slip dynamics and a discrete graphene membrane without the mesoscopic clamping asymmetry cannot deform realistically under the tip. To achieve a reasonable tradeoff between these two opposite requirements, we modeled the experimental membrane as a classical graphene sheet where the Adaptive intermolecular reactive empirical bond order (AIREBO) [226] potential describes intralayer interactions and Lennard-Jones (LJ) potential [201] interactions between the tip and graphene. To reproduce the asymmetric geometry, the membrane was finite in the x direction (orthogonal), and periodic in the y direction (parallel). To mimic the adhesion to the groove's crests, the membrane edges in the x direction were clamped with springs of constant $Q = 1602$ N/m to the equilibrium position, marked by black straight line in Fig. 5.3(a). Hence, the simulated membrane was suspended and the clamping springs provided the restoring force opposing the one exerted by the tip upon loading and sliding. In Fig. 5.3(a) the clamped side is the zigzag edge while the periodic side is the armchair edge. [1] The simulations were performed at zero temperature to obtain a clear signal and because the stick-slip dynamics is regulated by the energy barrier, while temperature introduces thermolubricity without qualitatively modifying the dynamics [224, 225]. As the tip in experiments moved orders of magnitude slower than the relaxation time of the atomistic motion, a viscous damping was applied to all the atoms. The crucial property we rely upon is the near independence of stick-slip friction upon velocity [223].

An external load P was applied to the model tip [as sketched in Fig. 5.3(b), which indents the membrane, as shown in Fig. 5.3(c-e) for increasing loads. The indentation shape follows the asymmetric geometry. The deformation is radial under the tip [green cross in Fig. 5.3(c-e)], but this symmetry is lost far away from it, in particular nearing the edges: The membrane forms an elongated "valley" in the parallel direction [white regions in Fig. 5.3(c-e)] and remains almost flat near the clamps [blue regions in Fig. 5.3(c-e)]. This characteristic indentation shape becomes more evident as the load increases, as shown in going from Fig. 5.3(c) to Fig. 5.3(e).

For each indentation load, the tip can slide in the orthogonal and parallel directions. The sliding was performed for a load from 0 to 2.24 nN. Note that the loads applied to a point-like tip do not relate directly to the experimental one. One can estimate the relative pressure and membrane vs tip-size ratio between MD and experiments. Taking the equilibrium tip-membrane distance according to the LJ potential $R = 0.35$ nm as tip radius in MD and assuming a Hertzian contact area (see Refs. [227, 228]), at the maximum load $P = 2.2$ nN the pressure was 12.8 GPa, much higher than experiments where the maximum estimated pressure was 28 MPa at load 20 nN. At the same time, in the experiments the load was applied on an extended tip of radius $R = 15$ nm, while the real contact area of the single asperity undergoing stick-slip is certainly smaller (and thus pressure is higher) but difficult to estimate [229]. A more meaningful quantity to compare between simulations and experiments is the ratio between the tip radius R and the membrane clamped length L. This ratio is $R/L = 0.011$ in simulations and $R/L = 0.01$ in experiments, with a groove distance $L = 1.5$ μm. The two values are comparatively close, suggesting that while the nominal pressure in the MD simulations is higher than the experimental one, the dimensional ratio is correctly described by the model. This geometrical element is crucial to address the anisotropy observed in experiments because the size relationship between the indenter and the intended membrane sets the shape of the indentation pattern and the strain distribution.

5.4 Results

Force traces along the orthogonal and parallel directions for selected loads are reported in Fig. 5.4(a-b), respectively. The atomistic stick-slip behavior is evident at all loads, owing to the damped, zero-temperature dynamics of the MD simulations. As the cantilever started to translate, the tip climbed the corrugation energy barrier; see the initial increase of all lines in Fig. 5.4(a-b). Once the cantilever restoring force overpowered the barrier, the system depinned, causing the first drop in all lines in Fig. 5.4(a-b). This is the onset of static friction. Afterwards, the tip moved by single-lattice slips, yielding the characteristic sawtooth force profile of stick-slip dynamics shown in Fig. 5.4(a-b). The membrane deformation instantaneously follows the tip motion[2]: There is an adiabatic separation between slow motion of the AFM tip and the fast relaxation of the membrane, as in experiments.

After an initial transient, the kinetic friction was calculated as the average sliding force shown in Fig. 5.4(a-b) as horizontal lines. The protocol to compute kinetic friction in this clamped system is described in detail

[1] We point out further effects of finite size, edge orientation, and full open-boundary conditions are discussed in [10] supplemental, in dependent of our conclusion here.

[2] Shown in detail in supplemental [10]

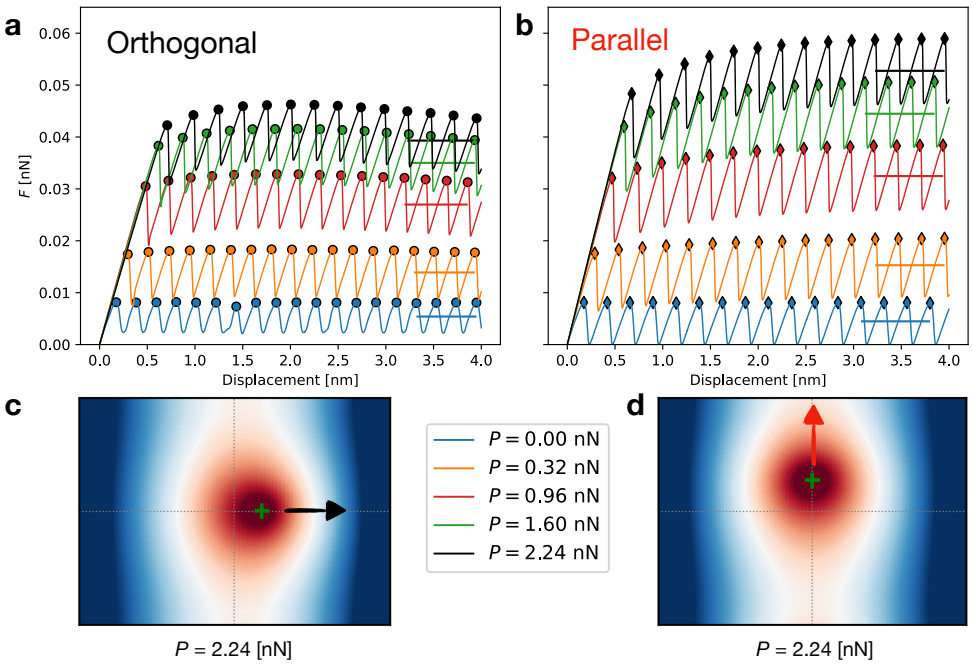

Figure 5.4: Simulated frictional response of the membrane perpendicular (a) and parallel (b) to the clamps. The y axis reports the force on the cantilever while x reports the cantilever position. Each colored line corresponds to a load, as reported in the legend in the bottom right. The friction traces are normalized by the elastic charging of the membrane – more detail in the Supplemental[10]. Color-matching horizontal lines show the average friction force at each load after the initial transient. Note that the average excludes the end of the simulation to limit the influence of the clamps in (a) and of the free edge in (b). Panels (c), (d) show the tip-sliding direction and the evolution from the indentation profile in Fig. 5.3(e) toward the end of the trajectory; color scale is the same as Fig. 5.3. Dashed horizontal and vertical gray lines indicate $x = 0$ and $y = 0$ as a guide to the eye.

Sec. 5.7. From Fig. 5.4(a-b) one can already see that the friction in the orthogonal direction is smaller than in the parallel one, as in experimental curves in Fig. 5.2(b). The force-load curves for the two directions are obtained by plotting the average friction force, horizontal lines in Fig. 5.4(a-b), against the applied load P. Fig. 5.5(a) reports the average friction vs load for the orthogonal (blue line) and parallel (orange line). For small loads ($P = 0 - 0.5$ nN), where the anisotropic mechanical constraint of the clamping is very modestly perceived, the two curves behave similarly; as the load increases, however, the average force in the parallel direction keeps rising, while in the orthogonal direction the growth slows down. This follows the experimental behavior in Fig. 5.2(b), where parallel force is higher while perpendicular is smaller. Even though the model force-load curves in Fig. 5.5(a) showed a clear nonlinear trend, as reasonable for the system, the concept of differential COF helps to establish a systematic comparison with experiment. Considering only the large-load limit [dashed lines in Fig. 5.4(a)], we obtained $COF_{\perp} = 0.013$ and $COF_{\parallel} = 0.023$, yielding a ratio $COF_{\parallel}/COF_{\perp} = 1.7$. We conclude that this minimal model is able to reproduce fairly well the experimental finding $COF_{\parallel} \gg COF_{\perp}$.

Note that the COFs from MD simulations are higher than in experiments. This discrepancy can be linked to the simulated system being an ideal crystal at zero temperature, providing an upper bound for the friction force in the real system. At the same, the agreement between trends found in experiments and in MD simulations are robust against variations of crystal orientation and boundary conditions[2] (see also Ref. [230]). Hence, we believe the physics underpinning the experimental results are well described by the theoretical model, while the assumptions of the model result in a qualitative rather than quantitative agreement.

These "*in silico* frictional experiments" were crucial to understand the origin of this asymmetric rheological response of suspended graphene in absence of prestrain. Fig. 5.5(b-c) report the model strain distribution in the membrane as the bond-length deviation from equilibrium, $\langle\delta\rangle_{nn} = \left\langle \frac{l-l_0}{l_0} \right\rangle_{nn}$, where $l_0 = 0.139$ nm is the

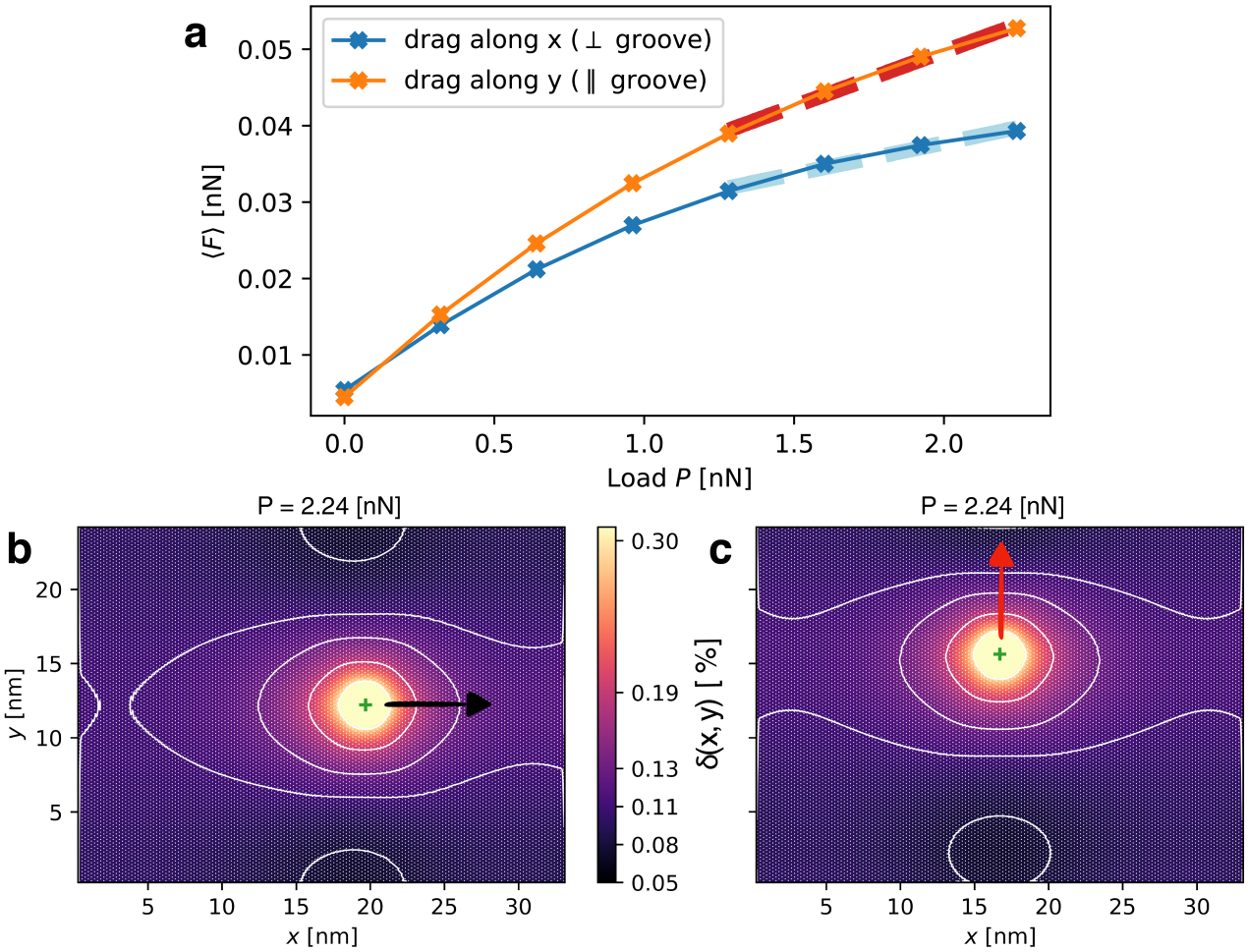

Figure 5.5: (a) Average friction vs load for the direction perpendicular (blue curve) and parallel (orange) to the clamp. COF perpendicular and parallel to the clamps is defined as the slope of the light-blue and red-dashed lines, respectively. (b), (c) Overall strain of each carbon atom as bond-length difference averaged over its nearest neighbors. (b) Final snapshot of orthogonal dragging, and (c) for parallel dragging; both snapshots refer to load $P = 2.24$nN [black curves in Fig. 5.4(a-b) and last point in (a)]. Green cross marks the tip position. Darker regions mark smaller strain, lighter regions higher strain. White lines mark the isoline at the values reported on the color bar.

equilibrium C − C bond length in MD and the $\langle\cdot\rangle_{nn}$ indicates the average over the nearest neighbors of each carbon atom. While no prestrain is present in the membrane, the tip indentation stretches the membrane up to $\delta \sim 2\%$ right below the tip as shown by the large yellow patch in Fig. 5.5(b-c). This tip-induced strain is larger in the orthogonal direction, as the graphene needs to comply with both the tip pressure and the clamps pull [see the brighter horizontal strip highlighted by the white contour lines in Fig. 5.5(b)]. Hence, the membrane is stiffer in the transverse direction. On the other hand, in the parallel direction the tip-induced strain is lower [see the black regions enclosed by the white contour lines in Fig. 5.5(c)]. When the tip was dragged along the transverse direction, the stiff substrate was not deformed significantly by the pushing tip and the force needed to slide was small. Conversely, when the tip was driven along the parallel direction the graphene membrane deformed easily under the action of the sliding probe, resulting in a higher force opposing sliding and, thus, a higher dissipation. As the load increases, the orthogonal direction becomes stiffer, enhancing this effect and leading to the smaller coefficient of friction shown in Fig. 5.5(a).

5.5 Discussion

The computational results indicate that the anisotropic stiffening of the membrane induced by the clamping during indentation, and not an anisotropic prestrain, which is absent in our case, is the mechanism underpinning

the different frictional response in the orthogonal and parallel directions. This argument is further corroborated by the experiments. Analyzing the effective piezoelongation as a function of the applied loads during the acquisition of friction vs load images[2], we can extract the tip-induced elastic deformations of graphene along both the orthogonal and parallel directions of the groove. This analysis provided an estimate of the effective elastic constant (K_{eff}) for the coupled graphene-cantilever system. The mechanics is that of two springs in series: One is given by the flexural constant K_{N} of the AFM cantilever; the other represents the elastic response of the graphene membrane subject to normal load, whose constant is termed here K_{Gr}.

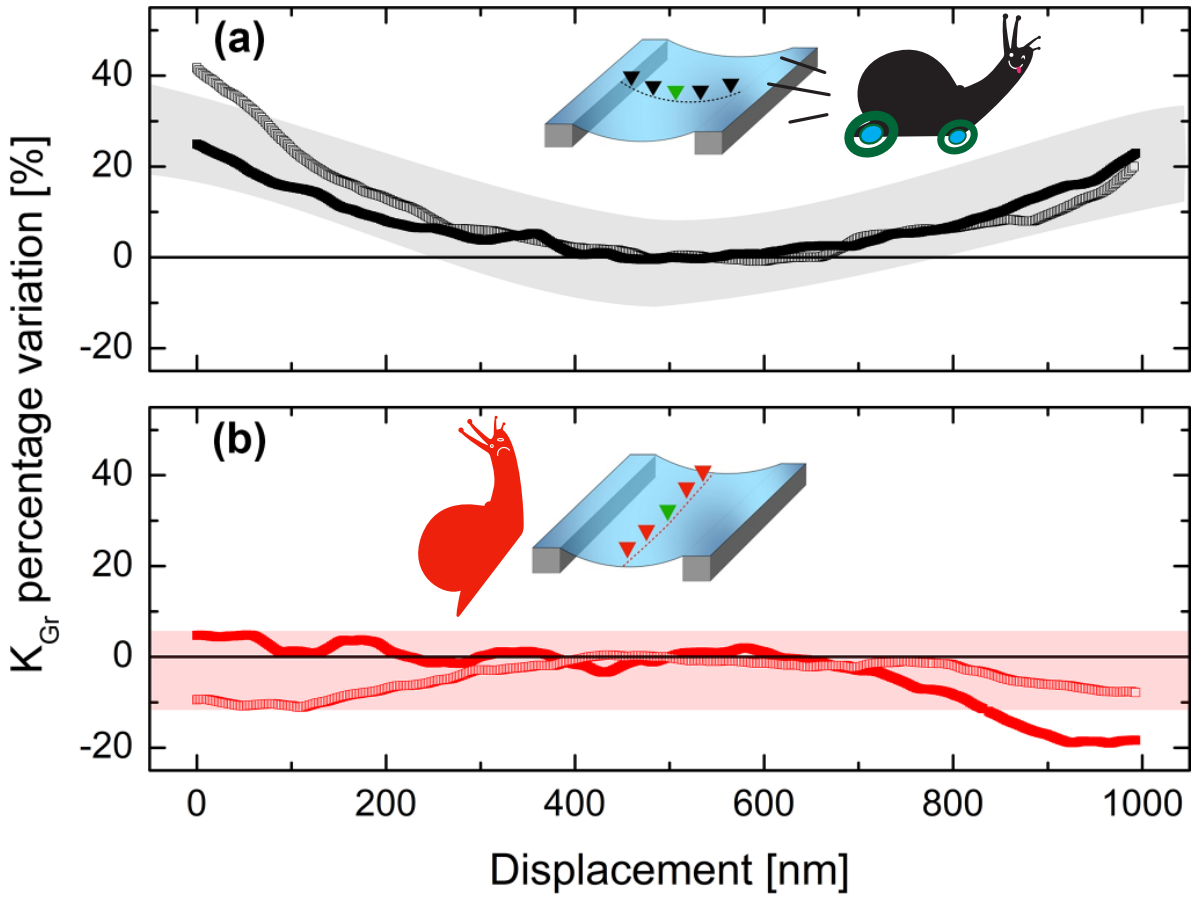

Figure 5.6: Elastic behavior of the graphene membrane along the orthogonal (black) and parallel (red) scan directions (light and dark lines correspond to different membranes). Elastic constant of the graphene membrane is evaluated as discussed. Data are normalized to the values evaluated at the membrane center (green triangle in the insets) and they are shown as relative percentage variation. In the orthogonal direction the relative variation of K_{Gr} near the clamping regions achieves 40% while along the parallel direction it is almost always contained within 10%. Reference values at the center are membrane 1 (dark line) $K_{\text{Gr}} = 0.455 \pm 0.05$(N/m); and membrane 2 (light line) $K_{\text{Gr}} = 0.46 \pm 0.15$(N/m).

Figure 5.6 reports the variation of the graphene elasticity K_{Gr} as a function of the positions along the orthogonal [Fig. 5.6(a)] and parallel direction [Fig. 5.6(b)] with respect to the value at the center of the path. In the orthogonal direction, the relative variation of K_{Gr} near the clamping regions achieves 40%, while along the parallel direction the variation is almost negligible (within 10% of the value at the center).

Hence, the intrinsic membrane elasticity as described by K_{Gr} strongly depends on the scan direction. In particular, the orthogonal scan reveals a nonuniform response along the profile: The center region is softer while the system gradually becomes effectively stiffer approaching the clamping constraints. On the contrary, in the parallel scan direction, the response is essentially constant, as expected from the model. The behavior described by the intrinsic membrane elasticity is consistent with computational results: The induced strain reported in Fig. 5.5(b-c) indicates anisotropic membrane stiffness along the two sliding directions. Tip sliding along the

orthogonal direction [Fig. 5.5(b)] moved toward higher strain regions near the clamps compared to the center: The membrane became stiffer. Conversely, when the tip slid along the parallel direction [Fig. 5.5(c)] the strain distribution just translated unchanged with the tip, yielding the same stiffness along the path.

5.6 Conclusions

The effect of in-plane strain on the frictional mechanics of free-standing 2D membranes has been addressed only recently. Within the effort of understanding the nanorheology of 2D materials under strain, graphene has been investigated in different conformations, from freely suspended on a circular hole to strained as the hole gets pressurized. We found unexpected results on the asymmetric tribological response of a single-layer CVD graphene freely suspended over a specially designed groove geometry. FFM measurements and friction vs load analysis performed at the membrane center reveal a remarkably large anisotropy with respect to the groove axis. A very low COF is measured by sliding transverse to the groove while an unexpected nearly threefold increase is obtained when moving parallel. As the prestrain discussed in the literature is absent in our system, a different mechanism is required to explain the observed anisotropy. Our MD model, corroborated by subsequent measurements, suggests that deformation induced by indenting and sliding action of the tip is anisotropic due to the asymmetric clamping conditions. This also reflects in anisotropic friction response of the graphene membrane. Sliding orthogonally to grooves produces a larger strain, where the membrane stiffens and the force needed to drive the tip drops. On the contrary, moving parallel to grooves the graphene membrane deforms easily and a larger force is needed to slide. This mechanism is amplified with increasing load, which results in an asymmetric dependence of friction vs load.

These experimental results complemented by numerical simulations demonstrate how strong adhesion (clamping) and decoupling (suspension) from the substrate can modulate the stiffness and the friction on these membrane-like systems. Strongly anisotropic geometries, such as that investigated here, are likely to occur in realistic systems. Hence, we believe that our results and analysis will be relevant to design and tune future graphene-based systems such as nanomechanical devices and ultralow-friction coatings.

5.7 Additional note

Methods

Non-equilibrium molecular dynamics (NEMD) simulations are performed using LAMMPS [225]. The graphene membrane is modeled using the AIREBO potential [46] and LJ for graphene-Si interaction $\varepsilon = 0.0087$ eV and $\sigma = 3.595$ Å[201].

To mimic the suspended graphene, we clamp and hold both sides of graphene in the Xdirection with strong springs of stiffness $K_c = 1602.17$ N/m. This large value is chosen as a compromise between vertical load and size of the system, which is also close to Young's modulus of graphene given its nanometric size. However, the overall features of simulations remain independent of this choice; smaller values would intuitively reproduce the same results for a smaller scale of vertical loads. Simulations with both open and periodic boundary conditions (OBC and PBC) along Y-direction are performed. To test the effect of the membrane crystalline orientation, all measurements are done for both armchair and zigzag orientations of graphene.

The relaxed indentation configurations are obtained in three steps; first, imposing an initial constant vertical load on the tip which allows preliminary shaping during N = 3000000 steps of MD simulation with the time step dt = 1fs. Second, using CG minimisation with tolerance 10^{-16} eV on the energy allows fast readjustments of the configurations. Third, a final MD run with N = 3000000 steps gives us realistic results, allowing for fine readjustment. To simulate frictional measurements, the system is kept at zero temperature using a Langevin thermostat with damping factor gamma = 0.05 ps. We performed more simulations for various values above and below this value, and the results of this work are confirmed to be independent of a specific choice. The tip is attached to a moving stage with constant velocity $v_{\mathrm{drag}} = 2.0$ m/s with a spring of stiffness $K_{\mathrm{drag}} \sim 0.08$ N/m. The friction force is computed as $F = K_{\mathrm{drag}}\,[v_{\mathrm{drag}}t - \ r_i(t)]$ where $r_i(t)$ is the instantaneous position of the tip along the direction i, which could be perpendicular (x axis) or parallel (y axis) to the clamps.

Finally, to confirm the consistency of results, the procedure is repeated back and forth many times to regain the same hysteresis. To estimate the contact area of atomically-thin tip adopted in MD simulation of the PT model, we adopt a simple Hertian model. The radius a of the contact area is expressed in terms of the applied load P and mechanical properties of the tip by $a = \left(\frac{3PR}{4E^*}\right)$, where R is the curvature radius

of the tip, here the LJ interaction R = 0.35 nm, and the effective Young modulus of the contact is given by $1/E^* = \left(1 - v_1^2\right)/E_1 + \left(1 - v_2^2\right)/E_2$. The Young and Poisson modulus for graphene and silicon tip, respectively, are taken from the Material Project [226, 227]: $E_1 = 371$ GPa, $v_1 = 0.19$, $E_2 = 151$ GPa, $v_2 = 0.20$.

Chapter 6

Buckling, Bending, and Topological Bands of Freestanding Twisted Bilayer Graphene

6.1 Introduction

Two-dimensional (2D) bilayers and multilayers with variable lattice mismatch and/or twist angles exhibit a host of physical properties that also hold promise for applications [231–234]. With exceptional electronic properties at the magic twist angle, twisted bilayers graphene (TBG) are prominent among them [63, 64, 235]. Experimental bilayers are generally studied in deposited/encapsulated configurations, which preserve a flat geometry and the twist-related moiré pattern plays no mechanical role. Yet, TBG may also be realized as freestanding [236, 237]. Below a critical twist angle θ_c, moiré related structural instabilities and a variety of "buckled" states were suggested by pioneering freestanding simulations [208, 238, 239], but the actual nature and properties of the true TBG buckled state remain unknown. We use here theory and simulation to show that the moiré buckled state formed at low twist angle is quite different from expectations. Mechanically, it is accompanied by the unanticipated collapse of the TBG macroscopic bending rigidity. Electronically, the magic twist angle narrow bands, now doubled in number, are unexpectedly degenerate at zone boundaries, the vanishing Bragg scattering symmetry motivated reflecting single valley physics.

6.2 Mechanical properties

Starting with molecular dynamics (MD) simulations, large size model TBGs with variable twist θ and variable numbers N_{moire} of moiré cells were constructed with periodic boundary conditions in the (x, y) plane. Based on well-tested interatomic interactions and protocols (detailed in Section 6.5) we sought the zero stress equilibrium T=0 structure versus θ. We found that, similar but not identical to suggestions [208, 238, 239], two regimes emerge, separated by a structural phase transition at a critical $\theta_c \approx 3.77°$. Above θ_c the two layers remain flat and specular relative to the central plane (Fig. 6.1b). Below θ_c the layers jointly buckle giving rise to a "moiré (2×1)" cell doubling along armchair direction x, leading to two inequivalent, z-antisymmetrical AA nodes, AA1 (up) and AA2 (down) per cell, as in Fig. 6.1a. The magnitude of buckling is large. At the magic twist angle $\theta_m \approx 1.08°$ for example the zigzag z-corrugation is ≈ 10 (Fig. 6.1a,c). A competing $(\sqrt{3} \times \sqrt{3})$ buckling distortion, with one AA1 (100 % up) hexagonally surrounded by AA2 and AA3 (50 % down), was also found. It led to a slightly lower energy gain, and its details are further discussed in Section 6.5.8– not discussed here.

The energy gain driving the buckling distortion at $\theta < \theta_c$ is interlayer, with increased AB and BA, Bernal stacked areas, relative to the flat, unbuckled state's. That gain is balanced by an intralayer cost concentrated at the AA nodes, now transformed into buckling "hinges" AA1 (up) and AA2 (down). As θ decreases, the 2D density of AA nodes, thus of hinges, drops $\sim \theta^2$, and so does the cost, eventually favoring buckling for $\theta \leq \theta_c$. The transition, simulated by maintaining zero external stress and zero temperature, was found to be continuous.

6.2.1 Buckling order parameter

We define the $T = 0$ K buckling order parameter Q_0 as the large-size average Fourier component of the (2×1) moiré corrugation

$$Q_0 = \frac{a_{\rm Gr}}{N_x N_y A} \left\langle \sum_{n=1}^{N_{\rm at}} z_n \exp\left(-\frac{2\pi i}{l_x} x_n\right) \right\rangle \tag{6.1}$$

where $a_{\rm Gr}$ is graphene's lattice constant, $l_x = \sqrt{3}\lambda$ is the size of the buckled unit cell along the armchair direction x (Fig. 6.1a,b), $\lambda \sim a_{\rm Gr}/\theta$ is the moiré lattice constant (Fig. 6.1a,b), x_n and z_n are coordinates of the n-th atom ($n = 1, 2, ...N_{\rm at}$), $A = \sqrt{3}\lambda^2$ is the buckled unit cell area, and N_x, N_y are the number of cell replicas along x and y. This $Q_0(\theta)$ is proportional to the buckling induced bilayer thickness increase $\langle (z_{AA1} - z_{AA2}) \rangle$ (inset of Fig. 6.1c). Simulation for a set of θ values (see Section 6.5.2) characterized by a sufficient numbers of moiré cells $N_{\rm moire}$ showed, at $T = 0$, a growth of $Q_0(\theta < \theta_c)$ (Fig. 6.1c) well approximated by a power-law rise $Q_0(\theta) \approx 0.48\Theta(\theta_c - \theta)(\theta_c - \theta)^\beta$, where Θ is Heaviside's function, and $\beta = 0.7(0)$ a critical exponent. Within fitting uncertainty, reflected by the second decimal in brackets, this exponent differs from $1/2$, that could be expected for a classical $T = 0$ transition.

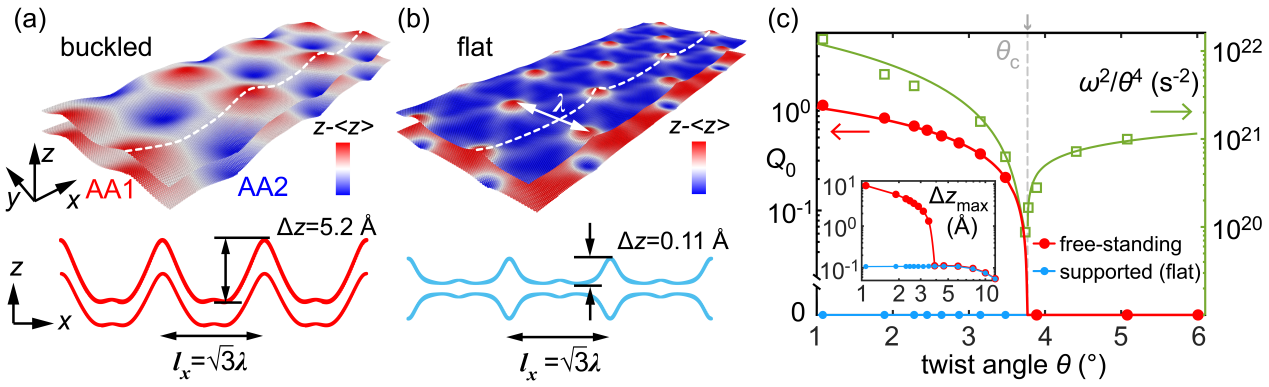

Figure 6.1: Visual models of small twist angle TBG structure at $T = 0$. Out-of-plane displacement of (a) optimal free-standing (2×1) buckled and (b) flat structures, magnified by factors 3 and 100 respectively, are sketched for twist angle $\theta_m = 1.08°$, where the moiré size $\lambda \approx a_{\rm Gr}/\theta_m \approx 13$ nm. (c) Twist angle dependence of the optimal buckling order parameter Q_0 (red and blue, left axis) for $N_x = N_y = 1$, $T = 0$ K, and of the normalized soft phonon frequencies ω^2/θ^4 (right axis, green). Critical twist angle $\theta_c \approx 3.77°$ marked by grey dashed line. Red and green lines are power law fits as described in text. Inset shows the maximum out-of-plane corrugation $\Delta z_{\rm max}$.

As in other displacive phase transitions, the local free energy around equilibrium supports a soft buckling phonon mode ω_i ($i = (+, -)$ refers to above or below θ_c), a mode which will also control critical fluctuations at $T > 0$. Its frequency was extracted from oscillations around equilibrium of a (2×1) moiré cell by starting the dynamics with $Q = Q_0 + \delta Q$, with $|\delta Q|/Q_0 \ll 1$, while maintaining $T = 0$ and zero stress. Because the cell area $A(\theta)$ varies as θ^{-2}, it is convenient to further normalize the soft mode frequencies to constant area in the form ω^2/θ^4. Power law fits near the singularity at θ_c yield (Fig. 6.1c), $\omega_i^2/\theta^4 \sim a_i|\theta - \theta_c|^{\gamma_i}$, with $\gamma_+ = 0.3(7)$, $\gamma_- = 1.3(0)$, with $a_+ = 8.58 \times 10^{20}$ s^{-2}, $a_- = 3.24 \times 10^{21}$ s^{-2}. Note the strongly asymmetric, again unusual exponents. We observe nevertheless that $\gamma_-/\beta \approx 2$ as in standard mean-field theory.

6.2.2 Bending stiffness collapse

Interestingly, the buckling amplitude Q_0 and its soft mode frequency are not the only critical quantities at $\theta \to \theta_c$. We found an unexpected collapse in its macroscopic partner, the bilayer's bending stiffness. Defined for direction $\mu = (x, y)$ as $D_\mu = {\rm d}F/{\rm d}[(\partial^2 h/\partial\mu^2)^2]$, where F is the Helmholtz free energy density, $\partial^2 h/\partial\mu^2$ is the μ-th component of the 2D Laplacian, and h the bilayer's corrugation profile $h(x, y)$ (Fig. 6.2). Controlling the membrane's deviations from planarity, D_μ determines the macroscopic flexural mode dispersion along μ, $\omega_\mu(q_\mu) = (D_\mu/\rho_{\rm 2D})^{1/2} q_\mu^2$, of an infinite membrane of 2D density $\rho_{\rm 2D}$.

The freestanding TBG bending stiffness D_μ was extracted by starting simulations with a slight x-compression (Fig. 6.2), i.e., $L_\mu = L_{0\mu} - \delta L$, of the bilayer's zero-pressure equilibrium size. Either the initial energy increase δE, or the ensuing flexural oscillation ω_μ yield $D_\mu = \lim_{\delta E \to 0} \frac{L_\mu^4 \delta E}{\pi^4 A h^2} = \frac{\rho_{\rm 2D} L_\mu^4 \omega_\mu^2}{16\pi^4}$ [240]. The resulting D_x is shown

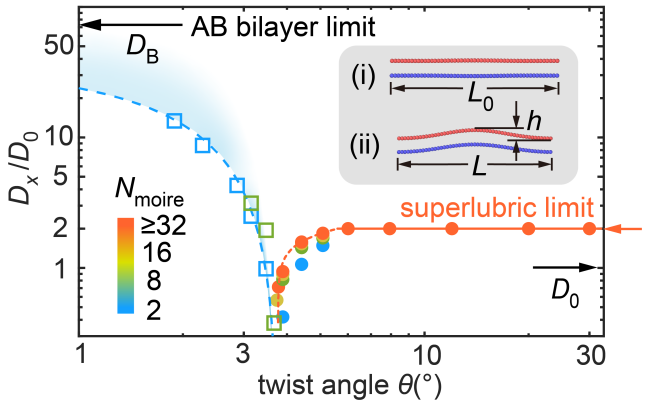

Figure 6.2: Freestanding TBG bending stiffness D_x/D_0, normalized to the monolayer's D_0, from zero stress simulations at $T = 0$. Note the critical collapse (red circles for $\theta > \theta_c$, blue squares for $\theta < \theta_c$). Dashed and dotted curves are power-law fits near θ_c. Multiplicity of circles at same twist angle shows convergence for simulation cells with increasing size $N_{\rm moire}$ (the $N_{\rm moire}$ dependence is weak for $\theta < \theta_c$). Inset: simulation protocol (see text).

in Fig. 6.2. For $6° < \theta < 30°$, D_x is close to $2D_0$, where $D_0 = 1.44$ eV is the bending stiffness of monolayer graphene [241], the factor 2 reflecting free sliding between the two layers[242, 243]. At the opposite end $\theta = 0°$, layers are instead locked in Bernal's AB stacking. That pushes D_x up to $D_{\rm B} \approx 100$ eV, now reflecting the large in-plane stiffness of graphene [244, 245]. The novelty is that between these extremes, D_x drops below $2D_0$ when $\theta \lessapprox 6°$, critically collapsing at θ_c, and rising immediately below towards $D_{\rm B}$. Near θ_c the collapse is critical

$$D_x(\theta) \sim c_i|\theta - \theta_c|^{\epsilon_i} \tag{6.2}$$

with exponents $\epsilon_+ = 0.2(2)$ and $\epsilon_- = 1.4(4)$, and c_+=2.4 eV and c_- =7.5 eV, for $\theta > \theta_c$ and $\theta < \theta_c$ respectively.

6.2.3 A model to relate buckling to bending

Why does a *macroscopic* mechanical parameter like $D_x(\theta)$ drop critically at the *microscopic* buckling transition? We developed an analytical "zigzag" model that explains it. As sketched in Fig. 6.3a the buckled structure can roughly be modeled as a zigzag shape where flat (AB-commensurate) regions are separated by maximally bent (AA-centered) hinges. The total length of the system along the buckling direction is $L_x = N_x l_x$. Upon bending along x both hinges and flats undergo deformation, and the free energy increase with bending angle Φ is $F(\Phi) = \frac{D_{\rm f} K l_y}{2N(2D_{\rm f} l_y + K l_x)}\Phi^2$ where $D_{\rm f}$ is the bending stiffness of the flat pieces, K the angular stiffness of the hinges, and l_y the bilayer size perpendicular to the bending direction x. Defining an effective bending stiffness $F = \frac{D_{\rm eff} l_y}{2L_x}\Phi^2$, one obtains, using $l_y = \lambda$,

$$D_{\rm eff} = \frac{D_{\rm f}}{1 + 2D_{\rm f}/\sqrt{3}K}. \tag{6.3}$$

We can now assume $D_{\rm f} = D_{\rm B} \approx 100$ eV of the flat pieces for $\theta < \theta_c$, dropping to $D_{\rm f} = 2D_0 = 2.88$ eV for $\theta > \theta_c$ (Fig. 6.3b). The collapse of $D_x(\theta)$ at θ_c is controlled by that of the hinge stiffness K, connected to the buckling frequency $\omega_\pm$ by simple mechanics

$$K \propto \rho_{\rm 2D} l_x^4 \omega_\pm^2. \tag{6.4}$$

Inserting $\omega_\pm$ into Fig. 6.3b, theoretical and simulated bending stiffnesses agree fairly well, both in magnitude and in critical scaling (details in Section 6.5.5). Thus the TBG bending stiffness collapse is a direct consequence of that of the buckling modes $\omega_\pm$. In return, the buckling criticality must be influenced by the bending one. The coexistence of these two coupled degrees of freedom, with important cross correlations, is likely to account for the unusual exponents.

We come next to two important properties predicted for the freestanding TBG buckled state, namely temperature behaviour, and the narrow band electronic structure at the magic twist angles.

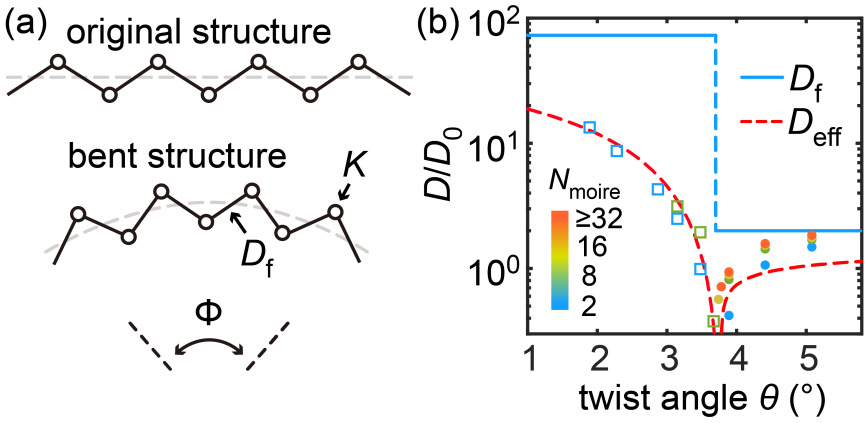

Figure 6.3: Zigzag model of bending stiffness D_{eff} in a buckled bilayer. (a) Unbent and bent models; (b) bending stiffness from real simulations of Fig. 6.2 (circles and squares) and from zigzag model, Eq. 6.3 (red dashed line). Assumed flat piece stiffness D_{f} (blue line) (more detail in Section 6.5.5).

6.2.4 Temperature effects

Finite temperature MD simulations show that at small twist angle the buckling persists up to high temperature. Flexural fluctuations, abundant and not gapped, do not cancel the buckling order parameter, which survives up to a remarkable ≈ 500 K at the magic twist angle (Fig. 6.4a). If bending could be ignored, this robust buckling order should drop at some T_c with 3-state Potts universality, whose behaviour is critical as opposed to first order, despite the presence of Landau 3rd order invariants [246] [1]. Unfortunately, size limitations obscure the precise high temperature buckling demise, replacing it with the smooth crossovers of Fig. 6.4a (see Section 6.5.4), equally compatible with either continuous or discontinuous decays. We also extracted the temperature dependence of bending stiffness (Fig. 6.4b). We do not deal with the long-wavelength anomaly of the freestanding bilayer as a membrane [247], but simply extract the buckling-related evolution, as predicted for observation in microscopic size samples. Contrary to the buckling robustness, bending stiffness changes dramatically with temperature. The singularity near θ_c is quickly wiped out (Fig. 6.4b), the two layers eventually bending independently despite the large buckling. Reflecting that, the flexural fluctuations of a TBG near θ_c should grow anomalously at low temperature, when D_x is small, but not above.

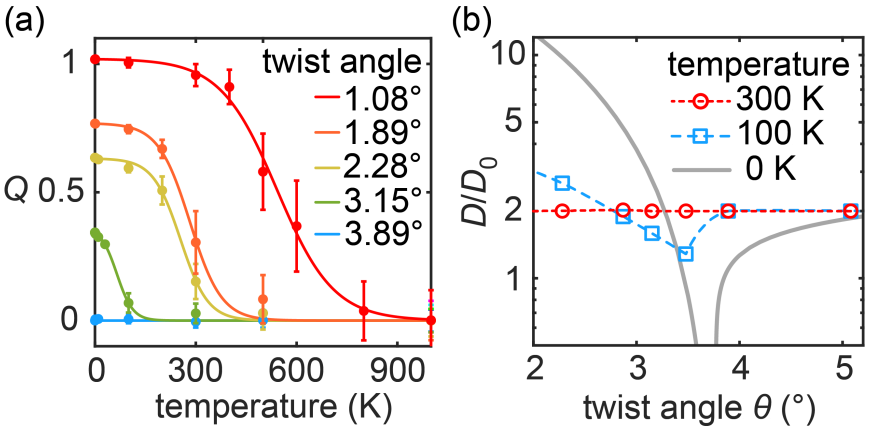

Figure 6.4: Effect of temperature. (a) Buckling order parameter at high temperatures. The expected critical behaviour is smoothened by small simulation size (three (2×1) cells at each θ). (b) Bending stiffness at $T = 0$ (gray, from Fig. 6.2), 100 K (blue) and 300 K (red). Note the extreme sensitivity to temperature.

[1] Under uniaxial stress or asymmetric boundary condition, such as sketched in Fig. 6.1a-b, that behavior might turn to Ising.

6.3 Electronic structure

Near the magic twist angle $\theta_m = 1.08°$, the flat TBG has four ultra-narrow bands, whose physics has been at the center of much attention [63, 235]. What will happen of these bands in the freestanding TBG, where the buckling sets in? We should anticipate eight narrow bands, separated by zone boundary gaps caused by the large (2×1) distortion. We carried out tight-binding calculations at θ_m and compared buckled and unbuckled TBG. The Hamiltonian, must be general enough to take into account the geometrical orientations of orbitals for the buckled TBG.

6.3.1 Hamiltonian

The tight binding Hamiltonian is $H = \sum_{i,j} -t_{ij}|i\rangle\langle j| + \text{H.c.}$, where t_{ij} is the transfer integral between sites i and j. Let $\boldsymbol{R}_j - \boldsymbol{R}_i = (l, m, n)d$ be the distance vector between two orbital, and $\hat{\boldsymbol{n}}_i = (n_i^l, n_i^m, n_i^n)$ be the direction of orbital $\boldsymbol{p}_i$, then using the Slater-Koster[248] formula

$$t_{ij} = \sum_{k}^{l,m,n} n_i^k \Big[n_j^k (k^2 V_{pp\sigma} + (1-k^2) V_{pp\pi}) + \sum_{g \neq k}^{l,m,n} n_j^g g k (V_{pp\sigma} - V_{pp\pi}) \Big] \tag{6.5}$$

where the out-of-plane (σ) and in-plane (π) hoppings are

$$V_{pp\sigma} = V^0_{pp\sigma} \ \exp\left(-\frac{d-d_0}{r_0}\right), \quad V_{pp\pi} = V^0_{pp\pi} \ \exp\left(-\frac{d-a_0}{r_0}\right) \tag{6.6}$$

where $V^0_{pp\pi} = -2.7$ eV and $V^0_{pp\sigma} = 0.48$ eV are are chosen to reproduce ab-initio curves in AA and AB stacked bilayer graphene similar to previous works [249], $d_0 = 3.344$ is the minimum distance between the two layers in the AB stacked region, $a_0 = a_{\text{Gr}}/\sqrt{3} \approx 1.42$ is the carbon-carbon bond length in the relaxed structure, and r_0 is the decay rate $\approx 0.184 a_{\text{Gr}}$.

In the particular case of unbuckled, flat bilayer $\hat{\boldsymbol{n}}_i \approx \hat{\boldsymbol{n}}_j \approx (0, 0, 1)$ therefore Eq. (6.5) reduces to $t_{ij} = n^2 V_{pp\sigma} + (1-n^2) V_{pp\pi}$ – see Fig. 6.5, where we show how the angle between two neighbouring local normals changes when they are buckled.

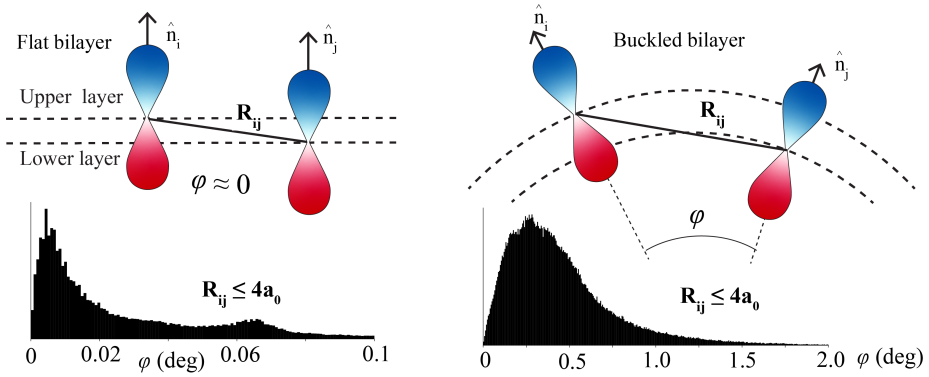

Figure 6.5: Unlike the flat bilayer (left panel), where local normals deviate very little from vertical, the deviation is much larger in the buckled state (right panel). The distribution of the included angle φ between two local normals $\hat{n}_i$ and $\hat{n}_j$ (within the cutoff range $R_{ij} \leq 4a_0$) is shown in the lower panel. The maximum φ for the buckled structure is more than one order of magnitude larger than the unbuckled structure – similar to what we discovered for the tilt angle ϕ.

6.3.2 Space group

The unit cell [2] of the (2×1) buckled TBG together with the Wyckoff positions in the $P2_12_12$ space group (no. 18) is shown in Fig. 6.6. We note that the 2a Wyckoff positions (red/blue circles) correspond to the AA stacked

[2] In order to be consistent with conventions of [63] (Cao, Nature, 2018) the x and y directions in the electronic section are exchanged with respect to the structural part.

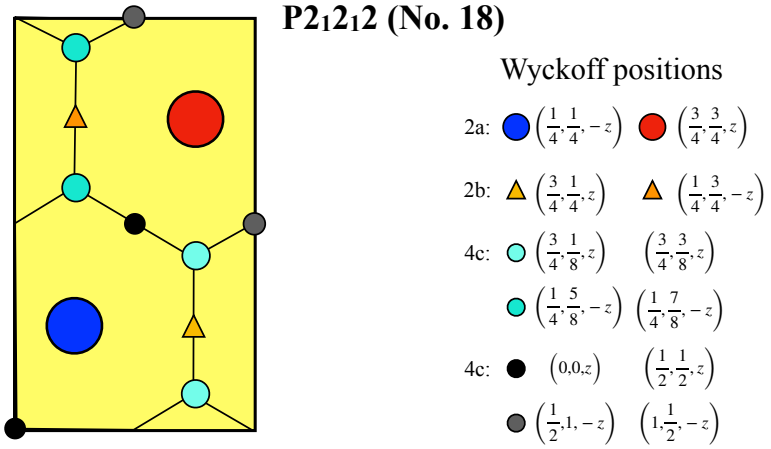

Figure 6.6: Unit cell and Wyckoff positions in the space group $P2_12_12$. Note that the 2a positions corresponds to the AA stacked regions, whereas the 4c positions in cyan to the Bernal stacked ones.

regions and the 4c positions (cyan circles) to the Bernal stacked ones. The 3f positions in the P622 space group (no. 177) of the unbuckled TBG split into the 2b and 4c (yellow triangles and black circles, respectively) in the space group of the buckled TBG. The non-symmorphic symmetry connects the two 2a positions, the two 2b ones, as well as the two sets with opposite z coordinates within the 4c Wyckoff positions (light cyan $\rightarrow$ dark cyan, as well as dark gray $\rightarrow$ black).

6.3.3 Flat Bnads

In Fig. 6.7(a) we show the flat bands of the *unbuckled* bilayer folded into the reduced BZ of the 2×1 buckled one, labelling the Bloch waves at the high symmetry point with the irreps of the $P2_12_12$ space group, (despite the correct space group in this case being $P622$, no. 177).

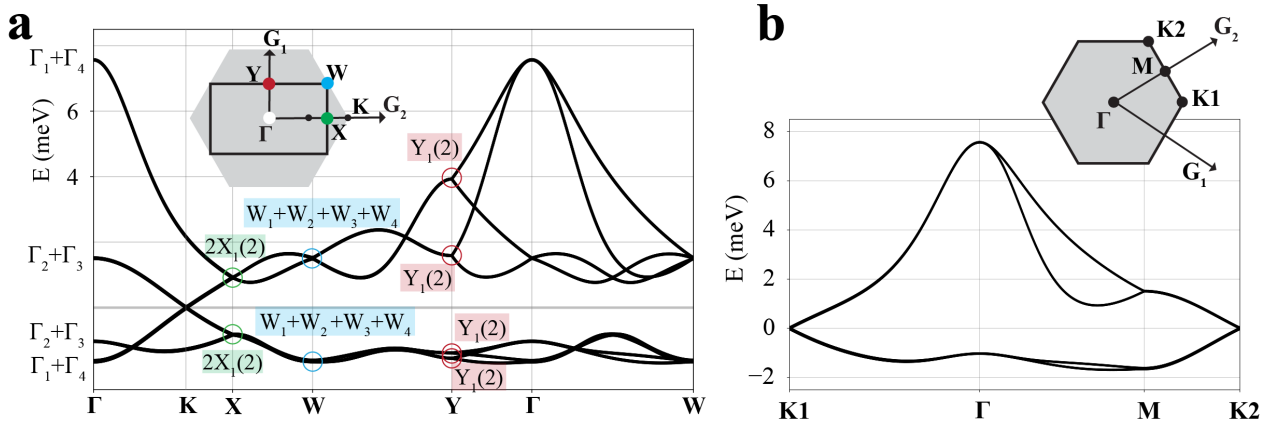

Figure 6.7: Flat bands for the bilayer graphene with twist angle $\theta = 1.08°$. (a): flat bands of the unbuckled bilayer folded into the (2×1) reduced Brillouin Zone. The additional crossings of the unbuckled bands arise because the actual space group is P622 (no. 177). (b): flat bands of the unbuckled bilayer in their natural (1×1) Brillouin Zone.

Shown in Fig. 6.8 are the 8 bands of the buckled state. The bands, almost a factor 2 wider, display important novelties. First, unlike the unbuckled TBG (or even the non-optimal (1×1) buckled state [208]) the Dirac zero gap, formerly at point K, is now split into two close-by points $K \pm k_y$ (see inset). Second, and striking, zone boundary splittings at W and X points – expected because (2×1) buckling removes the C_{3z} symmetry, and Bragg scattering should in principle take place – do not occur. This anomaly calls for a full symmetry analysis.

In the next section, we identify the flat bands corresponding to a given valley, magnetic space group $P2_12_1'2'$, no. 18.19. These single-valley bands can be generated by the atomic limit of Wannier orbitals centered at the

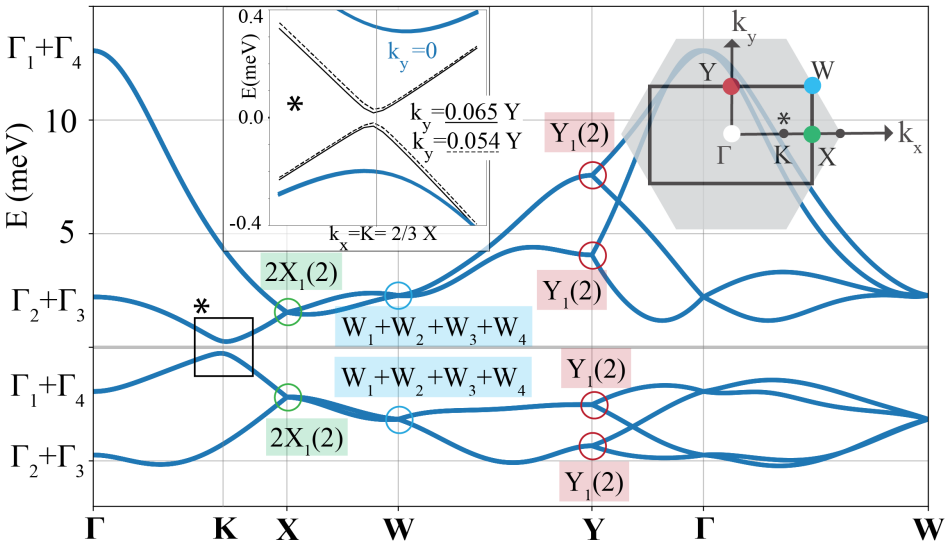

Figure 6.8: The eight narrow bands of the (2×1) buckled TBG at the twist angle $\theta = 1.08°$. Inset $*$ shows how the gap closing point is now split into two, above and below (not shown) the point K where it lies in the flat TBG.

Wyckoff positions $4c$ of space group $P2_12_1'2'$. Yet, this was not possible in the original unfolded band structure [249, 250]: and that was a clear symptom of non-trivial topological character of the unbuckled bilayer – *a property that should be independent of the arbitrary choice of unit cell and folding procedure*. For that reason, despite not having right tools to prove it, we conjecture that the bands of the buckled twisted bilayer graphene are likely to be topological as well.

6.3.4 Symmetries

The buckled structure has, unlike the flat one, a non-symmorphic space group $P2_12_12$ (no. 18) that includes $\{1 \mid 0\}$, $\{2_{010} \mid 0, 1/2, 0\}$, $\{2_{100} \mid 1/2, 0, 0\}$ and $\{2_{001} \mid 1/2, 1/2, 0\}$, (in Seitz notation, with fractional translations) which we shortly denote as E, C_{2y}, C_{2x} and C_{2z}, respectively. The Bloch states of the 8 bands at the high symmetry points transform as the irreducible representations (irreps) of the corresponding little groups.

	E	C_{2z}	C_{2y}	C_{2x}
Γ_1	1	1	1	1
Γ_2	1	1	-1	-1
Γ_3	1	-1	-1	1
Γ_4	1	-1	1	-1

	E	C_{2z}	C_{2y}	C_{2x}
W_1	1	1	i	i
W_2	1	1	$-i$	$-i$
W_3	1	-1	$-i$	i
W_4	1	-1	i	$-i$

	E	C_{2z}	C_{2y}	C_{2x}
$X_1(2)$	1	σ_3	σ_1	$-i\sigma_2$
$Y_1(2)$	1	σ_3	$-i\sigma_2$	σ_1

Table 6.1: Character table and irreducible representations at the high-symmetry points in space group $P2_12_12$.

In Table 6.1 we report the character table of the irreducible representations (irreps) at the high-symmetry points in space group $P2_12_12$, where σ_a, $a = 1, 2, 3$, are Pauli matrices that act in the space of two-dimensional irreps. The eigenstates of the Hamiltonian that we calculate do transform as one of the irreps at the corresponding high-symmetry points, see Fig. 6.8, supporting our identification of the space group.

In our reference frame only C_{2y} commutes with the generator of $U(1)$ valley symmetry, while C_{2x}, and thus C_{2z}, exchange the valley index – as time-reversal symmetry $\hat{T}$ also does. It follows that, e.g., at the $\mathbf{\Gamma}$-point, C_{2x} and valley $U(1)$ get promoted to $SU(2)$. That enforces degeneracy between eigenstates with opposite parity under C_{2x} and same parity under C_{2y} [249], making Γ_1 degenerate with Γ_4, and Γ_2 with Γ_3. The interplay between valley $U(1)$ and the non-symmorphic group's fractional translations has further consequences at zone boundary points $\mathbf{W}$ and $\mathbf{X}$. Physical insight is obtained by switching to a single valley representation where valley index is conserved [250]. This representation obeys the magnetic space group $P2_12_1'2'$ (no. 18.19)

generated by E, C_{2y}, $\hat{T}\,C_{2x}$ and $\hat{T}\,C_{2z}$. The four flat bands per valley can be generated by Wannier orbitals centered at the Bernal stacked regions. Their centers correspond to the Wyckoff positions $4c$ in the magnetic space group $P2_12_1'2'$ [251–253], whose co-representation contains just the identity and thus allows a single irrep. The single-valley elementary band representation is [251–253]: $2\Gamma_1(+) \oplus 2\Gamma_2(-)$ and $2Y_1(+) \oplus 2Y_2(-)$, where $(\pm)$ indicate the parity under C_{2y}; $X_1X_2(2)$ and $W_1W_2(2)$, transforming under C_{2y}, respectively, as σ_3, the third Pauli matrix, and $i\sigma_3$ (see Table 6.1). Along the path $\mathbf{X} \to \mathbf{W}$, $k_y \in 0 \to \pi$, the irreducible representation remains twofold degenerate and transforms under C_{2y} like $\mathrm{e}^{ik_y/2}\,\sigma_3$. This now yields double degeneracies within a single valley. Bearing in mind that the two valleys must be further degenerate at all high-symmetry points and paths that are invariant under C_{2x}, one readily recovers the fourfold degeneracy at $\mathbf{W}$. In fact all "accidental" degeneracies of the band structure in Fig. 6.8 are explained in terms of single valley physics, enforced by non symmorphycity.

These one-electron degeneracies, and the ways they might be broken by interactions, represent an interesting question for freestanding TBG experiments, where topology should also play a role. Since narrow bands do admit an elementary representation, the arguments used in the unbuckled case to diagnose a fragile topology [250] do not strictly apply here. The unexpected similarity of buckled bands to the (2×1) BZ folded unbuckled ones (Figures 6.7 and 6.8), nonetheless suggests that the topological properties remain similar. Thus [249, 254] the interplay between Coulomb repulsion and electron-phonon coupling to Kekulé modes should split the degeneracies and open the gaps that are absent at the one electron level, stabilising topological insulators in (2×1) buckled TBG, giving rise to novel fractional fillings absent in the flat state

6.4 Summary

In summary, several important phenomena are predicted to occur once freestanding TBG will be realized. First, a zigzag buckled state should set in with a critical behavior as a function of twist angle $\theta \to \theta_c \approx 3.7°$. At $\theta \approx 1°$ the normals to the bilayer should deviate from $\hat{z}$ by a sizeable $\sim \pm 3°$ (Section 6.5.7), experimentally observable. Second, the macroscopic bending stiffness, a crucial mechanical parameter for a membrane, should collapse at the buckling transition, giving rise to gigantic flexural fluctuations already at very low temperatures. Third, the buckling distortion should survive up to relatively high temperatures, whereas the bending stiffness anomaly will on the contrary dwindle upon heating. Fourth, narrow electronic bands are predicted for the buckled magic TBG displaying unexpected single-valley degeneracies, to be broken by interactions, with the possibility of doubling the number of quantized fillings upon gating. That should offer a richer playground for topological features and insulating states than for flat TBG. Other properties including kinetic and tribological behaviour will be addressed in follow-up work. Similar buckling phenomena could take place in freestanding bilayers of other 2D materials, now being pursued.

6.5 Additional notes

Here are some supplementary notes in case the reader wants to delve deeper into any particular section.

6.5.1 Simulation details

Twisted bilayer graphene (TBG) with periodic boundary conditions (PBC) along x and y directions are constructed for a discrete set of twist angles θ ranging from 1.08° to 30° chosen for supercells of reasonable sizes [255]. For the freestanding systems, no additional constraints are imposed along the out-of-plane (i.e., z) direction. To describe supported systems, z-direction springs with spring constant k_z are tethered to each carbon atoms to mimic the constraints from the substrate. The interlayer and intralayer interaction is described by the registry-dependent Kolmogorov-Crespi potential with local normals [256, 257] and REBO force field respectively [226]. All simulations are performed with open-source code LAMMPS [46, 258].

Structural optimization.

During the optimization, the simulation box adaptively changes size, so that the in-plane stress is fixed to zero, $p_{xx} = p_{yy} = 0$. The FIRE algorithm [259] is used to minimize energy during structural optimization (together with conjugate gradient algorithms with several loops to optimize the box size). Minimization stopped when the largest single atom force $|F_i| < 10^{-6}$ eV/. Unless otherwise specified, all structural optimization used this convergence criterion.

Bending simulation.

A compression protocol [242, 243] is used to extract the bending stiffness of TBG. As shown in Fig. 6.2, by compressing the simulation box (along x direction), the out-of-plane corrugation appears with height h (in bending simulations, $k_z = 0$). The compression strain $\varepsilon = (L_0 - L)/L_0$ in our bending simulations is chosen to be $\varepsilon \lesssim 0.1\%$, thus the ratio between the bending corrugation height ($h \sim L_0\sqrt{\varepsilon}/\pi$) and the length $h/L_0 \ll 1$. Since the free energy of the system increases during the compression-induced bending, the system will spontaneously oscillate after the release of the boundary constraints. From that we obtain the flexural oscillation frequency and thus the bending stiffness. In order to achieve free oscillations, the Nosé-Hoover thermostat and barostat are applied to the whole system during the simulation [260] with $T \to 0$ K and $p_{xx} = p_{yy} = 0$. The flexural frequencies are checked to be independent of the damping coefficient used.

6.5.2 Buckling order parameter at variable twist angle

As in main text, we start at finite temperature with the same order parameter definition Q^* for the (2×1) buckling distortion in the form:

$$Q^* = \frac{a_{\mathrm{Gr}}}{2L_xL_y}\left\langle\left|\sum_{n=1}^{N} z_n \exp\left(-\frac{2\pi i}{l_x}x_n\right)\right|\right\rangle \tag{6.7}$$

where $L_x = N_x l_x$ and $L_y = N_y l_y$ is the size of the box, $l_x \times l_y$ defines the size of one (2×1) moiré cell, N_x and N_y are the number of replicas along x and y directions. For the smallest simulation box ($N_x = N_y = 1$) and at $T = 0$ where the modulus is redundant, Eq. (6.7) coincides with Fig.1 in maintext. At nonzero temperatures, two problems arise with this definition of order parameter, a quantity that should represent the Bragg scattering magnitude produced by the symmetry breaking buckling distortion and nothing else. The first problem is that the coordinate difference of two separate TBG layer centers-of-mass exhibits a noticeable (x, y) random walk, permitted by the superlubric nature of their incommensurate contact, and by the finite supercell size. The larger the size, and the lower the temperature, the smaller this artifact. Because it gives rise to complex values of Q, we can eliminate it by taking the complex modulus as is done in Q^*.

The second problem is that temperature causes fluctuations with (2×1) periodicities, along with all other wavelengths, even in absence of distortions. This unwanted additional term had better be subtracted for the order parameter to yield correctly the distortion magnitude, representing the (2×1) Bragg reflection magnitude of a hypothetical scatterer. This correction will be discussed and eliminated in subsequent Section 6.5.3.

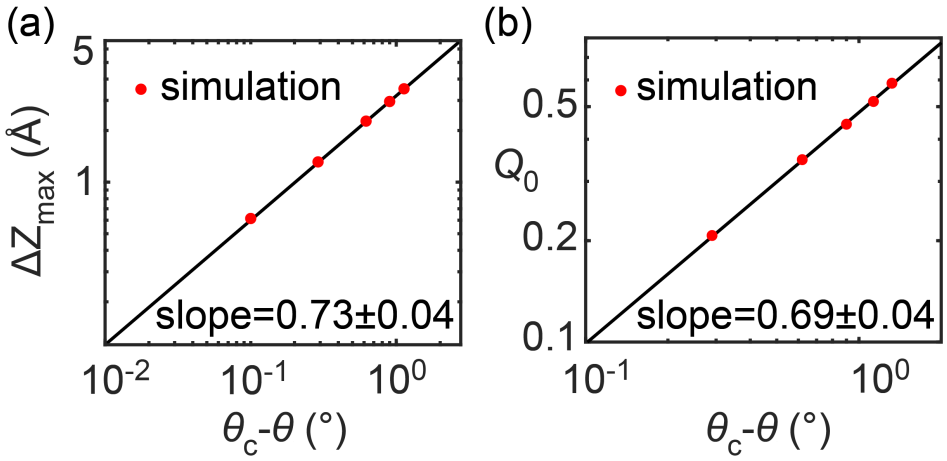

Figure 6.9: Fitting of the out-of-plane corrugation $\Delta z_{\max}$ and order parameters Q_0 of the buckling systems as a function of twist angle θ, at $T = 0$ K. The critical angle is $\theta_c = 3.77°$. Parameters used here are $T = 0$ K, $N_x = 3$ and $N_y = 1$.

From its definition, it is apparent that there is a positive correlation between the order parameter Q_0 and the maximum out-of-plane deformation $\Delta z_{\max} = \max(z) - \min(z)$. For systems at $T = 0$ K, we could use either parameter to represent the out-of-plane buckling magnitude. As shown in Fig. 6.9, for buckled structures ($\theta < \theta_c$), both $\Delta z_{\max}$ and Q_0 are well fit by power laws, with an exponent $\approx 0.7(0)$. For $\theta > \theta_c$, the order parameters is zero – no buckling.

6.5.3 Temperature corrected order parameter

As mentioned above, the order parameter definition needs to be corrected in the case of finite temperature.

A straight thermal fluctuation term $R(T)$ with buckling-unrelated (2×1) periodicity is to be subtracted from Q^*:

$$Q = Q^* - R \tag{6.8}$$

where R should be the nonzero (2×1) Fourier amplitude due to ordinary thermal fluctuations, if the TBG remained hypothetically unbuckled. As an approximation to that, we extrapolate to $T \leq T_c$ the (2×1) Fourier amplitude evaluated at $T \gtrsim T_c$, where the distortion has disappeared

$$R(T \lesssim T_c) = Q^*(T \gtrsim T_c) \tag{6.9}$$

This thermal fluctuation with $k = 2\pi/l_x$ further depends on the size of the bilayer and of course on temperature [261], $R(T) \propto l_x\sqrt{T}$, so that finally

$$R(T) \propto \theta^{-1}\sqrt{T} \tag{6.10}$$

The thermal (2×1) background R is extracted at $\theta = 3.89°$, and its temperature dependence, needed for the extrapolation, is further verified at $T > T_c$, where buckling is absent. As shown in Fig. 6.10, the scaling given by Eq. (6.10) is reasonable.

A direct comparison of the original Q^* and the correct Q is shown in Fig. 6.11.

6.5.4 Unbuckling temperature T_c

With the corrected parameter Q, we can estimate the unbuckling temperature T_c. First, it is generally seen that flexural fluctuations, large already at relatively low temperatures, play very little role and the buckling order parameter Q remains close to Q_0 so long as $(T \ll T_c)$. At very high temperatures $(T \gg T_c)$ conversely, buckling disappears, and Q =0.

The actual transition between the two regimes, ideally sharp at infinite size, (and presumably with order parameter exponent β either 1/8 if Ising, or 1/9 if 3-state Potts) is artificially smoothed into a soft crossover at our small simulation sizes. A size-smoothed Heaviside step function (approximated as a sigmoid) $S(T - T_c)$ is used to crudely account for this behaviour $Q(T) = Q_t S$, where $Q_t = Q_t(T)$ is the (unknown) true order parameter and $S(T - T_c) = \{1 + \exp[(T - T_c)/T_f]\}^{-1}$, with T_f a parameter characterizing the finite-size

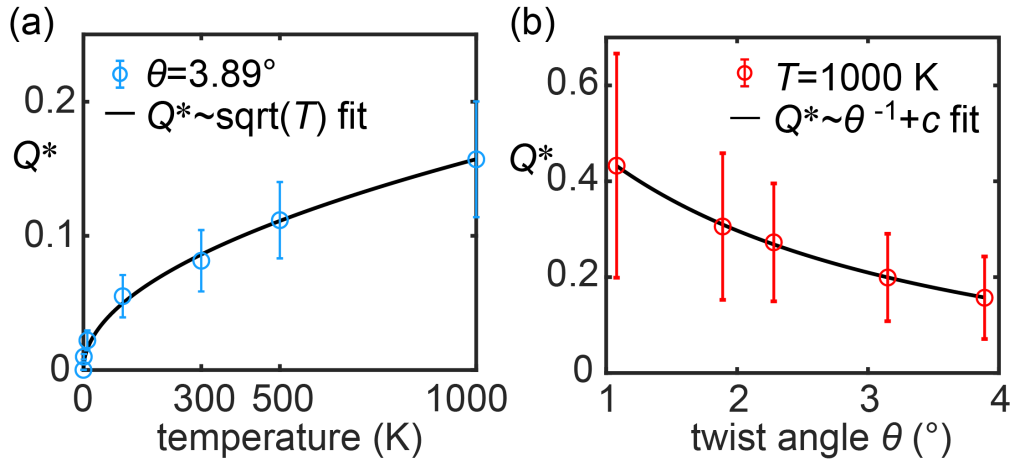

Figure 6.10: Verification of Eq. (6.10). (a) The simulated order parameter Q^* scales as $T^{1/2}$. (b) The simulated order parameter Q^* scales as θ^{-1}. Except for temperature, parameter used here are same as those in Fig. 6.9.

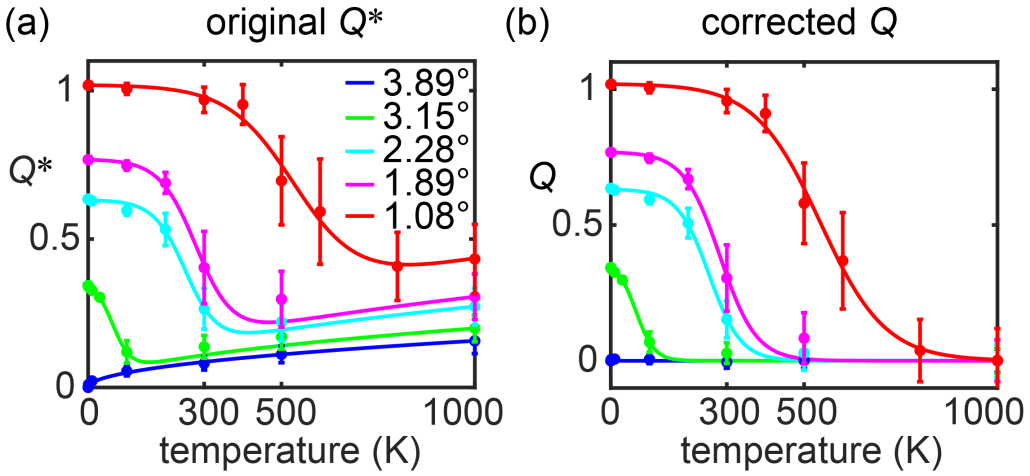

Figure 6.11: (a) Uncorrected order parameter Q^* for different twist angles. The solid line fit is based on a smoothed Heaviside step function (see text). (b) Corrected order parameter Q (thermal background term subtracted). Parameters used here are $N_x = 3$ and $N_y = 1$.

smoothing. We found that a good fit of the finite size crossover of Fig. 6.11b can already be obtained by crudely setting $Q_t(T) = Q_0$ (a choice compatible with a first order transition, but of course not proving it), with the transition temperature T_c as the only parameter. Values of T_c for different twist angles are shown, along with the fitting parameter T_f in Table 6.2.

As shown in Fig. 6.11b, fits based on this crude trial (solid lines) agree well with the MD simulations (color-matched points). The unbuckling transition temperature T_c so obtained for magic twist TBG (see Fig. 6.11b and Table 6.2) is as high as ≈ 500 K – one should by all means be able to observe this buckled structure at room temperature.

6.5.5 Zigzag model details

Here we give details about the zigzag model and discuss its applicability to understand the bending stiffness of TBG and the scaling exponents.

Effective bending stiffness

The model is illustrated in Fig. 6.12a – a simplified zigzag out-of-plane mechanical structure. When this model structure is bent (Fig. 6.12b), the hinge angles deform. The model (Fig. 6.12c) consists of flat (AB-like)

twist angle θ (°)	1.08	1.89	2.28	3.15	3.89
T_c (K)	541	283	254	65.2	0
T_f (K)	83.8	46.9	40.8	24.0	\

Table 6.2: Estimated unbuckling temperature T_c and finite size fitting parameter T_f for different twist angles.

regions and hinge (AA-like) regions. The total length of the system (along the bending direction) is L_x, where $L_x = N_x l_x$.

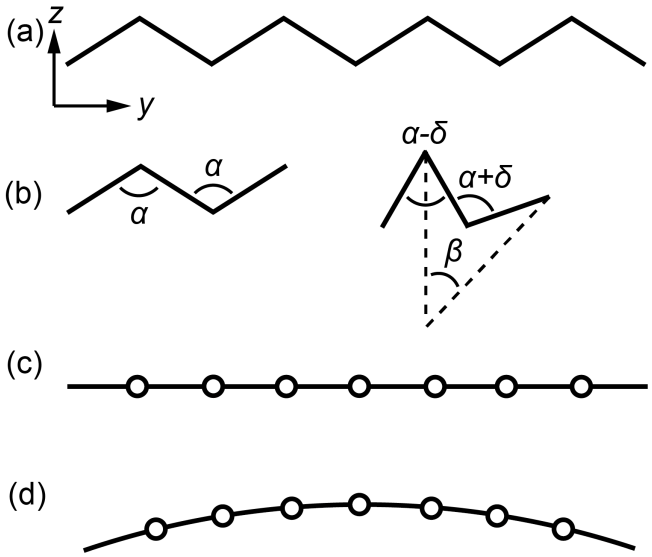

Figure 6.12: Schematic diagram of the hinge model for the buckling structure.

When the model is bent (Fig. 6.12d), both hinge and the flat regions undergo the bending deformations, the relative free energy increase of the system is

$$F(\Phi) = \frac{D_{\mathrm{f}} K l_x l_y \Phi^2}{2L_x(2D_{\mathrm{f}} l_y + K l_x)} \tag{6.11}$$

where D_{f} is the bending stiffness of the flat region, K is the angular stiffness of hinges, and Φ is the total bending angle. Compared to the bending energy expressed by the effective bending stiffness of the whole system,

$$E = \frac{D_{\mathrm{eff}} l_y \Phi^2}{2L_x} \tag{6.12}$$

one gets the effective bending stiffness for the zigzag buckled model:

$$D_{\mathrm{eff}} = \frac{D_{\mathrm{f}}}{1 + 2D_{\mathrm{f}}/\sqrt{3}K} \tag{6.13}$$

where we used $l_x = \sqrt{3}\lambda$ and $l_y = \lambda$. The bending stiffness of the flat region D_{f} is approximated by:

$$D_{\mathrm{f}} = \begin{cases} D_{\mathrm{B}} \approx 100 \text{ eV}, & (\theta < \theta_c) \\ 2D_0 = 2.88 \text{ eV}, & (\theta > \theta_c) \end{cases} \tag{6.14}$$

To estimate the bending stiffness from Eq. (6.13), the only undetermined parameter is the hinge stiffness K.

Hinge stiffness K

Here we provide simulation details that reveal the magnitude and θ-dependence of the hinge stiffness K. Since the stiffness is proportional to the square of buckling frequency, $K \propto \rho_{2\mathrm{D}} l^4 \omega_{\pm}^2$, one can firstly extract the θ-dependence of the buckling frequency $\omega(\theta)$.

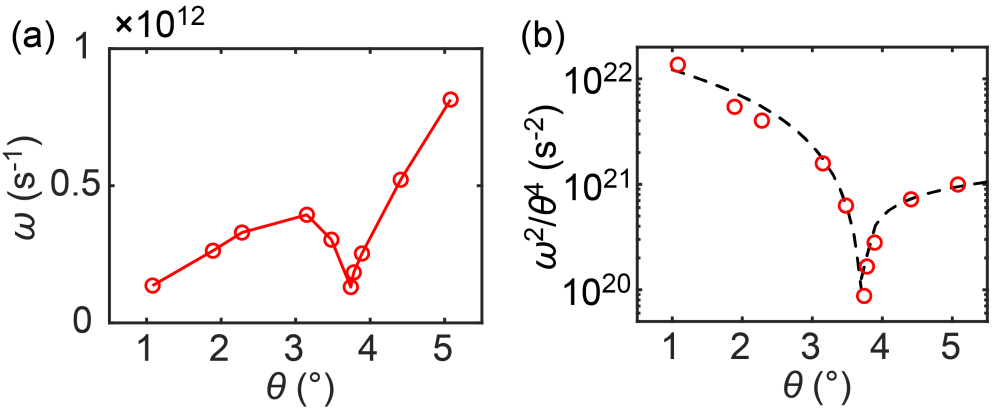

Figure 6.13: (a) Dependence of the buckling frequency ω upon the twist angle θ. (b)Twist angle dependence of the "normalized" buckling frequency, ω^2/θ^4 (red). The dashed lines are power-law fits given by Eq. (6.16).

For $\theta < \theta_c$, the buckling frequency can be extracted by small oscillations around equilibrium once the dynamics is started with $Q_0+\delta Q$ (with $\delta Q/Q_0 \ll 1$). For $\theta > \theta_c$, where the static buckling vanishes ($Q_0 = 0$), the buckling frequency can still be extracted by injecting a small initial amplitude buckling distortion ($\Delta z_{\max} \ll d_0$) and then tracking the damped oscillations as the TBG evolves towards its unbuckled ground state . Note that the frequency of the soft mode so injected, whose eigenvector has the wavelength of the (2×1) buckling unit cell (i.e., 2 moirés), does not change as N_{moire} increases. As shown in Fig. 6.13, the buckling frequency $\omega \to 0$ as $\theta \to \theta_c$.

The stiffness K can be expressed as

$$K = c\frac{\rho_{2D}}{16\pi^4}(\sqrt{3}a_{\text{Gr}})^4\frac{\omega^2}{\theta^4}\left(\frac{180}{\pi}\right)^4 \tag{6.15}$$

where c is a prefactor of $O(1)$. The last term is introduced so as to express the twist angle θ in degrees rather than radians. The twist dependence of K clearly reflects that of ω^2/θ^4. By fitting the simulation results (red circles in Fig. 6.13b), we get:

$$\frac{\omega^2}{\theta^4} = \begin{cases} 3.24 \times 10^{21}(\theta_c - \theta)^{1.30}\ \text{s}^{-2}, & (\theta < \theta_c) \\ 8.58 \times 10^{20}(\theta - \theta_c)^{0.37}\ \text{s}^{-2}, & (\theta > \theta_c) \end{cases} \tag{6.16}$$

With the twist angle dependence of K thus obtained, the predictions of the zigzag model are: (a) For $\theta \to \theta_c$, the buckling structure is infinitely soft ($K \to 0$), and it follows that $D_{\text{eff}} \to 0$. This agrees with the bending stiffness collapse discovered in bending simulations. (b) On the low θ side $\theta < \theta_c$, with $D_{\text{f}} \approx 100$ eV $\gg K$, the effective bending stiffness $D_{\text{eff}} \sim K$. According to Fig. 6.13b, K (and thus D_{eff}) increases as the twist angle decreases from θ_c, with an exponent $\gamma_- = 1.30$ – close to the bending simulation exponent $\epsilon_- = 1.44$. (c) On the large θ side $\theta > \theta_c$ with $D_{\text{f}} \approx 2D_0 = 2.88$ eV $\ll K$, the effective bending stiffness $D_{\text{eff}} \sim 2D_0$. According to Fig. 6.15b, D_{eff} decreases as the twist angle decreases approaching θ_c, with an exponent $\epsilon_+ = 0.2$ – not too far from the soft mode exponent $\gamma_+ = 0.3(7)$.

To fully address the magnitude of K and compare theory and bending simulations, we need to specify the value of parameter c in Eq. 6.15. To achieve this, we performed additional "elongation" simulations. The elongation simulations are constructed with quasi-static protocol – stretching the size of the simulation box along x direction by $\delta l_x = 0.002$ ($\delta l_x \ll l_x$) in each step and performing the structural optimization. The total elongation is $\Delta l_x = \delta l_x \times N_{\text{step}}$, where N_{step} is the number of stretching steps.

The elongation simulation is sketched in Fig. 6.14, where l_0 is the size of the (2×1) unbuckled structure (along x), l_x and H are the size and corrugation height of the buckled structure, l'_x and H' are the size and corrugation height during the elongation simulation, Δl_x is the elongation, α is the equilibrium angle of each

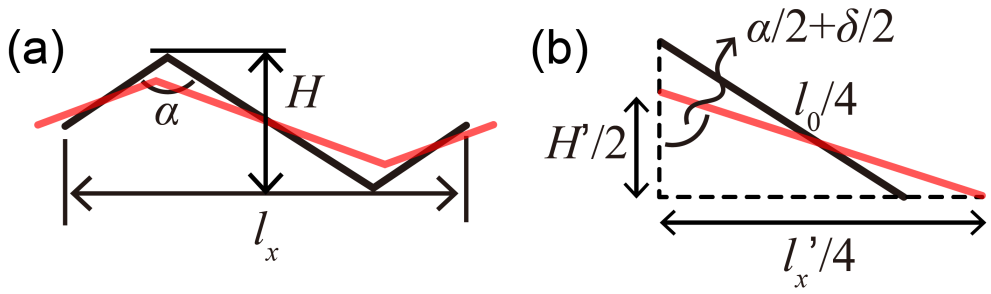

Figure 6.14: (a) Model for elongation zigzag model, where black and red represent the equilibrium and elongated structure. (b) The quarter part of the model.

hinge and δ is the increase of the angle. These parameters are related by

$$\begin{aligned} H &= l_0/2\cos(\alpha/2) \\ l_x &= l_0\sin(\alpha/2) \\ H' &= l_0/2\cos(\alpha/2+\delta/2) \\ l'_x &= l_0\sin(\alpha/2+\delta/2) \\ \Delta l_x &= l'_x - l_x \end{aligned} \tag{6.17}$$

where $\delta \ll \alpha$ and $\alpha+\delta \leq \pi$. From the elongation simulation, one can extract the tensile stiffness (of the buckled structure) A by fitting the energy increase $\Delta E = \frac{1}{2}A\Delta l_x^2$. Considering that the flat region can be regarded as a rigid body, this ΔE is mainly contributed by the increase of the hinge energy $2\times\frac{1}{2}K\delta^2$, where the prefactor 2 represents two hinges in a (2×1) moiré unitcell. Substituting the relationship $\delta = \Delta l_x/H$ (which can be derived from Eqs. 6.17 above) into ΔE and equating them, we finally have the hinge stiffness $K = AH^2/2$. The value of A and K from elongation simulations is listed in Table S2. Comparing the value of K in Table S2 with Eq. 6.15 and 6.16, we find that $c \approx 1.75$ gives the best match.

twist angle θ (°)	2.87	3.15	3.48	3.67
A (N/m)	39.12	41.36	47.66	46.13
H (Å)	2.958	2.272	1.323	0.6135
K (eV)	10.69	6.67	2.61	0.543

Table 6.3: hinge stiffness of several buckled structures.

6.5.6 Bending stiffness at finite temperature

At finite temperature, flexural fluctuations immediately grow for our very large supercells, where the out-of-plane deformation of the buckling structure is heavily influenced by the thermal noise. Thus, it is difficult to use either the oscillation frequency method or the energy method to extract bending stiffness. We introduced an alternative method that is more effective at higher temperatures ($T \gtrsim T_c$), where all soft buckling phonon modes are largely populated. Since we wish to extract the flexural phonon dispersion (thus the bending stiffness) from MD simulations, we turn to the power spectral density (PSD) method [262]. The PSD method projects the velocity of each carbon atom to graphene phonon modes:

$$P(\vec{k},\omega) = \frac{1}{4\pi\tau N}\sum_{\alpha}\sum_{l} m_l \left| \int_0^{\tau}\sum_{n=1}^{N} \dot{u}_{l\alpha\vec{R}_n}(t)\exp\left(i\vec{k}\cdot\vec{R}_n - i\omega t\right)\mathrm{d}t \right|^2 \tag{6.18}$$

where τ is the simulation time, N is the total number of the primitive cell, $u_{l\alpha\vec{R}_n}(t)$ is the displacement of carbon atom in the α direction ($\alpha = x, y, z$) of atom l (with mass m_l) inside primitive cell $\vec{R}_n$. Here l and n is the atom index inside one graphene primitive cell ($l = 1, 2$) and the index of the primitive cell ($n = 1, 2, ..., N$) respectively.

In this way, the distribution of kinetic energy in each mode can be directly displayed, yielding the dispersion relation of the system. The dispersion relation of the flexural mode $\omega \propto k^2$, and the bending stiffness of the system can be obtained by fitting the prefactor

$$D = \frac{\rho_{2\mathrm{D}}\omega^2}{k^4} \tag{6.19}$$

where $\rho_{2\mathrm{D}}$ is the mass of the bilayer per unit area. Several typical results of $\log_{10}[P(k,\omega)]$ (maxima used to identify the flexural mode) and the corresponding fit extracting the effective bending stiffness D are shown in Fig. 6.15.

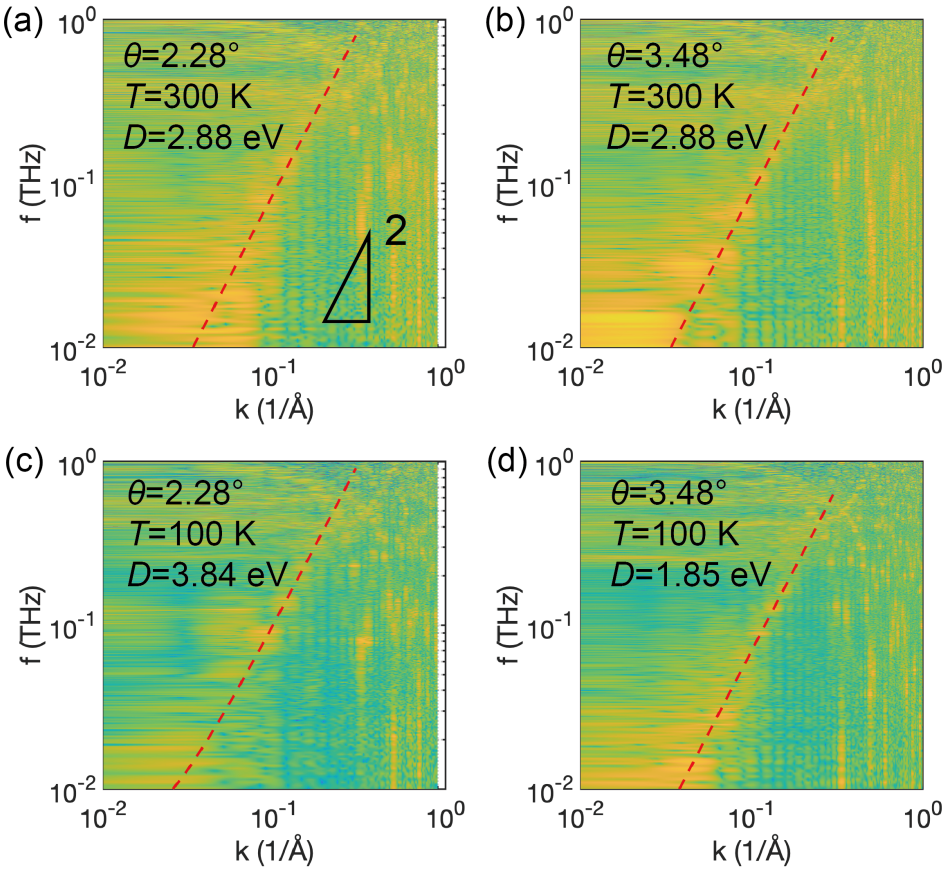

Figure 6.15: Power spectral density of the upper layer of a twisted graphene bilayer at finite temperature. (a, b) Room temperature results for $\theta = 2.28^\circ$ and $\theta = 3.48^\circ$. (c, d) $T = 100$ K results for $\theta = 2.28^\circ$ and $\theta = 3.48^\circ$. Here the frequency is $f = \omega/2\pi$. The spectrum for the lower layer is same as the upper layer.

For low temperature $T \ll T_c$, the buckling order parameter $Q \approx Q_0$, thus we expect that the bending stiffness of the system is dominated by the "hinge" stiffness K, and the value of D should be similar to $T = 0$ cases.

6.5.7 Tilt angle

Normal vector of the buckled (2×1) bilayer deviates locally from $\vec{\hat{z}}$, mainly due to tilt angle of flat AB and BA regions.

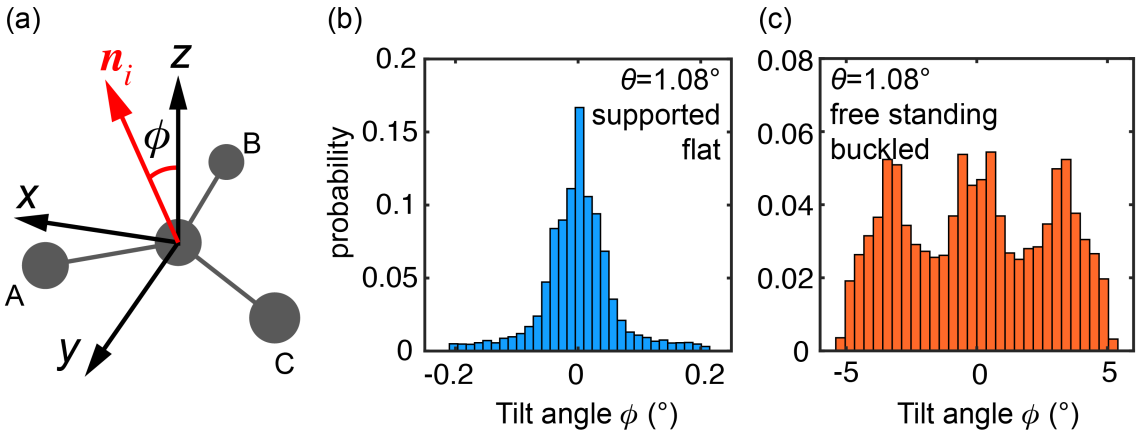

Figure 6.16: (a) Schematic diagram of the local normal $\vec{n}_i$ and the tilt angle ϕ. Probability distribution of ϕ for the magic angle (b) unbuckled and (c) buckled structures.

The tilt angle of i-th atom is defined as:

$$\phi_i = \arcsin\left(\frac{\vec{n}_i \cdot \vec{e}_x}{|\vec{n}_i|}\right) \tag{6.20}$$

where $\vec{n}_i$ is the local normal vector (Fig 6.16a, with A, B and C the nearest neighbors of the central carbon atom). Take $\theta_m = 1.08°$ TBG ($T = 0$) as an example, the distribution of ϕ for supported-flat structure and freestanding-buckling structure are shown in Fig. 6.16b and c respectively. The maximum and the most probable tilt angles of the buckling structure ($\phi_{\max} \approx 5°$ and $\phi_{\text{peak}} \approx 3°$) are more than an order of magnitude larger than the flat structure's ($\phi_{\max} \approx 0.2°$). In addition, the distribution is also different, single peak for the flat structure, split peaks for buckled structure. Experiments detecting the tilt angle of the surface should easily capture the buckled structure when present.

6.5.8 $\sqrt{3} \times \sqrt{3}$ Buckling

Besides the 2×1 buckling described in main text, energy minimization in larger simulation cells and zero planar stress found an alternative $\sqrt{3} \times \sqrt{3}$ buckled structure at only slightly higher total energy.

To convey a feeling for the relative difference, at $\theta = 3.15$ degrees for example, the total energy per atom E_{tot}/N_{at} is $E_i^{(\sqrt{3}\times\sqrt{3})} = -7.418088$ eV for $\sqrt{3} \times \sqrt{3}$ buckling, against $E_i^{(2\times1)} = -7.418090$ eV for 2×1 buckling and $E_i^{\text{flat}} = -7.418076$ eV for no buckling. These differences are not as imperceptible as they seem, once scaled with the large supercell size, and more importantly against the modest buckled-unbuckled entropy difference, resulting for example in an unbuckling temperature estimated to be as large as 65 K for the (2×1) bilayer at this twist angle (Table 6.2).

It might of course happen that, owing to contingent factors such as imperfect structure caused by ill-fitting of $\sqrt{3} \times \sqrt{3}$ buckling inside the rectangular simulation box, force field inaccuracy, different entropies of the two phases at finite temperature, etc., the balance could be reversed, with $\sqrt{3} \times \sqrt{3}$ slightly more stable than 2×1. Even then, the former would remain an isolated possibility, whereas most uniaxial perturbations, intentional or accidental, would generally stabilize the latter. For this additional reason we concentrated on the 2×1 buckling.

The detailed geometry of the two buckled structures at the same twist angle is shown in Fig. 6.17. In the $\sqrt{3} \times \sqrt{3}$ distortion, where C_{3z} symmetry is fully restored, the up-down symmetry is broken, with a triangular AA1 superlattice strongly raised out of plane, and a complementary honeycomb superlattice comprising two weakly lowered AA2 and AA3 per cell (Fig. 6.17b). Further below we will show in Fig. 6.18, for completeness, the 12 electronic bands of the $\sqrt{3} \times \sqrt{3}$ buckled structure, of course different from those of 2×1.

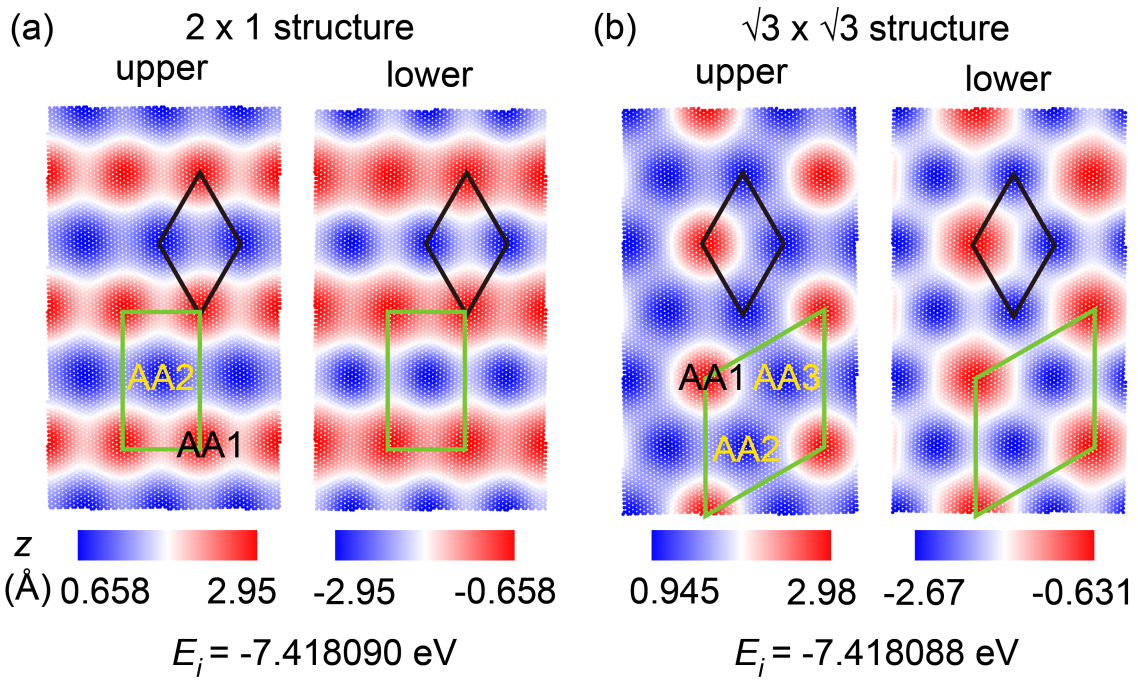

Figure 6.17: The 2×1 and $\sqrt{3}\times\sqrt{3}$ buckling structures for $\theta = 3.15°$. The moiré primitive cell is highlighted by the black rhombus; the corresponding 2-moiré and 3-moiré cells and simulation boxes are shown with green rectangle/rhombus. The corrugation height and the potential energy E_i per atom are listed at the bottom.

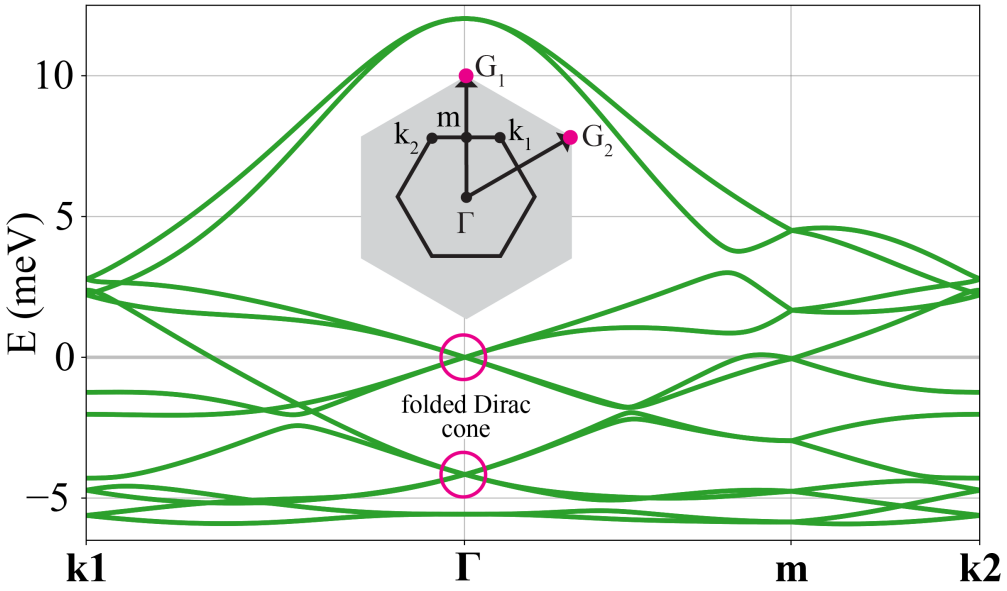

Figure 6.18: Flat bands for the $\sqrt{3}\times\sqrt{3}$ buckled bilayer with twist angle $\theta = 1.08°$. Note the double folding of the Dirac cone at Γ. Beware of the 90 degrees rotated convention compared with that of (2×1) bands of other figures.

6.5.9 Limiting behavior near zero twist angle

Our study yields quantitative predictions for the buckling magnitude and the bending stiffness of the graphene bilayer down to twist angle $\theta = 0.655°$ where simulations proved feasible. The behavior at smaller twists, from $0.655°$ to $\theta = 0$, is beyond reach of simulations owing to the diverging size $\lambda/a \sim \theta^{-1}$ of the moiré cell. In the lack of a specific theory, the small twist angle limit remains unknown. Nonetheless, it is instructive to see if small angle extrapolations of existing results might authorize reasonable conjectures about the possible limiting behaviour. We focus specifically on the buckling order parameter Q_0 – proportional to the moiré z-corrugation magnitude $\Delta z_{\max}$ (inset of Fig 1c)– and on the tilt angle $|\phi| = \tan^{-1}(\Delta z_{\max}/(\sqrt{3}\lambda/2))$ inside each moiré cell. The evolution of both quantities down to $0.655°$ is shown in Fig. 6.19 and 6.20 respectively.

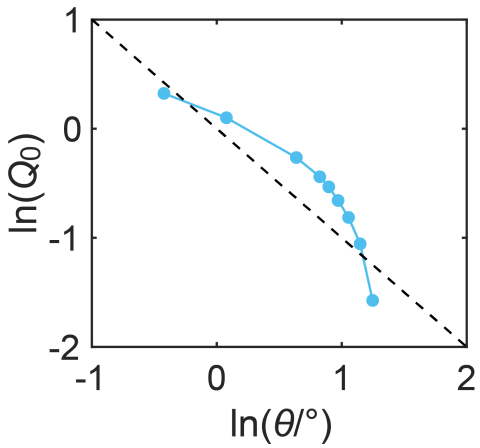

Figure 6.19: Growth of the (2×1) order parameter Q_0 for decreasing twist angle θ from T=0 simulations down to $0.655°$. The dashed line has the slope -1 expected for linear growth with moiré size $\lambda \sim a\theta^{-1}$. Extrapolation below $0.655°$ suggests a less than linear growth as $\theta \to 0$.

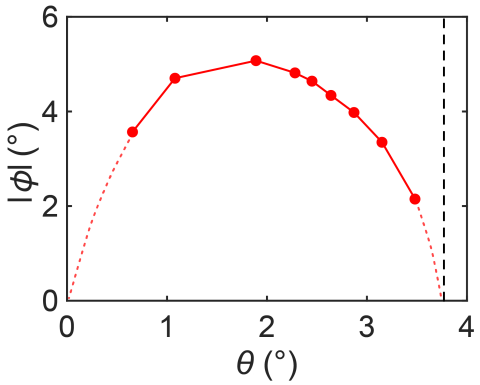

Figure 6.20: Tilt angle $|\phi| = \tan^{-1}(\Delta z_{\max}/(\sqrt{3}\lambda/2))$ of Bernal flat domains between positive and negative buckling lines (red and blue in Fig. 6.1a, see also Section 6.5.7). The extrapolation (red dashed line) is compatible with $\phi = 0$ at $\theta = 0$ (and of course at $\theta = \theta_c = 3.77$). The black dashed line marks the buckling-unbuckling transition at $\theta_c = 3.77°$.

Under the assumption, not unreasonable and yet not proven, that all quantities are already approaching at our smallest simulated twist angles their asymptotic behaviour towards $\theta \to 0$, then the relative buckling corrugation magnitude will grow indefinitely, albeit less than linearly with θ^{-1} (Fig. 6.19). Because of that, the tilt angle $|\phi|$ will tend to zero in the limit (Fig. 6.20) where therefore the bilayer will be essentially flat despite the buckling. In accord with that, the total energy will in the limit also coincide with that of the completely flat unbuckled $\theta = 0$ state. The latter unbuckled state would nonetheless represent a singular point, from which buckling would set in non analytically at infinitesimal twist θ.

Alternatively, we cannot exclude that a new unanticipated regime could set in at even smaller twists than those investigated, with a possible asymptotic demise of the buckling order parameter. That would represent an

analytically smooth limit joining the buckled bilayer at nonzero twist to the flat unbuckled state in the $\theta \to 0$ limit.

More work will therefore be necessary to ascertain the actual behaviour in this limit.

6.5.10 `LTB+Symm` code

For this work, we developed the `LTB+Symm` code (Large-scale Tight Binding and Symmetry validation). `LTB+Symm` is a useful tool to perform tight binding calculations with non-planar geometries in large-sized unit cells, thanks to its MPI implementation. `LTB+Symm` is an object-oriented, open-source Python3 software; its streamlined, geometry-agnostic implementation allows to easily implement *ad-hoc* solutions to capture system-specific features. A novel aspect of `LTB+Symm` is its ability to validate and label irreps at high-symmetry points of the Brillouin zone (once the right space group is defined). `LTB+Symm` is publicly accessible on GitHub: https://github.com/khsrali/LTB-Symm For more details and exmaple of this code, please see Appendix A.

Part III

Other Theoretical Problems

Chapter 7

Ring Population Statistics in an Ice Lattice Model

7.1 Introduction

In the high temperature, proton-disordered state of an ideal ice lattice, where Bernal-Fowler's "ice rule" constraint – two and only two hydrogens per oxygen – is strictly obeyed, all permitted configurations have equal probability. Predicting the ice properties in this limit is then just a matter of counting. Pauling[263] used this fact to evaluate the entropy to be $\ln(3/2) = 0.405$ per site, a mean-field estimate which, even if only an approximation to the actual value (very close for cubic and hexagonal lattices) of about 0.410, [264–266] still stands as a monumental achievement. The simplest conceptual improvement was perhaps the consideration [267] of the correlations introduced by closed N-member rings in the lattice, whose number is $N_{tot} = 1 + 3^N$, yielding an extra entropy $N^{-1}\ln(1 + 1/3^N)$. Restricting to the smallest, $N = 6$, each site participates in 12 hexagonal rings, for both I_h and I_c 3D ice lattices. Each such six-member ring is one of a total N_{tot} permitted realizations, whose presence however only adds to Pauling's entropy a small extra piece $1/(6 \times 3^6) = 0.00023$ [267]. More complex correlations and the infinite variety of larger rings of course improve the entropy estimates much further, as described by an immense literature, mathematically rooted in combinatorics and graph theory [265, 268–270].

The hexagonal 6-member ice rings, their nature and abundance in the ideal disordered state, nevertheless retain a special interest for their own sake, as the carriers of the shortest range correlations forced by the ice rules, in ice as well as in water[271]. Therefore it is of further interest to investigate in detail their population statistics.

7.2 Mean-field ring populations

In I_c and I_h perfect ice lattices the ("chair") rings occur in one of eight topological types, in turn belonging to one among four different order parameter values: 0,1,2,3 to be defined soon. This note presents a mean-field evaluation of the probability for any of these ring types to occur in the ideal 3D proton disordered cubic or hexagonal ice. While all elements for doing that are contained or implicit in past work[267, 268, 270], an explicit result remains of immediate use and interest. Firstly, because it allows to rationalize high temperature ring populations previously encountered in ab initio water simulations [271] and in Monte Carlo simulations of a cubic ice lattice model such as Ref. [11] – whose notation we shall adopt here. Secondly, because they shed indirect light on the anomalous string nucleation process that was recently predicted in that work, a process now candidate for possible observation.

In the lattice model, a binary variable $\phi_{ij} = \pm 1$, with the "arrow" property $\phi_{ji} = -\phi_{ij}$, is attached to each (hydrogen) bond between two neighboring (oxygen) sites (ij) on a diamond lattice. The $N_{tot} = 730$ hexagonal ring configurations are generated by all possible sequences of six consecutive bond signs $\phi_{ij} = \pm 1$ permitted by the ices rules. The quantity

$$S = 3 - |\frac{1}{2}\Sigma_{ij}\phi_{ij}| = 0, 1, 2, 3 \tag{7.1}$$

defines the order parameter, or family, to which each of these rings, a hexagon where each bond ϕ_{ji} is either $+$ or $-$, belongs. We will conventionally assume the sign of ϕ_{ij} is attributed to the left vertex i, while running clockwise along the ring (see Fig. 7.1). In other words, $\phi_{ji} = +1$ when the H atom (the "arrow head") lies close to site j)

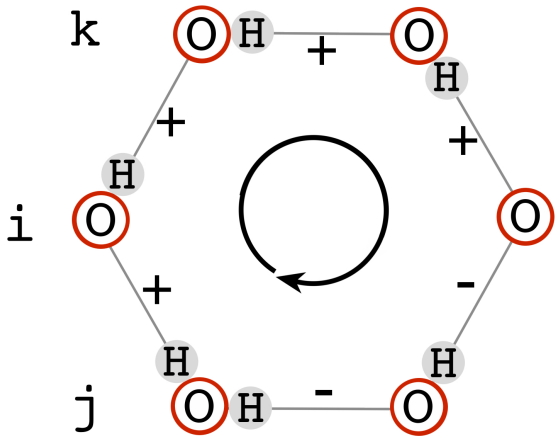

Figure 7.1: Hexagonal ring, here shown for type 3, order parameter $S = 2$. The probability of this particular ring in proton disordered ice is 192/730. That for all other rings is obtained from Eqs. (7.3-7.4)

To facilitate elementary enumeration and classification of rings, two elements are expedient. One is symmetry, the other is the ice rule. The first can be dealt with exactly. The second is treated within mean-field.

Symmetry first. Rotational C_6 symmetry of the hexagon demands that each configuration generates another five by applying 60 degree rotations. That gives a rotational multiplicity factor R, ranging case by case from 6 to 1. Sign inversion symmetry, in addition, turns a ring configuration into another equally valid by exchanging pluses and minuses –that is, turning all arrows around. That gives an inversion multiplicity factor I, that can be either 2 or 1, again case by case.

Second, the ice rule, which controls the multiplicity of the six hexagon vertices. Outside the hexagon, vertices are connected by paths in the ice lattice, giving rise to correlations among them. In the mean-field approximation, which we adopt, these correlations are ignored and each vertex is independent. It is therefore easy to determine six multiplicity factors F_i, $i = 1, 2 \ldots 6$, one per vertex. A vertex i across which the bond variable or arrow does not change sign, that is where $\phi_{ji}\phi_{ik} = +1$, entails two possibilities, corresponding to the remaining bond arrow entering that site i to be placed on either of the two off-ring bonds. The vertex factor taking care of that is thus $F_i = 2$ reflecting these two possibilities. Alternatively, a vertex i where the bond variable flips sign, that is where both arrows point either in or out, $\phi_{ji}\phi_{ik} = -1$, can occur only once because the two remaining off-ring bonds from site i can only be opposite, whence $F_i = 1$.

By identifying these factors for every ring type, the overall multiplicity of that type is the product

$$M = R\, I\, F, \text{ where } F = \Pi_{i=1}^{6}\, F_i \tag{7.2}$$

In this way it is now possible to enumerate each of the eight hexagonal ring types 1, 2,... 8 (note that, as explained above, the hexagon is run clockwise and bond signs are attributed to the left vertex, the arrow starting with H close to the O site, as in Fig. 7.1) :

$$1:(++++++); \qquad M_1 = 1\times 2\times 2^6 \qquad =128 \tag{7.3a}$$
$$2:(+++++-); \qquad M_2 = 6\times 2\times 2^4 \qquad =192 \tag{7.3b}$$
$$3:(++++--); \qquad M_3 = 6\times 2\times 2^4 \qquad =192 \tag{7.3c}$$
$$4:(+-++-+); \qquad M_4 = 3\times 2\times 2^2 \qquad =24 \tag{7.3d}$$
$$5:(+-++-+); \qquad M_5 = 6\times 2\times 2^2 \qquad =48 \tag{7.3e}$$
$$6:(+++---); \qquad M_6 = 6\times 1\times 2^4 \qquad =96 \tag{7.3f}$$
$$7:(+-+-+-); \qquad M_7 = 1\times 2\times 1 \qquad =2 \tag{7.3g}$$
$$8:(++--+-); \qquad M_8 = 6\times 2\times 2^2 \qquad =48 \tag{7.3h}$$

where the total number of configurations is correctly $\sum_{i=1}^{8} M_i = N_{tot} = 1+3^6 = 730$. The eight ring types can be further grouped according to their order parameter S defined in Eq. (7.1), yielding the theoretical abundance N_S of rings with order parameter S in any state of the ice lattice model, including the maximally disordered ones, which we are interested in. Rings of type 1 and 2 possess $S = 0$ and $S = 1$ respectively, whereas types 3,4,5 share the same order parameter $S = 2$, those of type 6,7,8 share the same $S = 3$. Therefore the ring probability $P(S) = N(S)/N_{tot}$ for each order parameter $S = 0, 1, 2, 3$ is

$$P_0 = \frac{N(S=0)}{N_{tot}} = \frac{M_1}{N_{tot}} = \frac{128}{730} = 0.1753 \tag{7.4a}$$
$$P_1 = \frac{N(S=1)}{N_{tot}} = \frac{M_2}{N_{tot}} = \frac{192}{730} = 0.2630 \tag{7.4b}$$
$$P_2 = \frac{N(S=2)}{N_{tot}} = \frac{M_3+M_4+M_5}{N_{tot}} = \frac{264}{730} = 0.3616 \tag{7.4c}$$
$$P_3 = \frac{N(S=3)}{N_{tot}} = \frac{M_6+M_7+M_8}{N_{tot}} = \frac{146}{730} = 0.2000 \tag{7.4d}$$

7.3 Comparison with Monte Carlo results

While direct measurements of these population probabilities are not available – and real ice is notoriously far from a perfect lattice –, this result can first be compared with that obtained in *ab initio* water simulations such as Ref [271] where P_0 is 0.165, only 5% different. More detailed and instructive comparisons can be made with populations $A_S = 12P_S$ of hexagonal ring type S numerically obtained in the Monte Carlo ice model simulation which we carried out extending those of Ref. [11] to achieve high accuracy, extrapolating to the high temperature and infinite cell size limits.

Table 7.1 summarizes our results, showing an overall agreement of the mean-field populations with accurate MC results that is remarkable, within about 1% in all cases. Interesting is the dependence on cluster and on lattice types of the deviation between mean-field and MC values. The mean-field population S_0 is essentially exact, indicating that for this type of cluster, where all arrows coherently concatenate, the inter-vertex correlations are close to zero. That is confirmed also by the coincidence of S_0 values in I_h and I_c lattices. In all other cases, where deviations from mean-field are detectable, they are accompanied by differences between I_h and I_c – different lattices implying different vertex-vertex correlations.

S	0	1	2	3
Mean-field	2.104	3.156	4.340	2.400
MC I_h	2.104 ± 0.001	3.191 ± 0.002	4.321 ± 0.003	2.388 ± 0.002
MC I_c	2.103 ± 0.001	3.182 ± 0.003	4.347 ± 0.002	2.3670 ± 0.0002

Table 7.1: Population $A_S = 12P_S$ of the 12 hexagonal rings threading each oxygen site, distributed among the four order parameters S values in the perfectly disordered state of I_c and I_h ice lattice model. Mean-field values are compared with Monte Carlo data, from simulations extending those of Ref. [11] to high temperature and large size extrapolations for diamond and hexagonal diamond oxygen lattices respectively. Error bars are conservative estimates of method-related errors. The corresponding populations of the $T = 0$ ordered (ferroelectric) state are $A_0 = 0$, $A_1 = 0$, $A_2 = 0$, $A_3 = 12$ in the cubic lattice I_c; for the hexagonal lattice I_h they are $A_0 = 0$, $A_1 = 6$, $A_2 = 0$, $A_3 = 6$ in case of $Cmc2_1$ symmetry , $A_0 = 0$, $A_1 = 6$, $A_2 = 6$, $A_3 = 0$ for $Pna2_1$ symmetry, and $A_0 = 0$, $A_1 = 0$, $A_2 = 6$, $A_3 = 6$ for $P1$ symmetry (see e.g., Ref. [272])

7.4 Discussion

These results shed some additional and interesting light on the proton disorder-order transformation in ice models. Following Ref. [11] and references therein, we focus on the cubic lattice I_c, where the ordered state is fully ferroelectrically polarized.

First, consider thermal equilibrium. Although impeded kinetically, the equilibrium phase transition between high temperature proton disorder and ferroelectric proton order below T_c – a value determined by the dipolar interaction J, is thermodynamically unharmed by the ice rules. In the ideally perfect ordered and ferroelectric state of ice all 12 rings have $S = 3$. More precisely, they all are of a smaller subset of $S = 3$, precisely the "$+z$-polarized" subclass of M_6 rings, a type which includes also $\pm x$,$\pm y$ and $-z$ orientations, as defined in Eq. (7.3f). Because there are 12 rings per site, the initial population of that ring type in the disordered state is $12(1/6)M_6/N_{tot} = 12(16/730) = 0.263$, quite small. The gap from this value to 12 in the ordered, fully polarized low-temperature state underlies and clarifies, in parallel to and beyond the mere entropy jump, the strong first order character of the disorder-order transition that was found by Monte Carlo.

Second, non-equilibrium, and the predicted anomalous string-like nucleation of ferroelectric order inside proton disordered low temperature ice. The ring distribution should play a role in the transformation kinetics. The disordered Pauling state, preserved by the ice rules as a metastable but infinitely long-lived state even at low temperatures, begins to transform to a partially ordered and ferroelectric state once an ice rule-breaking defect or impurity modeling, e.g., KOH doping, is inserted in the lattice. Simulations found that the impurity-nucleated transformation does not occur through the usual three dimensional cluster typical of regular first order transitions but rather, in the ice-rule conserving lattice, by a string of flipped bond signs, resembling a domino-like cascade of correspondingly flipped H-bonds. In its run, the propagating string head – a mimic of the mobile hydroxyl ion – overturns the order parameter of the rings it runs through, from their generally disordered varieties $S = 0, 1, 2, 3$ to S_3 rings with increased $+z$ polarization, like the fully "z-polarized" subset of rings of the $(+ + + - - -)$ M_6 variety. In essence, the string propagates, through complex trial-and-error moves including multiple passes, eventually transforming a chain of $(-)$ bonds to a chain of $(+)$ bonds left behind. In doing that, the polarized rings are preferentially installed where they did not exist. Concurrently, the dipole-dipole interaction J acts to select a preferential z-alignment of these overturned rings, so that they line up ferroelectrically. While the lower energy of the ordered state provides the thermodynamical force pushing meandering strings to proceed onwards and to transform more and more rings from disorder to order, they do encounter a large population of unsuitably configured rings. The complex trial-and error labor involved represents a factor that in this ice model slows down the Monte Carlo string progress, causing it to meander in search, as it were, of the best path. That appears to be, in essence, the reason why, in the Monte Carlo evolution of the doped ice model, ferroelectric order grows only partly and sluggishly once the disordered state is transformed away [11], a behaviour whose effects are also reminiscent of those observed in ice in real time [273]. Aware as one should be that the chemical and physical reality of real ice is substantially more complex [274–277] than the present cartoon lattice model, the topological elements and the importance of disordered ring population which the model demonstrates still retain a suggestive importance, particularly if the string-like nucleation of order which was previously suggested should be experimentally confirmed.

Appendix A: LTB-Symm Tight Binding and Symmetry Analysis Code

Introduction

Tight binding is a model used to describe the behavior of electrons in a solid, particularly in insulators and semiconductors. It is based on the assumption that the electrons in a solid are strongly bound to the atoms but can jump between atoms with some relatively small probability. In other words, the electrons are localised on the atomic lattice site and weakly hop between sites. This model is particularly useful to study the electronic properties of materials with a large size unit cell, where more sophisticated Density Functional Theory (DFT) methods become too expensive in terms of computation time.

Solving a tight binding model, always narrows down to diagonalizing the Hamiltonian. Resulting in eigenvalues and eigenvectors problem. The former produces the band structure of the solid, and the latter represent the probability amplitudes for the electrons to be found at each site in the crystal lattice, also reflecting the topological properties. Explict examples of such Hamiltonians are presented in the example section. The symmetry of eigenvectors, tells us how the electronic states of a crystal are is distributed in real space. By studying topology, we analyse how symmetry evolves across momentum space. The concepts and tools of group theory, allows us to systematically analyse the symmetries of the crystal lattice and their impact on the electronic structure. Namely spatial and time-reversal symmetries.

Most researchers in the field of twistronics, prefer to have a framework that not only diagonalises tight binding Hamiltonians, but also allows them to implement and investigate more topological and symmetry properties of the eigenvectors.

Installation

Requirements LTB-Symm is written in Python. To function properly “Python 3.8+“ is required.

Operating system LTB-Symm has been developed and tested on both **Linux** and **MacOS**. In both of these operating systems, installation process is similar. Although on **MacOS** there is an extra pre-step, i.e. make sure you have “pip“ installed by typing the command below in your terminal:

```
python -m ensurepip
```

In principle it should be possible to install the code on **Windows** machines, but we have not tested it, yet. Again you can install “pip“ by executing the following command in “cmd“:

```
> curl https://bootstrap.pypa.io/get-pip.py -o get-pip.py
> python get-pip.py
```

Install through pip You can simply install with:

```
pip install ltb-symm
```

If you have it already install, you may use option :code:‘–upgrade‘ to have the latest version.

If installation failed, please make sure all dependencies correctly installed. That includes;

```
numpy scipy matplotlib mpi4py tqdm primme
```

Required versions: NumPy 1.19.5+, Scipy 1.10.0+, Primme 3.2

Note you need a working MPI implementation for “mpi4py“ to succesfully function.

Source code LTB-Symm is publicly available at GitHub under GNU General Public License v3.0 : https://github.com/kh
Symm

How to run Simply write an input file (see examples) and run using you python interpreter:
For example:

```
python input.py
```

Or alternatively if you want to use MPI feature, for instance on a HPC with 32 core each node:

```
mpirun --map-by ppr:32:node python input.py
```

Example 1: Band structure of TBG

Here we demonstrate how to calculate band structre for magic angle twisted bilayer graphene (TBG).
First import ltbsymm and other libraries if you need, in this case also numpy:

```
import ltbsymm as ls
import numpy as np
```

Create an object of TightBinding class:

```
mytb = ls.TB()
```

Next, load the coordinate file. 1.08_1AA.data is an example of relaxed structure using LAMMPS.

```
mytb.set_configuration('1.08_1AA.data', r_cut = 5.7, local_normal=True)
```

r_cut used to detect neighbors within a circular range around each individual cites. local_normal=True clarifies whether to calculate the local normal vector, pointing out from surface locally (True) or use (0,0,1) as vertical normal to all sites (False). The former option is needed in case your structure is not flat, and out of plain deformations affects how orbitals interacts, see Slater-Koster[248]. The latter is suitable (and faster) for flat geometries with negligible corrugation.
Depending on size of your system, you may want to save this initial configuration! This will help you to save time for next runs with the same data file and setting.

```
mytb.save(configuration =True)
```

The heart of any band structure calculation is the Hamiltonian. In LTB-Symm you are completely free to define the Hamiltonian of your TB model! Define your it as you like, using features that are already developed. In the case of TBG we define the Hamiltonian – see our paper– as:

$$H_{ij} = \frac{V_{pp\sigma}}{2}\left[\left(\frac{\mathbf{d}_{ij}\cdot\hat{n}_i}{\mid \mathbf{d}_{ij} \mid}\right)^2 + \left(\frac{\mathbf{d}_{ij}\cdot\hat{n}_i}{\mid \mathbf{d}_{ij} \mid}\right)^2\right] + V_{pp\pi}\left[1 - \frac{1}{2}\left(\left(\frac{\mathbf{d}_{ij}\cdot\hat{n}_j}{\mid \mathbf{d}_{ij} \mid}\right)^2 + \left(\frac{\mathbf{d}_{ij}\cdot\hat{n}_j}{\mid \mathbf{d}_{ij} \mid}\right)^2\right)\right] \tag{7.5}$$

Where $V_{pp\sigma}$ and $V_{pp\pi}$ are defined as

$$V_{pp\sigma} = V^0_{pp\sigma}\ \exp\left(-\frac{\mid \mathbf{d}_{ij} \mid -d_0}{r_0}\right), \quad V_{pp\pi} = V^0_{pp\pi}\ \exp\left(-\frac{\mid \mathbf{d}_{ij} \mid -a_0}{r_0}\right) \tag{7.6}$$

This Hamiltonian translates into the following Python function:

```
# Define Hamiltonian and fix the parameters of the Hamiltonian that are the same for all pairs
def H_ij(v_ij, ez_i, ez_j, a0 = 1.42039011, d0 = 3.344, V0_sigam = +0.48, V0_pi = -2.7, r0 =
    0.184* 1.42039011 * np.sqrt(3) ):
    """
        Args:
            d0: float
                Distance between two layers. Notice d0 <= than minimum interlayer distance,
    otherwise you are exponentially increasing interaction!
            a0: float
                Equilibrium distance between two neghibouring cites.
            V0_sigam: float
                Slater-Koster parameters
            V0_pi: float
                Slater-Koster parameters
```

```
            r0: float
                Decay rate of the exponential
    """

    dd = np.linalg.norm(v_ij)
    V_sigam = V0_sigam * np.exp(-(dd-d0) / r0 )
    V_pi    = V0_pi    * np.exp(-(dd-a0) / r0 )

    tilt_1 = np.power(np.dot(v_ij, ez_i)/ dd, 2)
    tilt_2 = np.power(np.dot(v_ij, ez_j)/ dd, 2)
    t_ij =  V_sigam * (tilt_1+tilt_2)/2 + V_pi * (1- (tilt_1 + tilt_2)/2)

    return t_ij
```

Now that the Hamiltonian is defined, it is time to define the reciprocal space, i.e. the right Brillouin zone for our system. In the simple case of TBG, LTB-Symm is able to detect mini brillouin zone (MBZ) automatically.

```
# Define MBZ and set K-points
mytb.MBZ()
mytb.set_Kpoints(['K1','Gamma','M2', 'K2'] , N=32)
```

We may define a specific path inside the MBZ set_Kpoints(), with total N=32 K-points which will be automatically distributed along the segments.

Now the physics is set, and electronic bands are ready to calculate.

```
# For twisted bilayer graphene sigma=np.abs(V0_pi-V0_sigam)/2 . An approximate value where
    flat bands are located
mytb.calculate_bands(H_ij, n_eigns = 4, sigma=np.abs(-2.7-0.48)/2, solver='primme',
    return_eigenvectors = False)
```

It is always a good idea to save the calculation!

```
mytb.save(bands=True)
```

You could run this code in parallel using MPI. For example on 4 cores, this calculation should take only around 200 seconds

```
$ mpirun -n 4 python input_calculate.py
```

Before plotting, let us see if there are any flatbands

```
# Detect if there are any flatbands
mytb.detect_flat_bands()
```

Then you realize there are 4 flat bands, but are not centered around zero. This could happen, simply because the approximate value of sigma that is used in mytb.calculate_bands() has no knowledge of Fermi level. This can be easily fixed simply by recentering flat bands around a given K-point (in this case K1, where Dirac cone is centered):

```
# Set Fermi level by shifting E=0 to the avergage energies of flat bands at point e.g. 'K1'
mytb.shift_2_zero('K1', np.array([0,1,2,3]))
```

Finally, you can plot and save the band structure.

```
# Plot bands and modify figure as you like
plot = mytb.plotter_bands(color_ ='C0')
plot.set_ylim([-10,15])
plt.savefig('out_1.08_1AA/'+'Bands_'+ ".png", dpi=150)

plt.show()
```

Result are shown in Fig. 7.2a. For denser a calculation we could set N=1000 in set_Kpoints(), that requires a longer calculation Fig. 7.2b.

Alternatively you could close the session and load previously calculate bands:

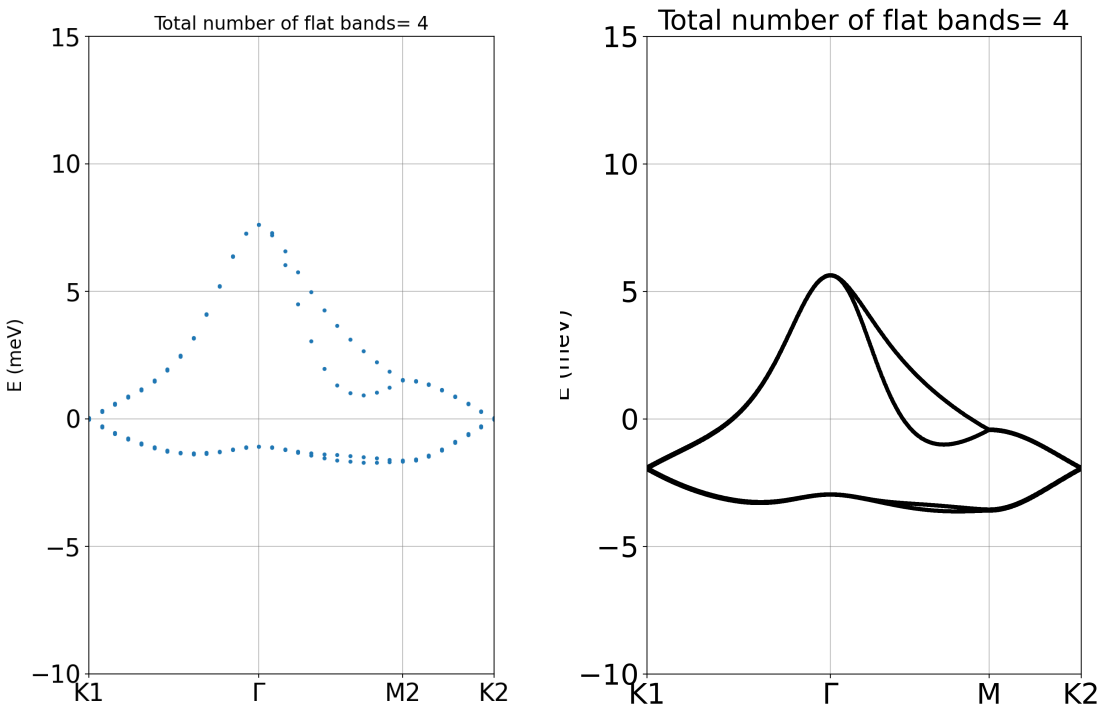

Figure 7.2: Band structutre of magic angle TBG in 1AA unitcell. (left) A fast calculation with N =32, only 200 Seconds. (right) denser calculation with N=1000

```
mytb = ls.TB()
mytb.load('out_1.08_1AA', bands='bands_.npz', configuration='configuration_.npz')
plot = mytb.plotter_bands(color_ ='C0')
```

Warning: In case of using *mpirun*, it is better to assign only one core for plotting functions:

```
import numpy as np
import ltbsymm as ls
import matplotlib.pyplot as plt
from mpi4py import MPI

comm = MPI.COMM_WORLD
rank = comm.Get_rank()

if rank == 0:
    mytb = ls.TB()
    mytb.load('out_1.08_1AA', bands='bands_.npz', configuration='configuration_.npz')
    plot = mytb.plotter_bands(color_ ='C0')
    plt.show()

MPI.Finalize()
```

Example 2: Symmetry operations and wavevector parity

This example shows how to investigate the parity of wavevectors under various symmetry operations at any given point of the Brillouin zone. Symmetry is useful to understand the topological properties of band structure.

As an example, here, we consider two unit cells of twisted bilayer graphene at the magic angle 1.08 degrees. At the time of writing this example, the project is under active development. “symmetry“ module is only fully

developed for the rectangular lattice.

First let's calculate eigenvectors at high symmetry points, like in the previous example:

```
import sys
import numpy as np
import ltbsymm as ls
from mpi4py import MPI

comm = MPI.COMM_WORLD
rank = comm.Get_rank()


# Start a TB object and set/load configuration
mytb = ls.TB()
mytb.set_configuration('1.08_2AA.data', r_cut = 5.7, local_normal=True, nl_method='RS')
mytb.save(configuration =True)

# Define Hamiltonian and fix the parameters of the Hamiltonian that are the same for all pairs
def H_ij(v_ij, ez_i, ez_j, a0 = 1.42039011, d0 = 3.344, V0_sigam = +0.48, V0_pi = -2.7, r0 =
    0.184* 1.42039011 * np.sqrt(3) ):
    """
        Args:
            d0: float
                Distance between two layers. Notice d0 <= than minimum interlayer distance,
    otherwise you are exponentially increasing interaction!
            a0: float
                Equilibrium distance between two neghibouring cites.
            V0_sigam: float
                Slater-Koster parameters
            V0_pi: float
                Slater-Koster parameters
            r0: float
                Decay rate of the exponential
    """
    #print(v_ij, ez_i, ez_j)
    dd = np.linalg.norm(v_ij)
    V_sigam = V0_sigam * np.exp(-(dd-d0) / r0 )
    V_pi    = V0_pi    * np.exp(-(dd-a0) / r0 )

    tilt_1 = np.power(np.dot(v_ij, ez_i)/ dd, 2)
    tilt_2 = np.power(np.dot(v_ij, ez_j)/ dd, 2)
    t_ij =  V_sigam * (tilt_1+tilt_2)/2 + V_pi * (1- (tilt_1 + tilt_2)/2)

    return t_ij



# Define MBZ and set K-points
mytb.MBZ()
mytb.set_Kpoints(['X','Gamma','Y', 'W'], N=0, saveH=True)


# For twisted bilayer graphene sigma=np.abs(V0_pi-V0_sigam)/2 . An approximate value that flat
     bands are located
mytb.calculate_bands(H_ij, n_eigns = 8, sigma=np.abs(-2.7-0.48)/2, solver='primme', tbt='type2
    ', return_eigenvectors = True)


mytb.save(bands=True)

MPI.Finalize()
```

For detailed explanation of the above function see Example 1.

Once a band structure calculation is done, you can always save using

```
mytb.save(bands=True, configuration=True)
```

This is very convenient, for later application or symmetry analysis you can simply load:

```
mytb.load('out_1.08_2AA', bands='bands_.npz', configuration='configuration_.npz')
```

There is no need to re-calculate from beginning.

Having wave vectors, we can proceed to create a Symm object from our TB model.

```
if rank == 0:

    sm = ls.Symm(mytb)

    sm.build_map('C2z',['-X+1/2*Rx','-Y+1/2*Ry','Z'], atol=0.3, plot = True)
    sm.build_map('C2y',['-X','Y+1/2*Ry','-Z'], atol=0.3)
    sm.build_map('C2x',['X+1/2*Rx','-Y','-Z'], atol=0.3)
```

You may define all symmetry operations of the space group. Note that the Symm object can also handle non-symmorphic operations. build_map() simply verifies if the suggest symmetry exists in real space, and if so, and how does it map with existing orbital indices.

The second argument of build_map() should be arithmetic math operations in following order: [operation for X, operation for Y, operation for Z] The Arithmetic symbols and namespaces below are acceptable:

```
    +, -, /, *, X, Y, Z, Rx, Ry, and Rz.
```

Rx, Ry, and Rz are lattice vectors along their directions. X, Y, and Z are coordinates of cites inside unitcell.

In our example 1/2*Rx applies a non-symmorphic translation in the x direction.

Next, build (N*N) matrices for the verified symmetry operations.

```
# Make the operation Matrix at a given point of receiprocal space
sm.make_Cmat('C2x', 'Gamma')
sm.make_Cmat('C2y', 'Gamma')
sm.make_Cmat('C2z', 'Gamma')
```

And we can simply check (up to the false tolerance error set by "ftol") if they make sense, by taking the square

```
# Check operations square and how they commute
sm.check_square('C2x', 'Gamma', ftol = 30)
sm.check_square('C2y', 'Gamma', ftol = 30)
sm.check_square('C2z', 'Gamma', ftol = 30)
```

We may need to know how the symmetry operations commute, or anti-commute !

```
sm.check_commute('C2x', 'C2y', 'Gamma', ftol=30)
sm.check_commute('C2z', 'C2y', 'Gamma', ftol=30)
sm.check_commute('C2x', 'C2z', 'Gamma', ftol=30)
```

In this case results like this:

```
    C2x @ C2x = identity at Gamma
    C2y @ C2y = identity at Gamma
    C2z @ C2z = identity at Gamma
    [C2x, C2y] do commute at Gamma
    [C2z, C2y] do commute at Gamma
    [C2x, C2z] do commute at Gamma
```

We are inerested in symmetry operation on wave vectors associated with flat bands, therefore first we detect if there are any flat bands:

```
mytb.detect_flat_bands()
```

Results in:

```
    8  flat bands detected
```

Now we can check if (flat) wave vectors respect the symmetries that we defined:

```
sm.vector_diag('Gamma', name1='C2x', subSize = 4, skip_diag = True)
```

Which results in:

```
======================
** vector_diag at Gamma **
======================


Subspace 1.0 with energies:
0.005687156959874318
0.005675662193339814
-0.0003969110247522556
-0.00041691802874066486
<psi| C2z |psi>
[[-0.8+0.j , 0.5-0.2j,-0. +0.j ,-0. +0.j ],
 [ 0.5+0.2j, 0.8+0.j , 0. -0.j ,-0. +0.j ],
 [-0. -0.j , 0. +0.j , 0.9+0.j , 0.3-0.j ],
 [-0. -0.j ,-0. -0.j , 0.3+0.j ,-0.9+0.j ]]
<psi| C2y |psi>
[[ 1.+0.j, 0.-0.j, 0.-0.j,-0.+0.j],
 [ 0.+0.j, 1.+0.j, 0.-0.j,-0.+0.j],
 [ 0.+0.j, 0.+0.j,-1.+0.j,-0.+0.j],
 [-0.-0.j,-0.-0.j,-0.-0.j,-1.+0.j]]
<psi| C2x |psi>
[[-0.8+0.j , 0.5-0.2j, 0. -0.j ,-0. +0.j ],
 [ 0.5+0.2j, 0.8+0.j , 0. -0.j , 0. -0.j ],
 [ 0. +0.j , 0. +0.j ,-0.9+0.j ,-0.3+0.j ],
 [-0. -0.j , 0. +0.j ,-0.3-0.j , 0.9+0.j ]]

Subspace 2.0 with energies:
-0.003000614802293855
-0.003018659755200659
-0.0035570670624436307
-0.0036018736346046243
<psi| C2z |psi>
[[-0.5+0.j ,-0.1+0.9j, 0. +0.j ,-0. +0.j ],
 [-0.1-0.9j, 0.5+0.j ,-0. +0.j ,-0. -0.j ],
 [ 0. -0.j ,-0. -0.j , 0.5+0.j ,-0.3+0.8j],
 [-0. -0.j ,-0. +0.j ,-0.3-0.8j,-0.5-0.j ]]
<psi| C2y |psi>
[[-1.+0.j, 0.-0.j, 0.+0.j,-0.+0.j],
 [ 0.+0.j,-1.+0.j,-0.+0.j,-0.-0.j],
 [ 0.-0.j,-0.-0.j, 1.+0.j,-0.+0.j],
 [-0.-0.j,-0.+0.j,-0.-0.j, 1.+0.j]]
<psi| C2x |psi>
[[ 0.5+0.j , 0.1-0.9j,-0. -0.j ,-0. +0.j ],
 [ 0.1+0.9j,-0.5+0.j , 0. -0.j ,-0. -0.j ],
 [-0. +0.j , 0. +0.j , 0.5+0.j ,-0.3+0.8j],
 [-0. -0.j ,-0. +0.j ,-0.3-0.8j,-0.5+0.j ]]
```

As you can see there are offdiagonal terms in ‘C2x‘ and ‘C2z‘ space, which don’t allow us to read parities. Unfortunately, there is no guarantee that “LANCZOS“ wave vectors would be diagonal in this subspace, especially in the case of degenerate vectors.

Hopefully, we perform successive diagonalisations to take care of subspaces of degenerate eigenvalues

```
# Diagonalize wave vectors respect to a given symmetry
sm.vector_diag('Gamma', name1='C2z', name2= 'C2x', subSize = 4, rtol=0.1, skip_diag = False)
```

```
======================
** vector_diag at Gamma **
======================


Diagonalizing flat bands subspace 1.0 with energies:
0.005687156959874318
0.005675662193339814
-0.0003969110247522556
```

```
-0.00041691802874066486
<psi| C2z |psi>
[[-0.8+0.j , 0.5-0.2j,-0. +0.j ,-0. +0.j ],
 [ 0.5+0.2j, 0.8+0.j , 0. -0.j ,-0. +0.j ],
 [-0. -0.j , 0. +0.j , 0.9+0.j , 0.3-0.j ],
 [-0. -0.j ,-0. -0.j , 0.3+0.j ,-0.9+0.j ]]
Diagonalizing respect to  C2z
eignvalues:  [-1.-0.j, 1.+0.j, 1.+0.j,-1.-0.j]

 Second off-diagonalizing respect to  C2x
upper_block is
 [[-1.+0.j, 0.-0.j],
 [ 0.+0.j, 1.+0.j]]
eignvalues:  [-1.-0.j, 1.-0.j]
lower_block is
 [[-1.+0.j,-0.+0.j],
 [-0.-0.j, 1.+0.j]]
eignvalues:  [-1.-0.j, 1.+0.j]

Final check if diagonalized respect to  C2z
[[-1.+0.j,-0.+0.j, 0.+0.j, 0.-0.j],
 [-0.-0.j, 1.+0.j,-0.+0.j, 0.+0.j],
 [ 0.-0.j,-0.-0.j, 1.+0.j,-0.+0.j],
 [ 0.+0.j,-0.-0.j,-0.-0.j,-1.+0.j]]

Final check if diagonalized respect to  C2y
[[ 1.+0.j, 0.-0.j, 0.-0.j,-0.+0.j],
 [ 0.+0.j, 1.+0.j,-0.+0.j, 0.-0.j],
 [ 0.+0.j,-0.-0.j,-1.+0.j,-0.+0.j],
 [-0.-0.j, 0.+0.j,-0.-0.j,-1.+0.j]]

Final check if diagonalized respect to  C2x
[[-1.+0.j, 0.+0.j,-0.+0.j, 0.-0.j],
 [ 0.+0.j, 1.+0.j,-0.+0.j, 0.-0.j],
 [-0.-0.j,-0.-0.j,-1.+0.j, 0.+0.j],
 [ 0.+0.j, 0.+0.j, 0.+0.j, 1.+0.j]]

Diagonalizing flat bands subspace 2.0 with energies:
-0.003000614802293855
-0.003018659755200659
-0.0035570670624436307
-0.0036018736346046243
<psi| C2z |psi>
[[-0.5+0.j ,-0.1+0.9j, 0. +0.j ,-0. +0.j ],
 [-0.1-0.9j, 0.5+0.j ,-0. +0.j ,-0. -0.j ],
 [ 0. -0.j ,-0. -0.j , 0.5+0.j ,-0.3+0.8j],
 [-0. -0.j ,-0. +0.j ,-0.3-0.8j,-0.5-0.j ]]
Diagonalizing respect to  C2z
eignvalues:  [-1.-0.j,-1.+0.j, 1.+0.j, 1.-0.j]

 Second off-diagonalizing respect to  C2x
upper_block is
 [[ 1.+0.j,-0.+0.j],
 [-0.-0.j,-1.+0.j]]
eignvalues:  [ 1.+0.j,-1.+0.j]
lower_block is
 [[-1.+0.j,-0.+0.j],
 [-0.-0.j, 1.+0.j]]
eignvalues:  [-1.+0.j, 1.-0.j]

Final check if diagonalized respect to  C2z
[[-1.+0.j, 0.-0.j, 0.-0.j,-0.-0.j],
 [ 0.+0.j,-1.+0.j,-0.+0.j,-0.+0.j],
 [ 0.+0.j, 0.-0.j, 1.+0.j, 0.-0.j],
 [-0.+0.j,-0.-0.j, 0.+0.j, 1.+0.j]]

Final check if diagonalized respect to  C2y
[[-1.+0.j, 0.-0.j,-0.+0.j, 0.+0.j],
 [ 0.+0.j, 1.+0.j, 0.-0.j, 0.+0.j],
 [-0.-0.j, 0.+0.j,-1.+0.j,-0.+0.j],
```

```
  [ 0.-0.j, 0.-0.j,-0.-0.j, 1.+0.j]]

 Final check if diagonalized respect to  C2x
 [[ 1.+0.j, 0.-0.j,-0.+0.j, 0.+0.j],
  [ 0.+0.j,-1.+0.j,-0.+0.j, 0.+0.j],
  [-0.-0.j,-0.-0.j,-1.+0.j, 0.+0.j],
  [ 0.-0.j, 0.-0.j, 0.-0.j, 1.+0.j]]
```

They are successfully diagonalized. So we can read the parities.

Acknowledgements

Formal:

My PhD fellowship is supported by European Research Council Advanced Grant ULTRADISS No. 8344023 under supervision of Prof. Erio Tosatti. Special thank to (International Centre for Theoretical Physics) ICTP, which made it possible for me to get admitted to the joint PhD program ICTP/SISSA.
Many thanks to Dr. Mehdi Vaez Allaei who introduced me to Prof. Tosatti in the first place. I would also like to thank Prof. Ernst Meyer and Dr. Marcin Kisiel, for many interesting discussions that we had.

Less formal:

Special thanks to my supervisors and good friends, professors Erio Tosatti, Andrea Vanossi, and Giuseppe Santoro. For infinite reasons, always being available to discuss physics with open heart and mind, whom I always perceived as close friends while discussing all the matters. They helped me to grow up a lot, both as a researcher and as a person. Erio is like the grandfather I never had, and Andrea the older brother.

Also thanks to the postdocs, Jin Wang, for his commitment and dedication to our jointly published papers, and being a good friend to whom I am close to the deepest layers of polite Chinese culture.
Andrea Silva, for collaborating on physics and being a good friend who introduced me to the climbing community, which certainly lubricated my life.

My warmest thanks to my parents Norollah and Zeinab; my two beautiful sisters Nafise and Fati; and my big brother Hamed; for their love, patience, continuous support, and understanding.

Bibliography

[1] E. Tosatti, S. Prestipino, S. Kostlmeier, A. Dal Corso, and F. D. Di Tolla. String tension and stability of magic tip-suspended nanowires. *Science*, 291(5502):288–290, 2001.

[2] E. Tosatti. Nanowire formation at metal-metal contacts. *Solid State Communications*, 135(9):610–617, 2005.

[3] A. I. Yanson, G. Rubio Bollinger, H. E. van den Brom, N. Agraït, and J. M. van Ruitenbeek. Formation and manipulation of a metallic wire of single gold atoms. *Nature*, 395(6704):783–785, 1998.

[4] Hideaki Ohnishi, Yukihito Kondo, and Kunio Takayanagi. Quantized conductance through individual rows of suspended gold atoms. *Nature*, 395(6704):780–783, 1998.

[5] Jean Comtet, Antoine Lainé, Antoine Niguès, Lydéric Bocquet, and Alessandro Siria. Atomic rheology of gold nanojunctions. *Nature*, 569(7756):393–397, 2019.

[6] Takaaki Sato, Tadashi Ishida, Laurent Jalabert, and Hiroyuki Fujita. Real-time transmission electron microscope observation of nanofriction at a single ag asperity. *Nanotechnology*, 23(50):505701, 2012.

[7] Danyang Yu, Jin Wang, Ming Ma, and Yonggang Meng. Effect of surface energy on shearing of metal asperities contact at the nanoscale. *The Journal of Physical Chemistry C*, 124(50):27436–27441, 2020.

[8] Jin Wang, Ali Khosravi, Andrea Vanossi, and Erio Tosatti. Sliding and pinning in structurally lubric 2d material interfaces. *Reviews of Modern Physics*, 2023.

[9] Martin Rejhon, Francesco Lavini, Ali Khosravi, Mykhailo Shestopalov, Jan Kunc, Erio Tosatti, and Elisa Riedo. Relation between interfacial shear and friction force in 2d materials. *Nature Nanotechnology*, 17(12):1280–1287, 2022.

[10] Andrea Mescola, Andrea Silva, Ali Khosravi, Andrea Vanossi, Erio Tosatti, Sergio Valeri, and Guido Paolicelli. Anisotropic rheology and friction of suspended graphene. *Physical Review Materials*, 7:054007, 2023.

[11] J. Lasave, S. Koval, A. Laio, and E. Tosatti. Proton strings and rings in atypical nucleation of ferroelectricity in ice. *Proceedings of the National Academy of Sciences*, 118(1):e2018837118, 2021.

[12] D. W. Pashley, M. J. Stowell, M. H. Jacobs, and T. J. Law. The growth and structure of gold and silver deposits formed by evaporation inside an electron microscope. *The Philosophical Magazine*, 10(103):127–158, 1964.

[13] Nicolás Agraït, Alfredo Levy Yeyati, and Jan M. van Ruitenbeek. Quantum properties of atomic-sized conductors. *Physics Reports*, 377(2-3):81–279, 2003.

[14] Ryan Requist, Pier Paolo Baruselli, Alexander Smogunov, Michele Fabrizio, Silvio Modesti, and Erio Tosatti. Metallic, magnetic and molecular nanocontacts. *Nature Nanotechnology*, 11(6):499–508, 2016.

[15] N. Agraït, G. Rubio, and S. Vieira. Plastic deformation of nanometer-scale gold connective necks. *Physical Review Letters*, 74(20):3995–3998, 1995.

[16] A. I. Mares, A. F. Otte, L. G. Soukiassian, R. H. M. Smit, and J. M. van Ruitenbeek. Observation of electronic and atomic shell effects in gold nanowires. *Physical Review B*, 70:073401, 2004.

[17] Yukihito Kondo and Kunio Takayanagi. Synthesis and characterization of helical multi-shell gold nanowires. *Science*, 289(5479):606–608, 2000.

[18] Yoshifumi Oshima, Keisuke Mouri, Hiroyuki Hirayama, and Kunio Takayanagi. Quantized electrical conductance of gold helical multishell nanowires. *Journal of the Physical Society of Japan*, 75(5):053705, 2006.

[19] Yoshihiko Kurui, Yoshifumi Oshima, and Kunio Takayanagi. One-by-one evolution of conductance channel in gold [110] nanowires. *Journal of the Physical Society of Japan*, 76(12):10–13, 2007.

[20] Tokushi Kizuka. Atomic configuration and mechanical and electrical properties of stable gold wires of single-atom width. *Physical Review B*, 77:155401, 2008.

[21] Yang Lu, Jian Yu Huang, Chao Wang, Shouheng Sun, and Jun Lou. Cold welding of ultrathin gold nanowires. *Nature Nanotechnology*, 5(3):218–224, 2010.

[22] J. M. van Ruitenbeek, A. Alvarez, I. Piñeyro, C. Grahmann, P. Joyez, M. H. Devoret, D. Esteve, and C. Urbina. Adjustable nanofabricated atomic size contacts. *Review of Scientific Instruments*, 67(1):108–111, 1996.

[23] Jiaming Liu, Jiaqi Zhang, Toyoko Arai, Masahiko Tomitori, and Yoshifumi Oshima. Critical shear stress of gold nanocontacts estimated by in situ transmission electron microscopy equipped with a quartz length-extension resonator. *Applied Physics Express*, 14(7):075006, 2021.

[24] Jiankuai Diao, Ken Gall, Martin L. Dunn, and Jonathan A. Zimmerman. Atomistic simulations of the yielding of gold nanowires. *Acta Materialia*, 54(3):643–653, 2006.

[25] Luis A. Zepeda-Ruiz, Alexander Stukowski, Tomas Oppelstrup, and Vasily V. Bulatov. Probing the limits of metal plasticity with molecular dynamics simulations. *Nature*, 550:492–495, 2017.

[26] S. M. Foiles, M. I. Baskes, and M. S. Daw. Embedded-atom-method functions for the fcc metals cu, ag, au, ni, pd, pt, and their alloys. *Physical Review B*, 33:7983–7991, 1986.

[27] Jiaqi Zhang, Keisuke Ishizuka, Masahiko Tomitori, Toyoko Arai, Kenta Hongo, Ryo Maezono, Erio Tosatti, and Yoshifumi Oshima. Peculiar atomic bond nature in platinum monatomic chains. *Nano Letters*, 21(9):3922–3928, 2021.

[28] F. Ercolessi, E. Tosatti, and M. Parrinello. Au (100) surface reconstruction. *Physical Review Letters*, 57:719–722, 1986.

[29] F. Ercolessi, M. Parrinello, and E. Tosatti. Simulation of gold in the glue model. *Philosophical Magazine A*, 58(1):213–226, 1988.

[30] Raju P. Gupta. Lattice relaxation at a metal surface. *Physical Review B*, 23:6265–6270, 1981.

[31] M W Finnis and V Heine. Theory of lattice contraction at aluminium surfaces. *Journal of Physics F Metal Physics*, 4(3):l37, 1974.

[32] Christoph Eisenmann, Chanjoong Kim, Johan Mattsson, and David A. Weitz. Shear melting of a colloidal glass. *Physical Review Letters*, 104:035502, 2010.

[33] Uzi Landman, W.D. Luedtke, and Eric M. Ringer. Atomistic mechanisms of adhesive contact formation and interfacial processes. *Wear*, 153(1):3–30, 1992.

[34] J. B. Pethica and A. P. Sutton. On the stability of a tip and flat at very small separations. *Journal of Vacuum Science & Technology A*, 6(4):2490–2494, 1988.

[35] H. W. Sheng, M. J. Kramer, A. Cadien, T. Fujita, and M. W. Chen. Highly optimized embedded-atom-method potentials for fourteen fcc metals. *Physical Review B*, 83:134118, 2011.

[36] Andrea Vanossi, Nicola Manini, Michael Urbakh, Stefano Zapperi, and Erio Tosatti. Colloquium: Modeling friction: From nanoscale to mesoscale. *Reviews of Modern Physics*, 85:529–552, 2013.

[37] S. Yu. Krylov, K. B. Jinesh, H. Valk, M. Dienwiebel, and J. W. M. Frenken. Thermally induced suppression of friction at the atomic scale. *Physical Review E*, 71:065101, 2005.

[38] L. Prandtl. Ein gedankenmodell zur kinetischen theorie der festen korper. *ZAMM - Journal of Applied Mathematics and Mechanics / Zeitschrift für Angewandte Mathematik und Mechanik*, 8(2):85–106, 1928.

[39] Nico Mosso, Ute Drechsler, Fabian Menges, Peter Nirmalraj, Siegfried Karg, Heike Riel, and Bernd Gotsmann. Heat transport through atomic contacts. *Nature Nanotechnology*, 12:430–433, 2017.

[40] Longji Cui, Wonho Jeong, Sunghoon Hur, Manuel Matt, Jan C. Klöckner, Fabian Pauly, Peter Nielaba, Juan Carlos Cuevas, Edgar Meyhofer, and Pramod Reddy. Quantized thermal transport in single-atom junctions. *Science*, 355(6330):1192–1195, 2017.

[41] Benjamin F Toler, Ronald A Coutu, and John W McBride. A review of micro-contact physics for microelectromechanical systems (MEMS) metal contact switches. *Journal of Micromechanics and Microengineering*, 23(10):103001, 2013.

[42] A. Basu, G. G. Adams, and N. E. McGruer. A review of micro-contact physics, materials, and failure mechanisms in direct-contact RF MEMS switches. *Journal of Micromechanics and Microengineering*, 26(10), 2016.

[43] W.H. Abbott. Materials, environment, motion, and electrical contact failure mechanisms. *Proceedings of the Thirty Fifth Meeting of the IEEE Holm Conference on Electrical Contacts*, pages 3–11, 1989.

[44] Yilin Zhou, Chuan Hong, Libiao Liu, and Liangjun Xu. The reliability investigation of gold plated electrical contacts under sliding conditions. *Proceedings of the IEEE 2012 Prognostics and System Health Management Conference (PHM-2012 Beijing)*, pages 1–6, 2012.

[45] Ruiting Tong and Geng Liu. Vibration induced reciprocating sliding contacts between nanoscale multi-asperity tips and a textured surface. *Microgravity Science and Technology*, 32(1):79–88, 2020.

[46] Steve Plimpton. Fast parallel algorithms for short-range molecular dynamics. *Journal of Computational Physics*, 117(1):1–19, 1995.

[47] Harold S. Park and Jonathan A. Zimmerman. Modeling inelasticity and failure in gold nanowires. *Physical Review B*, 72:054106, 2005.

[48] Daniel Gall. Electron mean free path in elemental metals. *Journal of Applied Physics*, 119(8):085101, 2016.

[49] Mark A. Lantz, Dorothea Wiesmann, and Bernd Gotsmann. Dynamic superlubricity and the elimination of wear on the nanoscale. *Nature Nanotechnology*, 4:586–591, 2009.

[50] Ming Ma, Igor M. Sokolov, Wen Wang, Alexander E. Filippov, Quanshui Zheng, and Michael Urbakh. Diffusion through bifurcations in oscillating nano- and microscale contacts: Fundamentals and applications. *Physical Review X*, 5:031020, 2015.

[51] Z. Tshiprut, A. E. Filippov, and M. Urbakh. Tuning diffusion and friction in microscopic contacts by mechanical excitations. *Physical Review Letters*, 95:016101, 2005.

[52] Rosario Capozza, Andrea Vanossi, Alessandro Vezzani, and Stefano Zapperi. Triggering frictional slip by mechanical vibrations. *Tribology Letters*, 48(1):95–102, 2012.

[53] Rosario Capozza, Andrea Vanossi, Alessandro Vezzani, and Stefano Zapperi. Suppression of friction by mechanical vibrations. *Physical Review Letters*, 103:085502, 2009.

[54] Bo N. J. Persson. *Sliding Friction Physical Principles and Applications*. Springer Berlin Heidelberg, 2000.

[55] Bo N. J. Persson (Editor) and Erio Tosatti (Editor). *Physics of Sliding Friction (NATO Science Series E:, 311)*. Springer Netherlands, 1996.

[56] Frank Philip Bowden and David Tabor. *The friction and lubrication of solids*, volume 1. Oxford university press, 2001.

[57] Takaaki Sato, Zachary B. Milne, Masahiro Nomura, Naruo Sasaki, Robert W. Carpick, and Hiroyuki Fujita. Ultrahigh strength and shear-assisted separation of sliding nanocontacts studied in situ. *Nature Communications*, 13(1):2551, 2022.

[58] B. N. J. Persson and J. Biele. Heat transfer in granular media with weakly interacting particles. *AIP Advances*, 12(10):105307, 2022.

[59] B. N. J. Persson. On the electric contact resistance. *Tribology Letters*, 70(3):88, 2022.

[60] Ali Khosravi, Antoine Lainé, Andrea Vanossi, Jin Wang, Alessandro Siria, and Erio Tosatti. Understanding the rheology of nanocontacts. *Nature Communications*, 13(1):2428, 2022.

[61] Sergey Yu. Krylov and Joost W. M. Frenken. The physics of atomic-scale friction: Basic considerations and open questions. *physica status solidi (b)*, 251(4):711–736, 2014.

[62] Tianren Fu, Kathleen Frommer, Colin Nuckolls, and Latha Venkataraman. Single-molecule junction formation in break-junction measurements. *The Journal of Physical Chemistry Letters*, 12(44):10802–10807, 2021.

[63] Yuan Cao, Valla Fatemi, Ahmet Demir, Shiang Fang, Spencer L. Tomarken, Jason Y. Luo, Javier D. Sanchez-Yamagishi, Kenji Watanabe, Takashi Taniguchi, Efthimios Kaxiras, Ray C. Ashoori, and Pablo Jarillo-Herrero. Correlated insulator behaviour at half-filling in magic-angle graphene superlattices. *Nature*, 556(7699):80–84, 2018.

[64] Yuan Cao, Valla Fatemi, Shiang Fang, Kenji Watanabe, Takashi Taniguchi, Efthimios Kaxiras, and Pablo Jarillo-Herrero. Unconventional superconductivity in magic-angle graphene superlattices. *Nature*, 556(7699):43–50, 2018.

[65] Alexander Kerelsky, Leo J. McGilly, Dante M. Kennes, Lede Xian, Matthew Yankowitz, Shaowen Chen, K. Watanabe, T. Taniguchi, James Hone, Cory Dean, Angel Rubio, and Abhay N. Pasupathy. Maximized electron interactions at the magic angle in twisted bilayer graphene. *Nature*, 572(7767):95–100, 2019.

[66] Matthew Yankowitz, Shaowen Chen, Hryhoriy Polshyn, Yuxuan Zhang, K. Watanabe, T. Taniguchi, David Graf, Andrea F. Young, and Cory R. Dean. Tuning superconductivity in twisted bilayer graphene. *Science*, 363(6431):1059–1064, 2019.

[67] Petr Stepanov, Ipsita Das, Xiaobo Lu, Ali Fahimniya, Kenji Watanabe, Takashi Taniguchi, Frank H. L. Koppens, Johannes Lischner, Leonid Levitov, and Dmitri K. Efetov. Untying the insulating and superconducting orders in magic-angle graphene. *Nature*, 583(7816):375–378, 2020.

[68] Jeong Min Park, Yuan Cao, Kenji Watanabe, Takashi Taniguchi, and Pablo Jarillo-Herrero. Tunable strongly coupled superconductivity in magic-angle twisted trilayer graphene. *Nature*, 590(7845):249–255, 2021.

[69] Shuai Zhang, Tianbao Ma, Ali Erdemir, and Qunyang Li. Tribology of two-dimensional materials: From mechanisms to modulating strategies. *Materials Today*, 26:67–86, 2019.

[70] Motohisa Hirano and Kazumasa Shinjo. Atomistic locking and friction. *Physical Review B*, 41:11837–11851, 1990.

[71] Martin Dienwiebel, Gertjan S. Verhoeven, Namboodiri Pradeep, Joost W. M. Frenken, Jennifer A. Heimberg, and Henny W. Zandbergen. Superlubricity of graphite. *Physical Review Letters*, 92:126101, 2004.

[72] Xuanyu Huang, Li Lin, and Quanshui Zheng. Theoretical study of superlubric nanogenerators with superb performances. *Nano Energy*, 70:104494, 2020.

[73] Xuanyu Huang, Xiaojian Xiang, Jinhui Nie, Deli Peng, Fuwei Yang, Zhanghui Wu, Haiyang Jiang, Zhiping Xu, and Quanshui Zheng. Microscale schottky superlubric generator with high direct-current density and ultralong life. *Nature Communications*, 12(1):2268, 2021.

[74] Zhanghui Wu, Xuanyu Huang, Xiaojian Xiang, and Quanshui Zheng. Electro-superlubric springs for continuously tunable resonators and oscillators. *Communications Materials*, 2(1):104, 2021.

[75] Quanshui Zheng and Qing Jiang. Multiwalled carbon nanotubes as gigahertz oscillators. *Physical Review Letters*, 88:045503, 2002.

[76] Andrea Vanossi, Clemens Bechinger, and Michael Urbakh. Structural lubricity in soft and hard matter systems. *Nature Communications*, 11(1):4657, 2020.

[77] Y. Liu, A. Erdemir, and E.I. Meletis. A study of the wear mechanism of diamond-like carbon films. *Surface and Coatings Technology*, 82(1):48–56, 1996.

[78] Mikael Eriksson, Filip Bergman, and Staffan Jacobson. On the nature of tribological contact in automotive brakes. *Wear*, 252(1):26–36, 2002.

[79] Yu Zhao, Hui Mei, Peng Chang, Chao Chen, Laifei Cheng, and Konstantinos G. Dassios. Infinite approaching superlubricity by three-dimensional printed structures. *ACS Nano*, 15(1):240–257, 2021.

[80] Gang He, Martin H. Müser, and Mark O. Robbins. Adsorbed layers and the origin of static friction. *Science*, 284(5420):1650–1652, 1999.

[81] Jacqueline Krim. Friction and energy dissipation mechanisms in adsorbed molecules and molecularly thin films. *Advances in Physics*, 61(3):155–323, 2012.

[82] Nicola Varini, Andrea Vanossi, Roberto Guerra, Davide Mandelli, Rosario Capozza, and Erio Tosatti. Static friction scaling of physisorbed islands: the key is in the edge. *Nanoscale*, 7:2093–2101, 2015.

[83] Matteo Pierno, Lorenzo Bruschi, Giampaolo Mistura, Guido Paolicelli, Alessandro di Bona, Sergio Valeri, Roberto Guerra, Andrea Vanossi, and Erio Tosatti. Frictional transition from superlubric islands to pinned monolayers. *Nature Nanotechnology*, 10(8):714–718, 2015.

[84] Thomas Bohlein, Jules Mikhael, and Clemens Bechinger. Observation of kinks and antikinks in colloidal monolayers driven across ordered surfaces. *Nature Materials*, 11(2):126–130, 2012.

[85] Andrea Vanossi and Erio Tosatti. Kinks in motion. *Nature Materials*, 11(2):97–98, 2012.

[86] Davide Mandelli, Andrea Vanossi, Nicola Manini, and Erio Tosatti. Friction boosted by equilibrium misalignment of incommensurate two-dimensional colloid monolayers. *Physical Review Letters*, 114:108302, 2015.

[87] T. Brazda, A. Silva, N. Manini, A. Vanossi, R. Guerra, E. Tosatti, and C. Bechinger. Experimental observation of the aubry transition in two-dimensional colloidal monolayers. *Physical Review X*, 8:011050, 2018.

[88] Xin Cao, Emanuele Panizon, Andrea Vanossi, Nicola Manini, and Clemens Bechinger. Orientational and directional locking of colloidal clusters driven across periodic surfaces. *Nature Physics*, 15(8):776–780, 2019.

[89] Serge Aubry. The twist map, the extended Frenkel-Kontorova model and the Devil's staircase. *Physica D: Nonlinear Phenomena*, 7(1):240–258, 1983.

[90] M Peyrard and S Aubry. Critical behaviour at the transition by breaking of analyticity in the discrete Frenkel-Kontorova model. *Journal of Physics C: Solid State Physics*, 16(9):1593–1608, 1983.

[91] J. B. Sokoloff, J. E. Sacco, and J. F. Weisz. Undamped lattice vibrations in systems with two incommensurate periodicities. *Physical Review Letters*, 41:1561–1564, 1978.

[92] M. H Müser. Structural lubricity: Role of dimension and symmetry. *Europhysics Letters*, 66(1):97–103, 2004.

[93] J. B. Sokoloff. Theory of energy dissipation in sliding crystal surfaces. *Physical Review B*, 42:760–765, 1990.

[94] Kazumasa Shinjo and Motohisa Hirano. Dynamics of friction: superlubric state. *Surface Science*, 283(1):473–478, 1993.

[95] Mehmet Z. Baykara, Mohammad R. Vazirisereshk, and Ashlie Martini. Emerging superlubricity: A review of the state of the art and perspectives on future research. *Applied Physics Reviews*, 5(4):041102, 2018.

[96] Jean Michel Martin and Ali Erdemir. Superlubricity: Friction's vanishing act. *Physics Today*, 71(4):40–46, 2018.

[97] Motohisa Hirano, Kazumasa Shinjo, Reizo Kaneko, and Yoshitada Murata. Observation of superlubricity by scanning tunneling microscopy. *Physical Review Letters*, 78:1448–1451, 1997.

[98] Ze Liu, Jiarui Yang, Francois Grey, Jefferson Zhe Liu, Yilun Liu, Yibing Wang, Yanlian Yang, Yao Cheng, and Quanshui Zheng. Observation of microscale superlubricity in graphite. *Physical Review Letters*, 108:205503, 2012.

[99] Changgu Lee, Qunyang Li, William Kalb, Xin-Zhou Liu, Helmuth Berger, Robert W. Carpick, and James Hone. Frictional characteristics of atomically thin sheets. *Science*, 328(5974):76–80, 2010.

[100] Cangyu Qu, Kunqi Wang, Jin Wang, Yujie Gongyang, Robert W. Carpick, Michael Urbakh, and Quanshui Zheng. Origin of friction in superlubric graphite contacts. *Physical Review Letters*, 125:126102, 2020.

[101] Elad Koren, Emanuel Lörtscher, Colin Rawlings, Armin W. Knoll, and Urs Duerig. Adhesion and friction in mesoscopic graphite contacts. *Science*, 348(6235):679–683, 2015.

[102] Michael Urbakh. Towards macroscale superlubricity. *Nature Nanotechnology*, 8(12):893–894, 2013.

[103] Rufan Zhang, Zhiyuan Ning, Yingying Zhang, Quanshui Zheng, Qing Chen, Huanhuan Xie, Qiang Zhang, Weizhong Qian, and Fei Wei. Superlubricity in centimetres-long double-walled carbon nanotubes under ambient conditions. *Nature Nanotechnology*, 8(12):912–916, 2013.

[104] T. Filleter, J. L. McChesney, A. Bostwick, E. Rotenberg, K. V. Emtsev, Th. Seyller, K. Horn, and R. Bennewitz. Friction and dissipation in epitaxial graphene films. *Physical Review Letters*, 102:086102, 2009.

[105] Shigeki Kawai, Andrea Benassi, Enrico Gnecco, Hajo Söde, Rémy Pawlak, Xinliang Feng, Klaus Müllen, Daniele Passerone, Carlo A. Pignedoli, Pascal Ruffieux, Roman Fasel, and Ernst Meyer. Superlubricity of graphene nanoribbons on gold surfaces. *Science*, 351(6276):957–961, 2016.

[106] Diana Berman, Sanket A. Deshmukh, Subramanian K. R. S. Sankaranarayanan, Ali Erdemir, and Anirudha V. Sumant. Macroscale superlubricity enabled by graphene nanoscroll formation. *Science*, 348(6239):1118–1122, 2015.

[107] Joost A van den Ende, Astrid S de Wijn, and Annalisa Fasolino. The effect of temperature and velocity on superlubricity. *Journal of Physics: Condensed Matter*, 24(44):445009, 2012.

[108] L. Consoli, H. J. F. Knops, and A. Fasolino. Onset of sliding friction in incommensurate systems. *Physical Review Letters*, 85:302–305, 2000.

[109] A. S. de Wijn. (in)commensurability, scaling, and multiplicity of friction in nanocrystals and application to gold nanocrystals on graphite. *Physical Review B*, 86:085429, 2012.

[110] Itai Leven, Dana Krepel, Ortal Shemesh, and Oded Hod. Robust superlubricity in graphene/h-bn heterojunctions. *The Journal of Physical Chemistry Letters*, 4(1):115–120, 2013.

[111] Oded Hod. The registry index: A quantitative measure of materials' interfacial commensurability. *ChemPhysChem*, 14(11):2376–2391, 2013.

[112] Davide Mandelli, Wengen Ouyang, Oded Hod, and Michael Urbakh. Negative friction coefficients in superlubric graphite–hexagonal boron nitride heterojunctions. *Physical Review Letters*, 122:076102, 2019.

[113] E. Gnecco, R. Bennewitz, T. Gyalog, Ch. Loppacher, M. Bammerlin, E. Meyer, and H.-J. Güntherodt. Velocity dependence of atomic friction. *Physical Review Letters*, 84:1172–1175, 2000.

[114] E. Riedo, E. Gnecco, R. Bennewitz, E. Meyer, and H. Brune. Interaction potential and hopping dynamics governing sliding friction. *Physical Review Letters*, 91:084502, 2003.

[115] Martin H. Müser. Velocity dependence of kinetic friction in the prandtl-tomlinson model. *Physical Review B*, 84:125419, 2011.

[116] Franco Pellegrini, Emanuele Panizon, Giuseppe E. Santoro, and Erio Tosatti. Thermally assisted lubricity and negative work tails in sliding friction. *Physical Review B*, 99:075428, 2019.

[117] Yi Sang, Martin Dubé, and Martin Grant. Thermal effects on atomic friction. *Physical Review Letters*, 87:174301, 2001.

[118] Peter Reimann and Mykhaylo Evstigneev. Nonmonotonic velocity dependence of atomic friction. *Physical Review Letters*, 93:230802, 2004.

[119] Yalin Dong, Ajay Vadakkepatt, and Ashlie Martini. Analytical models for atomic friction. *Tribology Letters*, 44(3):367, 2011.

[120] O.K. Dudko, A.E. Filippov, J. Klafter, and M. Urbakh. Dynamic force spectroscopy: a fokker–planck approach. *Chemical Physics Letters*, 352(5):499–504, 2002.

[121] Roberto Guerra, Ugo Tartaglino, Andrea Vanossi, and Erio Tosatti. Ballistic nanofriction. *Nature Materials*, 9(8):634–637, 2010.

[122] Yanmin Liu, Kang Wang, Qiang Xu, Jie Zhang, Yuanzhong Hu, Tianbao Ma, Quanshui Zheng, and Jianbin Luo. Superlubricity between graphite layers in ultrahigh vacuum. *ACS Applied Materials & Interfaces*, 12(38):43167–43172, 2020.

[123] Wen Wang and Xide Li. Interlayer motion and ultra-low sliding friction in microscale graphite flakes. *EPL (Europhysics Letters)*, 125(2):26003, 2019.

[124] D Dowson. *History of tribology*. Longman, London, 1979.

[125] Guillaume Amontons. De la resistance cause'e dans les machines. *Memoires De L'Acedemie Royale A*, pages 257–282, 1699.

[126] B. N. J. Persson and E. Tosatti. The effect of surface roughness on the adhesion of elastic solids. *The Journal of Chemical Physics*, 115(12):5597–5610, 2001.

[127] B N J Persson, O Albohr, U Tartaglino, A I Volokitin, and E Tosatti. On the nature of surface roughness with application to contact mechanics, sealing, rubber friction and adhesion. *Journal of Physics: Condensed Matter*, 17(1):R1, 2004.

[128] Binquan Luan and Mark O. Robbins. The breakdown of continuum models for mechanical contacts. *Nature*, 435(7044):929–932, 2005.

[129] Ali Erdemir and Jean-Michel Martin. *Superlubricity*. Elsevier, 2007.

[130] B. Derjaguin. Molekulartheorie der äußeren reibung. *Zeitschrift für Physik*, 88(9):661–675, 1934.

[131] Qunyang Li, Changgu Lee, Robert W. Carpick, and James Hone. Substrate effect on thickness-dependent friction on graphene. *physica status solidi (b)*, 247(11-12):2909–2914, 2010.

[132] Yinghui Sun, Rongming Wang, and Kai Liu. Substrate induced changes in atomically thin 2-dimensional semiconductors: Fundamentals, engineering, and applications. *Applied Physics Reviews*, 4(1):011301, 2017.

[133] Samir Mammadov, Jurgen Ristein, Julia Krone, Christian Raidel, Martina Wanke, Veit Wiesmann, Florian Speck, and Thomas Seyller. Work function of graphene multilayers on SiC(0001). *2D Materials*, 4(1):015043, 2017.

[134] Yang Gao, Suenne Kim, Si Zhou, Hsiang-Chih Chiu, Daniel Nélias, Claire Berger, Walt de Heer, Laura Polloni, Roman Sordan, Angelo Bongiorno, and Elisa Riedo. Elastic coupling between layers in two-dimensional materials. *Nature Materials*, 14(7):714–720, 2015.

[135] Damien Voiry, Hisato Yamaguchi, Junwen Li, Rafael Silva, Diego C. B. Alves, Takeshi Fujita, Mingwei Chen, Tewodros Asefa, Vivek B. Shenoy, Goki Eda, and Manish Chhowalla. Enhanced catalytic activity in strained chemically exfoliated WS2 nanosheets for hydrogen evolution. *Nature Materials*, 12(9):850–855, 2013.

[136] Wenzhong Bao, Jiayu Wan, Xiaogang Han, Xinghan Cai, Hongli Zhu, Dohun Kim, Dakang Ma, Yunlu Xu, Jeremy N. Munday, H. Dennis Drew, Michael S. Fuhrer, and Liangbing Hu. Approaching the limits of transparency and conductivity in graphitic materials through lithium intercalation. *Nature Communications*, 5(1), 2014.

[137] Chaochen Xu, Tao Xue, Wei Qiu, and Yilan Kang. Size effect of the interfacial mechanical behavior of graphene on a stretchable substrate. *ACS Applied Materials & Interfaces*, 8(40):27099–27106, 2016.

[138] Tao Jiang, Rui Huang, and Yong Zhu. Interfacial sliding and buckling of monolayer graphene on a stretchable substrate. *Advanced Functional Materials*, 24(3):396–402, 2013.

[139] J. Cho, J.J. Luo, and I.M. Daniel. Mechanical characterization of graphite/epoxy nanocomposites by multi-scale analysis. *Composites Science and Technology*, 67(11-12):2399–2407, 2007.

[140] E. J. Seldin and C. W. Nezbeda. Elastic constants and electron-microscope observations of neutron-irradiated compression-annealed pyrolytic and single-crystal graphite. *Journal of Applied Physics*, 41(8):3389–3400, 1970.

[141] G. Savini, Y.J. Dappe, S. Öberg, J.-C. Charlier, M.I. Katsnelson, and A. Fasolino. Bending modes, elastic constants and mechanical stability of graphitic systems. *Carbon*, 49(1):62–69, 2011.

[142] Zhiwei Peng, Xiaolin Chen, Yulong Fan, David J. Srolovitz, and Dangyuan Lei. Strain engineering of 2d semiconductors and graphene: from strain fields to band-structure tuning and photonic applications. *Light: Science & Applications*, 9(1), 2020.

[143] J. Scott Bunch, Arend M. van der Zande, Scott S. Verbridge, Ian W. Frank, David M. Tanenbaum, Jeevak M. Parpia, Harold G. Craighead, and Paul L. McEuen. Electromechanical resonators from graphene sheets. *Science*, 315(5811):490–493, 2007.

[144] Zenghui Wang and Philip X-L Feng. Design of black phosphorus 2d nanomechanical resonators by exploiting the intrinsic mechanical anisotropy. *2D Materials*, 2(2):021001, 2015.

[145] Changyao Chen, Sami Rosenblatt, Kirill I. Bolotin, William Kalb, Philip Kim, Ioannis Kymissis, Horst L. Stormer, Tony F. Heinz, and James Hone. Performance of monolayer graphene nanomechanical resonators with electrical readout. *Nature Nanotechnology*, 4(12):861–867, 2009.

[146] Nicholas R Glavin, Christopher Muratore, and Michael Snure. Toward 2d materials for flexible electronics: opportunities and outlook. *Oxford Open Materials Science*, 1(1), 2020.

[147] Ricard Alert and Jaume Casademunt. Role of substrate stiffness in tissue spreading: Wetting transition and tissue durotaxis. *Langmuir*, 35(23):7571–7577, 2018.

[148] Wenyang Qu, Soumendu Bagchi, Xiaoming Chen, Huck Beng Chew, and Changhong Ke. Bending and interlayer shear moduli of ultrathin boron nitride nanosheet. *Journal of Physics D: Applied Physics*, 52(46):465301, 2019.

[149] Xiaoming Chen, Chenglin Yi, and Changhong Ke. Bending stiffness and interlayer shear modulus of few-layer graphene. *Applied Physics Letters*, 106(10), 2015.

[150] J. Kunc, M. Rejhon, E. Belas, V. Dědič, P. Moravec, and J. Franc. Effect of residual gas composition on epitaxial growth of graphene on SiC. *Physical Review Applied*, 8(4), 2017.

[151] J. Kunc, M. Rejhon, and P. Hlídek. Hydrogen intercalation of epitaxial graphene and buffer layer probed by mid-infrared absorption and raman spectroscopy. *AIP Advances*, 8(4), 2018.

[152] Martin Rejhon and Jan Kunc. ZO phonon of a buffer layer and raman mapping of hydrogenated buffer on SiC(0001). *Journal of Raman Spectroscopy*, 50(3):465–473, 2018.

[153] J. Hass, F. Varchon, J. E. Millán-Otoya, M. Sprinkle, N. Sharma, W. A. de Heer, C. Berger, P. N. First, L. Magaud, and E. H. Conrad. Why multilayer graphene on $4h-\mathrm{SiC}(000\bar{1})$ behaves like a single sheet of graphene. *Physical Review Letters*, 100:125504, 2008.

[154] T. Filleter and R. Bennewitz. Structural and frictional properties of graphene films on SiC(0001) studied by atomic force microscopy. *Physical Review B*, 81(15), 2010.

[155] Suzhi Li, Qunyang Li, Robert W. Carpick, Peter Gumbsch, Xin Z. Liu, Xiangdong Ding, Jun Sun, and Ju Li. The evolving quality of frictional contact with graphene. *Nature*, 539(7630):541–545, 2016.

[156] Francesco Lavini, Annalisa Calò, Yang Gao, Edoardo Albisetti, Tai-De Li, Tengfei Cao, Guoqing Li, Linyou Cao, Carmela Aruta, and Elisa Riedo. Friction and work function oscillatory behavior for an even and odd number of layers in polycrystalline MoS_2. *Nanoscale*, 10(17):8304–8312, 2018.

[157] Yang Gao, Tengfei Cao, Filippo Cellini, Claire Berger, Walter A. de Heer, Erio Tosatti, Elisa Riedo, and Angelo Bongiorno. Ultrahard carbon film from epitaxial two-layer graphene. *Nature Nanotechnology*, 13(2):133–138, 2017.

[158] Filippo Cellini, Yang Gao, and Elisa Riedo. å-indentation for non-destructive elastic moduli measurements of supported ultra-hard ultra-thin films and nanostructures. *Scientific Reports*, 9(1), 2019.

[159] Filippo Cellini, Francesco Lavini, Elton Chen, Angelo Bongiorno, Filip Popovic, Ryan L. Hartman, Remi Dingreville, and Elisa Riedo. Pressure-induced formation and mechanical properties of 2d diamond boron nitride. *Advanced Science*, 8(2), 2020.

[160] O. L. Blakslee, D. G. Proctor, E. J. Seldin, G. B. Spence, and T. Weng. Elastic constants of compression-annealed pyrolytic graphite. *Journal of Applied Physics*, 41(8):3373–3382, 1970.

[161] J.R. Xiao, B.A. Gama, and J.W. Gillespie. An analytical molecular structural mechanics model for the mechanical properties of carbon nanotubes. *International Journal of Solids and Structures*, 42(11-12):3075–3092, 2005.

[162] P. H. Tan, W. P. Han, W. J. Zhao, Z. H. Wu, K. Chang, H. Wang, Y. F. Wang, N. Bonini, N. Marzari, N. Pugno, G. Savini, A. Lombardo, and A. C. Ferrari. The shear mode of multilayer graphene. *Nature Materials*, 11(4):294–300, 2012.

[163] K. V. Emtsev, F. Speck, Th. Seyller, L. Ley, and J. D. Riley. Interaction, growth, and ordering of epitaxial graphene on SiC{0001} surfaces: A comparative photoelectron spectroscopy study. *Physical Review B*, 77(15), 2008.

[164] P. Lauffer, K. V. Emtsev, R. Graupner, Th. Seyller, L. Ley, S. A. Reshanov, and H. B. Weber. Atomic and electronic structure of few-layer graphene on SiC(0001) studied with scanning tunneling microscopy and spectroscopy. *Physical Review B*, 77(15), 2008.

[165] P. Mallet, F. Varchon, C. Naud, L. Magaud, C. Berger, and J.-Y. Veuillen. Electron states of mono- and bilayer graphene on SiC probed by scanning-tunneling microscopy. *Physical Review B*, 76(4), 2007.

[166] I. Razado-Colambo, J. Avila, D. Vignaud, S. Godey, X. Wallart, D. P. Woodruff, and M. C. Asensio. Structural determination of bilayer graphene on SiC(0001) using synchrotron radiation photoelectron diffraction. *Scientific Reports*, 8(1), 2018.

[167] C. Virojanadara, R. Yakimova, J.R. Osiecki, M. Syvajarvi, R.I.G. Uhrberg, L.I. Johansson, and A.A. Zakharov. Substrate orientation: A way towards higher quality monolayer graphene growth on 6h-SiC(0 0 0 1). *Surface Science*, 603(15):L87–L90, 2009.

[168] F. Speck, J. Jobst, F. Fromm, M. Ostler, D. Waldmann, M. Hundhausen, H. B. Weber, and Th. Seyller. The quasi-free-standing nature of graphene on h-saturated SiC(0001). *Applied Physics Letters*, 99(12), 2011.

[169] Kayoung Lee, Seyoung Kim, M. S. Points, T. E. Beechem, Taisuke Ohta, and E. Tutuc. Magnetotransport properties of quasi-free-standing epitaxial graphene bilayer on SiC: Evidence for bernal stacking. *Nano Letters*, 11(9):3624–3628, 2011.

[170] R. W. Carpick, D. F. Ogletree, and M. Salmeron. Lateral stiffness: A new nanomechanical measurement for the determination of shear strengths with friction force microscopy. *Applied Physics Letters*, 70(12):1548–1550, 1997.

[171] E. Riedo, I. Palaci, C. Boragno, and H. Brune. The 2/3 power law dependence of capillary force on normal load in nanoscopic friction. *The Journal of Physical Chemistry B*, 108(17):5324–5328, 2004.

[172] Yalin Dong. Effects of substrate roughness and electron–phonon coupling on thickness-dependent friction of graphene. *Journal of Physics D: Applied Physics*, 47(5):055305, 2014.

[173] G.A. Tomlinson. CVI. a molecular theory of friction. *The London, Edinburgh, and Dublin Philosophical Magazine and Journal of Science*, 7(46):905–939, 1929.

[174] V. Zaloj, M. Urbakh, and J. Klafter. Atomic scale friction: What can be deduced from the response to a harmonic drive? *Physical Review Letters*, 81(6):1227–1230, 1998.

[175] David Andersson and Astrid S. de Wijn. Understanding the friction of atomically thin layered materials. *Nature Communications*, 11(1), 2020.

[176] Robert J. Young, Ian A. Kinloch, Lei Gong, and Kostya S. Novoselov. The mechanics of graphene nanocomposites: A review. *Composites Science and Technology*, 72(12):1459–1476, 2012.

[177] Qiang Cao, Xiao Geng, Huaipeng Wang, Pengjie Wang, Aaron Liu, Yucheng Lan, and Qing Peng. A review of current development of graphene mechanics. *Crystals*, 8(9):357, 2018.

[178] Shaohong Luo, Yarjan Abdul Samad, Vincent Chan, and Kin Liao. Cellular graphene: Fabrication, mechanical properties, and strain-sensing applications. *Matter*, 1(5):1148–1202, 2019.

[179] Costas Galiotis, Otakar Frank, Emmanuel N. Koukaras, and Dimitris Sfyris. Graphene mechanics: Current status and perspectives. *Annual Review of Chemical and Biomolecular Engineering*, 6(1):121–140, 2015.

[180] Changgu Lee, Xiaoding Wei, Jeffrey W. Kysar, and James Hone. Measurement of the elastic properties and intrinsic strength of monolayer graphene. *Science*, 321(5887):385–388, 2008.

[181] U. Ludacka, M. R. A. Monazam, C. Rentenberger, M. Friedrich, U. Stefanelli, J. C. Meyer, and J. Kotakoski. In situ control of graphene ripples and strain in the electron microscope. *npj 2D Materials and Applications*, 2(1), 2018.

[182] I V Gornyi, V Yu Kachorovskii, and A D Mirlin. Anomalous hooke's law in disordered graphene. *2D Materials*, 4(1):011003, 2016.

[183] Ke Cao, Shizhe Feng, Ying Han, Libo Gao, Thuc Hue Ly, Zhiping Xu, and Yang Lu. Elastic straining of free-standing monolayer graphene. *Nature Communications*, 11(1), 2020.

[184] Vesa-Matti Hiltunen, Pekka Koskinen, Kamila K. Mentel, Jyrki Manninen, Pasi Myllyperkiö, Mika Pettersson, and Andreas Johansson. Ultrastiff graphene. *npj 2D Materials and Applications*, 5(1), 2021.

[185] K. S. Novoselov, V. I. Fal'ko, L. Colombo, P. R. Gellert, M. G. Schwab, and K. Kim. A roadmap for graphene. *Nature*, 490(7419):192–200, 2012.

[186] Yuanlong Shao, Maher F. El-Kady, Lisa J. Wang, Qinghong Zhang, Yaogang Li, Hongzhi Wang, Mir F. Mousavi, and Richard B. Kaner. Graphene-based materials for flexible supercapacitors. *Chemical Society Reviews*, 44(11):3639–3665, 2015.

[187] Ahsan Mehmood, N.M. Mubarak, Mohammad Khalid, Rashmi Walvekar, E.C. Abdullah, M.T.H. Siddiqui, Humair Ahmed Baloch, Sabzoi Nizamuddin, and Shaukat Mazari. Graphene based nanomaterials for strain sensor application—a review. *Journal of Environmental Chemical Engineering*, 8(3):103743, 2020.

[188] Robin J. Dolleman, Dejan Davidovikj, Santiago J. Cartamil-Bueno, Herre S. J. van der Zant, and Peter G. Steeneken. Graphene squeeze-film pressure sensors. *Nano Letters*, 16(1):568–571, 2015.

[189] Zhen Yang, Yu Pang, Xiao lin Han, Yifan Yang, Jiang Ling, Muqiang Jian, Yingying Zhang, Yi Yang, and Tian-Ling Ren. Graphene textile strain sensor with negative resistance variation for human motion detection. *ACS Nano*, 12(9):9134–9141, 2018.

[190] Mufeng Liu, Zheling Li, Xin Zhao, Robert J. Young, and Ian A. Kinloch. Fundamental insights into graphene strain sensing. *Nano Letters*, 21(1):833–839, 2020.

[191] Xin Zhao, Boyang Mao, Mufeng Liu, Jianyun Cao, Sarah J. Haigh, Dimitrios G. Papageorgiou, Zheling Li, and Robert J. Young. Controlling and monitoring crack propagation in monolayer graphene single crystals. *Advanced Functional Materials*, 32(42), 2022.

[192] Chuan Liu, Bing Yao, Taige Dong, Haiguang Ma, Shaobo Zhang, Junzhuan Wang, Jun Xu, Yi Shi, Kunji Chen, Libo Gao, and Linwei Yu. Highly stretchable graphene nanoribbon springs by programmable nanowire lithography. *npj 2D Materials and Applications*, 3(1), 2019.

[193] Dmitry Kireev, Shideh Kabiri Ameri, Alena Nederveld, Jameson Kampfe, Hongwoo Jang, Nanshu Lu, and Deji Akinwande. Fabrication, characterization and applications of graphene electronic tattoos. *Nature Protocols*, 16(5):2395–2417, 2021.

[194] Dmitry Kireev, Jameson Kampfe, Alena Hall, and Deji Akinwande. Graphene electronic tattoos 2.0 with enhanced performance, breathability and robustness. *npj 2D Materials and Applications*, 6(1), 2022.

[195] Xuge Fan, Anderson D. Smith, Fredrik Forsberg, Stefan Wagner, Stephan Schröder, Sayedeh Shirin Afyouni Akbari, Andreas C. Fischer, Luis Guillermo Villanueva, Mikael Östling, Max C. Lemme, and Frank Niklaus. Manufacture and characterization of graphene membranes with suspended silicon proof masses for MEMS and NEMS applications. *Microsystems & Nanoengineering*, 6(1), 2020.

[196] F. M. D. Pellegrino, G. G. N. Angilella, and R. Pucci. Strain effect on the optical conductivity of graphene. *Physical Review B*, 81(3), 2010.

[197] Xin He, Li Gao, Ning Tang, Junxi Duan, Fujun Xu, Xinqiang Wang, Xuelin Yang, Weikun Ge, and Bo Shen. Shear strain induced modulation to the transport properties of graphene. *Applied Physics Letters*, 105(8), 2014.

[198] Hang Zhang, Jhao-Wun Huang, Jairo Velasco, Kevin Myhro, Matt Maldonado, David Dung Tran, Zeng Zhao, Fenglin Wang, Yongjin Lee, Gang Liu, Wenzhong Bao, and Chun Ning Lau. Transport in suspended monolayer and bilayer graphene under strain: A new platform for material studies. *Carbon*, 69:336–341, 2014.

[199] Robert Schmidt, Iris Niehues, Robert Schneider, Matthias Drüppel, Thorsten Deilmann, Michael Rohlfing, Steffen Michaelis de Vasconcellos, Andres Castellanos-Gomez, and Rudolf Bratschitsch. Reversible uniaxial strain tuning in atomically thin wse2. *2D Materials*, 3(2):021011, 2016.

[200] Fang Wang, Suhao Li, Mark A Bissett, Ian A Kinloch, Zheling Li, and Robert J Young. Strain engineering in monolayer WS_2 and WS_2 nanocomposites. *2D Materials*, 7(4):045022, 2020.

[201] Shuai Zhang, Yuan Hou, Suzhi Li, Luqi Liu, Zhong Zhang, Xi-Qiao Feng, and Qunyang Li. Tuning friction to a superlubric state via in-plane straining. *Proceedings of the National Academy of Sciences*, 116(49):24452–24456, 2019.

[202] Kunqi Wang, Cangyu Qu, Jin Wang, Wengen Ouyang, Ming Ma, and Quanshui Zheng. Strain engineering modulates graphene interlayer friction by moiré pattern evolution. *ACS Applied Materials & Interfaces*, 11(39):36169–36176, 2019.

[203] Chaochen Xu, Shuai Zhang, Hongzhi Du, Tao Xue, Yilan Kang, Yang Zhang, Pei Zhao, and Qunyang Li. Revisiting frictional characteristics of graphene: Effect of in-plane straining. *ACS Applied Materials & Interfaces*, 14(36):41571–41576, 2022.

[204] Philip Egberts, Gang Hee Han, Xin Z. Liu, A. T. Charlie Johnson, and Robert W. Carpick. Frictional behavior of atomically thin sheets: Hexagonal-shaped graphene islands grown on copper by chemical vapor deposition. *ACS Nano*, 8(5):5010–5021, 2014.

[205] G Paolicelli, M Tripathi, V Corradini, A Candini, and S Valeri. Nanoscale frictional behavior of graphene on SiO_2 and ni(111) substrates. *Nanotechnology*, 26(5):055703, 2015.

[206] Xuanye Wang, Khwanchai Tantiwanichapan, Jason W. Christopher, Roberto Paiella, and Anna K. Swan. Uniaxial strain redistribution in corrugated graphene: Clamping, sliding, friction, and 2d band splitting. *Nano Letters*, 15(9):5969–5975, 2015.

[207] Andrea Mescola, Guido Paolicelli, Sean P. Ogilvie, Roberto Guarino, James G. McHugh, Alberto Rota, Erica Iacob, Enrico Gnecco, Sergio Valeri, Nicola M. Pugno, Venkataramana Gadhamshetty, Muhammad M. Rahman, Pulickel Ajayan, Alan B. Dalton, and Manoj Tripathi. Graphene confers ultralow friction on nanogear cogs. *Small*, 17(47), 2021.

[208] Tawfiqur Rakib, Pascal Pochet, Elif Ertekin, and Harley T. Johnson. Corrugation-driven symmetry breaking in magic-angle twisted bilayer graphene. *Communications Physics*, 5(1):242, 2022.

[209] Ji Eun Lee, Gwanghyun Ahn, Jihye Shim, Young Sik Lee, and Sunmin Ryu. Optical separation of mechanical strain from charge doping in graphene. *Nature Communications*, 3(1), 2012.

[210] A. C. Ferrari, J. C. Meyer, V. Scardaci, C. Casiraghi, M. Lazzeri, F. Mauri, S. Piscanec, D. Jiang, K. S. Novoselov, S. Roth, and A. K. Geim. Raman spectrum of graphene and graphene layers. *Physical Review Letters*, 97(18), 2006.

[211] Krzysztof Gajewski, Stefan Goniszewski, Anna Szumska, Magdalena Moczala, Piotr Kunicki, John Gallop, Norbert Klein, Ling Hao, and Teodor Gotszalk. Raman spectroscopy and kelvin probe force microscopy characteristics of the CVD suspended graphene. *Diamond and Related Materials*, 64:27–33, 2016.

[212] Jiang-Bin Wu, Miao-Ling Lin, Xin Cong, He-Nan Liu, and Ping-Heng Tan. Raman spectroscopy of graphene-based materials and its applications in related devices. *Chemical Society Reviews*, 47(5):1822–1873, 2018.

[213] Stepháne Berciaud, Sunmin Ryu, Louis E. Brus, and Tony F. Heinz. Probing the intrinsic properties of exfoliated graphene: Raman spectroscopy of free-standing monolayers. *Nano Letters*, 9(1):346–352, 2009.

[214] Jakob Zabel, Rahul R. Nair, Anna Ott, Thanasis Georgiou, Andre K. Geim, Kostya S. Novoselov, and Cinzia Casiraghi. Raman spectroscopy of graphene and bilayer under biaxial strain: Bubbles and balloons. *Nano Letters*, 12(2):617–621, 2012.

[215] John E. Sader, James W. M. Chon, and Paul Mulvaney. Calibration of rectangular atomic force microscope cantilevers. *Review of Scientific Instruments*, 70(10):3967–3969, 1999.

[216] Christopher P. Green, Hadi Lioe, Jason P. Cleveland, Roger Proksch, Paul Mulvaney, and John E. Sader. Normal and torsional spring constants of atomic force microscope cantilevers. *Review of Scientific Instruments*, 75(6):1988–1996, 2004.

[217] Manoj Tripathi, Firas Awaja, Rafael A. Bizao, Stefano Signetti, Erica Iacob, Guido Paolicelli, Sergio Valeri, Alan Dalton, and Nicola Maria Pugno. Friction and adhesion of different structural defects of graphene. *ACS Applied Materials & Interfaces*, 10(51):44614–44623, 2018.

[218] Aitor Zambudio, Enrico Gnecco, Jaime Colchero, Rubén Pérez, Julio Gómez-Herrero, and Cristina Gómez-Navarro. Fine defect engineering of graphene friction. *Carbon*, 182:735–741, 2021.

[219] Zhao Deng, Nikolai N. Klimov, Santiago D. Solares, Teng Li, Hua Xu, and Rachel J. Cannara. Nanoscale interfacial friction and adhesion on supported versus suspended monolayer and multilayer graphene. *Langmuir*, 29(1):235–243, 2012.

[220] Udo D. Schwarz, Oliver Zwörner, Peter Köster, and Roland Wiesendanger. Quantitative analysis of the frictional properties of solid materials at low loads. i. carbon compounds. *Physical Review B*, 56(11):6987–6996, 1997.

[221] N. Manini, G. Mistura, G. Paolicelli, E. Tosatti, and A. Vanossi. Current trends in the physics of nanoscale friction. *Advances in Physics: X*, 2(3):569–590, 2017.

[222] Chaochen Xu, Zhijiang Ye, and Philip Egberts. Friction hysteretic behavior of supported atomically thin nanofilms. *npj 2D Materials and Applications*, 7(1), 2023.

[223] Andrea Vanossi, Nicola Manini, Michael Urbakh, Stefano Zapperi, and Erio Tosatti. Colloquium: Modeling friction: From nanoscale to mesoscale. *Reviews of Modern Physics*, 85(2):529–552, 2013.

[224] Martin H. Müser, Michael Urbakh, and Mark O. Robbins. Statistical mechanics of static and low-velocity kinetic friction. *Advances in Chemical Physics*, pages 187–272, 2003.

[225] A Vanossi and O M Braun. Driven dynamics of simplified tribological models. *Journal of Physics: Condensed Matter*, 19(30):305017, 2007.

[226] Donald W Brenner, Olga A Shenderova, Judith A Harrison, Steven J Stuart, Boris Ni, and Susan B Sinnott. A second-generation reactive empirical bond order (REBO) potential energy expression for hydrocarbons. *Journal of Physics: Condensed Matter*, 14(4):783–802, 2002.

[227] Maarten de Jong, Wei Chen, Thomas Angsten, Anubhav Jain, Randy Notestine, Anthony Gamst, Marcel Sluiter, Chaitanya Krishna Ande, Sybrand van der Zwaag, Jose J Plata, Cormac Toher, Stefano Curtarolo, Gerbrand Ceder, Kristin A. Persson, and Mark Asta. Charting the complete elastic properties of inorganic crystalline compounds. *Scientific Data*, 2(1), 2015.

[228] Anubhav Jain, Shyue Ping Ong, Geoffroy Hautier, Wei Chen, William Davidson Richards, Stephen Dacek, Shreyas Cholia, Dan Gunter, David Skinner, Gerbrand Ceder, and Kristin A. Persson. Commentary: The materials project: A materials genome approach to accelerating materials innovation. *APL Materials*, 1(1), 2013.

[229] Yifei Mo, Kevin T. Turner, and Izabela Szlufarska. Friction laws at the nanoscale. *Nature*, 457(7233):1116–1119, 2009.

[230] Clara M. Almeida, Rodrigo Prioli, Benjamin Fragneaud, Luiz Gustavo Cançado, Ricardo Paupitz, Douglas S. Galvão, Marcelo De Cicco, Marcos G. Menezes, Carlos A. Achete, and Rodrigo B. Capaz. Giant and tunable anisotropy of nanoscale friction in graphene. *Scientific Reports*, 6(1), 2016.

[231] A. K. Geim and I. V. Grigorieva. Van der waals heterostructures. *Nature*, 499(7459):419–425, 2013.

[232] K. S. Novoselov, A. Mishchenko, A. Carvalho, and A. H. Castro Neto. 2d materials and van der waals heterostructures. *Science*, 353(6298):aac9439, 2016.

[233] Matthew Yankowitz, Qiong Ma, Pablo Jarillo-Herrero, and Brian J. LeRoy. van der waals heterostructures combining graphene and hexagonal boron nitride. *Nature Reviews Physics*, 1(2):112–125, 2019.

[234] Yuan Liu, Nathan O. Weiss, Xidong Duan, Hung-Chieh Cheng, Yu Huang, and Xiangfeng Duan. Van der waals heterostructures and devices. *Nature Reviews Materials*, 1(9):16042, 2016.

[235] Rafi Bistritzer and Allan H. MacDonald. Moire bands in twisted double-layer graphene. *Proceedings of the National Academy of Sciences of the United States of America*, 108(30):12233–12237, 2011.

[236] Benjamin Butz, Christian Dolle, Florian Niekiel, Konstantin Weber, Daniel Waldmann, Heiko B. Weber, Bernd Meyer, and Erdmann Spiecker. Dislocations in bilayer graphene. *Nature*, 505(7484):533–537, 2014.

[237] Y. Ying, Z. Z. Zhang, J. Moser, Z. J. Su, X. X. Song, and G. P. Guo. Sliding nanomechanical resonators. *Nature Communications*, 13(1):6392, 2022.

[238] Shuyang Dai, Yang Xiang, and David J. Srolovitz. Twisted bilayer graphene: Moiré with a twist. *Nano Letters*, 16(9):5923–5927, 2016.

[239] Michael Lamparski, Benoit Van Troeye, and Vincent Meunier. Soliton signature in the phonon spectrum of twisted bilayer graphene. *2D Materials*, 7(2):025050, 2020.

[240] Lev Davidovich Landau, Evgenii Mikhailovich Lifshitz, Arnold Markovich Kosevich, and Lev Petrovich Pitaevskii. *Theory of elasticity*, volume 7. Elsevier, 1986.

[241] Qiang Lu, Marino Arroyo, and Rui Huang. Elastic bending modulus of monolayer graphene. *Journal of Physics D: Applied Physics*, 42(10):102002, 2009.

[242] Edmund Han, Jaehyung Yu, Emil Annevelink, Jangyup Son, Dongyun A. Kang, Kenji Watanabe, Takashi Taniguchi, Elif Ertekin, Pinshane Y. Huang, and Arend M. van der Zande. Ultrasoft slip-mediated bending in few-layer graphene. *Nature Materials*, 19(3):305–309, 2020.

[243] Jaehyung Yu, Edmund Han, M. Abir Hossain, Kenji Watanabe, Takashi Taniguchi, Elif Ertekin, Arend M. van der Zande, and Pinshane Y. Huang. Designing the bending stiffness of 2d material heterostructures. *Advanced Materials*, 33(9):2007269, 2021.

[244] Jae-Ung Lee, Duhee Yoon, and Hyeonsik Cheong. Estimation of young's modulus of graphene by raman spectroscopy. *Nano Letters*, 12(9):4444–4448, 2012.

[245] Guorui Wang, Zhaohe Dai, Junkai Xiao, ShiZhe Feng, Chuanxin Weng, Luqi Liu, Zhiping Xu, Rui Huang, and Zhong Zhang. Bending of multilayer van der waals materials. *Physical Review Letters*, 123:116101, 2019.

[246] F. Y. Wu. The potts model. *Reviews of Modern Physics*, 54:235–268, 1982.

[247] DR Nelson and L Peliti. Fluctuations in membranes with crystalline and hexatic order. *Journal de physique*, 48(7):1085–1092, 1987.

[248] J. C. Slater and G. F. Koster. Simplified lcao method for the periodic potential problem. *Physical Review*, 94:1498–1524, 1954.

[249] M. Angeli, E. Tosatti, and M. Fabrizio. Valley jahn-teller effect in twisted bilayer graphene. *Physical Review X*, 9:041010, 2019.

[250] Zhida Song, Zhijun Wang, Wujun Shi, Gang Li, Chen Fang, and B. Andrei Bernevig. All magic angles in twisted bilayer graphene are topological. *Physical Review Letters*, 123:036401, 2019.

[251] M.I. Aroyo, J.M. Perez-Mato, D. Orobengoa, E. Tasci, G. De La Flor, and A. Kirov. Crystallography online: Bilbao crystallographic server. *Bulgarian Chemical Communications*, 43(2):183 – 197, 2011. Cited by: 418.

[252] Mois Ilia Aroyo, Juan Manuel Perez-Mato, Cesar Capillas, Eli Kroumova, Svetoslav Ivantchev, Gotzon Madariaga, Asen Kirov, and Hans Wondratschek. Bilbao crystallographic server: I. databases and crystallographic computing programs. *Zeitschrift für Kristallographie - Crystalline Materials*, 221(1):15–27, 2006.

[253] Mois I. Aroyo, Asen Kirov, Cesar Capillas, J. M. Perez-Mato, and Hans Wondratschek. Bilbao Crystallographic Server. II. Representations of crystallographic point groups and space groups. *Acta Crystallographica Section A*, 62(2):115–128, 2006.

[254] Andrea Blason and Michele Fabrizio. Local kekulé distortion turns twisted bilayer graphene into topological mott insulators and superconductors. *Physical Review B*, 106:235112, 2022.

[255] G. Trambly de Laissardière, D. Mayou, and L. Magaud. Localization of dirac electrons in rotated graphene bilayers. *Nano Letters*, 10(3):804–808, 2010.

[256] Aleksey N. Kolmogorov and Vincent H. Crespi. Registry-dependent interlayer potential for graphitic systems. *Physical Review B*, 71:235415, 2005.

[257] Wengen Ouyang, Davide Mandelli, Michael Urbakh, and Oded Hod. Nanoserpents: Graphene nanoribbon motion on two-dimensional hexagonal materials. *Nano Letters*, 18(9):6009–6016, 2018.

[258] Aidan P. Thompson, H. Metin Aktulga, Richard Berger, Dan S. Bolintineanu, W. Michael Brown, Paul S. Crozier, Pieter J. in 't Veld, Axel Kohlmeyer, Stan G. Moore, Trung Dac Nguyen, Ray Shan, Mark J. Stevens, Julien Tranchida, Christian Trott, and Steven J. Plimpton. Lammps - a flexible simulation tool for particle-based materials modeling at the atomic, meso, and continuum scales. *Computer Physics Communications*, 271:108171, 2022.

[259] Erik Bitzek, Pekka Koskinen, Franz Gähler, Michael Moseler, and Peter Gumbsch. Structural relaxation made simple. *Physical Review Letters*, 97:170201, 2006.

[260] Glenn J. Martyna, Douglas J. Tobias, and Michael L. Klein. Constant pressure molecular dynamics algorithms. *The Journal of Chemical Physics*, 101(5):4177–4189, 1994.

[261] A. Fasolino, J. H. Los, and M. I. Katsnelson. Intrinsic ripples in graphene. *Nature Materials*, 6(11):858–861, 2007.

[262] John A. Thomas, Joseph E. Turney, Ryan M. Iutzi, Cristina H. Amon, and Alan J. H. McGaughey. Predicting phonon dispersion relations and lifetimes from the spectral energy density. *Physical Review B*, 81:081411, 2010.

[263] Linus Pauling. The structure and entropy of ice and of other crystals with some randomness of atomic arrangement. *Journal of the American ChemicalSociety*, 57(12):2680–2684, 1935.

[264] Jiří Kolafa. Residual entropy of ices and clathrates from monte carlo simulation. *Journal of Chemical Physics*, 140(20), 2014.

[265] Laurens Vanderstraeten, Bram Vanhecke, and Frank Verstraete. Residual entropies for three-dimensional frustrated spin systems with tensor networks. *Physical Review E*, 98:042145, 2018.

[266] Takuya Hayashi, Chizuru Muguruma, and Yuko Okamoto. Calculation of the residual entropy of ice ih by monte carlo simulation with the combination of the replica-exchange wang–landau algorithm and multicanonical replica-exchange method. *The Journal of Chemical Physics*, 154(4):044503, 2021.

[267] E. A. DiMarzio and F. H. Stillinger. Residual entropy of ice. *The Journal of Chemical Physics*, 40(6):1577–1581, 1964.

[268] J. F. Nagle. Lattice statistics of hydrogen bonded crystals. i. the residual entropy of ice. *Journal of Mathematical Physics*, 7(8):1484–1491, 1966.

[269] Jer-Lai Kuo, James V. Coe, Sherwin J. Singer, Yehuda B. Band, and Lars Ojamäe. On the use of graph invariants for efficiently generating hydrogen bond topologies and predicting physical properties of water clusters and ice. *The Journal of Chemical Physics*, 114(6):2527–2540, 2001.

[270] M. V. Kirov. Antisymmetry and stability of aqueous systems. iii. conformations of the hexagonal rings. *Journal of Structural Chemistry*, 49(6):650–655, 2008.

[271] Ali Hassanali, Federico Giberti, Jérôme Cuny, Thomas D. Kühne, and Michele Parrinello. Proton transfer through the water gossamer. *Proceedings of the National Academy of Sciences*, 110(34):13723–13728, 2013. Note that our definition of order parameter S differs from that in this work, and follows instead that of Ref [11].

[272] Tomas K. Hirsch and Lars Ojamäe. Quantum-chemical and force-field investigations of ice ih: Computation of proton-ordered structures and prediction of their lattice energies. *The Journal of Physical Chemistry B*, 108(40):15856–15864, 2004.

[273] Hiroshi Fukazawa, Susumu Ikeda, Mitsugu Oguro, Taku Fukumura, and Shinji Mae. Deuteron ordering in kod-doped ice observed by neutron diffraction. *The Journal of Physical Chemistry B*, 106(23):6021–6024, 2002.

[274] Lukasz Cwiklik, J. P. Devlin, and Victoria Buch. Hydroxide impurity in ice. *The Journal of Physical Chemistry A*, 113(26):7482–7490, 2009. PMID: 19368398.

[275] Rahul Dandekar and Ali A. Hassanali. Hierarchical lattice models of hydrogen-bond networks in water. *Physical Review E*, 97:062113, 2018.

[276] C. Knight and S. J. Singer. Theoretical study of a hydroxide ion within the ice-ih lattice. In Werner Kuhs, editor, *Physics and Chemistry of Ice*, pages 339–346. The Royal Society of Chemistry, 2007.

[277] Pablo M. Piaggi and Roberto Car. Enhancing the formation of ionic defects to study the ice ih/xi transition with molecular dynamics simulations. *Molecular Physics*, page e1916634, 2021.

List of publications

- Ring population statistics in an ice lattice model.
  Ali Khosravi, Jorge Lasave, Sergio Koval, and Erio Tosatti
  Journal of Chemical Physics 155, 224502 (December 2021)

- Understanding the rheology of nanocontacts.
  Ali Khosravi, Antoine Lainé, Andrea Vanossi, Jin Wang, Alessandro Siria, and Erio Tosatti
  Nature Communications 13, 2428 (May 2022)

- Relation between interfacial shear and friction force in 2D materials.
  Martin Rejhon, Francesco Lavini, Ali Khosravi, Mykhailo Shestopalov, Jan Kunc, Erio Tosatti, and Elisa Riedo
  Nature Nanotechnology 17, 1280–1287 (December 2022)

- Anisotropic rheology and friction of suspended graphene.
  Andrea Mescola, Andrea Silva, Ali Khosravi, Andrea Vanossi, Erio Tosatti, Sergio Valeri, and Guido Paolicelli
  Physical Review Materials 7, 054007 (May 2023)

- Bending stiffness collapse, buckling, topological bands of freestanding twisted bilayer graphene.
  Jin Wang, Ali Khosravi, Andrea Silva, Michele Fabrizio, Andrea Vanossi, and Erio Tosatti
  Physical Review B 108, L081407 (August 2023)

- Sliding and Pinning in Structurally Lubric 2D Material Interfaces.
  Jin Wang; Ali Khosravi; Andrea Vanossi; Erio Tosatti
  Reviews of Modern Physics, accepted, (September 2023)